Applications of Raman Microspectroscopy to the Study of Atmospheric Aerosol Particles

by

Rebecca L. Craig

A dissertation submitted in partial fulfillment
of the requirements for the degree of
Doctor of Philosophy
(Chemistry)
in the University of Michigan
2018

Doctoral Committee:

Assistant Professor Andrew P. Ault, Chair
Associate Professor Julie S. Biteen
Professor Zhan Chen
Assistant Professor Eric A. Kort

Rebecca L. Craig

craigre@umich.edu

ORCID iD: 0000-0002-4917-3223

Dedication

For my parents, in gratitude for their endless support and encouragement.

Acknowledgements

First, my advisor – Dr. Andrew Ault, and my committee members – Dr. Julie Biteen, Dr. Zhan Chen, and Dr. Eric Kort. Thank you to Andy for taking a chance on a Pittsburgh Steelers fan and pushing me to figure out my research, even when it led to ridiculous experimental set ups, like a cardboard box humidity chamber. Over the past four and a half years, I have learned how to think critically and creatively and without your mentorship, my graduate school success would not have been possible. Thank you to my committee for your advice, feedback, and support as I progressed through this program.

To Dotie Sipowska, thank you for teaching me how to be a better teacher over eight semesters of CHEM 130, supporting my future faculty GSI projects, all of the coffee dates, and most importantly, being an incredible role model as strong woman in science. To Karl Feierabend, my undergraduate advisor, thank you for your continued support and mentorship, even years after I have left Wooster.

To the members of the Ault and Pratt labs, who were not just great labmates, but even better friends, I am truly grateful. We've been through it all, from taco tours and extremely unsuccessful flag football teams to prepping trailers and thousands of substrates, and I could not have picked a better group of people to go through grad school with. Amy, who has been there since the beginning when our lab was a closet, thank you for doing all the microscopy work so I could avoid EMAL and for showing me how to get the best birthday deals. Matt, thanks for helping me replace pumps and fix the DMA. It was an honor to represent the Vatican City with you. To Nate, thank you for the Taylor Swift karaoke, epic meal times, and always being willing

to share a pitcher of beer when I needed it the most. Rachel, the Louise to my Thelma, thanks for all the Chela's and chocolate cake, the Pat Benatar soundtracked trips to Lowe's for garden supplies, and our yearly unsuccessful attempts to eat all the root veggies from the CSA. My postdocs, Jess and Peter, thank you for teaching me how to be a better scientist, but more importantly, for the Sporcle breaks, instituting happy hour, and for making MatLab so easy that even I could use it. Stephen, Ryan, and Garrett, thank you for the road trips, coffee breaks, and lengthy discussions of football, both real and fantasy. Nicole and Nancy, thank you for keeping me young, enabling my bubble tea addiction, and making me laugh this past year. My high school and undergraduate students, Darrell, Peter, Stephanie, Nick, and Mohammed, thank you for impressive work and contributions to several papers, and also for inspiring me with your enthusiasm and excitement to learn. In addition to the lab, I have to acknowledge my friends in the department – Kortney, BJ, Nathan, Molly, Jieming, Alex, Kevin. I hope you all know how much I have valued our friendship over the years.

To Brad, thank you for all the adventures, dinners, and bad puns that kept me laughing over the years, but more importantly, thank you for your understanding, kindness, and patience. Thank you to the Van Fleets, for welcoming me and including me in your family, even though I've been two states away this whole time. And finally, but most importantly, my family. My parents, my brother, and my grandma, have been a never-ending source of encouragement and support. They believed in me even when I did not believe in myself. Without them, I would not have been able to make it where I am today.

Table of Contents

List of Figures

List of Tables

List of Equations

List of Appendices

Abstract

Atmospheric aerosol particles impact climate by scattering or absorbing solar radiation and acting as cloud condensation and ice nuclei, but there is high uncertainty regarding the magnitude of these climate effects. The physicochemical properties of aerosol particles dictate their climate impacts, yet are challenging to accurately and quantitatively measure, as aerosols are highly complex in terms of chemical composition, size, phase, and morphology (i.e. mixing state). Methods enabling more detailed and quantitative investigations of aerosol particle properties are necessary in order to improve mechanistic understanding of multiphase aerosol processes occurring in the atmosphere. In this dissertation, novel Raman microspectroscopic techniques for improved analysis of the chemical composition of both laboratory-generated and ambient aerosol particles were developed to further understanding of aerosol mixing state, which will enable better predictions of the climate impacts associated with aerosols.

Computer-controlled Raman mapping (CC-Raman) and surface enhanced Raman microspectroscoy (SERS) were applied to the study of aerosol particles to improve characterization of chemical composition. CC-Raman used automated mapping to increase throughput and particle statistics by analyzing up to 100 particles per hour, in comparison to much slower manual characterization. CC-Raman analysis provides detailed information regarding functional groups present, size, morphology, and the mixing of secondary chemical species with primary components. SERS enables detection of trace organic and/or inorganic species present within particles, observation of complex inter- and intraparticle variability, and characterization of smaller, more atmospherically-relevant sized aerosol particles with diameters smaller than the diffraction limit (as small as 150 nm). In comparison to traditional vibrational spectroscopy techniques, these advances greatly increase the potential for characterization of aerosol particle physicochemical properties with Raman analysis.

A Raman microspectroscopic method for measuring single particle pH was developed. Aerosol pH plays an important role in many multiphase processes, such as secondary organic aerosol (SOA) formation, but is difficult to measure due to the minute volumes of aerosol

particles and the non-conservative nature of the hydronium ion. Traditional indirect measurement methods and predictions of aerosol pH via thermodynamic modeling often disagree and are associated with limitations regarding measurement inputs and equilibrium assumptions. In contrast, this method coupling Raman microspectroscopy with extended Debye-Hückel activity calculations allows for direct determination of acidity of individual particles based on measurements of acid and conjugate base vibrational modes. Several atmospherically relevant inorganic and organic acid-base equilibria systems are compatible with this method, including HNO_3/NO_3^-, HSO_4^-/SO_4^{2-}, $HC_2O_4^-/C_2O_4^{2-}$/ CH_3COOH/CH_3COO^-/ and HCO_3^-/CO_3^{2-}, covering a broad pH range (-1 to 10). A second complementary method for direct measurement of size-resolved bulk aerosol pH using quantitative colorimetric image processing of aerosol particles collected on pH indicator paper was also developed. In addition to aerosol pH measurements, these methods were used to investigate the effect of RH on particle acidity, gas-particle partitioning of acidic chemical species, the relationship between ionic strength and H^+ activity coefficients, and other aspects of ion behavior under non-ideal conditions. Direct measurement of aerosol pH through these methods will improve fundamental mechanistic understanding of critical pH-dependent aerosol processes.

The methods developed in this dissertation and their application to the study of atmospheric aerosol particles will yield more detailed measurements of particle physicochemical properties, providing new insights into the mechanisms of multiphase atmospheric processes and improving understanding of the impact of aerosols on climate.

Chapter 1. Introduction

1.1 Characteristics of Atmospheric Aerosol Particles

A solid or liquid particle suspended in a gas, such as the atmosphere, is defined as an aerosol. Atmospheric aerosol particles affect climate directly by scattering and absorbing solar radiation and indirectly by acting as cloud condensation and ice nuclei (CCN and IN) (Ramanathan et al., 2001; Pöschl, 2005; Andreae and Rosenfeld, 2008; Myhre et al., 2013). As shown in Figure 1.1, according to the International Panel on Climate Change (IPCC), both direct and indirect aerosol contributions to radiative forcing are still associated with high uncertainty, in comparison to other contributors, such as greenhouse gases (Myhre et al., 2013). In addition to climate effects, aerosols also negatively impact human health, as exposure to atmospheric particulate matter can lead to serious health issues, such as respiratory and cardiovascular disease, and is responsible for 10% of annual deaths globally (Pöschl, 2005; Pope and Dockery, 2006; Kim et al., 2015). Despite the importance of aerosols, mechanistic understanding of many key atmospheric processes remains low, in part due to challenges associated with measuring their physicochemical properties.

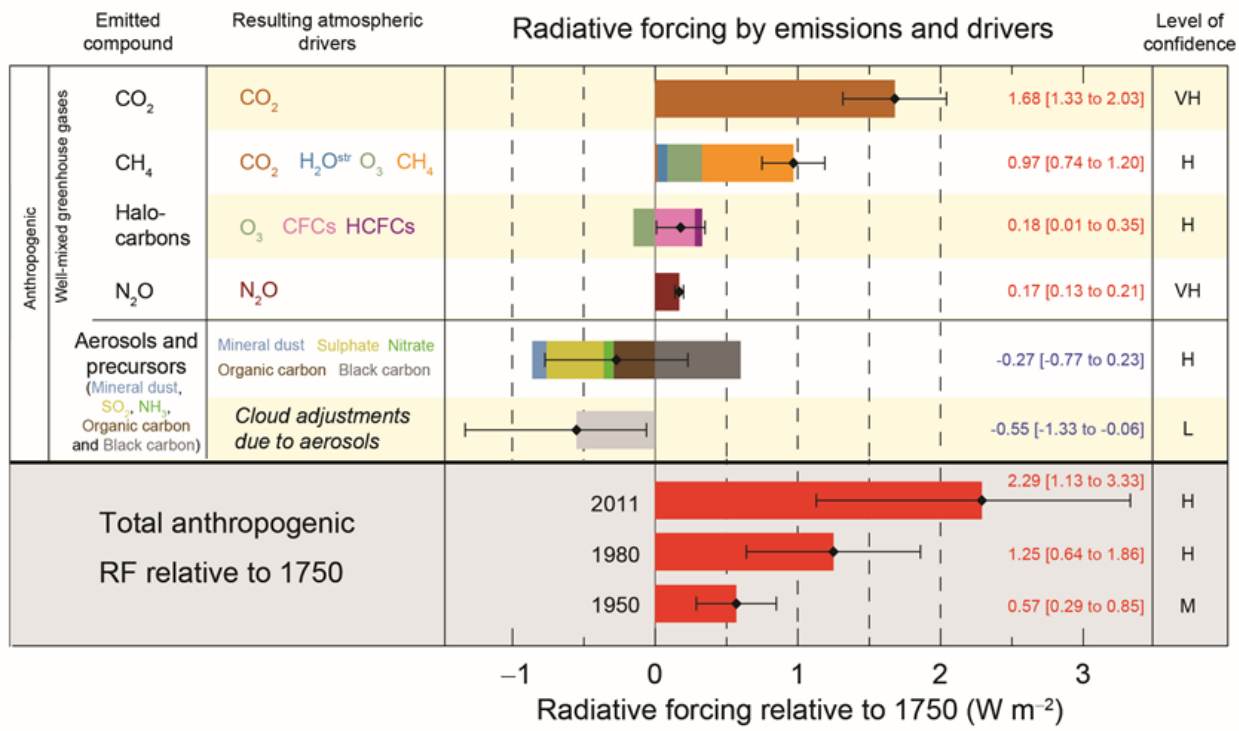

Figure 1.1 Radiative forcing estimates and uncertainties for greenhouse gases and aerosols. Adapted from Myhre et al. (2013).

Atmospheric aerosols have an array of sources, both natural and anthropogenic, ranging from sea spray aerosol and dust to emissions from fossil fuel combustion (Pöschl, 2005; Andreae and Rosenfeld, 2008). Primary aerosols are emitted directly into the atmosphere, while secondary aerosols are formed from the condensation of gaseous precursors (Pöschl, 2005; Andreae and Rosenfeld, 2008). One common type of secondary aerosol, secondary organic aerosol (SOA), is formed from the condensation of low volatility gaseous oxidation products of volatile organic compounds (VOCs) onto existing particles, usually composed of inorganic salts, such as $(NH_4)_2SO_4$ (Hallquist et al., 2009; Ziemann and Atkinson, 2012; McNeill, 2015). Figure 1.2 provides an illustration of aerosol sources and atmospheric processes that lead to climate effects. In addition to secondary aerosol formation, aerosol particles can undergo modifications during multiphase chemical and physical processing, such as hydrolysis reactions or phase changes, depending on atmospheric conditions (Pöschl, 2005; McNeill, 2015).

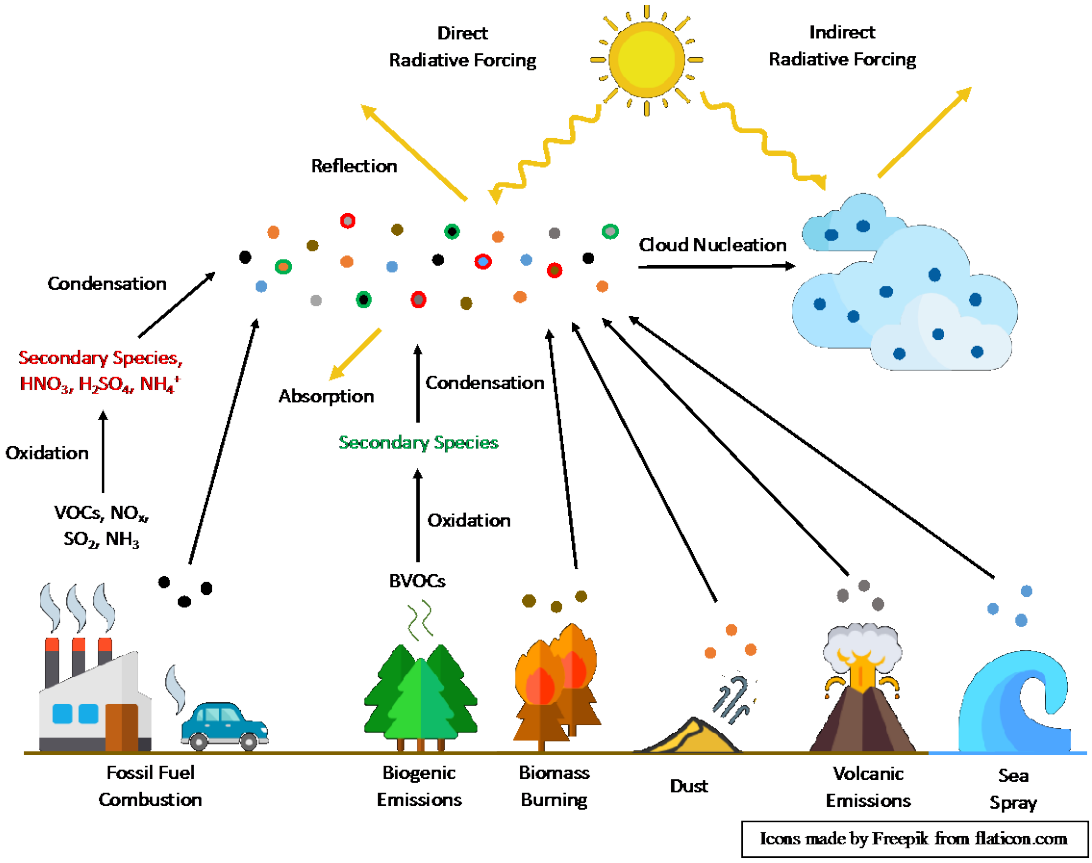

Figure 1.2 Illustration of anthropogenic and natural sources of aerosol particles, as well as atmospheric processing, and how aerosols impact climate through radiative forcing. Icons for schematic made by Freepik from flaticon.com.

The many sources of aerosols and subsequent atmospheric processing of aerosols leads to a wide range of sizes, structures, phase states, and chemical compositions. Atmospheric aerosol particles range in size from 1 nm – 100 μm, with the mode for particle number concentration centered at ~100 nm and particle mass concentration ranging from ~500 nm and ~6 μm (Hinds, 1999; Seinfeld and Pandis, 2016). Aerosol particles have a range of possible morphologies, from nearly spherical, like SOA, to chain agglomerates, like soot (Hinds, 1999; Zhang et al., 2008; Kwamena et al., 2010). Additionally, differing viscosities within particles lead to a variety of phase states, including liquid, aqueous, glassy (or semi-solid), and solid, such as crystalline salts (Buajarern et al., 2007; Virtanen et al., 2010; Seinfeld and Pandis, 2016). As a result of particle phase state and physical processes like efflorescence and deliquescence, a range of aerosol particle structures have also been observed, such liquid-liquid phase separated (LLPS), which

includes structures like core-shell and semi-engulfed (Kwamena et al., 2010; You et al., 2012, 2013). Many of the physical properties of aerosol particles, like viscosity and phase, are dependent on chemical composition. As mentioned previously, the wide range of sources and atmospheric processing leads to complex compositions, with aerosol particles often containing hundreds to thousands of different chemical species, both inorganic and organic (Prather et al., 2008). Aerosol mixing state refers to inter- and intraparticle variability in terms of both chemical composition and structure and can be challenging to measure and quantify (Riemer and West, 2013; O'Brien et al., 2015a; Fierce et al., 2016; Ault and Axson, 2017). Aerosol acidity is also interconnected with chemical composition, as the chemical species present influence particle pH, upon which many atmospheric processes that impact chemical mixing state are dependent (Gao et al., 2004; Surratt et al., 2007b; Gaston et al., 2014; Ghorai et al., 2014; Losey et al., 2016). Herein, aerosol mixing state and aerosol acidity, their atmospheric implications, and traditional measurement methods are discussed in greater detail.

1.2 Aerosol Mixing State

1.2.1 Definition of Aerosol Mixing State

Aerosol mixing state refers to the distribution of chemical species within an aerosol population. For chemical composition, mixing state can be described in terms of external and internal mixtures. External mixtures consist of particles that each contain only one chemical species (but may be different species for different particles), while internal mixtures consist of particles that each contain different species present within one particle (Riemer and West, 2013). If all particles in an internal mixture consist of the same chemical species present at the same relative abundance, it is considered to be fully internally mixed (Riemer and West, 2013). However, internal and external mixtures are idealized cases, and neither are representative of most ambient aerosol. Mixing state index is the first quantitative measure of chemical mixing state and can be used to characterize aerosol particles on the spectrum between fully internal and fully external mixtures (Riemer and West, 2013; O'Brien et al., 2015a). In addition to chemical mixing state, aerosol particles can vary in terms of physical properties, such as phase, internal structure, and viscosity. Physicochemical mixing state is an all-encompassing term that refers to the distribution of both chemical and physical features within an aerosol population (Ault and Axson, 2017). Figure 1.3, from a recent review by Ault and Axson, illustrates the different

chemical and physical aspects that can be incorporated into aerosol mixing state (Ault and Axson, 2017).

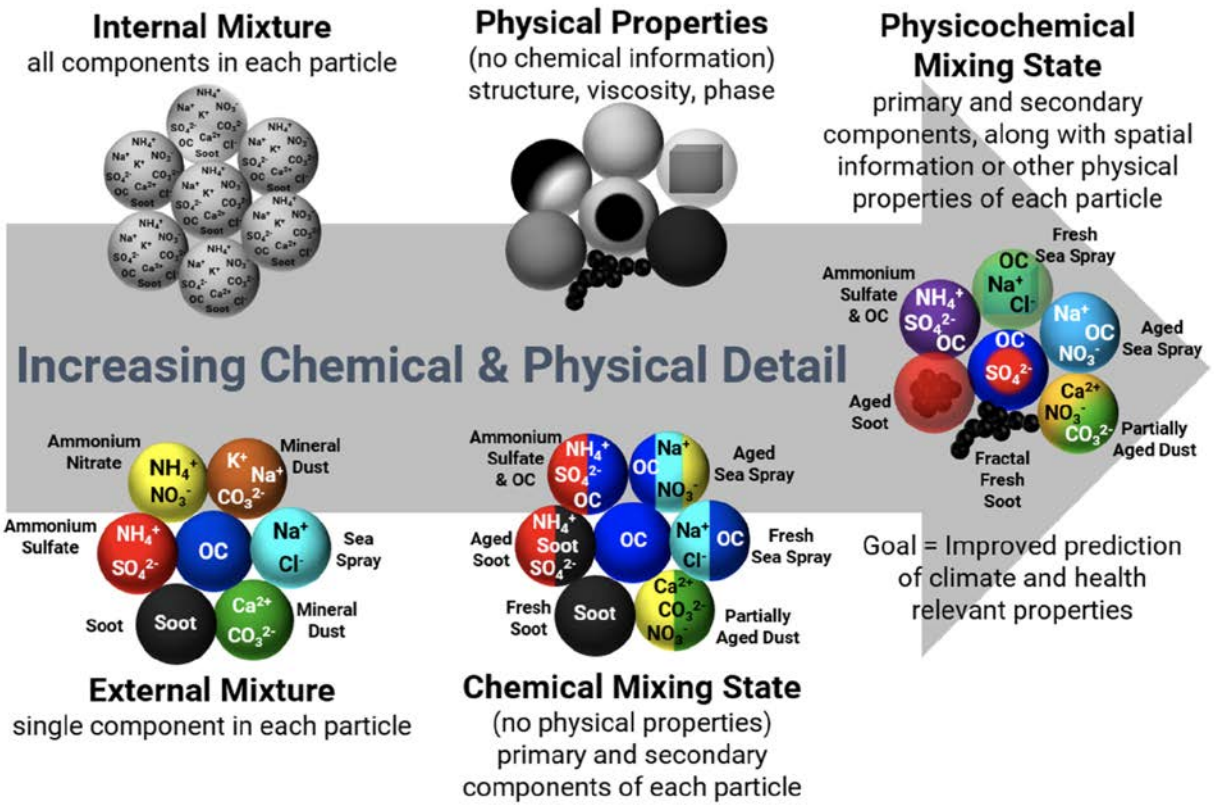

Figure 1.3 Representations of particle composition with increasing complexity and detail. Chemical mixing state provides information on primary versus secondary components, but does not provide spatial information or other physical properties. Physicochemical mixing state provides both chemical detail and spatial information or physical properties. Note that the locations of the colors in the chemical mixing state particles are not meant to convey spatial distribution, only the presence of both primary and secondary components. Reproduced from Ault and Axson (2017).

1.2.2 Mixing State Measurement Techniques

Different aspects of aerosol mixing state have been measured by many different analytical techniques, even before the term “mixing state” was defined and used widely. These include both direct and indirect measurements of chemical composition, morphology, and other properties, such as hygroscopicity and light scattering or absorption. Herein, some of these

techniques, often used in combination, and notable advances in aerosol particle characterization related to mixing state are discussed.

One of the earliest aerosol measurements related to mixing state was reported in 1974 by Bigg et al., who used electron microscopy and a thin film vapor method of chemical testing to detect a range of compounds, such as sulfuric acid, sulfates, nitrates, halides, and persulfates, in ambient particles (Bigg et al., 1974). Further developing electron microscopy applications to study aerosol particles, in 1983, computer-controlled scanning electron microscopy (CCSEM) coupled with energy dispersive X-ray spectroscopy (EDX) was used for quantitative size and elemental composition characterization of a statistically-relevant number of particles, allowing for source apportionment based on differing chemical compositions (Casuccio et al., 1983). Through research using both transmission electron microscopy (TEM) and a nephelometer, Okada was able to observe two distinct particle types present within an aerosol population - both containing sulfate, but with differing size distributions and hygroscopicity (Okada, 1985). Electron microscopy was applied with increasing frequency to the study of aerosol particles from the 1990s and on, characterizing the constituents of specific types of aerosol, such as marine, mineral, and biomass (Pósfai et al., 1994, 2003; Buseck and Pósfai, 1999; Li et al., 2003). In 1999, atomic force microscopy (AFM), was used to classify aerosol particles as organic, graphitic, or inorganic, as well as obtain size distributions (Lehmpuhl et al., 1999). Microscopy studies of aerosol particles have since advanced greatly, allowing for the study of internal mixing (Pósfai et al., 1999; Deboudt et al., 2010), phase transitions (Wise et al., 2005), hygroscopic behavior (Semeniuk et al., 2007), phase separation (You et al., 2012),and other important aerosol physicochemical properties that impact mixing state.

Mass spectrometry (MS) has been used since the 1980s to characterize aerosol particles. One of the earliest studies in 1985 is laser microprobe mass analysis (LAMMA) to identity distinct sulfate and nitrate layers within marine aerosol particles (Bruynseels and Van Grieken, 1985). Connecting more directly with aerosol chemical mixing state, in 1997, Murphy and Thomson observed no ambient particle classes characterized as fully externally or fully internally mixed through MS analysis (Murphy and Thomson, 1997). Over the past several decades, many unique mass spectrometers, such as the aerosol mass spectrometer (AMS), particle analysis by laser mass spectrometer (PALMS), single particle laser ablation time-of-flight mass spectrometer (SPLAT), and aerosol time-of-flight mass spectrometer (ATOFMS), have been developed and

used for bulk and single particle aerosol classification, with numerous studies providing chemical mixing state information for aerosol populations all over the world (Noble and Prather, 2000; Pratt and Prather, 2012a, 2012b). Because of its ability for real-time online characterization, MS has also been applied to study mixing state evolution during changing environmental conditions and atmospheric processing, including heterogeneous reactions and nucleation events (Gard et al., 1998; Song et al., 1999; Hughes et al., 2000; Zhang et al., 2005; Broekhuizen et al., 2006; Shiraiwa et al., 2007; Wang et al., 2010a; Baustian et al., 2012; Cappa et al., 2012).

Spectroscopy techniques were first applied to the study of aerosol mixing state in 2002, when Maria et al. used Fourier transform infrared spectroscopy (FTIR) to characterize functional groups and organic mass in aerosol samples (Maria et al., 2002). Since then, FTIR and other spectroscopic techniques, including Raman microspectroscopy, X-ray photoelectron spectroscopy (XPS), and scanning transmission X-ray microscopy with near edge X-ray absorption fine structure spectroscopy (STXM-NEXAFS), have be used to map organic coatings of aerosol particles (Russell et al., 2002), characterize internally and externally mixed particle types through composition and structure (Deboudt et al., 2010; Moffet et al., 2010a; Song et al., 2010; Baustian et al., 2012), and analyze variation in particle surface chemical composition (Song and Peng, 2009). Optical trapping and tweezing spectroscopy techniques have also been used to characterize mixing state of single aerosol droplets during dynamic multiphase processes, such as coagulation and uptake of water or organics (Hopkins et al., 2004; Mitchem et al., 2006).

In addition to the methods for direct measurement, many techniques that probe various physicochemical properties of aerosol particles have been used to infer information about mixing state. These indirect methods include particle sizing instrumentation, mass analyzers, ion chromatography (IC), nephelometers, absorption photometers, and cloud condensation nuclei (CCN) counters. These methods, often used in tandem and with direct measurement techniques, have been used to determine aerosol mixing state through measurements of particle size distributions, particle nucleation and growth, ion composition, scattering albedo and absorption, aerosol optical depth, hygroscopicity, phase transitions, such as deliquescence and efflorescence, and mass ratios of chemical components within particles, as well as the evolution of these aerosol properties under changing environmental conditions (Lightstone et al., 2000; Abel et al., 2003; Clarke et al., 2004; Marcolli et al., 2004; Schnaiter et al., 2005; Möhler et al., 2005;

Broekhuizen et al., 2006; Cheng et al., 2006; Moteki and Kondo, 2007; Shiraiwa et al., 2007; Moffet and Prather, 2009; Wang et al., 2010a; Petzold et al., 2011; Koop et al., 2011; Liu et al., 2017a).

Even though a broad range of analytical techniques, such as those discussed here, can be used to study different aspects of aerosol mixing state, there are still many challenges and limitations associated with current methods. For example, each technique has boundaries in terms of particle sizes and compositions that can be analyzed, often due to sample preparation or instrumentation limitations, meaning no single technique is robust enough to provide a complete picture of aerosol mixing state. Improved methods or the development of complementary techniques are required in order to address the knowledge gaps associated with fully characterizing aerosol mixing state.

1.3 Aerosol Acidity

Adapted from Craig, R. L. and Ault, A. P. Aerosol Acidity: Direct Measurement from Spectroscopic Methods. In *Multiphase Environmental Chemistry in the Atmosphere*. Hunt, S., Nizkorodov, S., Laskin, A., Eds. ACS Symposium Series, submitted. Copyright 2018 American Chemical Society.

1.3.1 pH Dependent Atmospheric Processes

Acidity impacts many multiphase chemical processes of atmospheric aerosols; the most well-known and studied being secondary organic aerosol (SOA) formation. Overall, increased acidity levels are associated with enhanced SOA yields due to acid-catalyzed heterogeneous reactions, such as epoxide ring-opening reactions (Eddingsaas et al., 2010; Mael et al., 2015) or reactions of carbonyls (Jang et al., 2002). This phenomenon has been observed for a wide range of SOA precursors, including isoprene (Edney et al., 2005; Surratt et al., 2007a; Jaoui et al., 2010; Kuwata et al., 2015; Xu et al., 2016), specifically its photooxidation products methacroelin (Zhang et al., 2012b), methyl vinyl ketone (Chan et al., 2013), and isoprene epoxydiols (IEPOX) (Riva et al., 2016d), monoterpenes (such as α-pinene) (Czoschke and Jang, 2006; Northcross and Jang, 2007; Offenberg et al., 2009; Lal et al., 2012; Han et al., 2016), sesquiterpenes (such as β-caryophyllene) (Offenberg et al., 2009; Chan et al., 2011), 1,3-butadiene (Lewandowski et al.,

2015), 2-methyl-3-buten-2-ol (MBO) (Zhang et al., 2012a, 2014), aromatics (such as toluene) (Cao and Jang, 2007), and aldehydes (Jang et al., 2003a). In addition to increased kinetics of acid-catalyzed reactions, SOA yield can be enhanced in terms of mass due to the formation of larger oligomers (Gao et al., 2004; Chan et al., 2013; Kuwata et al., 2015).

One particular class of chemical species that is formed via pH-dependent reactions in SOA is organosulfates. Organosulfate abundance is strongly correlated with acidity, as formation often occurs only under acidic conditions (Iinuma et al., 2007a, 2009; Surratt et al., 2008). Although acidic conditions dictate organosulfate formation in SOA, these compounds can form via photooxidation and/or ozonolysis of many precurors, including α-pinene (Surratt et al., 2007b, 2008; Iinuma et al., 2009; Lal et al., 2012; Duporté et al., 2016), β-pinene (Iinuma et al., 2007a, 2009; Surratt et al., 2008), limonene (Iinuma et al., 2007b; Surratt et al., 2008) and other monoterpenes, as well as isoprene (Surratt et al., 2007b, 2008; Darer et al., 2011; Kuwata et al., 2015; Li et al., 2016), β-caryophyllene (Chan et al., 2011), MBO (Zhang et al., 2012a; Mael et al., 2015), alkanes (Riva et al., 2016a), alkylamines (Wang et al., 2010b), and polycyclic aromatic hydrocarbons (PAHs), such as naphthalene (NAP) and 2-methylnaphthalene (2-MeNAP) (Riva et al., 2015). While organosulfate formation has been observed and studied to a greater extent, formation and hydrolysis of organic nitrate compounds also occurs under acidic conditions (Mael et al., 2015; Rindelaub et al., 2015; Han et al., 2016). Though acid-catalyzed SOA formation has primarily been studied through laboratory and chamber work, it has been observed in ambient data globally (Edney et al., 2005; Zhang et al., 2007a; Tanner et al., 2009; Ding et al., 2011; Pathak et al., 2011; Budisulistiorini et al., 2015), including the formation of oligomers (Liggio and Li, 2013), organosulfates (Surratt et al., 2008), and organic nitrates (Kiendler-Scharr et al., 2016).

In addition to SOA formation, pH also plays an important role in many other multiphase chemical and physical atmospheric processes. Examples include changes to gas-particle partitioning equilibria leading to increased reactive uptake of organic compounds (Liggio and Li, 2006; Wang et al., 2012; Gaston et al., 2014; Liu et al., 2015; Marais et al., 2016; Chen et al., 2017), heterogenerous reactions of non-SOA particle types, such as chloride depletion in sea spray aerosol (SSA) (Gard et al., 1998; Laskin et al., 2012; Ault et al., 2014; Bondy et al., 2017b), acid-catalyzed hydrolysis reactions (Hu et al., 2011; Jacobs et al., 2014; Rindelaub et al., 2015, 2016b; Cortés and Elrod, 2017), and increased metal ion dissolution and solubility under

acidic conditions (Chen et al., 2012; Longo et al., 2016; Fang et al., 2017). Other multiphase processes affected by particle acidity include water uptake (Prenni et al., 2003; Ghorai et al., 2011, 2014), liquid-liquid phase separation (LLPS) (Ault et al., 2013a; You et al., 2014; Dallemagne et al., 2016; Losey et al., 2016), light absorption (Song et al., 2013; Lin et al., 2014), as well as photolysis and OH radical reaction chemistry (Liu et al., 2017c; Rapf et al., 2017; Witkowski and Gierczak, 2017). Despite the evidence for enhanced SOA formation and other multiphase atmospheric processes that occur under acidic conditions, more specific correlation to acidity is not well characterized, in part due to the challeneges associated with measuring aerosol pH.

1.3.2 Determining Aerosol pH

Aerosol pH is difficult to determine due to the small size of particles (attoliter or smaller volumes) and the non-conservative nature of H^+ with respect to other chemical species present, as it is dependent on aerosol liquid water content and relative humidity (RH). As a result of these challenges, indirect measurements, proxy methods, and thermodynamic equilibrium models have often been used to predict aerosol acidity (Hennigan et al., 2015). Indirect measurements from filter-based extraction and extrapolation are associated with high uncertainty, often due to changes in ion distribution during extraction or sampling artifacts (Koutrakis et al., 1988; Keene et al., 2002; Pathak et al., 2004; Hennigan et al., 2015). Proxy methods, such as ion balance and molar ratio, which infer H^+ concentration, and subsequently pH, by balancing measured concentrations of inorganic anions and cations (Kerminen et al., 2001; Trebs et al., 2005; Metzger et al., 2006; Feng et al., 2012), are also associated with high uncertainty and often cannot predict aerosol pH with more precision than “acidic” or “basic” classification (Hennigan et al., 2015). Additionally, the ion balance and molar ratio methods typically disagree with thermodynamic equilibrium model predictions of pH, and the discrepancy between the two methods can be attributed to lack of considerations for aerosol liquid water content and ion activity coefficients and inability to differentiate between free and bound H^+ (e.g. protons associated with bisulfate, HSO_4^-, or other inorganic ions) (Keene et al., 2004; Trebs et al., 2005; Metzger et al., 2006; Pathak et al., 2009; Hennigan et al., 2015).

In contrast, a third proxy method, phase partitioning, which uses measurements of semivolatile compounds in the gas and aerosol phase, such as NH_3/NH_4^+, to indirectly predict

pH, has yielded much better agreement with models (Keene et al., 2004; Young et al., 2013; Hennigan et al., 2015). Thermodynamic models, such as E-AIM (Clegg et al., 1998; Wexler and Clegg, 2002) and ISORROPIA-II (Nenes et al., 1998; Fountoukis and Nenes, 2007), use measurements of both gas and aerosol phase chemical species, temperature, and RH to predict aerosol pH. Although the phase partitioning method and thermodynamic models show the best agreement and are widely considered to be the most accurate of the current methods for indirect prediction of aerosol pH, they are not without limitations (Hennigan et al., 2015). Both methods are most accurate when constrained by measurements of gas and aerosol phase chemical components (Hennigan et al., 2015; Murphy et al., 2017), but are sensitive to the respective measurement input values and their associated uncertainties. Additionally, both methods assume gas-particle phase equilibrium, which is not always accurate under conditions of low liquid water content or high ionic strength (Keene et al., 2004; Virtanen et al., 2010; Perraud et al., 2012; Hennigan et al., 2015; Shiraiwa et al., 2017), and neither method accounts for the potential influence of organic components (Hennigan et al., 2015; Silvern et al., 2017), such as organic acids, which are ubiquitous in ambient aerosol (Zhang et al., 2007b; Kolb and Worsnop, 2012).

The phase partitioning method and thermodynamic models have been applied to evaluate ambient aerosol acidity and variability globally (Guo et al., 2015, 2016, 2017; Vieira-Filho et al., 2016; Liu et al., 2017b). Overall, aerosol particles are often acidic, but there is variability due to differing source contributions (Bougiatioti et al., 2016, 2017; Pozzer et al., 2017; Shi et al., 2017), regional location, such as urban versus rural areas (Bougiatioti et al., 2016; Battaglia et al., 2017), and seasonality (Kumar and Raman, 2016; Wu et al., 2017). These predictions indicate that acidity-dependent chemistry can occur readily in most ambient aerosol, as pH levels are low enough, despite decreasing atmospheric gaseous SO_2 emissions and subsequent condensed-phase sulfate concentrations in some regions, such as the southeast United States, where SOA formation is prevalent (Weber et al., 2016). Direct measurement of aerosol pH is needed to constrain model and proxy method predictions of acidity, particularly when there is disagreement, and will help further understanding of the impact of pH on multiphase atmospheric processes.

Currently, there are few methods for direct measurement of aerosol acidity. One method measures proton concentration in particle samples collected on dyed filters through a colorimetric analysis integrated with a reflectance UV-Visible spectrometer (Jang et al., 2008; Li

and Jang, 2012). A second method monitors acidity via fluorescence spectroscopy with a pH-sensitive dye (Dallemagne et al., 2016). However, application of these methods has been limited and more refined techniques for direct measurement of aerosol pH are necessary to constrain model predictions and improve understanding of pH-dependent atmospheric processes.

1.4 Research Objectives and Scope of the Dissertation

In this dissertation, several Raman microspectroscopic methods were developed and applied to study the chemical mixing state and acidity of both laboratory-generated and ambient aerosol particles. Chapter 2 describes a novel method for automated mapping for Raman microspectroscopic characterization and its application to ambient aerosol particles collected during the Southern Oxidant and Aerosol Study (SOAS). Chapters 3 and 4 detail the application of surface enhanced Raman spectroscopy (SERS) to improve detection and characterization of previously unidentifiable vibrational modes within aerosol particles, as well as the first measurements of atmospheric particles with diameters small than the diffraction limit. Chapters 5 and 6 describe the development a spectroscopic method to measure single particle aerosol pH by quantitatively probing the vibrational modes that correspond to the acid and conjugate base species for several inorganic and organic equilibrium systems. Through pH measurements with this method, the effect of RH on particle acidity, gas-particle partitioning of acidic chemical species, and the relationship between ionic strength and H^+ activity could also be studied and are discussed in Chapters 5 and 6. Chapter 7 details a novel quantitative pH indicator paper method for measuring size-resolved bulk aerosol pH and the subsequent direct observation of a relationship between particle size and acidity. Finally, Chapter 8 concludes the dissertation and discusses on-going projects.

Chapter 2. Computer Controlled Raman Microspectroscopy (CC-Raman): A Method for the Rapid Characterization of Individual Atmospheric Aerosol Particles

Adapted with permission from Craig, R. L., Bondy, A. L., and Ault, A. P.: Computer-controlled Raman microspectroscopy (CC-Raman): A method for the rapid characterization of individual atmospheric aerosol particles, *Aerosol. Sci. Technol.*, 51:9, 1099-1112, 2017. https://doi.org/10.1080/02786826.2017.1337268

2.1 Introduction

Atmospheric aerosol particles play an important role in climate by scattering and absorbing solar radiation and acting as cloud condensation nuclei (CCN) or ice nuclei (IN) (Ramanathan et al., 2001; Prather et al., 2008). Climate-relevant properties, such as hygroscopicity, ice nucleation ability, and light scattering, are dependent on the physical and chemical properties of individual aerosol particles, such as size, chemical composition, and morphology (Pöschl, 2005). Knowledge of the primary components in individual aerosols is often not sufficient to infer their climate properties (Prather et al., 2008; Bauer et al., 2013; Ault and Axson, 2017), as a particle's chemical mixing state, the secondary chemical species present, and their internal spatial distribution influence behavior in the atmosphere, such as the ability to act as CCN or IN (Wang et al., 2010a; Schill et al., 2015). For example, partitioning between phases and different types of internal structure, such as core-shell morphology, can inhibit heterogeneous reactivity and/or water uptake (McNeill et al., 2006; Davies et al., 2013; Ruehl and Wilson, 2014; Ryder et al., 2014, 2015). Spectroscopic analysis has great potential to probe particle mixing state and provide important information on particle composition and structure (Lee and Allen, 2012), while ideally being non-destructive, which can allow for further analysis at a future date.

Raman microspectroscopy has been increasingly applied to study chemical composition and mixing state by probing the functional groups present in individual aerosol particles (Ivleva

et al., 2007b; Sobanska et al., 2012; Ault et al., 2013b, 2014; Ebben et al., 2013; Laskina et al., 2013; Zhou et al., 2014; Catelani et al., 2014; Deng et al., 2014; Craig et al., 2015; Rindelaub et al., 2016a). Raman microspectroscopy not only measures the vibrational frequencies of functional groups present, but also provides the spatial distribution of the measured functional groups within a particle through spectral mapping (Stefaniak et al., 2009; Ault et al., 2014; Jung et al., 2014; Sobanska et al., 2014). Raman is particularly sensitive to secondary chemical species, and spectra of the fingerprint region (500-1500 cm^{-1}) (Smith and Dent, 2005) can be used to identify organic functional groups and, thus, infer classes of organic compounds present based on the detected vibrational modes (McLaughlin et al., 2002; De Gelder et al., 2007; Avzianova and Brooks, 2013). Additionally, elemental carbon (EC), especially graphitic species, have very large Raman scattering cross sections, making even small amounts of EC in particles easily detectable (Rosen and Novakov, 1977; Rosen et al., 1978). Raman can also distinguish species, such as sulfate and bisulfate, which gravimetric and mass spectrometry-based methods cannot, allowing pH to be probed (Rindelaub et al., 2016a). While various infrared spectroscopy techniques, such as attenuated total reflectance Fourier transform infrared spectroscopy (ATR-FT-IR), diffuse reflectance FT-IR, or optical microscopy coupled with FT-IR (micro-FT-IR), can also probe chemical composition and are sensitive to organic compounds, these methods must overcome a strong absorbance interference from water and are limited to bulk analysis or larger (> 5 μm) particles with spatial resolution varying across the spectral window (Ryu and Ro, 2009; Ghorai et al., 2011; Takahama et al., 2013; Jung et al., 2014; Gaffney et al., 2015).

In comparison, the diffraction limit for commonly used wavelengths for Raman analysis (532, 633, and 640 nm) allows for analysis of ≥ ~0.8 μm particles (projected area diameter, for confocal Raman microscopy with a 100x objective). Methods such as surface enhanced Raman spectroscopy (SERS) (Craig et al., 2015) and tip enhanced Raman spectroscopy (TERS) (Ofner et al., 2016) have been extending the lower size limit for individual particle Raman analysis further into the submicron size range. Additional advantages of Raman microspectroscopy include non-destructive analysis at ambient temperature and pressure, as well as minimal sample preparation. Although Raman microspectroscopy is a powerful analytical technique, it can be time-intensive and difficult to perform uniform analysis for an entire particle population (Ault and Axson, 2017). Very recently, work by Doughty and Hill has shown the potential of automated Raman analysis for field samples using a 40 x 1 μm beam and advancing tape

(Doughty and Hill, 2017). Development of an automated Raman microspectroscopic method that couples morphological measurements of individual submicron sized particles with detailed Raman spectra has the potential to improve efficient and thorough characterization of aerosol particle physicochemical properties.

Due to the benefits of spectroscopic analysis, several microspectroscopy techniques have already been automated and applied to the study and characterization of individual aerosol particles. These methods include computer controlled scanning electron microscopy (CCSEM) with energy dispersive X-ray analysis (EDX) and scanning transmission X-ray microscopy coupled with near-edge X-ray absorption fine structure spectroscopy (STXM-NEXAFS) (Casuccio et al., 1983, 2004; Germani and Buseck, 1991; Laskin and Cowin, 2001; Mamane et al., 2001; Laskin et al., 2006; Moffet et al., 2010a). SEM yields images with high spatial resolution that can be used to determine size and morphology of both coarse and fine mode particles (Jambers et al., 1995; Laskin and Cowin, 2001; Casuccio et al., 2004; Laskin et al., 2006). When coupled with EDX, SEM can also provide information on elemental composition, and is particularly well-suited to particles containing metals (Ault et al., 2012; Guasco et al., 2014; Shen et al., 2016). However, detailed chemical characterization of particles, particularly mixed carbon-containing particles, is limited (Jambers et al., 1995; Casuccio et al., 2004; Laskin et al., 2006). Another microscopy technique coupled with electronic spectroscopy, TEM–EELS (transmission electron microscopy with electron energy loss spectroscopy) uses inelastically scattered electrons, which provides better chemical detail than EDX, such as the ability to distinguish between organic carbon and soot, but still cannot differentiate organic carbon species and has yet to be automated (Katrinak et al., 1992; Alexander et al., 2008). As organosulfates and organonitrates have been identified as a larger than previously realized portion of secondary organic aerosol (Surratt et al., 2010; Darer et al., 2011; Hatch et al., 2011; Glasius and Goldstein, 2016), the inability of EDX to distinguish inorganic sulfate and nitrate from organosulfates and organic nitrates represents another limitation. An additional disadvantage of CCSEM is that it requires samples to be under vacuum, even the relatively less-intense vacuum used for environmental SEM (ESEM), which can result in transformation or loss of volatile or unstable compounds (Stefaniak et al., 2009).

Another automated microspectroscopic technique, STXM-NEXAFS, is a non-destructive x-ray technique that yields two-dimensional maps of particle composition and morphology with

high spatial resolution, as well as information on bonding and oxidation state (Takahama et al., 2007; Moffet et al., 2010a, 2011). This electronic spectroscopy technique is best for investigating oxidation state and evolution of aerosol mixing state, which can be difficult to study with SEM or other methods of microscopy (Takahama et al., 2007; Moffet et al., 2011). The automated aspect of these methods allows for individual particle analysis while also providing information on the overall particle population through characterization of thousands of particles (Jambers et al., 1995; Moffet et al., 2010a). While both electronic spectroscopy methods (CCSEM-EDX and STXM-NEXAFS) can provide some chemical information (elemental and bonding/ oxidation state, respectively), neither provides the detailed molecular information of vibrational spectroscopy methods, such as Raman microspectroscopy. Specifically Raman modes provide insight into functional groups within organic molecules and other secondary components (e.g. nitrate, sulfate), or bonding environment (aqueous versus solid, binding to different cations). This has led multiple studies to use coupled electron beam and Raman microspectroscopy measurements of the same samples, but the statistics for particles analyzed by Raman has typically been limited when compared with EDX or electron probe X-ray microanalysis (EPMA) (Sobanska et al., 2012; Ault et al., 2013b; Jung et al., 2014; Eom et al., 2016).

This study describes an automated method for single particle Raman microspectroscopic analysis. Computer-controlled Raman microspectroscopy (CC-Raman) is a method that can provide detailed chemical composition and size for a representative population of aerosol particles. Our initial publication of CC-Raman was validated by comparison with numerous other characterization techniques during the analysis of insoluble residues in snow from the California Sierra Nevada (Creamean et al., 2016), but has not been applied to atmospheric aerosols or quantitatively characterized. Herein, the potential of CC-Raman is demonstrated by analysis of laboratory generated aerosol particle standards and mixtures of varying chemical composition, as well as ambient particles collected during the Southern Oxidant and Aerosol Study (SOAS). CCSEM was also used to analyze the standard and ambient aerosol particle samples and is shown to be a valuable complementary technique to CC-Raman, which can provide a more detailed understanding of primary chemical species present for source apportionment. Overall, this study aims to highlight the unique detailed molecular characterization measurements possible with CC-Raman and to demonstrate the potential for

CC-Raman to help improve understanding of the chemical composition, mixing state, and climate-relevant properties of atmospheric aerosol particles.

2.2 Methods

2.2.1 Laboratory-Generated Aerosol Particle Samples

Standard solutions were prepared from 18.3 MΩ Milli-Q water and the following chemicals: sodium nitrate ($NaNO_3$), L-alanine ($C_3H_7NO_2$), and sodium sulfate (Na_2SO_4) (Sigma-Aldrich); calcium sulfate ($CaSO_4$) (Acros Organics); ammonium sulfate $(NH_4)_2SO_4$ (Alfa Aesar); and magnesium sulfate ($MgSO_4$) (Fisher Scientific). All chemicals were > 98.0% purity and used without further purification. The nitrate and sulfate salts were selected for this study as NO_3^- and SO_4^{2-} are common inorganic species present in aerosol particles. L-alanine was selected as it contains organic functional groups corresponding to vibrational modes commonly observed in aerosol particles, including ν(C-H), δ(C-H), ν(C-C), ν(C-O), and ν(O-C-O). Particles were generated from 0.05 M solutions atomized using HEPA-filtered air. After atomization, particles were size selected at 0.791 μm (electrical mobility diameter) with an electrostatic classifier (Model 3080, TSI Corporation) equipped with a long differential mobility analyzer (Model 3082, TSI Corporation) at sample to sheath flow ratio of 1:8.3 (0.3 to 2.5 lpm). and then impacted onto quartz substrates or Formvar transmission electron microscopy (TEM) grids (Ted Pella, Inc.) using a Microanalysis Particle Sampler (MPS-3, California Measurements, Inc.). Stage 2 of the MPS (0.40-2.8 μm equivalent aerodynamic diameter cut-point) was analyzed for each of the following samples: 1) mixed standards (L-alanine, ammonium sulfate, and sodium nitrate) and 2) sulfate standards (ammonium sulfate, calcium sulfate, magnesium sulfate, and sodium sulfate). For each sample, particles of each standard type were generated one compound at a time and impacted onto the same quartz substrate or the same TEM grid to achieve an externally mixed distribution. All MPS samples were collected with low enough aerosol concentrations and short enough sampling times to ensure minimal particle overlap (< 3% of particles had overlap).

2.2.2 Ambient Aerosol Particle Samples

Samples of airborne particles were collected on quartz substrates and TEM grids during the SOAS field campaign in Centreville, AL in 2013 using a Micro-Orifice Uniform Deposit Impactor (MOUDI, Model 110, MSP Corp.). Samples were frozen and stored prior to analysis. Stage 7 (aerodynamic size cut of 0.56 μm) for the following six samples were analyzed: June 06,

8:00 PM – 7:00 AM; June 12, 12:00 PM – 3:00 PM; June 14, 12:00 – 3:00 PM; June 20, 8:00 AM – 7:00 PM; June 26, 8:00 PM – 7:00 AM, and July 08, 8:00 PM – 7:00 AM.

2.2.3 Computer-Controlled Raman Microspectroscopy (CC-Raman)

This study used a Horiba LabRAM HR Evolution Raman spectrometer coupled with a confocal optical microscope (100x long working distance Olympus objective, 0.9 numerical aperature) and equipped with a Nd:YAG laser source (50 mW, 532 nm) and CCD detector. A 600 groove/mm diffraction grating yielded spectral resolution of ~1.8 cm^{-1}. The instrument was calibrated against the Stokes Raman signal of pure Si at 520 cm^{-1} using a silicon wafer standard. Laser power was adjusted accordingly with a neutral density filter to prevent damage to the sample (incident laser power ~35 mW). Spectra were collected for the range 500 to 4000 cm^{-1} with three accumulations at 5 s acquisition time for the standard samples and four accumulations at 15 s acquisition time for the ambient samples for each particle analyzed.

The CC-Raman method is facilitated by improved software, which applies the Particle Finder and Multivariate Analysis modules of LabSpec6 software (Horiba) that accompanies the spectrometer. An optical image was collected (Figure 2.1a) and aerosol particles were identified based on specified contrast, size, and morphological features (Figure 2.1b). The spatial resolution of the image was about 9.7 pixels/μm, which allowed for easy identification of ~1 μm particles. In terms of contrast, arbitrary light and dark thresholds that scaled the contrast of the image within a range of 1-100 were set to identify dark particles against a light background or light particles against a dark background. For size, the minimum particle area was set to 0.5 μm^2 and morphological filters were applied to better detect particle edges. A Raman spectrum was collected for each identified particle, as well as measurements of projected area diameter, circularity, and other morphological characteristics. In comparison to standard Raman mapping techniques, the identified particles form an irregularly shaped map area with variable step size between points (particles) analyzed. Only the particles within the image are analyzed and as settings identifying particles can be controlled by the user, false positive and false negative particle identification is reduced, and if unavoidable, at least able to be taken into account. Automation of particle analysis increased the number of particles analyzed per hour by a factor of four in comparison to manual Raman analysis, with ~80 and ~20 particles per hour analyzed for the standard and ambient samples, respectively, by CC-Raman. Divisive clustering analysis (DCA), a K-means partitional clustering method, was used to cluster and classify particles based

on distinct features in their Raman spectra (Figure 2.1c and 2.1d). Spectra were not processed prior to clustering analysis and the number of clusters was arbitrarily chosen by the user after testing several numbers of clusters and determining when clusters began to be distinguished by differing intensity of spectral features, rather than the spectral features themselves. Multiple CC-Raman maps were collected for each sample. 323, 151, and 1391 particles were analyzed for the mixed standards sample, the sulfate standards sample, and the ambient samples, respectively. Further discussion of the spectra is provided in the Results section.

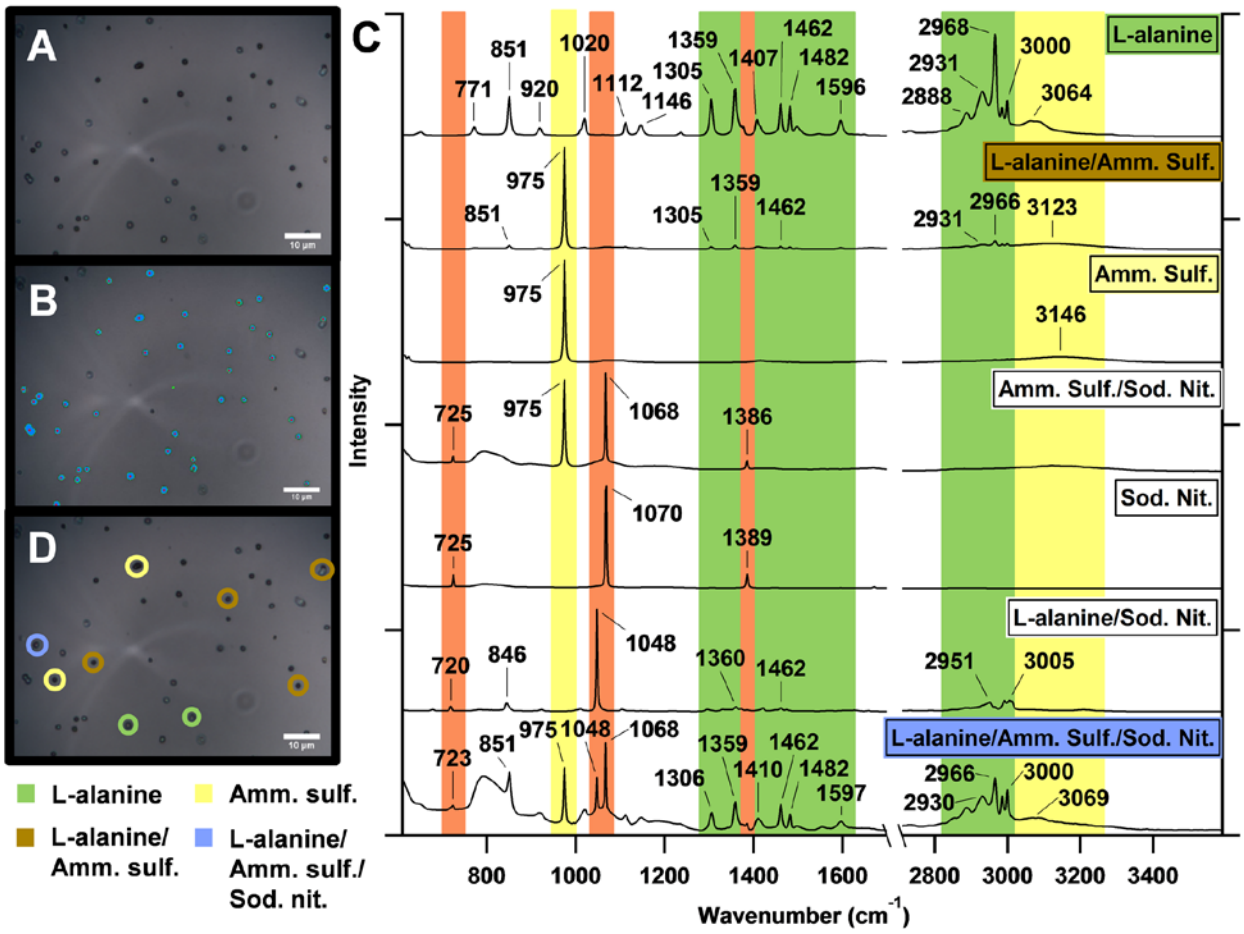

Figure 2.1 A) Optical image of laboratory generated aerosol particles composed of L-alanine, $(NH_4)_2SO_4$, and $NaNO_3$. B) The same image now with aerosol particles to be analyzed identified by the particle area (blue), particle perimeter (green), and the center of the particle where the Raman spectrum is collected (red). C) DCA-clustered Raman spectra of the analyzed aerosol particles, showing individual and mixed particles including: L-alanine, L-alanine/$(NH_4)_2SO_4$, $(NH_4)_2SO_4$, and L-alanine/$(NH_4)_2SO_4$/ $NaNO_3$. Vibrational modes are shown for $NaNO_3$ (orange), $(NH_4)_2SO_4$ (yellow), and L-alanine (green). D) Optical image with some identified particle types with four identified clusters - L-alanine particles, L-alanine/$(NH_4)_2SO_4$ mixed particles, $(NH_4)_2SO_4$ particles, and L-alanine/$(NH_4)_2SO_4$/ $NaNO_3$ mixed particles.

2.2.4 Computer-Controlled Scanning Electron Microscopy (CCSEM)

The laboratory-generated standards were analyzed at the Michigan Center for Materials Characterization $(MC)^2$ at the University of Michigan using a FEI Helios 650 nanolab SEM/FIB equipped with a field emission gun operating at 10 kV and a high angle annular dark field (HAADF) detector. The instrument was equipped with an EDX spectrometer (EDAX, Inc.) which allowed for X-ray detection of elements with atomic numbers (Z) higher than Be. EDX spectra from individual particles were analyzed to determine the relative abundance of elements within each of the standard samples. 271 and 226 particles were analyzed for the mixed standard and sulfate standard samples, respectively. The elements quantified in the mixed standards sample were: C, N, O, Na, S and the elements quantified in the sulfate standards sample were: N, O, Na, Mg, S, and Ca. Single-particle data from the CCSEM analysis was analyzed in MATLAB R2013b (MathWorks, Inc.) using k-means clustering of the elemental composition following a previously published method (Ault et al., 2012). Clusters were identified as a single compound or mix of compounds based on their elemental composition and the number of clusters was arbitrarily chosen to minimize both cluster number and error. Clustering analysis was performed on the square root of the matrix of atomic percent to emphasize differences due to lower atomic percent elements.

The ambient samples were analyzed at the Environmental Molecular Sciences Laboratory (EMSL) at the Pacific Northwest National Laboratory (PNNL) using a FEI Quanta environmental SEM equipped with a field emission gun operating at 20 kV, a HAADF detector, and an EDX spectrometer (EDAX, Inc.). For the six ambient samples, a total of 4830 particles were analyzed. EDX spectra from individual particles were analyzed to determine the relative abundance of the following 15 elements: C, N, O, Na, Mg, Al, Si, P, S, Cl, K, Ca, Ti, Fe, and Zn. K-means clustering of the particles resulted in clusters that were grouped into source-based classes by elemental composition, including mineral dust, secondary organic aerosol (SOA), biomass burning aerosol, fly ash, biological particles, sea spray aerosol (SSA), and lake spray aerosol (LSA), identified by comparison with literature from previous studies (Li et al., 2003; Pósfai et al., 2003; Sobanska et al., 2003; Utsunomiya et al., 2004; Laskin et al., 2006, 2012; Hopkins et al., 2008; Coz et al., 2009; Edgerton et al., 2009; Ault et al., 2012, 2013c; Moffet et al., 2013; Allen et al., 2015; Shen et al., 2016; Axson et al., 2016a, 2016b).

2.2.5 Condensation Particle Counter (CPC)

Particle number concentration and counts for each atomized and size selected standard compound were measured using a condensation particle counter (CPC) (Model 3775, TSI Corporation). Samples were tested in triplicate. The particle number counts for each standard were summed over the sampling time to determine the total possible number of particles of the respective compound for the laboratory generated standard sample. The total particle number count for each compound in a sample was compared and used as a preliminary prediction of particle composition of the sample.

2.3 Results and Discussion

2.3.1 Standard Aerosol Particle Samples

To test the ability of the CC-Raman to distinguish particle types during rapid analysis, a laboratory-generated, mixed-standard aerosol particle sample of L-alanine, $(NH_4)_2SO_4$, and $NaNO_3$ was characterized (Figure 2.1). The sample was compared with CCSEM characterization and the predicted composition of the sample based on CPC particle concentration measurements prior to impaction (Figure 2.2). The CC-Raman method identified clusters of L-alanine particles, L-alanine/$(NH_4)_2SO_4$ mixed particles, $(NH_4)_2SO_4$ particles, $(NH_4)_2SO_4/NaNO_3$ mixed particles, $NaNO_3$ particles, L-alanine/$NaNO_3$ mixed particles, and L-alanine/$(NH_4)_2SO_4/NaNO_3$ mixed particles (Figures 1c and 2a). These clusters were determined based on the functional groups identified by the different vibrational modes present in the Raman spectra (Figure 2.1c). $NaNO_3$ was identified by the presence of the $\nu_s(NO_3^-)$ symmetric stretching mode at 1068 cm^{-1} (solid) or 1048 cm^{-1} (free, aqueous NO_3^- ion) (Rousseau et al., 1968; Jentzsch et al., 2013; Deng et al., 2014). $\nu_a(NO_3^-)$ asymmetric stretching modes were also often present at ~725 cm^{-1} and ~1386 cm^{-1}, respectively (Rousseau et al., 1968; Jentzsch et al., 2013; Ault et al., 2014). $(NH_4)_2SO_4$ was identified by the presence of the $\nu_s(SO_4^{2-})$ symmetric stretching mode at 975 cm^{-1} and the ν(N-H) stretching mode, a broad peak around 3000-3200 cm^{-1} (Venkateswarlu et al., 1975; Sobanska et al., 2012; Ault et al., 2013b; Jentzsch et al., 2013; Zhou et al., 2014). As the only organic compound present in this sample, L-alanine, was identified by the presence of peaks in the 1300-1600 cm^{-1} and 2800-3000 cm^{-1} regions. The 1300-1600 cm^{-1} region contains many different vibrational modes, such as carbon-carbon and carbon-oxygen stretches, including ν(C-C), ν(C-O), and ν(O-C-O), as well as carbon-hydrogen bending modes (δ(C-H)), and others

(Devillepin et al., 1982; McLaughlin et al., 2002; De Gelder et al., 2007; Larkin, 2011; Ault et al., 2013b; Avzianova and Brooks, 2013; Laskina et al., 2013). Vibrational modes in the 2800-3000 cm^{-1} region more often represent symmetric and asymmetric $\nu(CH_3)$ and $\nu(CH_2)$ stretches (McLaughlin et al., 2002; Larkin, 2011; Ault et al., 2013b; Ebben et al., 2013; Laskina et al., 2013). It is important to note that simple assignments relating each vibrational mode to a specific compound can be made for this laboratory generated standard sample, as the compounds dictating the chemical composition of the particles were controlled.

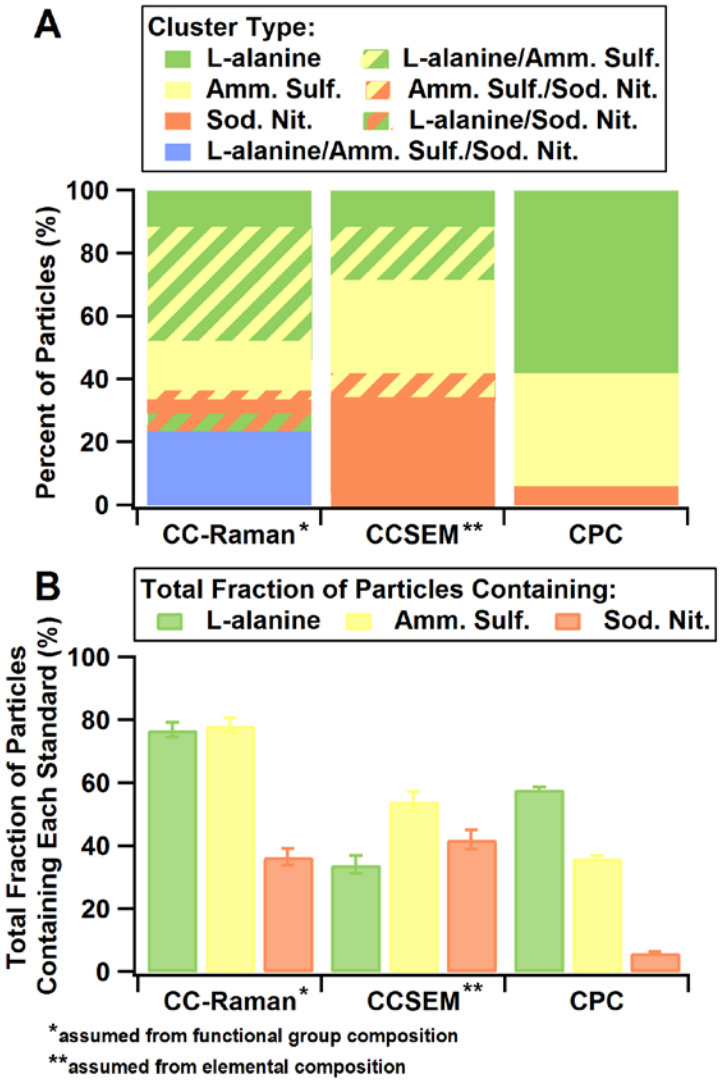

Figure 2.2 A) Percent fraction of cluster types as determined using CC-Raman, CC-SEM, and CPC techniques. B) Total fraction of particles containing each compound regardless of mixing state as determined by each method.

CCSEM analysis, which identified particles based on their elemental composition, resulted in similar clustering as CC-Raman. Particles of each individual compound and particles with mixtures of two compounds were distinguished, but CCSEM was not sensitive to particles containing all three compounds. The simple predicted sample composition based on CPC measured particle number counts did not account for multiple particles impacting on each other or any partitioning and thus did not include particles of mixed composition. For further comparison between the methods, the total fraction of particles containing each compound (L-alanine, $(NH_4)_2SO_4$, and $NaNO_3$) was calculated, regardless of whether the particle contained one compound or was mixed (meaning the total fraction for all the compounds will sum greater than 100% for the CC-Raman and CCSEM data due to the presence of mixed particles) (Figure 2.2b). Differences between CC-Raman and CCSEM identified cluster fractions with the CPC predicted cluster fractions can mainly be attributed to challenges from particle impaction. The CPC prediction was based on the total number of particles counted for each generated aerosol population prior to impaction onto substrates, while CC-Raman and CCSEM analysis was performed on particles after impaction, during which losses most likely occurred as some particle types impacted more efficiently than others, dependent on both particle composition and substrate material (Chang et al., 1999; Hinds, 1999; Virtanen et al., 2011). Impaction of particles also led to mixed chemical composition, which the CPC method was unable to predict. CC-Raman was consistent with the CPC predictions in that there was significantly less $NaNO_3$ (37%) than L-alanine (77%) and $(NH_4)_2SO_4$ (78%) present overall in the sample. While CCSEM detected a similar fraction of $NaNO_3$ (42%), it was much less sensitive towards L-alanine (34%) and $(NH_4)_2SO_4$ (54%). This is most likely due to CCSEM sensitivity issues with low Z elements, such as H, C, O, and N (Ro et al., 1999; Mamane et al., 2001), interference with detection of C and O due to the Formvar TEM grid substrate, and poor stability of these compounds under the electron beam. In comparison, CC-Raman most likely had minimal issues with sensitivity towards certain particle types due to all compounds containing functional groups with easily detected Raman active vibrational modes and lack of interference from the quartz substrate. Differences in the size of particles analyzed by each technique could also contribute to discrepancies in the particle types observed by CC-Raman in comparison to CCSEM. As shown in the size distributions for particles analyzed by each technique (Figure A.1), CC-Raman detected only supermicron particles, while CCSEM detected both sub- and supermicron

particles. Cluster percent fraction and total fraction of particles containing each compound with standard error for each method for the mixed standards sample are included in Tables A.1 and A.2.

Limitations of manual Raman microspectroscopy include: user biases due to hand selecting particles for analysis and time expenses limiting particle statistics and samples analyzed. Both are essentially eliminated by the ability of the CC-Raman method to increase the number of individual particles analyzed under identical analysis conditions. Figures of merit are given in Figure 2.3 and Table 2.1, including accuracy and precision (reproducibility) of the CC-Raman method. Figure 2.3a illustrates the cluster percent fractions for three trials of the CC-Raman method in comparison with the cumulative total CC-Raman analysis that was shown in Figure 2.2. Trials 1, 2, and 3 characterized 107, 111, and 105 particles, respectively. Cluster percent fraction values with standard error, with comparison to the cumulative total mixed standards CC-Raman analysis, are listed in Table A.3. Figure 2.3b shows the total fraction of particles containing each compound, whether as a single or mixed component, for each trial and the cumulative total. Values with standard error for the total fraction of particles containing each compound are provided in Table 2.1. While there are some differences between the cluster percent fractions, most likely due to the particle variability within the sample, the total fraction of particles containing each compound are mostly within error for each trial and the cumulative total. The consistency between trials for the total fraction of particles containing each compound demonstrates the reliability of the CC-Raman method.

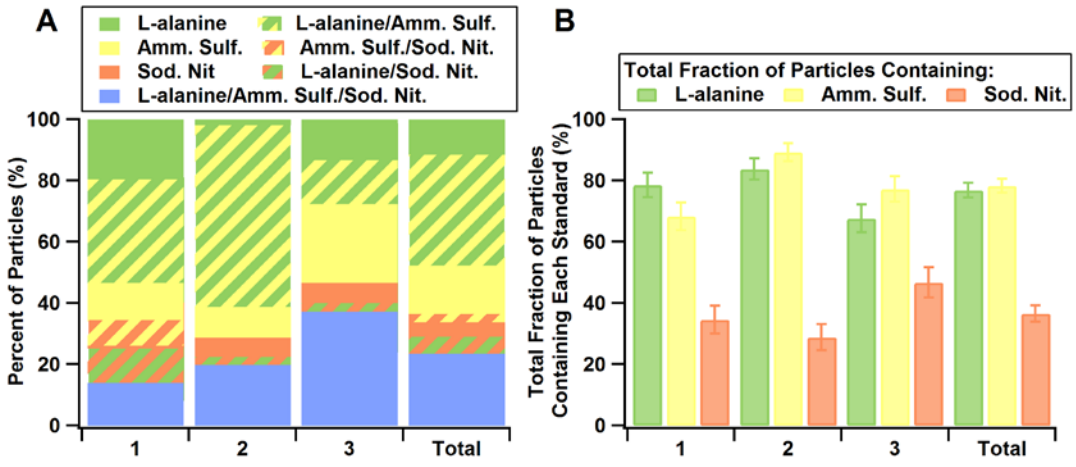

Figure 2.3 A) Cluster percent fractions for three trials of ~100 particles each and cumulative total particles analyzed. B) Total fraction of particles containing each compound for the three trials and cumulative total for the mixed standards sample.

Table 2.1 Total fraction of particles containing each compound type with standard error for each trial and cumulative total for CC-Raman of the mixed standards sample.

Sample	L-alanine (%)	Amm. Sulf. (%)	Sod. Nit. (%)
1	79 ± 4	68 ± 5	35 ± 5
2	84 ± 4	89 ± 3	29 ± 4
3	68 ± 5	77 ± 4	47 ± 5
Total	77 ± 2	78 ± 2	37 ± 3

As inorganic sulfate can be present in different bonding environments (liquid, solid, and mixed phase particles) in the atmosphere, the ability to distinguish the counter ion that sulfate is bonded to is important. CC-Raman was applied to characterize a laboratory-generated standard sample composed of different types of sulfate aerosol particles: $(NH_4)_2SO_4$, calcium sulfate ($CaSO_4$), magnesium sulfate ($MgSO_4$), and sodium sulfate (Na_2SO_4). Raman can detect shifts in the $\nu_s(SO_4^{2-})$ frequency in the Raman spectrum that are caused by the corresponding cation (Jentzsch et al., 2013; Mabrouk et al., 2013). Raman is also capable of probing bonding environment present in the particle, such as by identifying the presence of a free SO_4^{2-} ion based on the $\nu_s(SO_4^{2-})$ location. The ability to differentiate particles that contain the same anion is unique compared to other single particle analysis techniques, such as CCSEM, STXM-NEXAFS, and ATOFMS (aerosol time-of-flight mass spectrometer) that can only identify the presence of the anion and not the bonding cation, and will be valuable for investigations of particle reactivity, phase, and acidity of both laboratory generated and ambient aerosol particles.

Similar to the mixed aerosol particle standard sample, the results of this characterization were also compared to CCSEM characterization and CPC predicted aerosol population composition (Figures 2.4a and 2.4b). CC-Raman analysis identified clusters of $(NH_4)_2SO_4$ particles, $(NH_4)_2SO_4/CaSO_4$ mixed particles, $CaSO_4/MgSO_4$ mixed particles, $CaSO_4/MgSO_4/Na_2SO_4$ mixed particles, Na_2SO_4 particles, and $(NH_4)_2SO_4/CaSO_4/MgSO_4/Na_2SO_4$ mixed particles (Figure 2.4c). The $\nu_s(SO_4^{2-})$ for $(NH_4)_2SO_4$ is located at 975 cm^{-1} (Ault et al., 2013b; Jentzsch et al., 2013; Zhou et al., 2014), for Na_2SO_4 at 996 cm^{-1} (Sobanska et al., 2012; Jentzsch et al., 2013), for $CaSO_4$ at 1008 cm^{-1} (Sobanska et al.,

2012; Jentzsch et al., 2013), and for $MgSO_4$ at 1014 cm^{-1} (Jentzsch et al., 2013). The $\nu(SO_4^{2-})$ mode located at 983 cm^{-1} is indicative of free, aqueous sulfate ion (Jentzsch et al., 2013). The peak location for each sulfate compound's $\nu_s(SO_4^{2-})$ mode was also confirmed by comparison with Raman spectra collected from individual particles from samples of each pure compound.

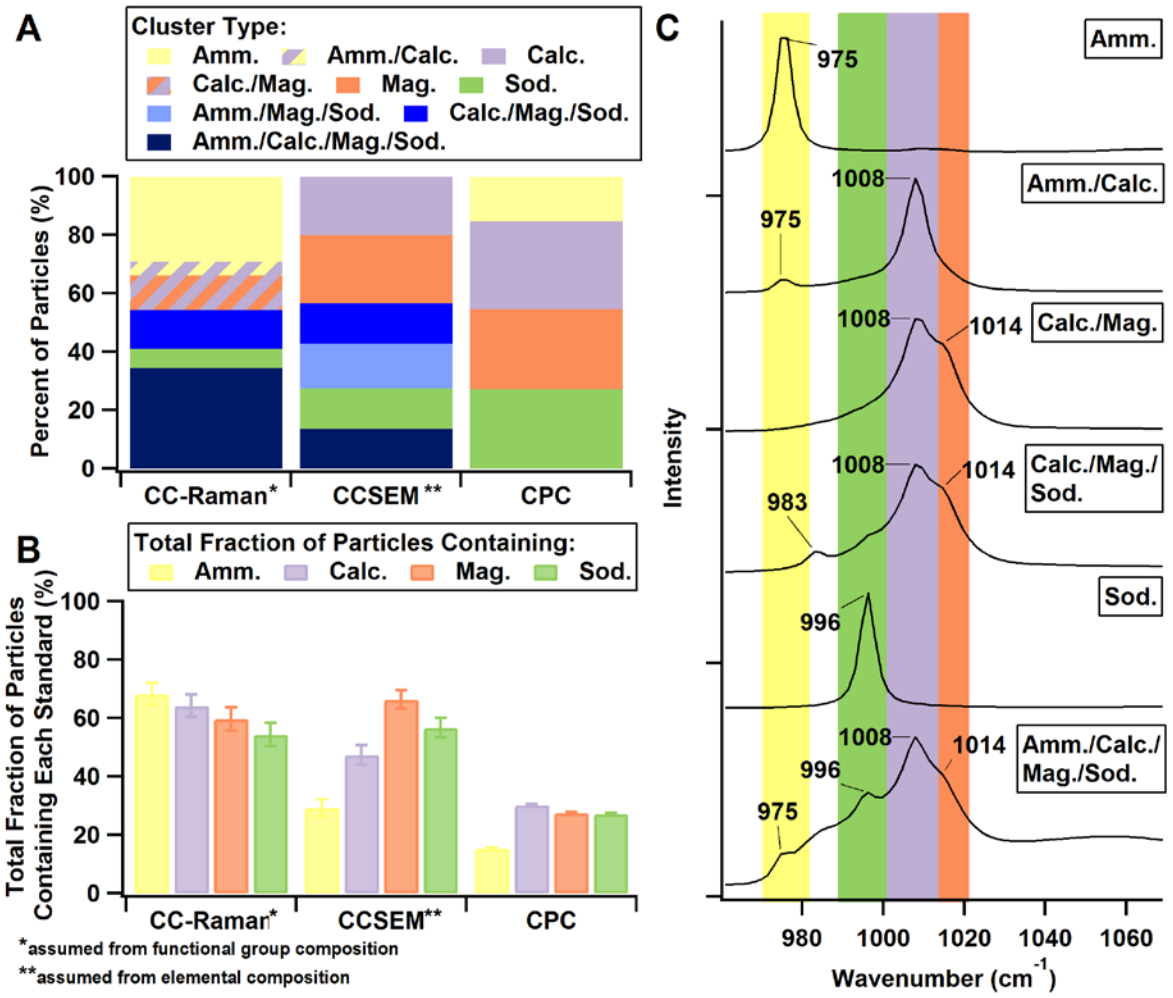

Figure 2.4 A) Percent fraction of cluster types as determined by the CC-Raman, CCSEM, and CPC methods. B) Total fraction of particles containing each compound regardless of mixing state as determined by each method. C) Example spectra (focused on the spectral region where the $\nu(SO_4^{2-})$ vibrational mode is present) for each CC-Raman identified. The highlights represent regions where intensity in the Raman spectrum are indicative of the $\nu_s(SO_4^{2-})$ vibrational mode of ammonium sulfate (yellow), sodium sulfate (green), calcium sulfate (purple), and magnesium sulfate (orange).

CCSEM is unable to differentiate different types of sulfates, except indirectly by identifying the cation element. CCSEM analysis yielded clusters of $CaSO_4$ particles, $MgSO_4$ particles, Na_2SO_4 particles, $(NH_4)_2SO_4/MgSO_4/Na_2SO_4$ mixed particles, $CaSO_4/MgSO_4/Na_2SO_4$

mixed particles, and $(NH_4)_2SO_4/CaSO_4/MgSO_4/Na_2SO_4$ mixed particles. CCSEM did not detect any mixed particles containing only two components nor was CCSEM able to identify any free sulfate anions. Both the cluster percent fractions (Figure 2.4a) and total fraction of particles containing each sulfate compound (Figure 2.4b) show CCSEM's poor sensitivity for ammonium sulfate compared to CC-Raman. As with the previously discussed mixed standard sample, this is most likely due to the fact that NH_4^+ cation is composed solely of low Z elements and that it is an unstable compound under the electron beam (Ro et al., 1999; Mamane et al., 2001). Also similar to the mixed standard sample, discrepancy between the CC-Raman and CCSEM methods compared to the CPC predictions can mainly be attributed to inefficiencies in the particle impaction process (Chang et al., 1999; Hinds, 1999; Virtanen et al., 2011) and differences in the size of particle analyzed by each technique (Figure A.2). Cluster percent fraction and the total fraction of particles containing each compound with standard error for each method for the sulfate standards sample are included in Tables S4 and S5.

2.3.2 Ambient Aerosol Particle Samples

To further demonstrate the potential of CC-Raman, the method was applied to study ambient aerosol particles collected during the SOAS field campaign in Centreville, AL in 2013. 1391 particles from six different samples were characterized, yielding clusters of trace organic particles, organic particles, organic/mineral mixed particles, particles containing graphitic soot, and particles that exhibited fluorescence (Figure 2.5). The graphitic soot cluster also includes particles that exhibit artifacts of burning, due to the similarity of these spectral features to those of soot and graphitic carbon species (discussed further later). Cluster fraction values with standard error can be found in Table A.6. A size distribution, ranging from 0.8 to 8.7 μm with a mode of 1.5 μm, based on the CC-Raman measured projected area diameter, is shown in Figure A.1. The measured particle sizes are consistent with the expected particle sizes based on the MOUDI stage 7 nominal size cut of 0.56 μm when spreading upon impaction, which can be three or four times the aerodynamic diameter (Sobanska et al., 2014), is taken into account.

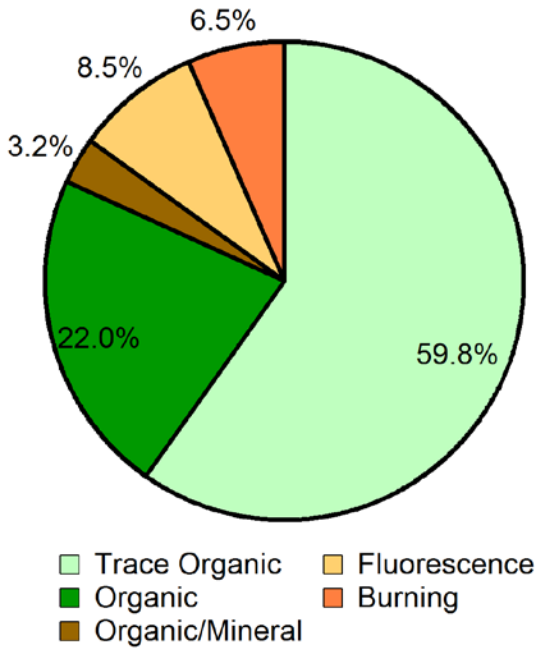

Figure 2.5 CC-Raman identified clusters for aerosol particles from the ambient SOAS samples.

The trace organic cluster was composed of particles that yielded spectra with intensity in both the fingerprint and higher frequency regions of the Raman spectrum that would correspond to the vibrational modes of organic functional groups, but the intensity was too low to resolve specific peaks. The low intensity is most likely due to the organic components of the particle contributing only a small fraction to the overall particle composition, with the remaining components potentially being water, SSA, mineral (non-fluorescing), or other types that either cannot be detected or are difficult to detect with Raman. For example, the small fraction of organic/mineral particles exhibited strong peaks at 518 and 636 cm^{-1} indicative of either aluminum-containing and silicon-containing minerals (Frost et al., 1997; Laskina et al., 2013), but peaks corresponding to various unresolved organic vibrational modes were also present. The organic/mineral particle spectra can be found in Figure A.4, along with example spectra of the different types of fluorescence and graphitic soot observed. With detailed post-analysis, useful information can be obtained from spectra that exhibit fluorescence (Doughty and Hill, 2017) and fluorescence microscopy or other techniques can potentially be used in correlation with Raman analysis to identify soot, biological, and other types of particles. For the EC-containing particles, peaks around 1350 and 1600 cm^{-1} corresponding to the D "disorder" band of the breathing vibrational mode and the G "graphitic" band of the stretching and bending vibrational modes of honeycomb framework carbon atoms, respectively, can be used to identify soot and various types

of ordered graphitic carbon (Ivleva et al., 2007b; Pimenta et al., 2007; Malard et al., 2009; Catelani et al., 2014; Gaffney et al., 2015; Doughty and Hill, 2017). A few optical images highlighting particles identified as graphitic soot are included in Figure A.5.

The organic cluster, which was almost a quarter fraction of the particles detected, was composed of many particles with diverse and rich spectra. As seen in the example spectra shown in Figure 2.6, these particles contained $\nu(SO_4^{2-})$, $\nu(NO_3^-)$, ν(N-H), and ν(O-H) stretching modes, as well as a variety of modes in the organic fingerprint region and different combinations of $\nu(CH_2/CH_3)$ symmetric and asymmetric stretching modes. The vibrational modes in the organic fingerprint region are difficult to identify with certainty due to the many different functional groups that exhibit Raman activity within that spectral window (Larkin, 2011). However, based on the functional groups of carboxylic acids, long chain aliphatics, fatty acids, organonitrates, and other compounds common to SOA, these vibrational modes are most likely stretching modes, such as ν(C-C), ν(C=C), ν(C-O), ν(C=O), $\nu(CO_2^-)$, and ν(C-OH), and bending, wagging, and rocking modes, such as $\delta(CH_2/CH_3)$, δ(C-C), δ(O-H), and δ(O-C-O) (Devillepin et al., 1982; McLaughlin et al., 2002; De Gelder et al., 2007; Ault et al., 2013b; Avzianova and Brooks, 2013; Laskina et al., 2013; Deng et al., 2014; Zhou et al., 2014). Figure 2.7 shows the further classification of the different types of organic particles based on their secondary components, with smaller clusters broken out on the right-hand side of the figure for clarity. Cluster fraction values with standard error can be found in Table A.7. A brief comparison of the CC-Raman analysis with CCSEM analysis for two days, June 14 and July 8, is included in Figure A.6. This comparison shows that according to CCSEM, SOA comprises a large component of the SOAS aerosol population and CC-Raman can be used to further classify the SOA particles based on their secondary composition. As this work is focused on demonstrating the potential for CC-Raman to be applied to the study ambient aerosol particles, a forthcoming publication will provide further details on the chemical composition of the SOA, mixing state and atmospheric implications of the SOAS aerosol population. Just as there are challenges with directly comparing CC-Raman and CCSEM analysis due to the limitations and capabilities of each technique, direct comparison of CC-Raman analysis with other work characterizing SOA particles from SOAS, such as studies of organic nitrates (Lee et al., 2016), IEPOX derived SOA (Lopez-Hilfiker et al., 2016), and dust and sea spray aerosol (Allen et al., 2015) may be difficult

due to differences in the size of particles analyzed and the specific properties characterized by each technique.

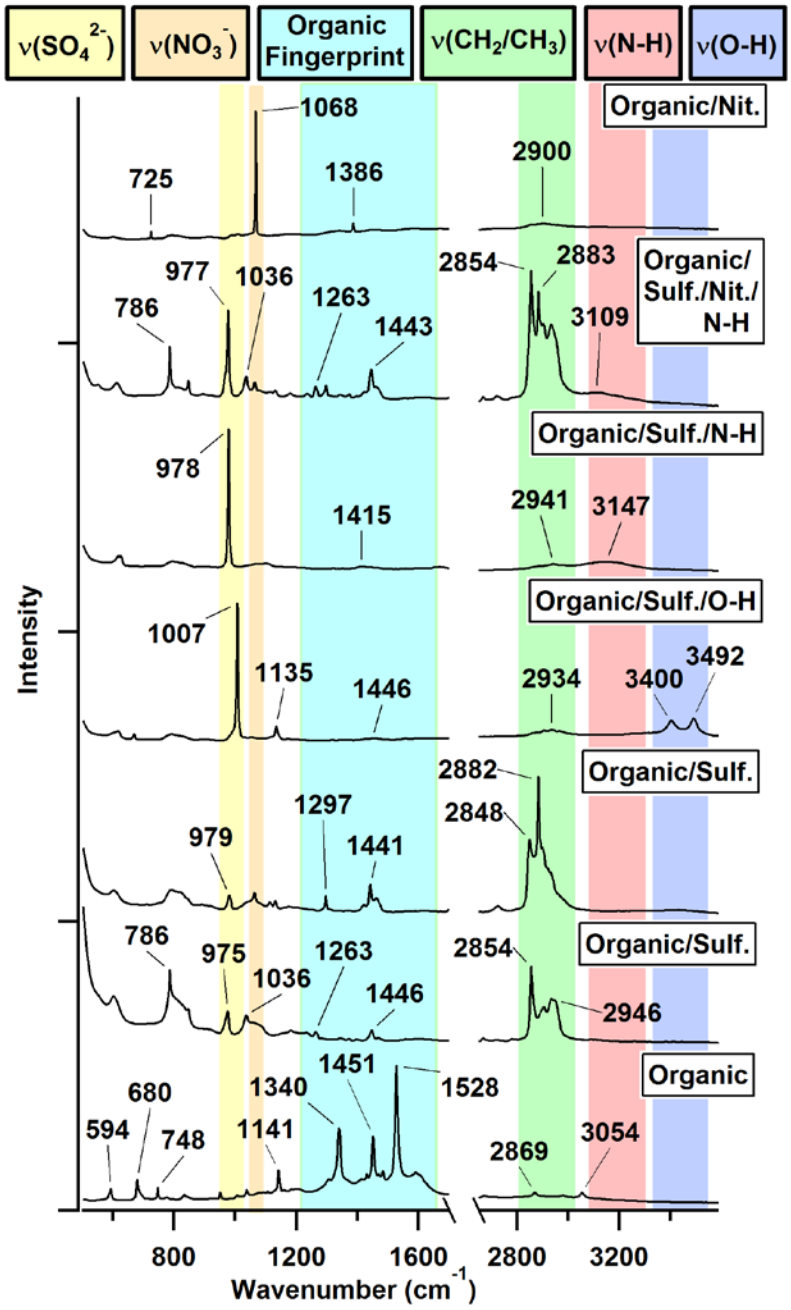

Figure 2.6 Example Raman spectra of the fingerprint region (<1600 cm^{-1}) and higher energy region (2700-3600 cm^{-1}) of particle types identified within the organic class of SOAS aerosol particles. Each spectrum was normalized to the highest intensity peak.

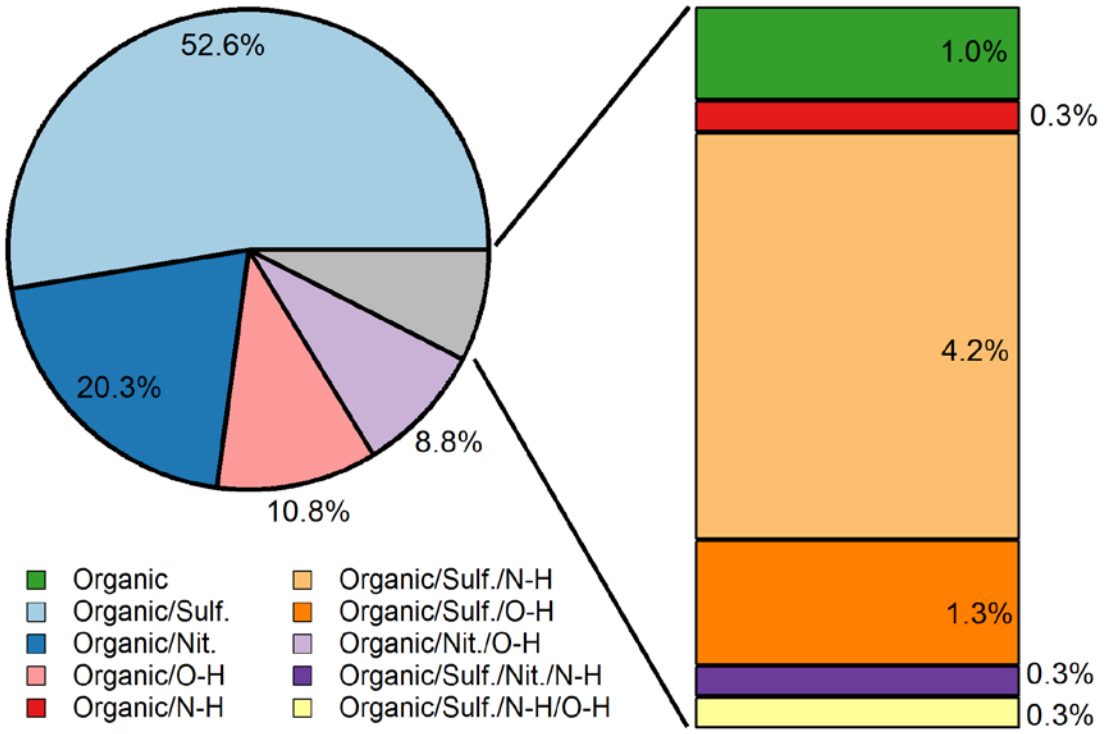

Figure 2.7 Further classification of the SOAS organic cluster based on the secondary components identified from the vibrational modes present in the Raman spectra.

For the ambient samples, CC-Raman provided less information on the primary components and general classification of aerosol particle types. For example, sea spray aerosol (SSA) was difficult to identify by CC-Raman since key SSA components, such as NaCl and $MgCl_2$, do not contain Raman-active vibrational modes. Additionally, while Raman is sensitive to many vibrational modes of mineral components, due to the high photon energy of the 532 nm laser, the Raman spectra of mineral-containing dust particles are often overwhelmed by fluorescence features (Bozlee et al., 2005; Doughty and Hill, 2017). Other particle types also susceptible to fluorescence and/or burning interference include biological and biomass (Poehlker et al., 2012). As discussed above, soot particles typically have a distinct spectral signature but it can be challenging to distinguish that signature from the burning features of previously mentioned laser sensitive components (Sadezky et al., 2005; Ivleva et al., 2007b; Catelani et al., 2014; Gaffney et al., 2015; Doughty and Hill, 2017). Despite these limitations, there is great potential for CC-Raman to detect the secondary components of aerosol particles, especially those of secondary organic aerosol or other organic-containing particles, as demonstrated in Figures 6 and 7. In contrast to CCSEM, which can only identify the elemental

composition, CC-Raman can distinguish between the functional groups present in a particle that might consist of similar elemental composition. For example, CC-Raman can differentiate between nitric acid (HNO_3), nitrate (NO_3^-), nitrite (NO_2^-), or ammonium (NH_4^+) based on the different vibrational modes corresponding to each functional group, whereas CCSEM can only detect nitrogen and oxygen (and oxygen can be difficult to differentiate from signal due to the substrate). Probing secondary speciation with CC-Raman will allow for investigations to improve understanding of important physicochemical properties, including chemical mixing state and internal structure, as well as atmospheric processes such as water uptake and particle phase reactions.

2.4 Conclusions

This study demonstrates a new method, CC-Raman, for automated single particle aerosol analysis using information dense Raman microspectroscopy. CC-Raman maximizes the potential of Raman microspectroscopy for aerosol particle characterization, specifically in terms of identifying secondary chemical components in SOA and other organic-containing particles that can be difficult to detect. CC-Raman uses uniform, improved throughput analysis to provide information on the vibrational modes that can be used to identify the functional groups present in individual aerosol particles. In addition to identifying secondary species in SOA, CC-Raman can also be applied to study inorganic and non-fluorescing mineral components as well. Because of its ability to probe secondary species and properties of particles that other single particle techniques struggle to determine, CC-Raman can be used for investigations that will answer questions regarding the organic and inorganic molecular species present in aerosol particles, particle aging, and mixing of secondary species with primary components. Additional advantages of CC-Raman include minimal sample preparation and analysis at ambient temperature and pressure. CC-Raman, as a stand-alone technique or used in tandem with other methods, has the potential to be a powerful tool for studying important chemical and physical properties of aerosol particles to further understanding of their role in climate change and other atmospheric processes.

2.5 Acknowledgements

University of Michigan startup funds supported this project. RLC performed all CC-Raman research. ALB performed CCSEM research and the Michigan Center for Materials

Characterization (MC^2) is acknowledged for assistance. Funding for SOAS sampling was provided by the Environmental Protection Agency (EPA) (R835409). Professors Paul Shepson, Steve Bertman, Kerri Pratt, Ann Marie Carlton, as well as Manelisi Nhliziyo are thanks for assistance with SOAS sampling. The SOAS CCSEM analysis was performed at the Environmental Molecular Sciences Laboratory (EMSL), with assistance from Prof. Alex Laskin and Dr. Bingbing Wang, a Department of Energy (DOE) national user facility sponsored by the Office of Biological and Environmental Research at Pacific Northwest National Laboratory (PNNL). PNNL is operated for DOE by Battelle Memorial Institute under Contract No. DE-AC06-76RL0 1830. The University of Michigan Graduate School and Office of the Provost provided travel funds to PNNL.

Chapter 3. Surface Enhanced Raman Spectroscopy Enables Observations of Previously Undetectable Secondary Organic Aerosol Components at the Individual Particle Level

Adapted with permission from Craig, R. L., Bondy, A. L., and Ault, A. P.: Surface enhanced Raman spectroscopy enables observations of previously undetectable secondary organic aerosol components at the individual particle level, *Anal. Chem.*, 87, 15, 7510-7514, 2015. https://doi.org/10.1021/acs.analchem.6b01507

3.1 Introduction

Secondary organic aerosol (SOA) particles in the atmosphere are complex mixtures of organic and inorganic components (Surratt et al., 2010), with hundreds to thousands of different species present in individual particles, often at femtogram to attogram levels (Prather et al., 2008). In remote forested regions, biogenic volatile organic compounds (BVOC) contribute to 90% of SOA formation by mass (Virtanen et al., 2010), and SOA particles play an important role in climate by scattering solar radiation and nucleating cloud droplets which modify the properties of clouds (Carslaw et al., 2010). Yet, the specific organic species formed in the particle phase (Surratt et al., 2010), particle-to-particle variability (Prather et al., 2008), internal structure, phase state (i.e. liquid-liquid phase separations) (Virtanen et al., 2010; You et al., 2014), and particle evolution in the atmosphere remain poorly understood (Carslaw et al., 2010; Surratt et al., 2010). Single particle level analysis is particularly important as the particles composition, mixing state, and internal structure determines optical properties and water uptake (Jacobson, 2001; Prather et al., 2008).

Vibrational spectroscopy, and Raman microspectroscopy specifically, has potential to probe the moieties present and the molecular environment (phase state, protonation, etc.) at ambient temperature and pressure (Liu and Laskin, 2009; Worobiec et al., 2010; Ault et al., 2014). Unlike bulk infrared (IR) measurements of atmospheric particles, Raman does not have complications due to strong water absorption or interference in the fingerprint region, as with commonly used Teflon filters (Russell et al., 2009; Takahama et al., 2013). Raman microspectroscopy has been used primarily to probe the distribution of species within single

atmospheric particles > 1 μm in diameter (Baustian et al., 2012; Laskina et al., 2013; Jung et al., 2014; Sobanska et al., 2014).

However, despite this potential, Raman measurements of individual particles to date have been limited due to insufficient sensitivity to key trace species. Most Raman microspectroscopy measurements of atmospheric particles have focused on highly Raman-active modes, such as $\nu_s(SO_4^{2-})$, $\nu_s(NO_3^-)$, and the ν(C-H) region (Batonneau et al., 2006; Baustian et al., 2012; Ault et al., 2013b; Jung et al., 2014). These modes provide only a limited understanding of the species present and the reactions that occur within particles. To elucidate particle-phase processes requires measurements that produce greater intensity for organic modes in the fingerprint region. Additionally, the vast majority of secondary particles in the atmosphere, as well as those with the longest lifetimes, are < 1 μm in diameter. The optical and cloud nucleating properties of these small particles must be linked with chemical speciation to reduce aerosol climate uncertainties (Prather et al., 2008). Thus, methods need to measure < 1 μm particles, as well as intra-particle spatial variability with < 0.5 μm resolution (Veghte et al., 2013).

The use of surface enhanced Raman spectroscopy (SERS) to study atmospheric aerosols has the potential to overcome both major limitations of Raman microspectroscopy: insufficient detection limits and spatial limitations due to the diffraction limit. SERS offers strong enhancements in Raman signal (up to 10^{10}) due to localized surface plasmon resonances (LSPRs) that activate over small spatial regions (< 10 nm) (Pierre et al., 2011; Sharma et al., 2012; Kleinman et al., 2013; Schlucker, 2014). SERS offers great promise to detect key functional groups in complex mixtures. Examples of compounds present in SOA with functional groups that SERS can probe include epoxides, organosulfates, and organonitrates. These species have been observed primarily on extracted samples with liquid chromatography coupled to high resolution mass spectrometry (Surratt et al., 2010; Staudt et al., 2014), as well as other mass spectrometry and spectroscopy techniques (Hatch et al., 2011; Takahama et al., 2013).

Herein, we show the first use of SERS to probe atmospheric aerosol particles. These proof-of-concept results demonstrate signal enhancement of key species, allowing for the measurement of previously undetectable functional groups and < 0.5 μm spatial variation of species within individual atmospheric particles. Figure 3.1 shows a schematic of an atmospheric particle deposited on quartz coated with Ag nanoparticles to generate SERS enhancement. However, not all Ag nanoparticles are SERS active (Kleinman et al., 2013; Schlucker, 2014), so

Raman signal enhancement is not uniform across a single particle, but rather is dependent on the distance from a SERS hot spot. Because of the dependence on hot spot location, a statistically significant number of particles and particle regions must be analyzed in order to determine representative speciation within the deposited particle population. However, greater quantification will be possible as more uniform surfaces are created with more complex SERS substrate preparation that increase the number of hot spots and create more homogeneous distributions of enhanced regions.

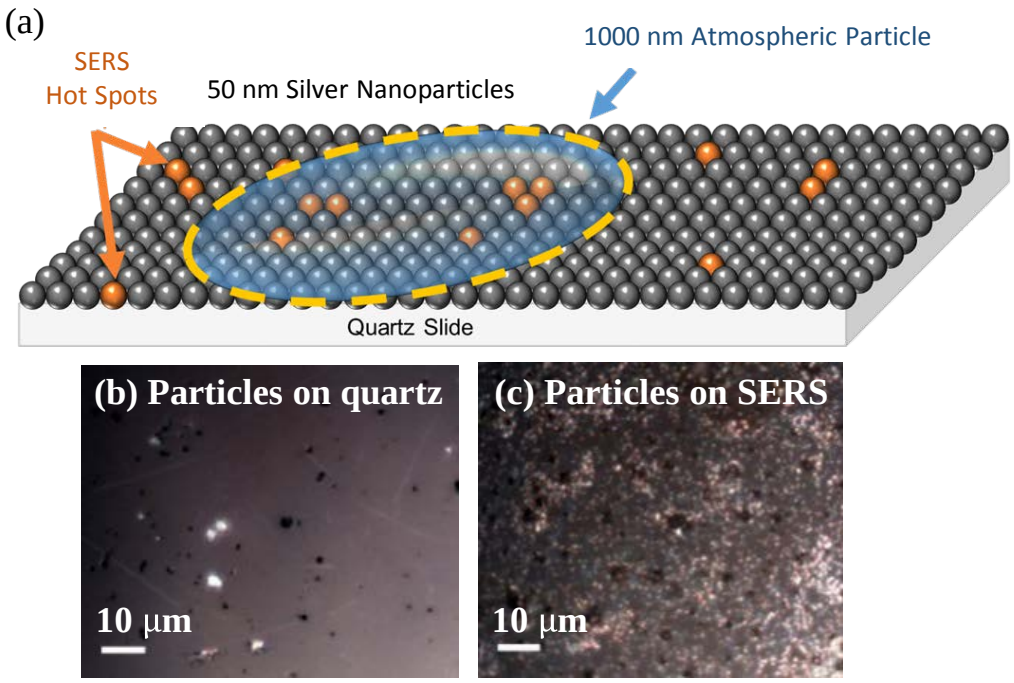

Figure 3.1 (a) Schematic of an aerosol particle impacted onto a SERS Ag nanoparticle coated quartz substrate. Optical image of aerosol particles impacted onto (b) quartz substrate and (c) Ag nanoparticle coated quartz substrate.

3.2 Methods

3.2.1 SERS Substrates

Ag nanoparticles were prepared by reduction of silver nitrate with hydroxylamine hydrochloride (Leopold and Lendl, 2003) and drop coated onto quartz substrates. The Ag nanoparticles were characterized with transmission electron microscopy (TEM), confocal optical microscopy, and UV-Visible spectroscopy. Details on the characterization are given in the Supplemental Information (Appendix B). An optical microscopy (100x objective) image of atmospheric particles impacted on a quartz substrate without Ag nanoparticles is shown in Figure

1b. Most aerosol particles appear dark, except for those containing minerals that fluoresce/scatter strongly. In contrast, the Ag nanoparticles are observed as bright particles on the quartz substrate (Figure 3.1c), with orange features indicating particularly SERS-active regions.

3.2.2 Aerosol Samples

Aerosolized $(NH_4)_2SO_4$ and $NaNO_3$ particles were generated in the laboratory using an atomizer. The particles passed through two diffusion dryers to remove excess water and impacted onto quartz and Ag nanoparticle coated quartz substrates using a Microanalysis Particle Sampler (MPS-3). Ambient aerosol particles were impacted onto quartz and Ag nanoparticle coated quartz substrates using a Micro-Orifice Uniform Deposit Impactor (MOUDI 110) at the University of Michigan Biological Station in Pellston, MI at the PROPHET Tower.

3.3 Results and Discussion

3.3.3 SERS of Standard Aerosol

Atomized ammonium sulfate and sodium nitrate were used to probe enhancement due to the SERS effect at the single particle level. Figure 3.2 shows a comparison of non-enhanced to SERS-enhanced spectra for the $\nu(SO_4^{2-})$ and $\nu(NO_3^-)$ modes, with average enhancement factors of 2.0 and 3.6, respectively. Two spectra exhibited large enhancement for $\nu(NO_3^-)$ (enhancement factors of 13 and 30). The $\nu(NO_3^-)$ peak red shifted from 1067 cm^{-1} to 1054 cm^{-1}, which has been observed previously in enhanced spectra of bulk aqueous nitrate and becomes more prominent with increased enhancement (Gajaraj et al., 2013), although an explanation for this shift has yet to be determined. The range of enhancement factors is most likely due to varying distance between particle and hot spot location.

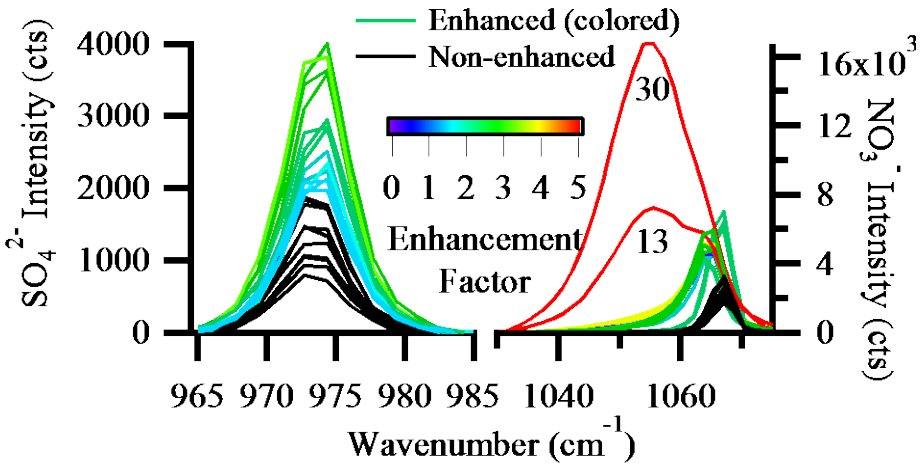

Figure 3.2 Non-enhanced and SERS-enhanced spectra for sulfate (left) and nitrate (right) stretching modes, derived from aerosolized $(NH_4)_2SO_4$ and $NaNO_3$. The color of the SERS-enhanced spectra corresponds to its enhancement factor, with those greater than 5 labeled above the spectra.

3.3.2 SERS of Ambient Aerosol

Ambient atmospheric particles were collected at a remote northern Michigan forested site, with sampling occurring above the forest canopy during a field study at the University of Michigan Biological Station (UMBS) near Pellston, MI. Enhancements were observed in the Raman signal due to the SERS effect for particles analyzed with a Raman microspectrometer using a 532 nm laser source (50 mW) and averaging 2 x 1 second acquisitions. The enhancements were observed across the Raman spectrum, both for modes previously studied for atmospheric particles, ($\nu_s(NO_3^-)$, ν_s(C-H), and ν(O-H)) (Batonneau et al., 2006; Baustian et al., 2012; Ault et al., 2013b; Jung et al., 2014), as well as modes not previously observed for organic functional groups in the fingerprint region (discussed below). Figure 3.3a establishes the enhancement in previously observed modes for a particle impacted on a region without Ag nanoparticles (blue) and spectra from particles deposited on the SERS-active Ag nanoparticles (red) (full spectra in Supplemental Information (Appendix B)). The enhancement in SERS spectra is shown for $\nu_s(NO_3^-)$, ν(O-H), and ν_s(C-H) with enhancement factors of 7, 12, and 14. A feature that is often barely detectable with conventional Raman microspectroscopy, δ(C-C), is also shown, with an enhancement factor of 8. It should be noted that the non-enhanced spectrum had the most intense signal of all spectra collected for particles not impacted on the Ag nanoparticles. Thus, comparison to that particle represents a lower limit regarding the enhancements observed. If comparisons were made to the mean non-SERS-enhanced spectrum

(by intensity), the signal is more than 10 times lower and many features were not present. This indicates average enhancements of 10^1-10^3 for these modes, which enable the detection of expected functional groups that have only been observed by extracting material from high volume samples (Surratt et al., 2010).

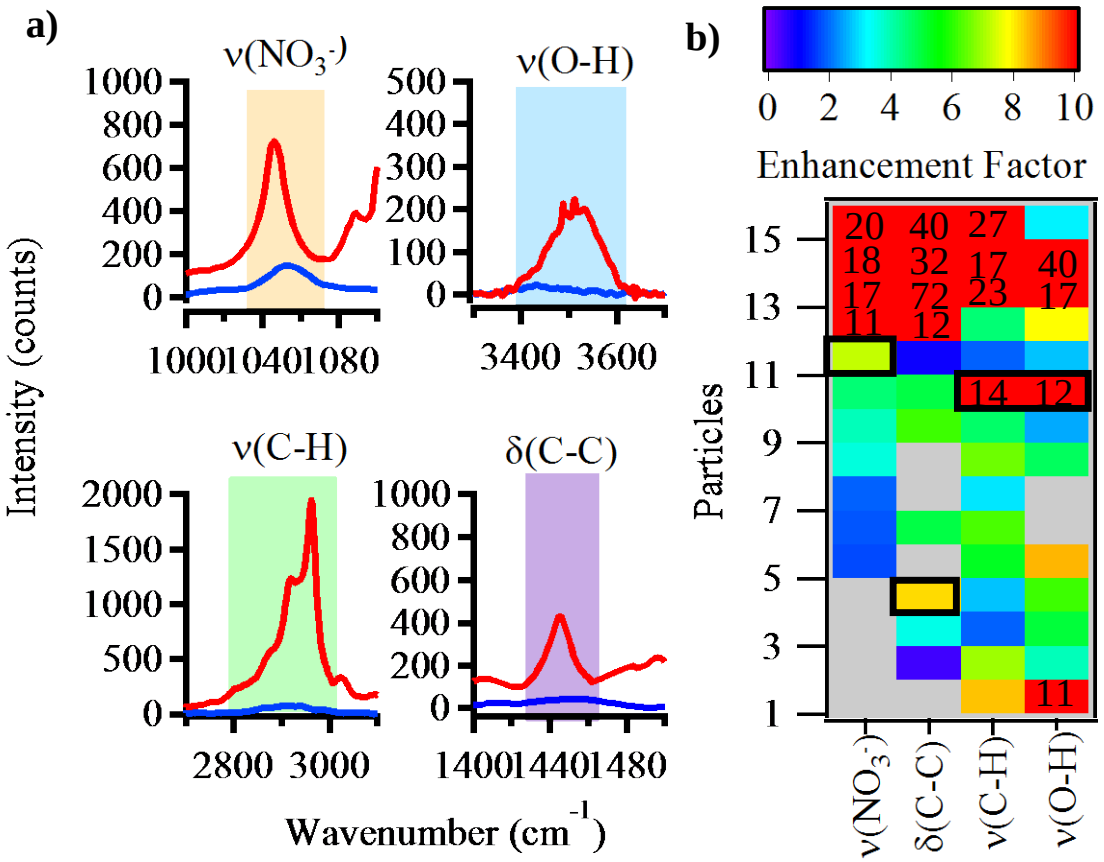

Figure 3.3 (a) Non-enhanced (blue) and SERS-enhanced (red) spectra of four different vibrational modes: ν(NO_3^-), ν(O-H), ν(C-H), and δ(C-C). The enhancement factor, 7.2, 11.7, 13.9, and 4.0, respectively, for the spectra represent median enhancement factor values for the 15 analyzed aerosol particles. (b) Calculated enhancement factor for 15 aerosol particles for the four vibrational modes of interest. Gray indicates the vibrational mode was not present in the Raman spectrum for a particular particle. The Raman spectra for vibrational modes highlighted by the black box is shown in (a).

As evidence that enhancement was widely observed for particles on SERS-active substrates, the enhancement factor was quantified for 15 particles compared to the most intense non-SERS enhanced particle from Figure 3.3a. The enhancement factors for the different regions from Figure 3.3a are shown as a heat map in Figure 3.3b (gray indicates no peak for a mode in that particle). The spectra exhibited a wide range of enhancements, with ~31% of modes being enhanced by more than a factor of 10; the largest observed enhancement factor was 72. The

vibrational modes highlighted by black boxes in Figure 3.3b, represent median enhancement factor values and correspond to the spectra shown in Figure 3.3a. The enhancement factor is not consistent across all vibrational modes, which can be attributed to particle-to-particle compositional variability and the non-uniform coupling of species from the different particles to the LSPRs (Haes and Van Duyne, 2004). Atmospheric particles frequently have complex internal structures, but have primarily been studied under the vacuum of electron microscopes (at times with cryo-stages) or with fluorescence microscopy on particles much larger than those present in the atmosphere (~40 um) (Ault et al., 2013a; Veghte et al., 2013; You et al., 2014). The small distance where SERS enhancement is localized (<10 nm) will allow Raman microspectroscopy to probe structure and phase state for particles in the size range (0.2 - 1.0 μm) where liquid-liquid phase separations and other complex morphologies are observed under atmospherically-relevant conditions (Veghte et al., 2013; You et al., 2014).

While Figure 3.3 focuses on modes that have already been studied, the previously unobserved peaks corresponding to other modes that were enhanced in the particles on the SERS-active substrate represent the most exciting results of this proof-of-concept study. Figure 3.4 shows spectra corresponding to four different SERS-enhanced particles, with the fingerprint region (500-1800 cm^{-1}) shown on the left and the higher energy, ν(C-H) and ν(O-H), stretching region on the right. It is important to note the peaks that are observed in the fingerprint region are of greater intensity than those of any previously studied atmospheric aerosol particles with Raman microspectroscopy. Due to the multitude of peaks in this region, only specific peaks are discussed here, with full assignment using standard molecules and a comparison with density functional theory calculations to be presented in a forthcoming paper. Peaks between 500-800 cm^{-1} correspond to δ(Si-O-Al) modes of aluminosilicate minerals present in dust particles, as well as bending modes of organic species, such as δ(O-C-O) of carboxylic acids (Frost et al., 1997; Laskina et al., 2013). The peaks in the low 900 cm^{-1} range are likely due to δ(O-H) (Larkin, 2011). Peaks at 998 cm^{-1} and 1051-1053 cm^{-1} are characteristic of $\nu_s(SO_4^{2-})$ and $\nu_s(NO_3^-)$, respectively (Ault et al., 2013b, 2014). Future work will utilize standards of non-volatile and low-volatility organic species predicted to be in the particle phase (i.e. organonitrates) to gain further insight into the functional groups from different species present. Preliminary assignment of peaks in the fingerprint region indicates the following functional groups/modes: carbonyls, aromatics, alcohols, methyl rocking and scissoring modes, and organonitrates, ν_s(N-O) at ~1650

cm^{-1}. Details on peak assignments and supporting SEM/EDX data are given in the Supplemental Information (Appendix B). These functional groups are consistent with the expected organic species in SOA particles from a high BVOC site (Surratt et al., 2010).

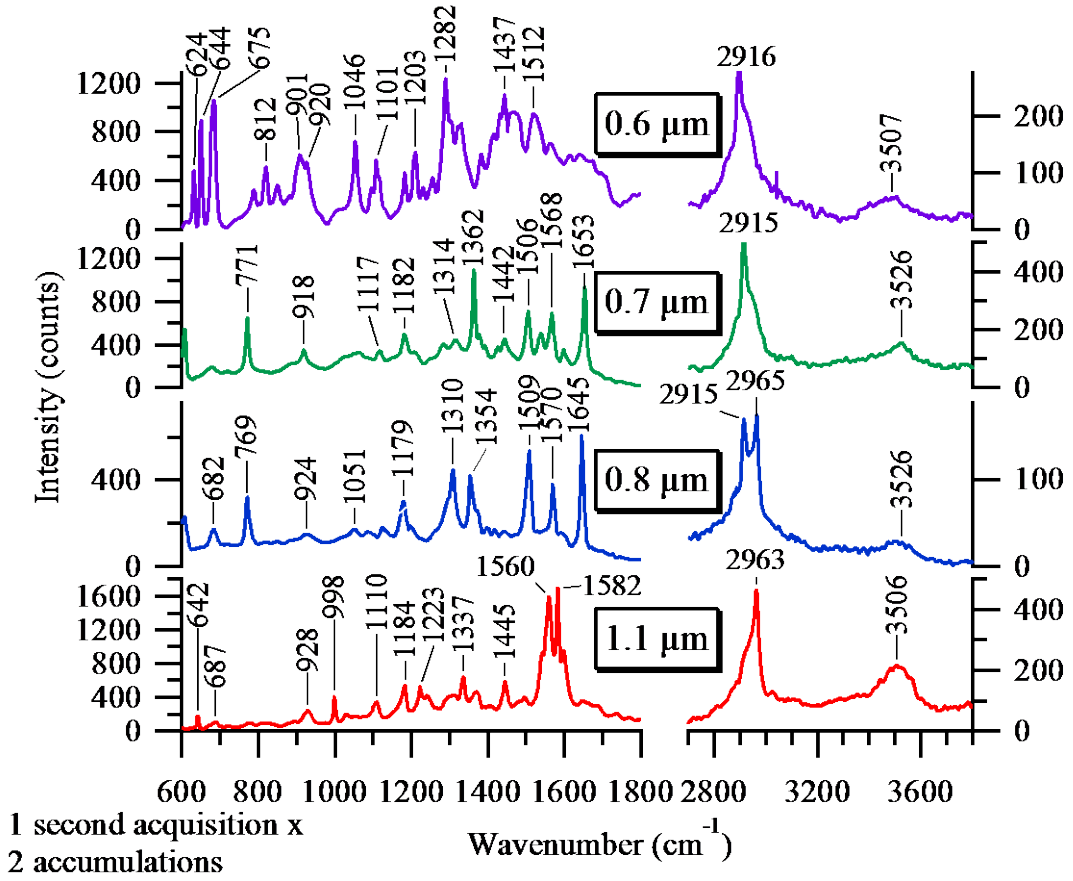

Figure 3.4 Raman spectra of the fingerprint region (500-1800 cm^{-1}) and higher energy region (2700-3800 cm^{-1}) of four ambient aerosol particles exhibiting enhancement.

The ν(C-H) and ν(O-H) stretching regions in Figure 3.4 contain information related to previous Raman microspectroscopy studies of atmospheric particles. The peaks at 2915 cm^{-1} and 2965 cm^{-1} are characteristic of $\nu_a(CH_2)$ and $\nu_a(CH_3)$, respectively (Larkin, 2011; Ault et al., 2013b). The peaks for the asymmetric stretches are much more intense than for the symmetric stretches, $\nu_s(CH_2)$ and $\nu_s(CH_3)$ (2850 and 2870 cm^{-1}, respectively). This indicates that there are few organic molecules with long, straight-chain alkanes (without gauche defects), as expected based on predicted particle phase products of isoprene oxidation (Surratt et al., 2010; O'Brien et al., 2013). Although organic –OH groups, such as polyols, could contribute to the broad peak centered around 3500 cm^{-1} indicative of ν(O-H), it is most likely from the presence of water (Ault et al., 2013b). The water content of SOA particles is important for determining key particle

phase processes, including hydrolysis rates and phase separations (Jacobs et al., 2014; You et al., 2014). By making measurements at ambient temperature and pressure, Raman microspectroscopy can probe these water-mediated processes directly.

Figure 3.5 shows the intra-particle distribution of functional groups for an SOA particle, which SERS can be used to study with 0.5 μm spatial resolution. An optical image and a spectral map representing the intensity for specific peaks across the particle are shown in Figure 5a and 5b, respectively. The green, blue, and red intensities of the spectral map represent the spectral intensity at 1022 cm^{-1} corresponding to $\nu_w(CH_2)$, 1480 cm^{-1} for δ(C-C), and 1370 cm^{-1} for $\nu_a(NO_3^-)$ (Larkin, 2011). Spectra collected from the red region also have a peak for the aqueous symmetric stretch of nitrate, $\nu_s(NO_3^-)$ at 1051 cm^{-1} (Ault et al., 2014). The spectra in Figure 3.5c represent a point from each of the colored regions in Figure 3.5b; these show the complexity and variability of spectra that can be observed within individual particles on submicron spatial scales with SERS. It should be noted that particle impaction and drying on the substrate can modify the distribution of species within a particle, though relative humidity control in future studies will minimize potential effects. This data highlights the potential for mapping atmospheric particles with < 1 μm resolution.

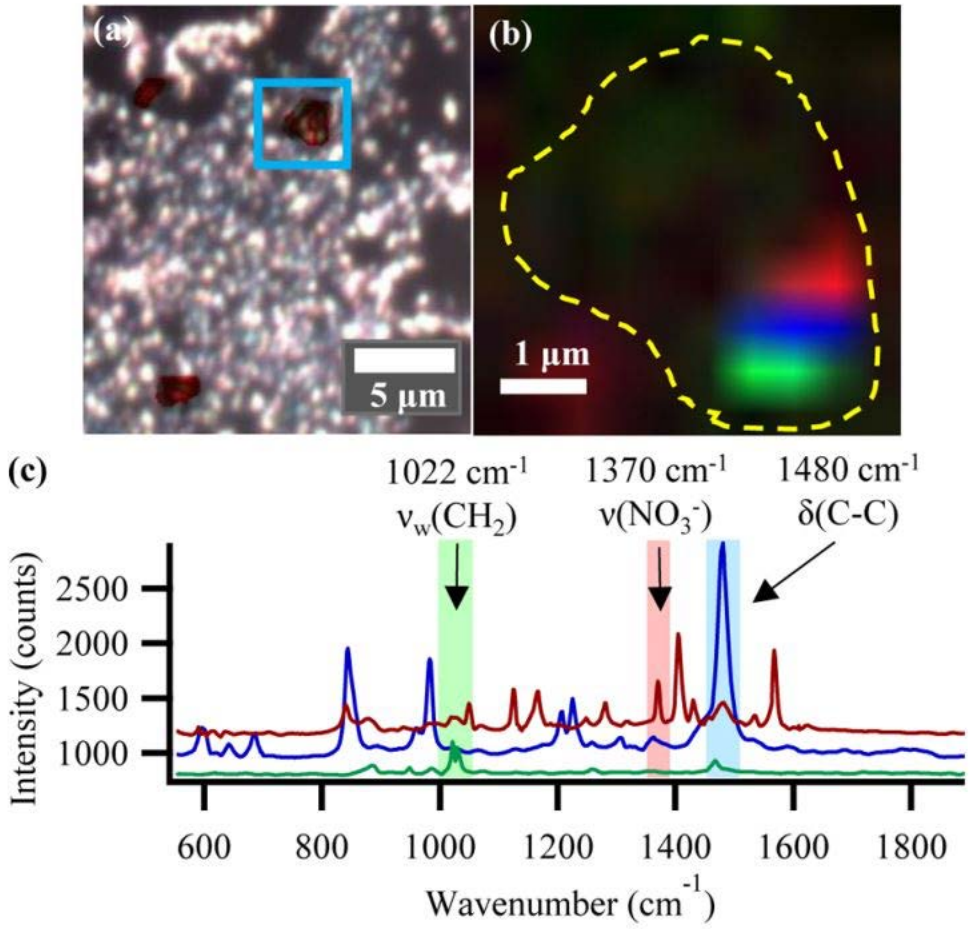

Figure 3.5 (a) Optical image of aerosol particle (highlighted in red) against SERS substrates and mapped area (blue box). (b) Map of the aerosol particle (outlined in yellow dashes) showing the location of the three different enhancec chemical species at 1022 cm^{-1} (green), 1370 cm^{-1} (red), and 1480 cm^{-1} (blue). (c) Raman spectra accompanying mapped intensities.

A separate challenge for this method is that particle depth is not even across its diameter. Atomic force microscopy has shown that a ratio of 3:1 (width:height, at particle center) is often observed for impacted particles meaning the thickness varies from a few nm to 750 nm for a 3 µm particle (Sobanska et al., 2014). The photons from the SERS enhancement must pass through a greater thickness of particle at the center of the particle versus the edge and could explain why enhancement in Figure 3.5b is strongest at the edge of the particle, though hot spot location is also important.

It is important to consider the amount of a functional group needed to obtain a detectable signal. Assuming a density of ~ 1.2 g/cm^3 (typical for SOA particles (McMurry et al., 2002)), the

particle highlighted in Figure 3.5 has an area of ~ 7 μm^2 and mass of 1.7 pg. Enhancement is correlated to distance from an active SERS Ag nanoparticle. Assuming (generously) that only the 10 nm closest to the Ag nanoparticle exhibits enhancement, the volume and mass of the particle's enhanced region was calculated to be < 0.07 μm^3 and < 8 fg. Assuming the presence of 10's to 100's of species in that region, detection limits on the order of 10-100 attograms may be observed. Calculation details are in the Supplemental Information (Appendix B). Detection limit quantification, detailed species identification, and improved substrates will be presented in a future publication. Raman microspectroscopic detection of species at attogram to femtogram levels is unprecedented for atmospheric particles, showing the power of SERS.

3.4 Conclusions

The development of spectroscopic analytical methods, particularly with functional group characterization, has been cited as a needed complement to mass spectrometry-based analysis of aerosols (Lee and Allen, 2012). Raman microspectroscopy has great potential to fill this need by analyzing species within individual particles at ambient temperature and pressure. This technique has been limited by the inability to measure key spectral modes in the fingerprint region that can be used to study the functional groups of SOA. SERS represents a possible solution by enhancing signal in modes of previously undetectable organic species in atmospheric particles. As shown in this study, SERS was applied to studies of individual atmospheric aerosol particles for the first time, allowing for the detection of functional groups from previously undetectable species. This new analytical method produced the observation of greater than expected inter- and intra-particle variability of organic species present in SOA from a BVOC-rich field site. While previous studies expected homogeneity of organic species between and within single particles, the substantial particle-to-particle variability and changes in chemical composition on scales < 1 μm indicate the importance of phase state, internal structure, and viscosity for organic species distributions. The enhanced detection limits and spatial scales for SERS of atmospheric particles have the potential to provide key insights regarding particle-phase reactions of SOA and the role that phase and structure play in determining climate-relevant properties, such as light scattering or cloud activation.

3.5 Acknowledgements

University of Michigan's MCubed program funded sampling at the UMBS PROPHET Laboratory. Dr. David M. Gates provided a fellowship to support RLC's work at UMBS. University of Michigan startup funded the remainder of the project. RLC performed all SERS research. ALB performed microscopy analysis. Daniel Gardner, Jillian Cellini, Stephanie Schmidt, Matthew Gunsch, Nathaniel May, Kerri Pratt, and Steven Bertman assisted with fieldwork. UM's Electron Microbeam Analysis Laboratory (EMAL) is acknowledged for assistance with TEM. The authors thank Renee Frontiera for insightful discussions and Joel Rindelaub and Paul Shepson for providing SOA standards to assist with spectral assignments.

Chapter 4. Surface Enhanced Raman Spectroscopy of Submicron Sized Aerosol Particles: Breaking the Diffraction Limit

Adapted with permission from Tirella, P. N., Craig, R. L., Tubbs, D. B., and Ault, A. P.: Investigation of Submicron Sized Aerosol Particles with Surface Enhanced Raman Spectroscopy (SERS), *Analyst*, 2018, under review with journal.

4.1 Introduction

Atmospheric aerosol particles impact climate by scattering and absorbing solar radiation and acting as cloud condensation and ice nuclei (Ramanathan et al., 2001; Pöschl, 2005; Andreae and Rosenfeld, 2008; Prather et al., 2008). However, these impacts are difficult to quantify due to the complex physicochemical properties of aerosols, particularly in terms of chemical composition, as individual particles can contain hundreds to thousands of different chemical species (Prather et al., 2008). An important example is secondary organic aerosol (SOA), which forms when oxidation products of volatile organic compounds (VOCs) condense onto existing aerosol particles composed of inorganic salts (i.e. ammonium sulfate) (Hallquist et al., 2009; Ziemann and Atkinson, 2012; McNeill, 2015). These particles contain both organic and inorganic components, but particle-to-particle variability in chemical composition, referred to as mixing state (Bauer et al., 2013; Riemer and West, 2013; O'Brien et al., 2015a; Fierce et al., 2016), due to different atmospheric processes is not well understood (Hallquist et al., 2009; Virtanen et al., 2010; You et al., 2014). In addition, aerosols can have intraparticle chemical variability through processes such as liquid-liquid phase separation (Smith et al., 2013; You et al., 2014; O'Brien et al., 2015b; Zhang et al., 2018). More detailed investigations of particle chemical composition are needed to improve understanding of multiphase aerosol processes, such as heterogeneous reactions, water uptake, phase transitions, and gas-particle partitioning.

Over the past decade, Raman microspectroscopy has been increasingly applied as an analytical technique for chemical characterization of aerosol particles (Stefaniak et al., 2009; Ault and Axson, 2017). This technique uses inelastically scattered light to detect vibrational modes present within a sample, which can then be used to identify functional groups and

chemical species. Raman microspectroscopy has been applied to characterize many different particle types, such as sea spray and other marine aerosol (Ault et al., 2013b; Deng et al., 2014; Sobanska et al., 2014; Bondy et al., 2017b), soot and elemental carbon (EC) particles (Rosen and Novakov, 1977; Rosen et al., 1978; Ivleva et al., 2007a; Catelani et al., 2014), mineral dust (Sobanska et al., 2012; Laskina et al., 2013; Catelani et al., 2014; Jung et al., 2014), and SOA (Craig et al., 2017a). as well as specific compounds commonly found in aerosols, including biological molecules (De Gelder et al., 2007) and various organic compounds like organic nitrates (McLaughlin et al., 2002), organosulfates (Bondy et al., 2018), and glyoxal oligomers (Avzianova and Brooks, 2013). Raman analysis has also been used to study hygroscopic properties (Jordanov and Zellner, 2006; Lee et al., 2008; Yeung and Chan, 2010; Bones et al., 2012; Chu et al., 2015), phase separations (Ciobanu et al., 2009; Bertram et al., 2011; Zhou et al., 2014), heterogeneous reactions (Lee and Chan, 2007; Ault et al., 2014; Bondy et al., 2017b), ice nucleation (Baustian et al., 2012), and acidity of aerosols (Rindelaub et al., 2016a; Craig et al., 2017b). Advantages of this technique include minimal sample preparation and non-destructive analysis under ambient temperature and relative humidity (RH) conditions. However, detection limits in terms of both particle size and concentration of chemical species present can make Raman microspectroscopic studies of aerosol particles challenging. The majority of aerosol particles, particularly those with lifetimes long enough to react and undergo atmospheric processing, are <1 μm, but Raman microspectroscopy has been applied mostly to the study of particles >1 μm, often 10-30 μm, due to the diffraction limit of wavelengths commonly used for Raman analysis (532 or 640 nm with a confocal microscope with 100x objective). Furthermore, even in supermicron atmospheric particles, chemical species are often present in very low concentration, making it difficult to detect Raman signal with enough intensity to determine the identity of vibrational modes and corresponding functional groups. Lastly, important particle properties, such as deliquescence relative humidity, can be size-dependent, limiting the ability to translate studies on large particles to atmospherically relevant sizes (Laskina et al., 2015). If SERS can be used to overcome the detection limit challenges associated with small particle sizes, the potential for Raman microspectroscopic analysis of aerosol particles to improve understanding of chemical composition and mixing state will greatly increase.

Surface enhanced Raman spectroscopy (SERS) can be used to improve the limit of detection of low concentration chemical species (Schlucker, 2014). Through SERS, weak Raman

signals are enhanced via interactions with localized surface plasmon resonances (LSPRs), which are generated by excited electrons in metallic substrates (Nie and Emory, 1997; Sharma et al., 2012; Kleinman et al., 2013; Schlucker, 2014; Keller et al., 2015). The metallic substrates are often silver, gold, or copper and can be in the form of foils, geometric nanoparticles, and colloids (Sharma et al., 2012, 2013; Kleinman et al., 2013). SERS has applications in many different fields, from biosensing to art preservation, and enhancement factors (EFs) for vibrational intensities of analytes are reported to be as large as $10^2 - 10^{12}$, and even up to 10^{15} for single molecule SERS (Nie and Emory, 1997; Pierre et al., 2011; Sharma et al., 2012; Kleinman et al., 2013; Schlucker, 2014; Keller et al., 2015). With SERS, limitations of spatial resolution and detection of chemical species present in trace amounts in aerosol particles can be overcome.

After a few preliminary qualitative studies showing its potential with bioaerosols (Ayora et al., 1997; Sengupta et al., 2005; Schwarzmeier et al., 2013), SERS has recently been applied to the study of aerosol particles more broadly and in a more quantitative manner. In 2015, Craig et al. used silver nanoparticle coated quartz substrates to investigate both ammonium sulfate and sodium nitrate aerosol particle standards as well as ambient aerosol (Craig et al., 2015) and in 2016, Fu et al. used Klarite, a commercially available Au substrate of structured gold inverted pyramids, to study ammonium sulfate and naphthalene mixed particles (Fu et al., 2017). A few variations of SERS, such as tip-enhanced Raman spectroscopy (TERS) (Ofner et al., 2016), electrospray SERS (ES-SERS) (Gen and Chan, 2017), and surface-enhanced resonance Raman spectroscopy (SERRS) of trapped and suspended particles (Sivaprakasam et al., 2017), have also been applied to study aerosol particles. Reported EFs ranged from 2.0 – 70 for $\nu_s(SO_4^{2-})$, $\nu_s(NO_3^-)$, ν(C-H), ν(O-H), and δ(C-C) vibrational modes (Craig et al., 2015; Fu et al., 2017; Gen and Chan, 2017) and 10^5 for vibrational modes of Rhodamine 590 chloride (R6G), a dye with a large scattering cross-section commonly used for SERS studies (Sivaprakasam et al., 2017). However, most particles probed in these studies were supermicron, not in the submicron size range typical for ambient aerosol, and further work can be done to increase EFs for vibrational modes corresponding to more atmospherically-relevant chemical compounds.

In this study, silver SERS substrates, including Ag nanoparticles and roughened Ag foil, were tested with both organic and inorganic species commonly observed in aerosols. Additionally, laboratory-generated and ambient aerosol particles <1 μm were analyzed to explore the lower limit in terms of particle size for SERS using these simple methods. The results of this

study highlight the potential for SERS analysis of aerosol particles with atmospherically-relevant sizes (down to 150 nm) to improve understanding of chemical composition, mixing state, and other physicochemical properties that impact aerosol climate effects.

4.2 Methods

4.2.1 Materials and Reagents

Quartz slides (Ted Pella, Inc.) and silver foil (ESPI Metals) were purchased and used as substrates. Silver nitrate ($Ag(NO_3)_2$) (Sigma-Aldrich), hydroxylamine hydrochloride (Sigma-Aldrich), and sodium hydroxide (Fischer) were used for silver nanoparticle (AgNP) synthesis. Polystyrene latex sphere (PSL) standards (Polysciences, Inc.), ammonium sulfate ($(NH_4)_2SO_4$) (Alfa Aesar), and sodium nitrate (Sigma Aldrich) were used chemical standards. All chemicals were >98% purity and used without further purification.

4.2.2 Substrate Preparation

Quartz coverslips were cut and cleaned prior to use as either a common Raman substrate or a base for a silver nanoparticle (AgNP) SERS substrate. AgNPs were synthesized by reducing silver nitrate with hydroxylamine hydrochloride, according to the method by Leopold and Lendl (Leopold and Lendl, 2003). The resulting colloidal solution of AgNPs was drop-coated onto clean quartz slides and dried in a desiccator to create SERS substrates in the same manner as Craig et al. (Craig et al., 2015). Silver foil was cut for use as SERS substrates.

4.2.3 Laboratory-Generated Aerosol Particle Samples

Organic aerosol particle standards were generated from colloidal solutions of PSLs of varying size (400 nm, 600 nm, and 800 nm). Inorganic aerosol particle standards were generated from solutions of 30 mM $(NH_4)_2SO_4$ or 30 mM $NaNO_3$. All solutions were made with 18.3 MΩ Milli-Q water. Aerosol particles were generated with a Collison nebulizer operated with HEPA-filtered air and then passed through two diffusion dryers to remove excess water before being impacted onto substrates with a microanalysis particle sampler (MPS-3, California Instruments, Inc.). Prior to impaction, the inorganic standard particles were size-selected at 400 nm, 600 nm, or 800 nm (electrical mobility diameter) with an electrostatic classifier (Model 3080, TSI Corporation) equipped with a long differential mobility analyzer (Model 3082, TSI Corporation) at sample to sheath flow ratio of 1:8.3 (0.3 to 2.5 lpm).

4.2.4 Ambient Aerosol Particle Samples

Ambient samples were collected from outside the University of Michigan Chemistry Building (930 N. University Ave. Ann Arbor, MI 48109). Samples were size selected at 150 nm (electrical mobility diameter) and then collected on Ag foil via impaction with the MPS-3.

4.2.5 Raman Microspectroscopy

Raman analysis was performed with a Horiba Labram HR Evolution Raman spectrometer (Horiba Scientific) coupled to a confocal optical microscope (100x Olympus objective, 0.9 N.A.). The spectrometer was equipped with a Nd:YAG laser source (50mW, 532nm) and a CCD detector. 600 groove/mm diffraction grating yielded spectral resolution of ~ 2 cm^{-1}. Calibration was carried out daily against the Stokes Raman signal of a pure silicon standard at 520 cm^{-1}. Laser power was attenuated with neutral density (ND) filters ranging from 1 to 100 to prevent sample damage. Spectra were collected for the range of 500 to 4000 cm^{-1} for 3 accumulations with 15 s acquisition time. 8-15 particles were analyzed for each sample. Raman maps were collected with computer-controlled XY Raman mapping, with spectra recorded on a point-by-point scanning mode with a 0.25 μm step size. Map spectra were also collected across a range of 500 to 4000 cm^{-1} for 3 accumulations with 15 s acquisition time.

SERS EFs were calculated for vibrational modes of interest according to Equation 1, I_{SERS} and I_{RC} are the Raman signal under SERS and non-SERS conditions, respectively, and c_{SERS} and c_{RC} are the analyte concentration under SERS and non-SERS conditions, respectively (Le Ru et al., 2007).

Equation 4.1
$$EF = \frac{I_{SERS}/c_{SERS}}{I_{RS}/c_{RS}} = \frac{I_{SERS}}{I_{RC}}$$

Since sample preparation for SERS and non-SERS conditions was identical, c_{SERS} can be assumed to be equal to c_{RC} and the equation to calculate EFs can be simplified to a comparison of I_{SERS} and I_{RC}. I_{SERS} and I_{RC} are represented by the integrated peak area for the respective vibrational modes. Integrate peak areas were determined along the natural baseline of the spectra using a multipeak fitting software package (Igor Pro, WaveMetrics). The average integrated peak area for Raman spectra collected under non-SERS conditions was used for I_{RC}.

4.3 Results and Discussion

4.3.1 Ag Substrate Testing

Laboratory-generated aerosol particle standards were used to investigate various Ag SERS substrates, including AgNP coated quartz and Ag foil, and their application to aerosol particle studies. Raman spectra of standard PSL particles collected from each substrate showed that, while both Ag SERS substrates enhanced the Raman signal across all vibrational modes, Ag foil yielded significantly higher EFs (Figure 4.1). For the symmetric ring stretching modes, ν_s(C-C) (Jasse et al., 1978; Sears et al., 1981; Larkin, 2011) at 1000 cm^{-1} and ν_s(C=C) (Jasse et al., 1978; Sears et al., 1981; Larkin, 2011) at 1602 cm^{-1}, average EFs were 21 for both modes for the Ag foil and 2 and 3 for the AgNP substrate, respectively. In comparison to the ring stretching modes, C-H bending and stretching modes showed greater enhancement in response to the SERS effect. Average EFs for the C-H bending mode (δ(C-H), 1452 cm^{-1}) (Jasse et al., 1978; Larkin, 2011), C-H stretching mode (ν(C-H), 2908 cm^{-1}) (Jasse et al., 1978; Larkin, 2011), and aromatic C-H stretching mode (ν(C-H) aromatic, 3054 cm^{-1}) (Jasse et al., 1978; Larkin, 2011) were 103, 123 and 70, respectively, for the Ag foil and 7, 5, and 2, respectively, for the AgNP substrate. The EF values for the AgNP substrate samples are consistent with previously reported EF values for $(NH_4)_2SO_4$ and $NaNO_3$ standard particles analyzed with SERS using similar substrates (Craig et al., 2015). The large variability in EFs, particularly evident for the Ag foil samples, could be attributed to varying degrees of coupling between LSPRs with analytes due to the roughened surface of the Ag foil or inconsistent distribution of AgNPs. Preliminary work testing several other Ag SERS substrates is included in Appendix C and results were, at best, comparable to the AgNP enhancement shown here. Despite the variability in enhancement, the Ag foil substrate yielded the highest EFs and thus, was used as the SERS substrate for all subsequent experiments in this work.

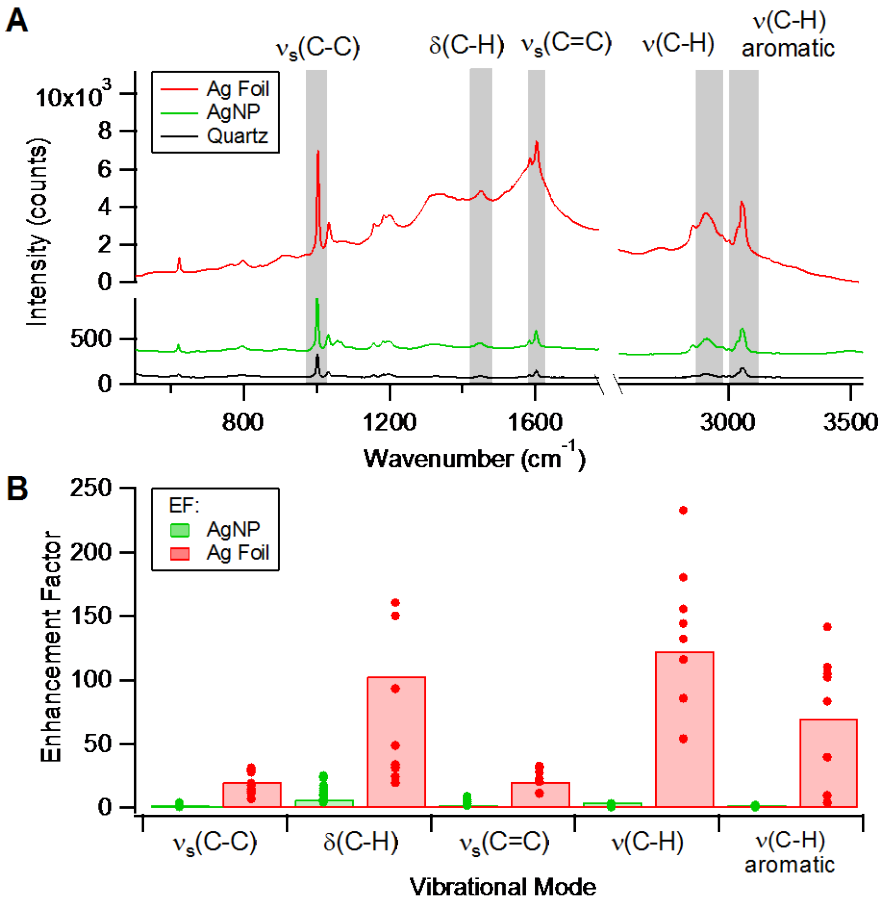

Figure 4.1 (A) Raman spectra of PSL particles on quartz, AgNP, and Ag foil substrates. (B) Comparison of calculated EFs for vibrational modes of interest for the AgNP and Ag foil SERS substrates. The points represent individual EF values and the bar indicates the average EF.

4.3.2 SERS of 400 – 800 nm Sized Laboratory-Generated Aerosol Particles

To investigate the potential of using SERS to study particles smaller than the size range typical for Raman analysis, <1 μm sized PSL particles were impacted on quartz and Ag foil substrates for SERS analysis. 400 nm, 600 nm, and 800 nm particles were tested and, as shown in Figure 4.2, spectra were successfully collected from particles at all sizes. Even though Raman signal was detected for PSL particles on plain quartz substrate, intensity was very low and vibrational modes were difficult to distinguish from background noise, particularly for the 400 nm sized particles. SERS enhancement was observed for all sized particles and average EFs for the five PSL vibrational modes ranged from 8 to 123. Similar to the PSL analysis in Figure 4.1, the δ(C-H) and ν(C-H) modes exhibited the largest enhancements. All Raman spectra, for PSL

particles on both quartz and Ag foil, are provided in Appendix C. It should be noted that both the 400 nm and 600 nm particles are smaller than the 721 nm diameter of the laser spot (for 532 nm laser with 0.9 N.A. objective).

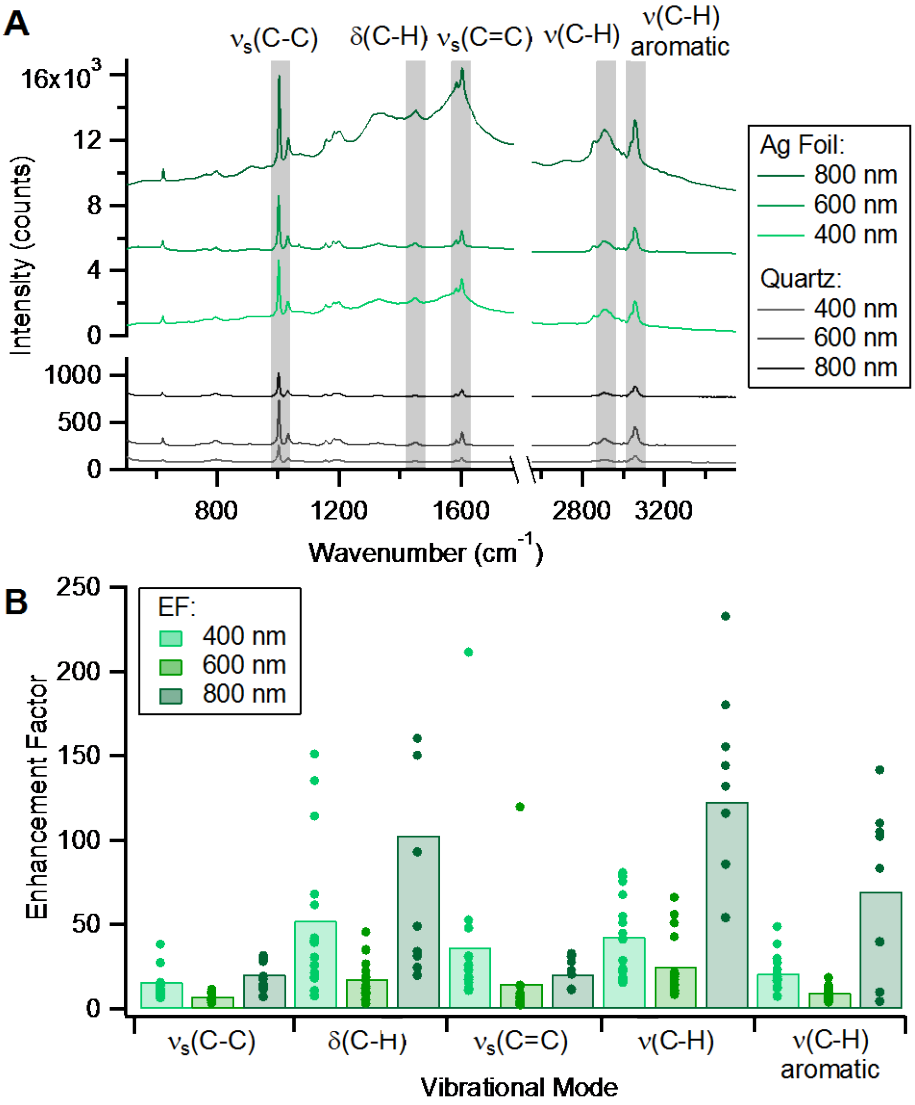

Figure 4.2 (A) Average Raman spectra for 400 nm, 600 nm, and 800 nm PSL particles on quartz and Ag foil substrates. (B) Calculated EFs for vibrational modes of interest for all particle sizes. The points represent individual EF values and the bar indicates the average EF.

Across all vibrational modes, there was no clear relationship between particle size and enhancement. Enhancement was expected to increase with increasing particle size, as the higher number of analyte molecules present in the larger particles could enable more opportunities for coupling to LSPRs and lead to greater enhancement of the Raman signal. This trend was

observed for the largest and smallest sized PSL particles analyzed, as the 800 nm particles were consistently more enhanced than the 400 nm particles, but the 600 nm particles exhibited the lowest levels of enhancement. The cause for the low enhancement observed for the 600 nm PSL particles is unclear at this time, but could possibly be due to crowding effects or the arrangement of PSL molecules hindering coupling between LSPRs and analyte molecules. The low enhancement for the 600 nm PSL particles could also be an anomaly, as the inorganic particles investigated as part of this study and discussed later were consistent with the 400 nm and 800 nm PSL particles, with larger sized particles yielding more enhanced spectra.

In addition to PSL particles, which are primarily organic, $(NH_4)_2SO_4$ and $NaNO_3$ particles were also tested since atmospheric aerosol particles often contain these inorganic components (Laskin et al., 2016). $(NH_4)_2SO_4$ and $NaNO_3$ particles were generated from solution and size-selected at 400 nm, 600 nm, and 800 nm for SERS analysis. For $(NH_4)_2SO_4$, the $\nu(SO_4^{2-})$ and the ν(N-H) stretching mode of NH_4^+ were studied (Figure 4.3). The $\nu_1(SO_4^{2-})$ (Venkateswarlu et al., 1975; Ault et al., 2013b; Jentzsch et al., 2013; Deng et al., 2014; Craig et al., 2017a) mode at 963 cm^{-1} had average EFs ranging from 128 to 324. There was a red shift in peak location for the SERS enhanced $\nu_1(SO_4^{2-})$ mode, shifting from 975 cm^{-1} to 963 cm^{-1}, along with an increase in peak broadness. This shift is possibly attributed to charge-transfer interactions between Ag and the $(NH_4)_2SO_4$ molecules and is consistent with earlier work studying SERS enhancement of $(NH_4)_2SO_4$/sucrose particles (Gen and Chan, 2017). The ν(N-H) (Venkateswarlu et al., 1975; Jentzsch et al., 2013) mode centered at 3130 cm^{-1} had average EFs ranging from 161 to 389. It should be noted that ν(N-H) is broader due to hydrogen bonding and can be difficult to quantify in low-intensity spectra. For $NaNO_3$, three stretches corresponding to NO_3^- were studied (Figure 4.4). $\nu_1(NO_3^-)$ (Rousseau et al., 1968; Jentzsch et al., 2013; Deng et al., 2014) at 1067 cm^{-1} had average EFs ranging from 11 to 23. There was a slight blue shift in peak location for the SERS enhanced $\nu_1(NO_3^-)$ mode, shifting from 1056 cm^{-1} to 1067 cm^{-1}. Interestingly, this result is inconsistent with previous work that observed a red shift from 1067 cm^{-1} to 1054 cm^{-1} for $\nu_1(NO_3^-)$ (Gajaraj et al., 2013; Craig et al., 2015). The 1054 cm^{-1} mode corresponds to aqueous, free NO_3^-, while the 1067 cm^{-1} mode corresponds to Na^+-bound NO_3^- (Jentzsch et al., 2013; Ault et al., 2014). Previous work proposed that $NaNO_3$ cannot couple as effectively as NO_3^- with the Ag substrate due to interaction with sodium or incorporation into a $NaNO_3$ amorphous solid or crystal, leading to a red shift occurring with increased enhancement

(Craig et al., 2015). Experimental conditions, such as RH impacts on particle phase, could play a role, but further work is needed to characterize this phenomenon and reconcile the discrepancy in observed peak shifting. $\nu_3(NO_3^-)$ (Rousseau et al., 1968; Jentzsch et al., 2013) at 1386 cm^{-1} and $\nu_4(NO_3^-)$ (Rousseau et al., 1968; Jentzsch et al., 2013) at 725 cm^{-1} had larger average EFs, ranging from 15 to 71. All Raman spectra, for $(NH_4)_2SO_4$ and $NaNO_3$ particles on both quartz and Ag foil, are provided in Appendix C.

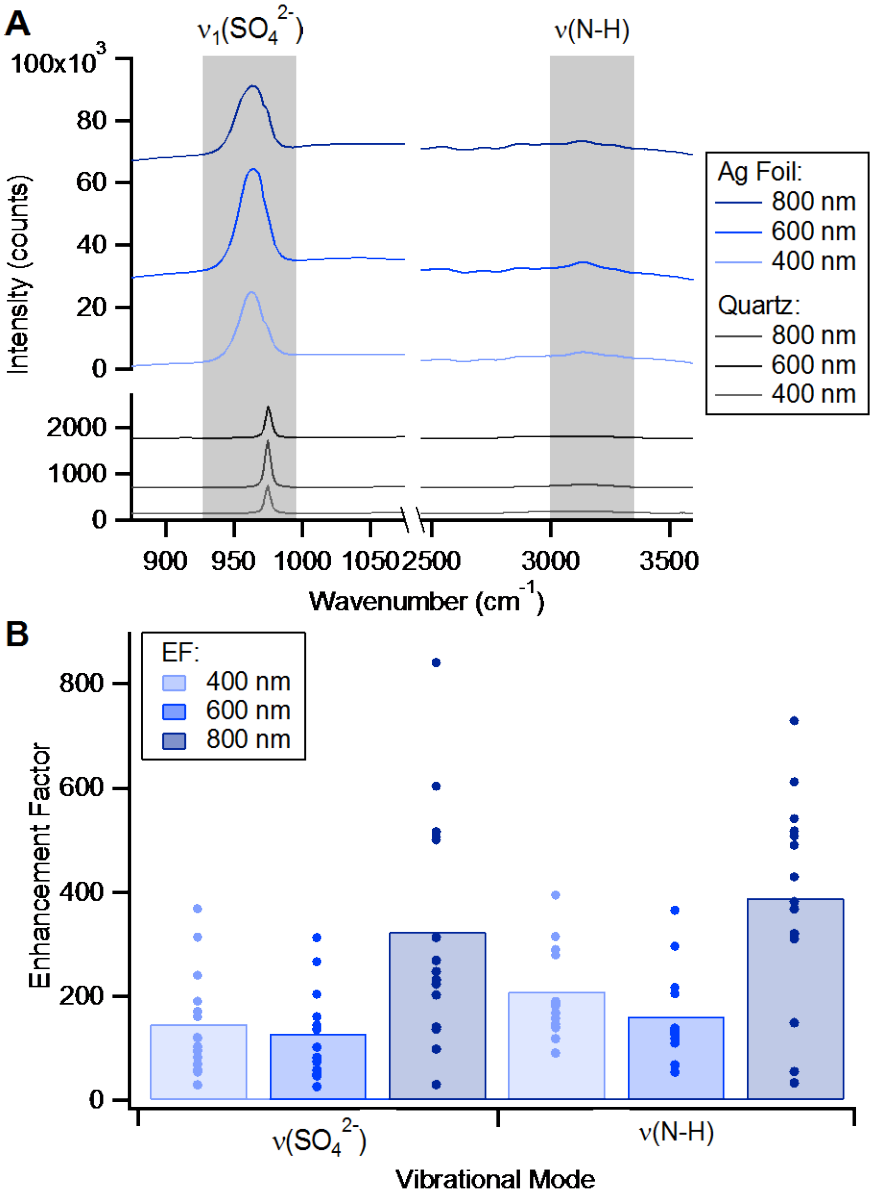

Figure 4.3 (A) Average Raman spectra for 400 nm, 600 nm, and 800 nm $(NH_4)_2SO_4$ particles on quartz and Ag foil substrates. (B) Calculated EFs for vibrational modes of interest for all particle sizes. The points represent individual EF values and the bar indicates the average EF.

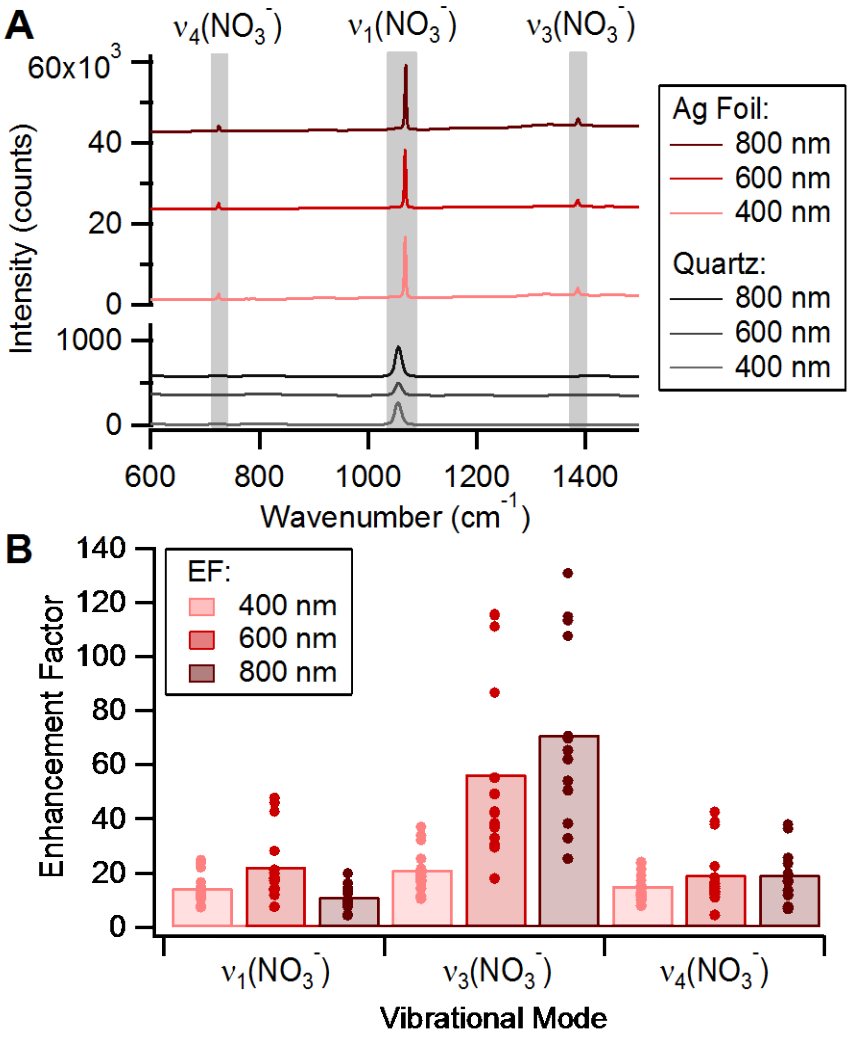

Figure 4.4 (A) Average Raman spectra for 400 nm, 600 nm, and 800 nm $NaNO_3$ particles on quartz and Ag foil substrates. (B) Calculated EFs for vibrational modes of interest for all particle sizes. The points represent individual EF values and the bar indicates the average EF.

EFs increased with increasing particle size for nearly all vibrational modes studied for the $(NH_4)_2SO_4$ and $NaNO_3$ particles. As discussed previously, this could be attributed to the higher number of analytes present in the larger particles, enabling more opportunities for interaction with LSPRs and leading to greater observed enhancement. Also, as with the PSL particles, there was a high level of variability in enhancement for all of the $(NH_4)_2SO_4$ and $NaNO_3$ vibrational modes.

4.3.3 SERS of 150 nm Sized Laboratory-Generated and Ambient Aerosol Particles

Thus far in this study, through SERS, the smallest particle size shown has been 400 nm, which is about 2-3 times smaller than the size of aerosol particles typically characterized through Raman analysis. However, SERS is capable of single molecule detection and so, should allow for Raman analysis of aerosol particles <400 nm. To test this limit, 150 nm PSL particles were collected on Ag foil. It should be noted that a 150 nm sized particle is well below to the diffraction limit of 361 nm for the Raman spectrometer used in this study (532 nm laser with 0.9 N.A./100x objective). Automated point-by-point mapping with a step size of 0.25 μm was used over a larger region of the substrate, enabling spectra to be collected for the 150 nm particles that were difficult to distinguish optically due to low spatial resolution. A representative spectrum for a 150 nm PSL particle and its corresponding location are shown in Figure 4.5. The five vibrational modes focused on in the earlier analysis are indicated, though other vibrational modes were also enhanced and present. In the optical image, the yellow box highlights the mapped region, while the red circle indicates the point corresponding to the SERS PSL spectrum. The small, dark spots are individual 150 nm PSL particles, while the larger spots are most likely agglomerates and were avoided for this specific analysis. It should also be noted that marks and scratches to the Ag foil can lead to intensity in the Raman spectra that make it difficult to identify vibrational modes corresponding to the particles. To reduce substrate interference, smooth regions of the Ag foil were selected for mapping analysis.

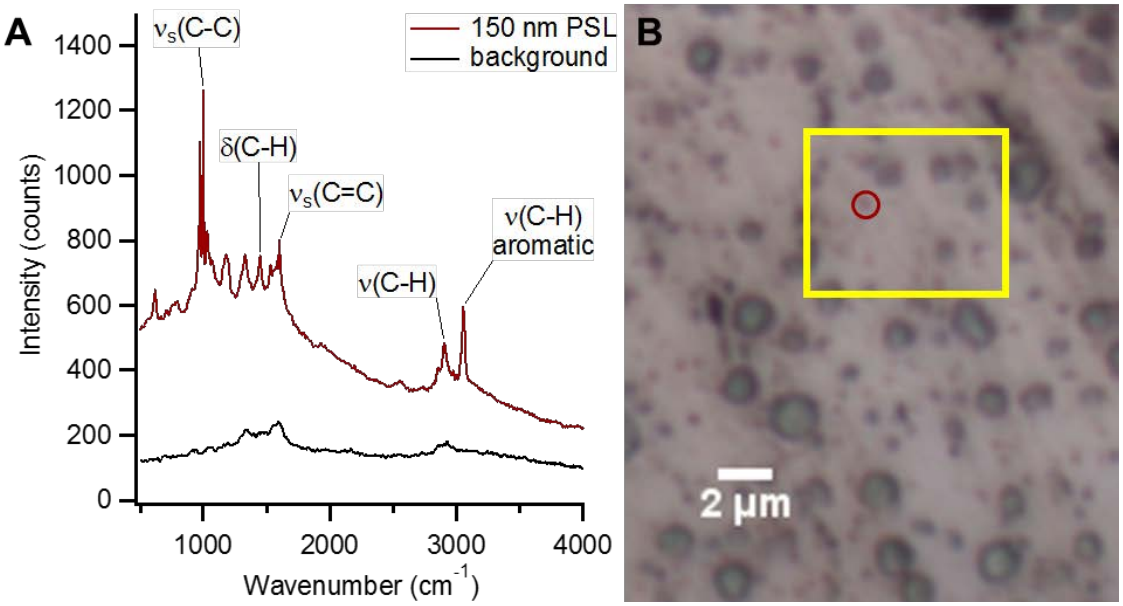

Figure 4.5 (A) SERS spectrum collected via automated point-by-point mapping of a 150 nm PSL particle on Ag foil substrate. (B) Optical image of 150 nm PSL sample on Ag foil, with the yellow box highlighting the mapped area and the red circle indicating the location of the Raman spectrum shown in (A).

In addition to testing SERS with laboratory-generated aerosol standards below the diffraction, ambient aerosol particles were also sampled, size-selected at 150 nm, and analyzed in the same manner (Figure 4.6). The corresponding optical image for the ambient aerosol sample is provided in Appendix C. With SERS, many previously indistinguishable vibrational modes were able to be identified within the spectra collected for the ambient aerosol particles. While it is difficult to definitively identify vibrational modes in ambient aerosol due to their complex chemical composition (hundreds to thousands of species per particle) and overlapping regions where modes can be present, tentative assignments are proposed. Peaks in the 500-900 cm^{-1} region could correspond to ν(Si-O-Si), δ(Si-O-Al), and other lattice vibrations of fly ash or silicon and aluminosilicate minerals (Michaelian, 1986; Frost, 1995; Frost et al., 1997; Larkin, 2011; Laskina et al., 2013), δ(C-O) of carbonates and carboxylic acids (Larkin, 2011; Laskina et al., 2013; Craig et al., 2015), or "breathing" modes of aromatic rings (De Gelder et al., 2007). The peaks at 963 – 988 cm^{-1} most likely correspond to ν(SO_4^{2-}) (Venkateswarlu et al., 1975; Ault et al., 2013b; Jentzsch et al., 2013; Deng et al., 2014; Craig et al., 2017a) and are exhibiting the same red shift observed for the $(NH_4)_2SO_4$ standard particles discussed earlier (Gen and Chan, 2017). Peaks in the 1000-1700 cm^{-1} region could correspond to a range of vibrational modes of

organic functional groups, including stretching modes, such as ν(C-O), ν(C-C), ν(C=C), ν(COO^-), and ν(C-OH), and bending and twisting modes, such as δ(CH_2), δ(CH_3), δ(C-C), δ(O-C-O), and δ(O-H) (Koenig and Angood, 1970; de Villepin and Novak, 1971; McLaughlin et al., 2002; De Gelder et al., 2007; Larkin, 2011; Ault et al., 2013b; Avzianova and Brooks, 2013; Laskina et al., 2013; Zhou et al., 2014; Deng et al., 2014; Bondy et al., 2018). Peaks in the higher energy 2700-3000 cm^{-1} region correspond to symmetric and asymmetric ν(CH_2) and ν(CH_3) modes (De Gelder et al., 2007; Larkin, 2011; Ault et al., 2013b; Laskina et al., 2013; Deng et al., 2014; Bondy et al., 2018). Specific compounds present in the ambient aerosol particles related to these functional groups could include long chain aliphatics, glyoxal oligomers, peroxides, organic sulfates, and minerals associated with dust (Lee and Chan, 2007; Avzianova and Brooks, 2013; Laskina et al., 2013; Deng et al., 2014; Bondy et al., 2018). To our knowledge, this is the first SERS-enhanced spectroscopic analysis of aerosol particles that have a smaller diameter than the diffraction limit. Additionally, for these ambient spectra, vibrational modes attributed to organic species exhibited greater enhancement in the lower frequency region (1000 – 1800 cm^{-1}) than the higher frequency region (2700 – 3000 cm^{-1}), which is consistent with previous work with SERS of ambient particles (Craig et al., 2015). This demonstrates the potential for SERS to enable the study of vibrational modes that are not as well characterized in the literature due to the difficulties associated with detecting them in aerosol particles via traditional microspectroscopic methods.

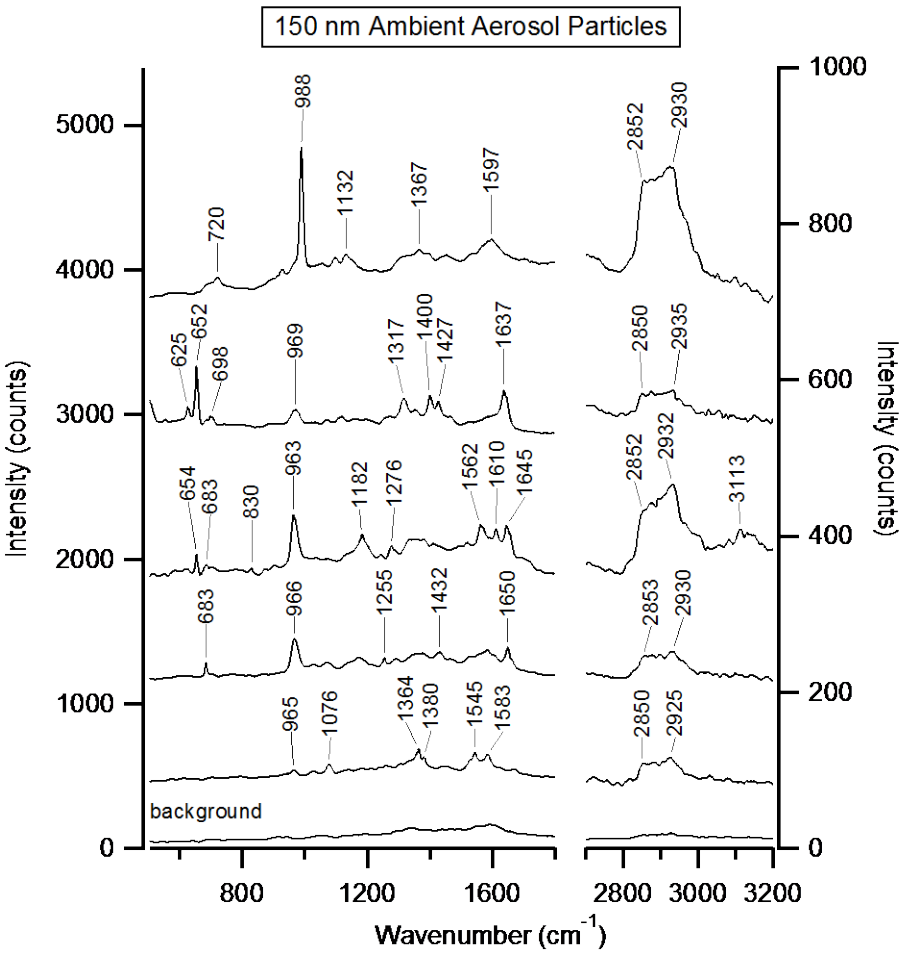

Figure 4.6 SERS-enhanced spectra obtained from Raman mapping of 150 nm size-selected ambient aerosol particles.

4.4 Conclusions

SERS was applied to the study of atmospheric aerosol particles to improve the limit of detection in terms of particles size. 400 nm, 600 nm, and 800 nm size-selected laboratory-generated aerosol particle standards of PSLs, ammonium sulfate, and sodium nitrate were collected on Ag foil SERS substrates and analyzed. Average enhancement factors for a range of inorganic and organic vibrational modes were calculated to be on the order of 10^2 and as large as 530. SERS enhancement increased with increasing particle size for the inorganic standards, while there was no observed consistent trend between SERS enhancement and particle size for the organic standard, likely due to variability in LSPRs on the foil surface and subsequent

coupling with analyte molecules. Ag foil substrates were also used for SERS analysis of 150 nm PSL and ambient aerosol particles via automated Raman mapping. All five PSL vibrational modes characterized with the larger sized particles were identified in the SERS enhanced spectra of the 150 nm particles. For the ambient aerosol, a range of inorganic and organic vibrational modes were detected, and corresponding functional groups were proposed. To our knowledge, this is the first vibrational spectroscopic analysis of aerosol particles smaller than the diffraction limit. These results show the potential for SERS to enable improved analysis of aerosol particle chemical composition and mixing state for the most atmospherically abundant particle sizes to better understand multiphase atmospheric processing and aerosol impacts on climate and human health.

4.5 Acknowledgements

This work was supported by the National Science Foundation Grant No. CAREER-1654149 and startup funds from the University of Michigan. RLC was partially supported by the Susan Lipschutz Fellowship Award from the University of Michigan Rackham Graduate School. DBT was partially supported by the Detroit Research Internship Summer Experience (D-RISE) program, funded by the NSF (CHE-1305777) to Dr. Nicolai Lehnert at UM, the UM College of Literature, Science and the Arts, the UM Office of the Provost, and Cass Technical High School in Detroit, MI. The Pratt Lab at the University of Michigan is acknowledged for assistance with ambient aerosol sampling. PNT and DBT performed sample preparation and Raman analysis under mentorship by RLC. RLC prepared the manuscript.

Chapter 5. Direct Measurement of pH in Individual Particles via Raman Microspectroscopy and Variation in Acidity with Relative Humidity

Adapted with permission from Rindelaub, J. D., Craig, R. L., Nandy, L., Bondy, A. L., Dutcher, C. S., Shepson, P. B., and Ault, A. P.: Direct measurement of pH in individual particles via Raman microspectroscopy and variation in acidity with relative humidity, *J. Phys. Chem. A*, 120, 6, 911-917, 2016. https://doi.org/10.1021/acs.jpca.5b12699

5.1 Introduction

Assessing the pH of atmospheric aerosol particles is of great interest, due to the impact of acidic particles on the environment and human health. Many atmospheric particle phase chemical processes are dependent on acidity, such as secondary organic aerosol (SOA) formation (Jang et al., 2002; Limbeck et al., 2003; Tan et al., 2009; Surratt et al., 2010), specifically organosulfate formation and organic nitrate hydrolysis (Surratt et al., 2008; Rindelaub et al., 2015). Acid-dependent particle phase processes also affect the equilibrium of gas-particle partitioning (Jang et al., 2002). As aerosol chemical composition determines hygroscopicity and contributes to cloud condensation nuclei activity, the pH of a particle can impact composition, cloud droplet nucleation and, ultimately, climate forcing (Jang et al., 2002; Pöschl, 2005).

Currently, there are not reliable methods to directly measure aerosol particle pH. Measuring the pH of aqueous filter extracts indirectly assesses particle acidity, but is associated with high uncertainty, due to the non-conservative nature of H^+ and changes to the ion distribution during filter extraction (Koutrakis et al., 1988; Keene et al., 2002; Jang et al., 2008; Hennigan et al., 2015). Additional artifacts, such as evaporation of particle phase components or impurities in the extraction solvent, can also jeopardize the integrity of filter-based measurements (Pathak et al., 2004). Similar to indirect measurements, proxy methods, such as ion balance, molar ratio, thermodynamic equilibrium models, or phase partitioning, are often used to estimate acidity, but have been shown to have major flaws or limitations (Hennigan et al., 2015). The ion balance and molar ratio methods are also associated with high uncertainty in

their estimations of aerosol particle pH and do not have good agreement with current thermodynamic equilibrium models (Fountoukis et al., 2009), such as E-AIM (Clegg et al., 1998; Wexler and Clegg, 2002) and ISORROPIA-II (Fountoukis and Nenes, 2007), often estimating pH to be less acidic than thermodynamic model predictions (Hennigan et al., 2015). Both the ion balance and molar ratio methods are frequently used and the discrepancy between these proxy methods and model estimations is attributed, in part, to the inability to differentiate between free and bound H^+ (e.g. protons associated with bisulfate, HSO_4^-, or other inorganic ions), exclusion of organic acids, and lack of consideration for both aerosol liquid water content and ion activity coefficients in the pH calculation (Kerminen et al., 2001; Keene et al., 2004; Trebs et al., 2005; Metzger et al., 2006; Zhang et al., 2007a; Pathak et al., 2009; Froyd et al., 2010; Feng et al., 2012; Hennigan et al., 2015). While thermodynamic equilibrium models, E-AIM and ISORROPIA-II, provide more accurate representations of aerosol partitioning and composition, there are still biases associated with aerosol pH predictions, due to the large model sensitivity to input values and their associated uncertainties (Fountoukis et al., 2009; Guo et al., 2015; Hennigan et al., 2015). The phase partitioning method is more consistent with thermodynamic models (Keene et al., 2004; Fountoukis et al., 2009; Young et al., 2013; Guo et al., 2015; Hennigan et al., 2015), but still involves an indirect measurement of particle pH and infers that the gas/particle system has reached a stable equilibrium, which may not occur in SOA systems, especially those involving particle phase acid-catalyzed reactions or viscous organic material (Virtanen et al., 2010; Koop et al., 2011; Perraud et al., 2012; Ziemann and Atkinson, 2012; O'Brien et al., 2014; Cheng et al., 2015; Dette and Koop, 2015; Hennigan et al., 2015; Rindelaub et al., 2015; Saukko et al., 2015). A recent critical review of aerosol acidity proxies suggests that, in the absence of reliable direct aerosol pH measurement techniques, thermodynamic models and phase partitioning provide the best estimation of particle acidity, despite their inherent biases (Hennigan et al., 2015).

To improve our fundamental understanding of aerosol acidity, specifically at the single particle level, we present a direct spectroscopic method for measuring the pH of individual aerosol particles using Raman microspectroscopy. There has been a recent increase in Raman microspectroscopy of aerosol particles due to its non-destructive nature and potential for determining chemical composition and structure of individual particles (Ault et al., 2013b, 2014; Ebben et al., 2013). For this study, Raman microspectroscopy has the advantage of directly

measuring the HSO_4^- anion and its conjugate base, SO_4^{2-}. The HSO_4^-/SO_4^{2-} acid/base pair system, which has been well characterized through both Raman and modeling studies, has clearly distinguishable vibrational shifts for $\nu_s(SO_4^{2-})$ and $\nu_s(HSO_4^{2-})$ at ~980 and ~1050 cm^{-1}, respectively (Irish and Chen, 1971; Kruus et al., 1985; Knopf et al., 2003). The pH of each individual particle was determined from the concetration of each anion within laboratory-generated aerosol particles based on integrated peak area and subsequent calculations for ionic strength, activity coefficients, and, subsequently, $[H^+]$. This spectroscopic approach has the potential to improve the fundamental understanding of aerosol acidity, which is currently lacking, and to eventually improve understanding of key atmospheric processes, such as SOA formation and phase behavior in liquid droplets.

5.2 Methods

5.2.1 Aerosol Samples

Laboratory-generated aerosol samples were created by atomizing standard solutions of $MgSO_4$ and H_2SO_4 and impacting aerosol particles onto quartz substrates using a microanalysis particle sampler (MPS-3, California Measurements, Inc.). Standard solutions were based on the "highly acidic aerosol" (Surratt et al., 2008), which consisted of 30 mM $MgSO_4$ and varying concentrations of H_2SO_4 for a range of bulk solution pH values: 0.44, 0.89, 1.15, 1.64, and 1.99 (Figure 1). All chemicals were purchased from Sigma Aldrich, Inc. at high purity (>99%). Generated aerosol particles were passed through two diffusion dryers (drying to ~15% RH) prior to impaction on quartz substrates, Particles with diameters ranging from 10-30 μm at ambient RH were selected for study in these experiments.

5.2.2 Raman Microspectroscopy

Once impacted on quartz substrates, the aerosol particles were probed using a Raman microspectrometer (LabRAM HR Evolution, HORIBA, Ltd.), initially at ambient temperature and pressure. The Raman spectrometer was equipped with a Nd:YAG laser source (50mW, 532 nm) and CCD detector and coupled with a confocal optical microscope (100x SLMPlan N Olympus objective). A 600 g/mm diffraction grating yielded spectral resolution of ~1.7 cm^{-1}. The instrument was calibrated against the Stokes Raman signal of pure Si at 520 cm^{-1} using a silicon wafer standard. Spectra were collected for the range 500 to 1400 cm^{-1} with three

accumulations at 5 s acquisition time. An environmental stage (Linkham Scientific Instruments, Inc.) was used to adjust RH, which was monitored with an RH sensor (EK-H5, Sensiron). Five to eight separate particles were investigated as a function of RH per sample.

5.2.3 Aerosol pH Calculation

Since $[HSO_4^-]/[SO_4^{2-}]$ is directly related to $[H^+]$ through the dissociation constant, the pH of individual aerosol particles could be easily calculated for an equilibrium system (Equation 5.1), where $K_a = 0.01$ for HSO_4^- (Lide, 2009).

Equation 5.1

$$K_a = \frac{a_{H^+} * a_{SO_4^{2-}}}{a_{HSO_4^-}} = \frac{([H^+] * \gamma_{H^+})([SO_4^{2-}] * \gamma_{SO_4^{2-}})}{[HSO_4^-] * \gamma_{HSO_4^-}}$$

The activity of each species is represented by α_i and the activity coefficient by γ_i in Equation 5.1. To determine the activity coefficients for each species within the particle, the ionic strength, I, of the aerosol was calculated from the concentration of each ion, C_i, and its corresponding charge, z_i, via Equation 5.2.

Equation 5.2

$$I = \frac{1}{2} \sum C_i z_i^2$$

Standard solutions of $MgSO_4$ and H_2SO_4 were used to create calibration curves relating $[SO_4^{2-}]$ and $[HSO_4^-]$ to integrated peak area of the $\nu_s(SO_4^{2-})$ and $\nu_s(HSO_4^-)$ modes (Figure 5.1). The sulfate calibration curve was created first and used to determine the amount of sulfate present in the SO_4^{2-}/HSO_4^- equilibrium, which was then used to determine $[HSO_4^-]$ and generate the bisulfate calibration curve. The ratio of the concentration of Mg^{2+} to the total concentration of sulfates ($[HSO_4^-]$ + $[SO_4^{2-}]$) in each bulk solution was used to determine $[Mg^{2+}]$ in the particles based on measured $[HSO_4^-]$ and $[SO_4^{2-}]$. The bulk solutions used for atomization to generate aerosol particles consisted of 30 mM $MgSO_4$ and varying concentrations of sulfuric acid (Table D.1). The ratio of Mg^{2+} concentration to total sulfate concentration ($[Mg^{2+}]/([SO_4^{2-}$ + $HSO_4^-]$) of the bulk solution was assumed to be the same ratio for aerosol particles. Molality units were used for the concentration of each species, determined by converting molarity to molality using the density of H_2SO_4 and $MgSO_4$ aqueous mixtures as a function of water activity according to models in the literature (Laliberte and Cooper, 2004; Laliberte, 2009). Activity coefficients for each species were determined using the extended Debye-Hückel relationship

(Equation 5.3) (Garrels and Christ, 1965) and then used to elucidate the corresponding H^+ concentrations via Equation 5.1.

Equation 5.3 $$-log\gamma_i = \frac{Az_i^2\sqrt{I}}{1+\text{å}_i B\sqrt{I}}$$

In Equation 5.3, *A* and *B* are constants characteristic of the solvent (water) and å_i is the effective diameter of the ion in solution, found in literature (Garrels and Christ, 1965). Using the ionic activity coefficients found from Equation 5.3, it should be noted that $[H^+]$ was iteratively solved in Equation 5.1, as $[H^+]$ also appears in the calculations for ionic strength in Equation 5.2. Once γ_{H^+} and $[H^+]$ were determined, aerosol pH was calculated using Equation 5.4.

Equation 5.4 $$\text{pH} = -log(a_{H^+}) = -log(\gamma_{H^+} * [H^+])$$

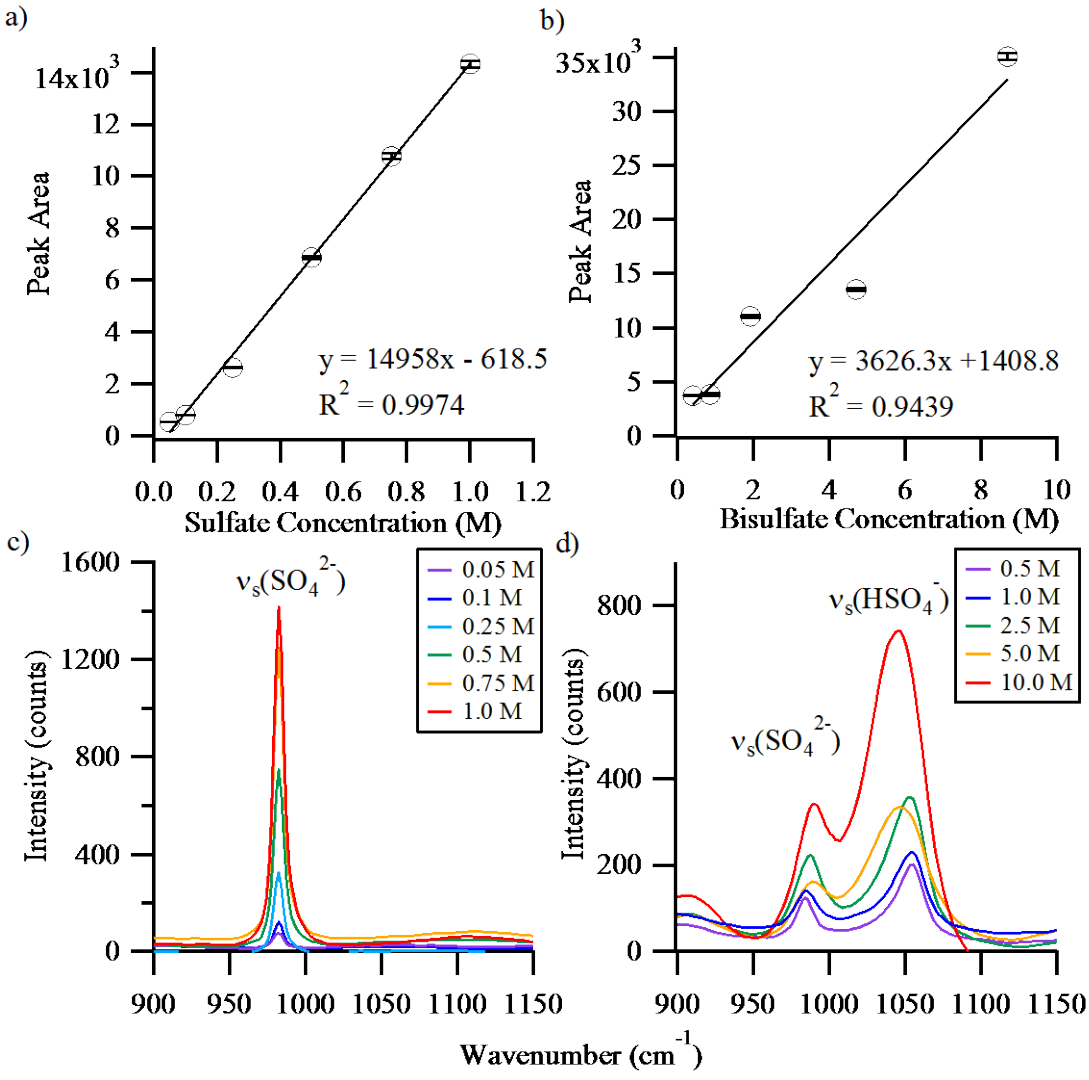

Figure 5.1 Calibration curves relating integrated peak area to concentration for a) SO_4^{2-} and b) HSO_4^{2-}, along with corresponding Raman spectra (c,d) for $\nu(SO_4^{2-})$ at ~985 cm^{-1} and $\nu(HSO_4^{-})$ at ~1050 cm^{-1}.

5.3 Results and Discussion

The modeled relative fraction for each species of the HSO_4^-/SO_4^{2-} system and associated *I* are shown in Figure 5.2 as a function of pH. The measured pHs of the aerosolized bulk solutions are referred to as the bulk solution hereafter.

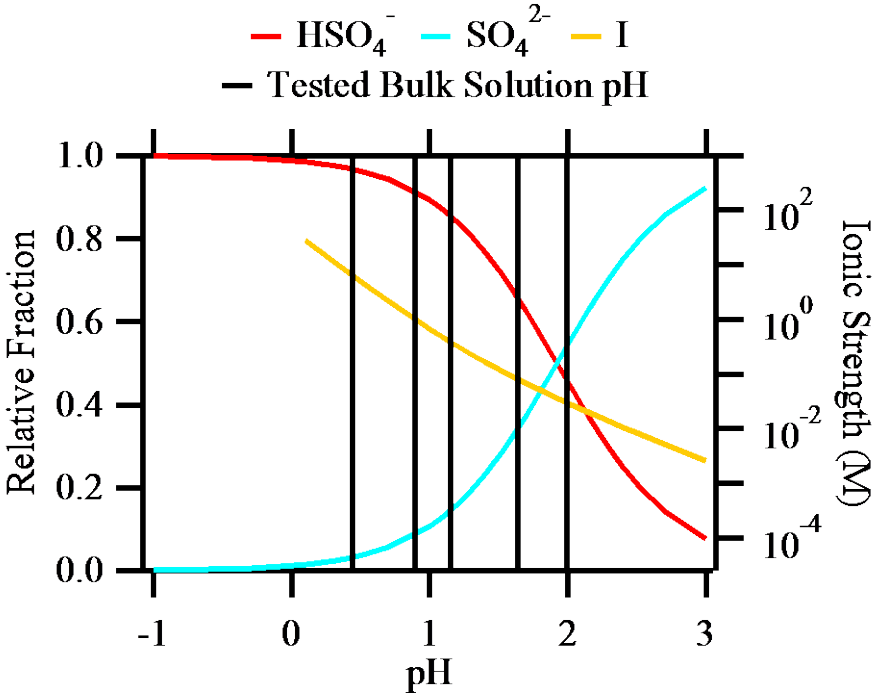

Figure 5.2 Relative fraction for HSO_4^- (red) and SO_4^{2-} (blue) concentrations, as well as ionic strength (I) (yellow), as a function of pH using the dissociation constant (K_a = 0.01) assuming equilibrium conditions. Each tested bulk solution pH (0.44, 0.89, 1.15, 1.64, and 1.99) is highlighted in black.

5.3.1 Aerosol pH Measurements at Ambient Relative Humidity

Average particle pH values after aerosolization and impaction varied from 0.18 to 0.79, based on the bulk solution at ambient relative humidity (55-65%). The corresponding Raman spectra of the region containing $\nu_s(SO_4^{2-})$ and $\nu_s(HSO_4^-)$ are displayed in Figure 5.3a, showing an increase in the intensity of the $\nu_s(HSO_4^-)$ mode (~1050 cm^{-1}) with decreasing pH. Figure 5.3b shows aerosol pH decreasing with decreasing $[SO_4^{2-}]/[HSO_4^-]$, following the equilibrium shift towards HSO_4^- as the particle becomes more acidic.

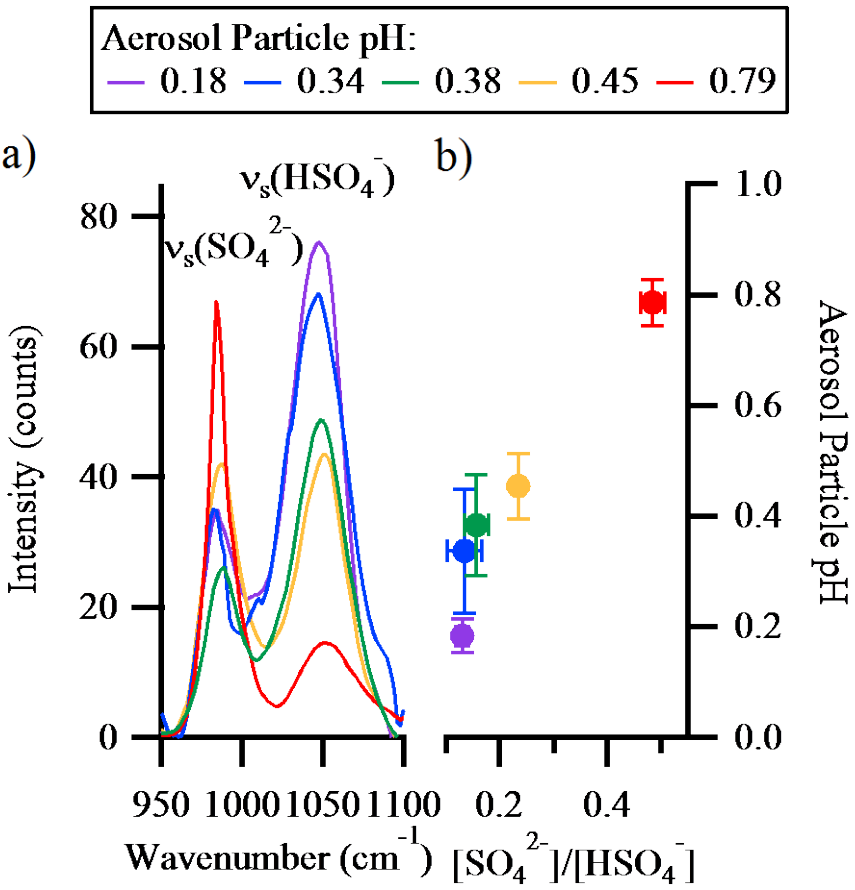

Figure 5.3 Raman spectra of $\nu_s(SO_4^{2-})$ and $\nu_s(HSO_4^-)$ for initial aerosol particles generated from each seed aerosol bulk solution (left) and average aerosol pH as a function of $[SO_4^{2-}]/[HSO_4^-]$ (right). Error bars are based on the standard deviation for multiple trials.

5.3.2 Aerosol pH Measurements with Varying Relative Humidity

After initial measurements, particles were exposed to varying RH conditions using a sealed environmental cell. The RH was reduced to ~30% and increased to ~90% at increments of ~10%, with spectra collected at each RH interval. Representative sets of Raman spectra, one each for bulk solution pH, are shown at different RH values in Figure 5.4 (left), along with average particle pH for each set of samples as a function of RH (right). As the RH was increased, water uptake occurred, causing dissociation of HSO_4^- and a subsequent increase in SO_4^{2-} concentration (as indicated by change in peak intensity), as well as an increase in average particle pH. For all seed particles, an increase in pH was observed with increasing RH (up to ~1 pH unit). Linear regressions were applied to the relationship between average aerosol particle pH

and RH for each bulk solution. The slopes for each regression were comparable, ~0.01 pH unit/% RH, indicating similar changes in aerosol pH with changing RH, regardless of initial pH.

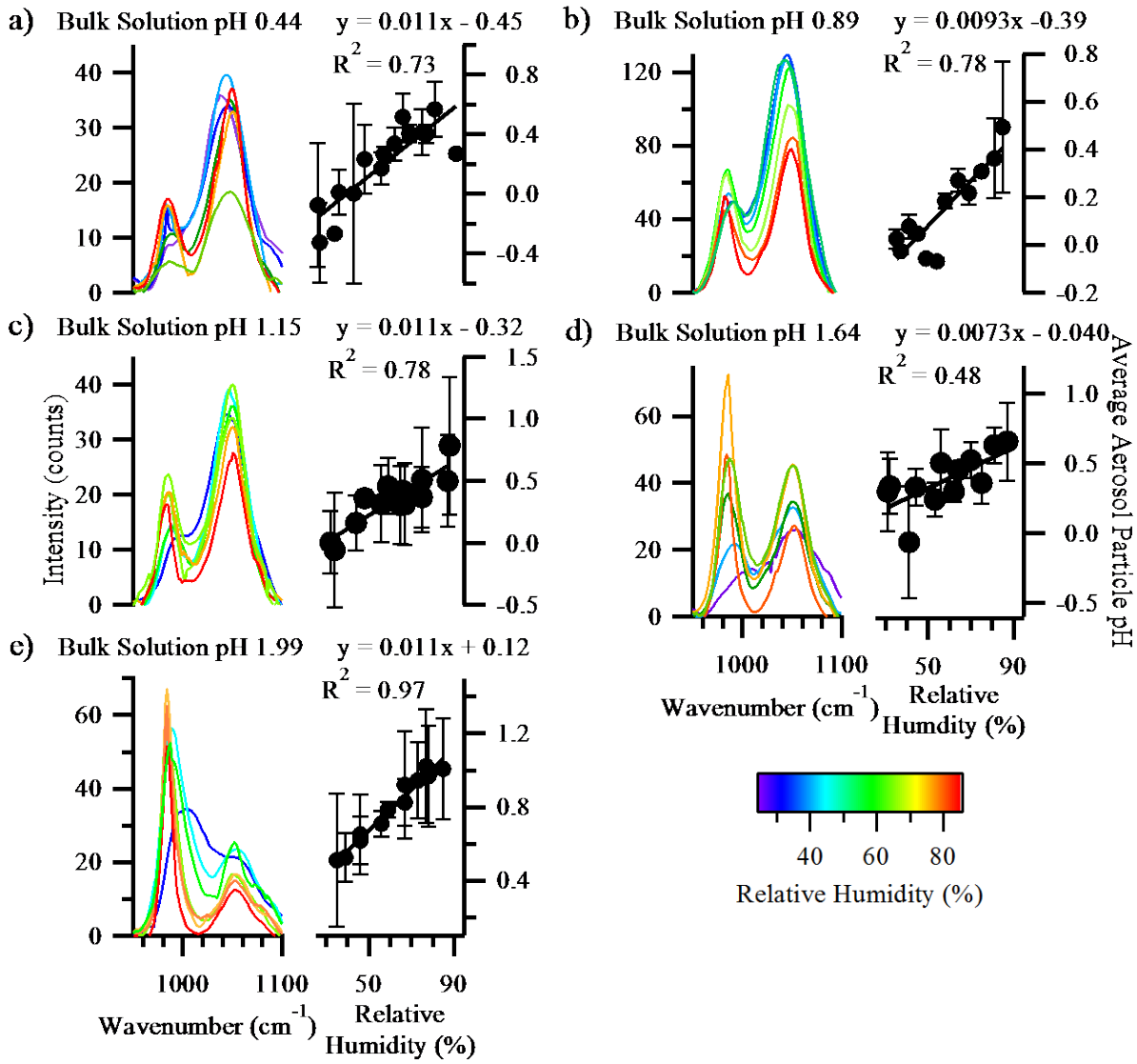

Figure 5.4 Raman spectra (left) of $\nu_s(SO_4^{2-})$ and $\nu_s(HSO_4^-)$ at varying RH for aerosol particles generated from bulk solution pH (a) 0.44, (b) 0.89, (c) 1.15, (d)1.64, and (e) 1.99. Average aerosol pH as a function of RH (right) for each bulk solution. Error bars are based on the standard deviation for multiple trials.

For comparison, the molar ratio and ion balance proxy methods for determining aerosol particle were also applied to determine the relationship between aerosol particle pH and relative humidity. The molar ratio method, which is qualitative, yielded particle acidities that increased with bulk solution pH, however the method is not capable of differentiating particle acidity at

variable RH. Specifically, the molar ratio method relates the total molar concentration of cations to the total molar concentration of anions (usually with only the most abundant ions in aerosols accounted for), with lower ratio values indicative of higher levels of acidity. Using [Mg^{2+}], [SO_4^{2-}], and [HSO^-], the molar ratio method yielded the same value for all particles within a given bulk solution pH, regardless of RH. [H^+] was not used for this calculation, as it is unknown when the molar ratio method is applied and, thus, not typically included. The ratio values were 0.08, 0.13, 0.36, 0.63, and 0.88 for bulk solution pH 0.44, 0.89, 1.15, 1.64, and 1.99, respectively. This indicates that the molar ratio method can show that particle acidity has the same trend as measured bulk solution acidity, but as noted in Hennigan et al., is not an accurate way to determine actual pH and certainly would not be sensitive enough to detect changes in particle acidity at different RH values (Hennigan et al., 2015). The ion balance method, which calculates [H^+] by taking the difference between the concentration of anions and the concentration of cations, yielded highly variable results, producing negative [H^+] values for two trials and larger [H^+] values, yielding lower pH values compared to Figure 5.4, in the other instances. The calculated particle pH values from the ion balance method are displayed in Figure D.1, showing limited sensitivity to RH. Ion balance could only be applied to particles associated with bulk solution pH 0.44, 0.89, and 1.15, as it resulted in negative [H^+] values for bulk solution pH 1.64 and 1.99 particles, showing its limitations. A comparison to the thermodynamic models, E-AIM and ISORROPI-II, could not be made as the models were not compatible with the data from this study.

For the measurements described above, connecting measured aerosol particle pH with bulk solution pH is important. The increase in particle pH with RH is related to the uptake of water, which led to a decrease in both [H^+] and *I*, due to increased solvent volume. The loss of aerosol water content induced an opposite effect on pH, a phenomenon that was observed when aerosol particles were passed through diffusion dryers prior to deposition, resulting in aerosol pH values lower than the bulk solution pH in each aerosol generation. The decrease in system pH after water loss is shown in Figure 5.5, which compares measured pH at 50% RH to the corresponding bulk solution pH.

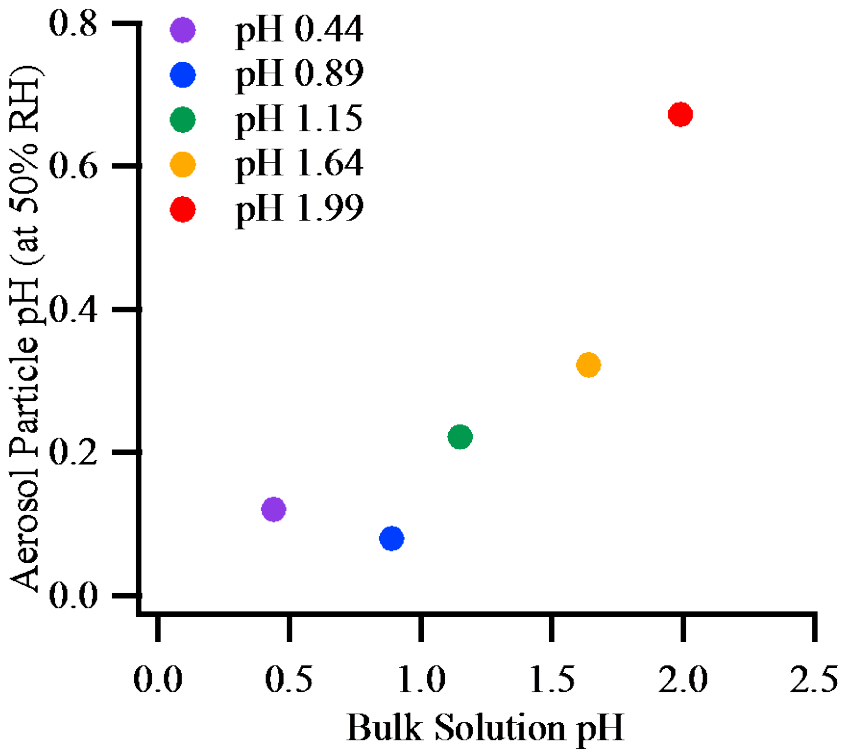

Figure 5.5 Calculated aerosol pH at 50% RH as a function of bulk solution pH. Aerosol pH was calculated from the linear regression (Figure 5.4) of each pH sample set.

For the HSO_4^-/SO_4^{2-} system, measurable particle pH values range from -0.68 to 1.33, based on the limit of detection for each ion species. This range has overlap with the range of recently reported ambient aerosol pH from indirect methods, which varied from 0.5 to 3, depending on the season (Guo et al., 2015). Thus, our method is very applicable to atmospherically-relevant aerosol properties and has potential for ambient aerosol particle pH measurements. However, applying this technique to ambient aerosol particles will be challenging, as Raman microspectroscopy of ambient samples can yield complex spectra with many vibrational modes that can be difficult to identify, overlapping Raman modes, fluorescence interference, and the potential for burning.

RH cycles of the laboratory-generated $MgSO_4/H_2SO_4$ aerosol also revealed that the particles created are metastable aqueous droplets, rather than crystalline solids, and have a continuous uptake of water with increasing RH (i.e. more water vapor present), following a smooth growth curve instead of discrete deliquescence and efflorescence RHs, as observed for systems such as $(NH_4)_2SO_4$ and NaCl. These results are consistent with previous investigations of the hygroscopic properties of $MgSO_4$ and $MgSO_4$ mixed aerosol particles, which have been

shown to form a gel at low RH due to polymeric contact ion pair chains (Chan et al., 2000; Zhang et al., 2002; Zhao et al., 2006). The observed liquid/amorphous state indicates that the aerosol does not completely lose water (at 26% RH, the lowest value tested) within the system and that, for chamber studies, water can be present in see aerosol, even at low RH. This result is in line with many studies showing water present in particles at low RHs (Parsons et al., 2004; Virtanen et al., 2010; Slade and Knopf, 2014; Chu et al., 2015; Saukko et al., 2015; You and Bertram, 2015). This phenomenon can help explain the observation of organic nitrate hydrolysis within laboratory-generated particles (from similar seeds) at RH values <10% in previous literature (Rindelaub et al., 2015). Assuming particles generated in this study have similar behavior as ambient particles, this indicates that ambient aerosol is likely to retain liquid water across atmospherically-relevant RHs and that water-induced chemistry should be at the forefront of studies concerning atmospheric aerosol processing.

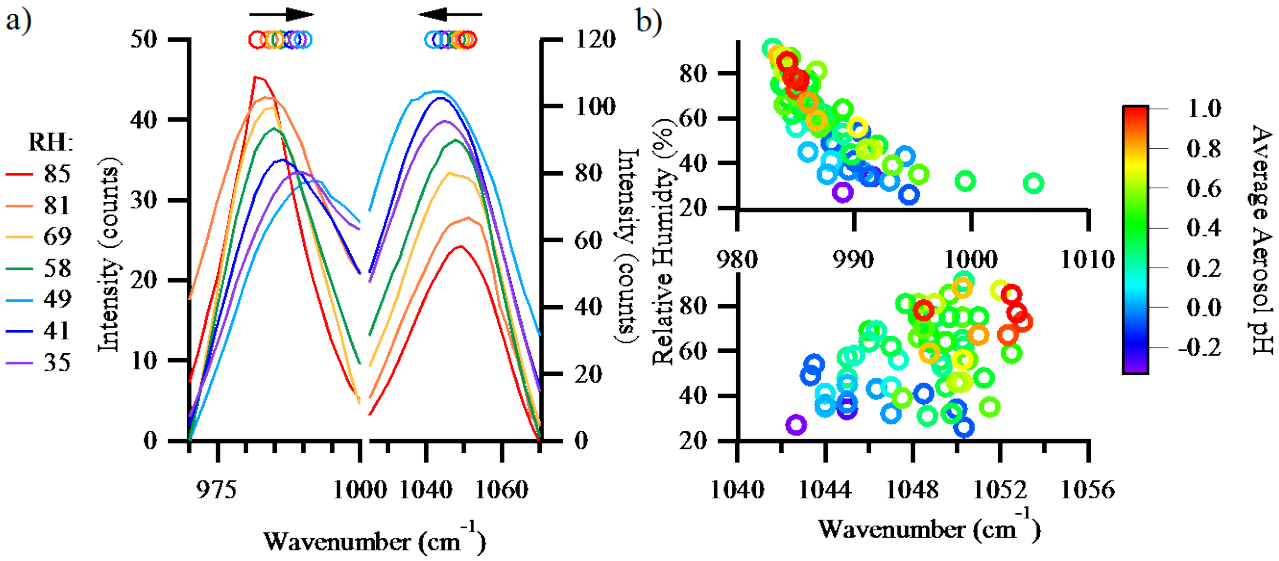

Figure 5.6 a) Raman spectra of $\nu_s(SO_4^{2-})$ and $\nu_s(HSO_4^-)$ at varying RH, with the colored dots and arrows above the peaks highlighting the blue and red shifts of $\nu_s(SO_4^{2-})$ and $\nu_s(HSO_4^-)$, respectively, with decreasing RH. b) RH plotted against absolute wavenumber, with average aerosol pH indicated by the color scale.

In addition to influencing particle pH, the uptake of water caused shifts in the peak positions of $\nu_s(SO_4^{2-})$ and $\nu_s(HSO_4^-)$, though, interestingly, in opposite directions. A decrease in RH led to a blue shift for $\nu_s(SO_4^{2-})$, from (on average) 984 to 989 cm^{-1} (Figure 5.6a). A study of the contact-ion-pairs in supersaturated $MgSO_4$ solutions (that lead to the formation of a gel at low RH) found that $\nu_s(SO_4^{2-})$ exhibited a blue shift as water-to-solute mole ratios and RH

decreased (Zhang and Chan, 2000). This shift was attributed to the formation of contact ion pairs with different structures (Zhang and Chan, 2000), a phenomenon that could play a role in these aerosol particles and induce a blue shift for $\nu_s(SO_4^{2-})$. Conversely, a decrease in RH corresponded to a red shift for $\nu_s(HSO_4^-)$, from (on average) 1052 to 1044 cm^{-1}. This red shift could be a result of increased hydrogen bonding (Larkin, 2011), as the concentration of HSO_4^- increased with decreasing RH. Hydrogen bonding could stabilize the HSO_4^- molecule, making it more symmetric, thus inducing the shift towards lower frequencies for the $\nu_s(HSO_4^-)$ mode. The formation of contact ion pairs with SO_4^{2-} molecules could have limited the impact of hydrogen bonding on the $\nu_s(SO_4^{2-})$ mode, but this is a preliminary explanation and further calculations are needed to confirm this. Additionally, the effect of hydrogen bonding on HSO_4^-, and not SO_4^{2-} molecules, might explain the difference in peak broadness, which can be seen by comparing the peak widths, as $\nu_s(HSO_4^-)$ with an average full width half maximum (FWHM) of 47.1 $\pm$ 6.1 cm^{-1} was significantly broader than the $\nu_s(SO_4^{2-})$ FWHM of 28.4 $\pm$ 6.4 cm^{-1}. The $MgSO_4$ and water system and the sulfate/bisulfate/water system have been extensively studied for clusters, revealing information regarding the structure prior to solvation (Miller et al., 2007; Yacovitch et al., 2011; DePalma et al., 2015), which will guide future simulations to explain these experimental results.

Several other acid/base systems have potential to be studied with respect to particle pH, such as HNO_3/NO_3^-, (pK_a = -1.3), $H_2CO_3/HCO_3^-/CO_3^{2-}$, ($pK_a$ = 6.4, 10.2) or organic acids, e.g. acetic acid/acetate (pK_a = 4.7) (Rudolph et al., 2008; Wren and Donaldson, 2012a). The direct measurement of particle pH has great potential to facilitate a large step forward in understanding aerosol aqueous phase chemistry. As an example, the formation of organosulfates has only occurred in photochemical chamber experiments employing “acidic seed aerosol” (Surratt et al., 2008). The same acidic seed aerosol solution was used in this study with an average particle pH measured as ~0.43 at ~65% RH. Understanding the pH at which these atmospherically-relevant compounds form is vital to replicating larger scale experiments focusing on production kinetics, precursors, and mechanistic formation pathways. For instance, if organosulfates only form under very acidic conditions, at pH < 2.0, the nucleophilic attack of HSO_4^- is likely to govern their formation within aerosol particles. While recent research by Xu et al. suggests the sulfate ion is instrumental in particle phase chemistry (Xu et al., 2015), it is worth noting that the measurements in that study could not differentiate SO_4^{2-} and HSO_4^- ions. As the ambient aerosol

pH in that study was < 2.0, the impact of the HSO_4^-/SO_4^{2-} equilibrium (which would be shifted to HSO_4^-) on biogenic SOA formation should be studied further. Additionally, our study was conducted at pHs relevant to other particle-phase chemical reactions, such as acid-catalyzed hydrolysis, oligomerization, and oxidation, which can now be studied with much greater certainty in laboratory experiments.

5.4 Conclusions

This study provides a non-destructive method for the determination of aerosol particle acidity in a laboratory setting and changes with respect to water content. Through these studies new insight was provided into the fundamental properties of the $\nu_s(SO_4^{2-})$ and $\nu_s(HSO_4^-)$ modes in particles of different ionic strengths, which will aid studies of aerosol acidity and the role of sulfate in particle-phase chemistry. The demonstrated potential of this method for laboratory studies has promise for direct measurements of pH in ambient particles, though ambient samples are far more complex, making the measurements and interpretation much more challenging. Recently there have been calls for more physical chemistry approaches to single particle analysis under ambient conditions for improved understanding of physical processes in these unique, complex systems (Grassian, 2015), which the direct measurement of particle pH in this study helps to address. These results, and future studies it will enable, will aid in elucidating processes governing SOA formation and water uptake, which ultimately determine climate-relevant properties of aerosols that impact radiative forcing.

5.5 Acknowledgements

This work was supported by startup funds from the University of Michigan and by the National Science Foundation grant No. AGS-1228496. RLC performed Raman microspectroscopy research with assistance from JDR and ALB. LN performed modeling and calculations with assistance from CSD.

Chapter 6. Spectroscopic Determination of Aerosol pH from Acid-Base Equilibria in Inorganic, Organic, and Mixed Systems

Adapted with permission from Craig, R. L., Nandy, L., Axson, J. L., Dutcher, C. S., and Ault, A. P.: Spectroscopic determination of aerosol pH from acid-base equilibria in inorganic, organic, and mixed systems, *J. Phys. Chem. A*, 121, 30, 5690-5699, 2017. https://doi.org/10.1021/acs.jpca.7b05261

6.1 Introduction

Atmospheric aerosols impact both climate and human health, yet many of the chemical mechanisms occurring within aerosols remain poorly understood (Prather et al., 2008). Many key multiphase chemical processes in aerosol particles are pH-dependent, such as secondary organic aerosol (SOA) formation (Jang and Kamens, 2001; Jang et al., 2003b; Gao et al., 2004; Cao and Jang, 2007; Tan et al., 2009; Lin et al., 2012; Lewandowski et al., 2015; Wong et al., 2015; Riva et al., 2016c, 2016d), which makes understanding aerosol acidity important for assessing the impact of aerosols on climate (Surratt et al., 2010). Specific pH-dependent processes include acid-catalyzed ring-opening reactions of epoxides (e.g. isoprene epoxydiol) (Iinuma et al., 2009; Eddingsaas et al., 2010; Surratt et al., 2010), formation and hydrolysis of organosulfates and organic nitrates (Surratt et al., 2008; Hu et al., 2011; Rindelaub et al., 2015, 2016b; Riva et al., 2016b), water uptake (Prenni et al., 2003; Ghorai et al., 2011), liquid-liquid phase separations (You et al., 2014; Losey et al., 2016), and gas-particle partitioning (Jang et al., 2002). One of the challenges for predicting the kinetics and overall importance of these processes is that methods to experimentally determine aerosol acidity are limited, but the available data suggest considerable variation between regions globally (Guo et al., 2015, 2016, 2017; Hennigan et al., 2015; Liu et al., 2017b). As an example, sulfate, which is formed from oxidation of $SO_{2(g)}$, is a large contributor to the acidity of aerosols, yet, despite decreasing atmospheric gaseous SO_2 emissions and subsequent condensed phase sulfate concentrations in the southeast US, aerosol pH has remained low (pH 0-2) over the past 15 years (Weber et al., 2016). Considering the complex mixture of emissions and atmospheric reactions that ultimately determine aerosol pH,

more refined techniques for measuring aerosol pH are necessary to evaluate the overall impact on atmospheric multiphase chemical processes.

Until recently, evaluation of aerosol pH has been primarily through indirect filter-based measurements or proxy methods, such as ion balance, molar ratio, phase partitioning, or thermodynamic equilibrium models (Hennigan et al., 2015). Upon examination of these methods, Hennigan et al. concluded that thermodynamic models and the phase partitioning method provide the most accurate estimations of aerosol pH (Hennigan et al., 2015). Thermodynamic equilibrium models, such as ISORROPIA-II (Fountoukis and Nenes, 2007) and E-AIM (Clegg et al., 1998; Wexler and Clegg, 2002), use temperature, relative humidity (RH), and measured concentrations of aerosol species and gas-phase precursors to predict concentrations of chemical species in both gas and aerosol phases, aerosol water, and aerosol pH. These models have been increasingly applied to evaluate aerosol acidity during several field campaigns, including MILAGRO (Hennigan et al., 2015), SOAS (Guo et al., 2015), WINTER (Guo et al., 2016), and CALNEX (Guo et al., 2017), as well as recent haze events in China (Liu et al., 2017b). The phase partitioning method uses measurements of gas and aerosol phase components to estimate aerosol pH from the phase partitioning of semi-volatile compounds, such as HNO_3/NO_3^- and NH_3/NH_4^+ (Keene et al., 2004; Young et al., 2013). Limitations for both the thermodynamic models and phase partitioning method include sensitivity to input values and the uncertainty associated with those measurements (Keene et al., 2004; Guo et al., 2015; Hennigan et al., 2015). Additionally, the phase partitioning method follows the assumption that the gas-particle phase system is at equilibrium, which is not necessarily accurate, particularly in conditions of high ionic strength or low liquid water content common in the atmosphere (Keene et al., 2004; Virtanen et al., 2010; Perraud et al., 2012; O'Brien et al., 2014; Shiraiwa et al., 2017). In comparison to the phase partitioning method, estimations of aerosol pH using filter-based measurements (Keene et al., 2002, 2004; Jang et al., 2008) and the ion balance (Trebs et al., 2005; Metzger et al., 2006; Feng et al., 2012) and molar ratio (Kerminen et al., 2001; Zhang et al., 2007a) proxy methods are all associated with higher degrees of uncertainty and disagreement with model predictions. These disagreements are mainly due to challenges associated with predicting $[H^+]$ since it is not conserved relative to other chemical species that are more easily measured (Hennigan et al., 2015). For filter-based measurements, uncertainty can also be attributed to sampling artifacts (Pathak et al., 2004). Additional limitations of the ion

balance and molar ratio methods include lack of consideration for aerosol liquid water content and ion activity coefficients, exclusion of organic acids, and inability to differentiate types of H (e.g., whether or not H^+ is a dissociated ion), though all of these factors are important for determining aerosol pH (Keene et al., 2004; Trebs et al., 2005; Metzger et al., 2006; Pathak et al., 2009; Hennigan et al., 2015).

In contrast to these indirect and proxy methods, Rindelaub et al. (Rindelaub et al., 2016a) recently developed a novel method utilizing Raman microspectroscopy, a technique that has been increasingly applied for analysis of individual laboratory and ambient particles in recent years (Ault et al., 2013b, 2014; Ebben et al., 2013; Craig et al., 2015, 2017a; Creamean et al., 2016; Ault and Axson, 2017). Wren and Donaldson have also used a spectroscopic technique to study pH of air-ice interfaces, but it involves indirect measurement through glancing-angle laser-induced fluorescence in conjunction with pH sensitive fluorescent dyes (Wren and Donaldson, 2012b, 2012c). Rindelaub et al. directly measured the pH of laboratory-generated $MgSO_4$-H_2SO_4 aerosol particles, a common seed aerosol used in SOA chamber studies (Surratt et al., 2008). Measured peak areas of the $\nu_s(SO_4^{2-})$ and $\nu_s(HSO_4^-)$ vibrational modes were used to determine SO_4^{2-} and HSO_4^- ion concentrations, respectively (Rindelaub et al., 2016a). The acid (HSO_4^-) and conjugate base (SO_4^{2-}) concentrations were then used, along with activity coefficients determined via the extended Debye-Hückel relationship and the acid dissociation constant (K_a), to calculate $[H^+]$ and pH (Rindelaub et al., 2016a). This method overcomes limitations of the previously discussed proxy methods, such as differentiating types of H^+ and accounting for aerosol liquid water content, and has potential to provide insight into chamber and ambient aerosol particle pH, which would be a valuable comparison to current predictions of aerosol pH, but has only been applied to one, relatively simple acid-base equilibrium system over a limited pH range (Rindelaub et al., 2016a).

In this work, the spectroscopic method described above for determining aerosol particle pH (Rindelaub et al., 2016a) has been applied to inorganic and organic acids with a range of pKa's in individual aerosol particles (Figure 6.1). These systems include nitric acid/nitrate (HNO_3/NO_3^-, pKa -1.3), bioxalate/oxalate ($HC_2O_4^-/C_2O_4^{2-}$, pKa 3.81), acetic acid/acetate (CH_3COOH/CH_3COO^-, pKa 4.76), and bicarbonate/carbonate (HCO_3^-/CO_3^{2-}, pKa 10.30) (Hood et al., 1954; Lide, 2009). These systems cover a wide pH range, including the typical range for atmospheric aerosols (pH -0.5 – 5) (Guo et al., 2015, 2016, 2017; Hennigan et al., 2015; Liu et

al., 2017b). The aerosol acidity predicted by thermodynamic models for several field campaigns are also indicated in Figure 6.1 and fall well within the range of several of the acid-base systems. A large fraction of aerosols are a mixture of inorganic and organic species, thus, in addition to these single acid-conjugate base systems, a two-component mixture of bisulfate/sulfate (HSO_4^- /SO_4^{2-}, pKa 2.0) (Lide, 2009) and $HC_2O_4^-/C_2O_4^{2-}$ was characterized to study the impact of increasing chemical complexity of the particles on the spectroscopic pH measurements. Observations of ion behavior in terms of ionic strength, H^+ activity, and solvent interactions were also made for each acid-base system. This work responds to a recent call for more physical chemistry approaches to single particle measurements (Grassian, 2015) and will enable future studies to improve understanding of pH of more chemically complex aerosol particles.

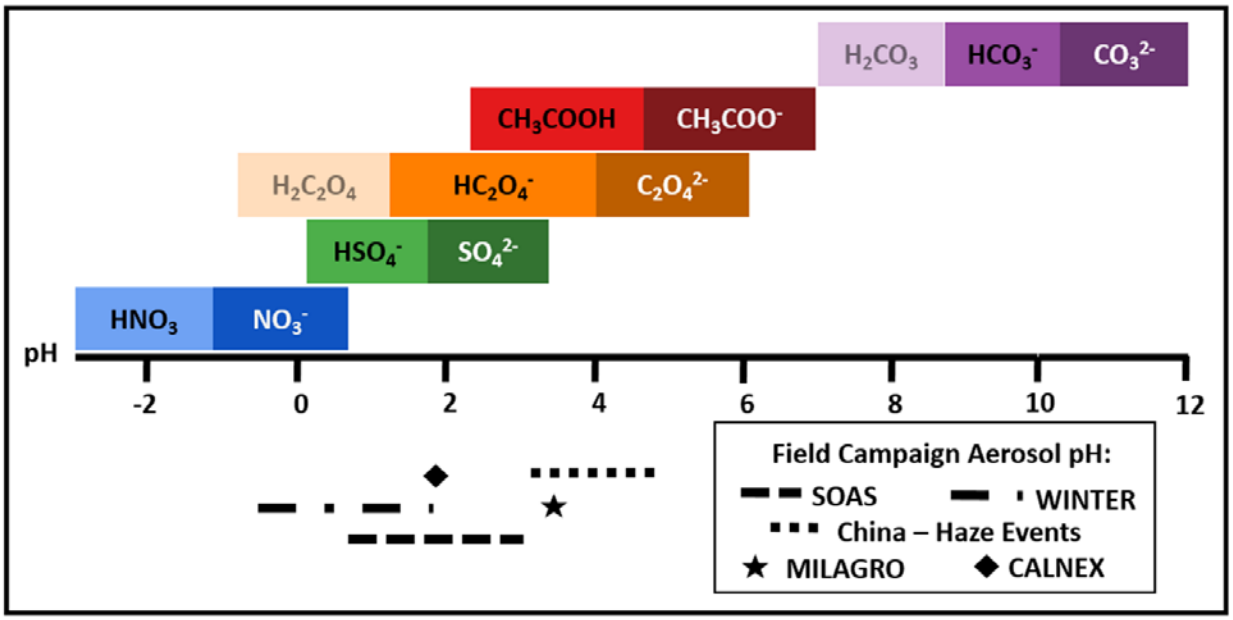

Figure 6.1. Schematic showing dominant species present as a function of pH for each acid-base system studied, as well as a comparison to the aerosol pH predicted by thermodynamic models for several field campaigns. $H_2C_2O_4$ and H_2CO_3 are included but cannot be quantified with this method.

6.2 Methods

6.2.1 Aerosol Sample Preparation

Standard solutions were prepared using 18.3 MΩ Milli-Q water and the following chemicals: ammonium oxalate ($(NH_4)_2C_2O_4$), sodium acetate ($NaCH_3COO$), sodium bicarbonate

($NaHCO_3$), sodium nitrate ($NaNO_3$), hydrochloric acid (HCl), nitric acid (HNO_3), and sulfuric acid (H_2SO_4) (Sigma-Aldrich); oxalic acid ($H_2C_2O_4$) (Acros Organics); ammonium sulfate ($(NH_4)_2SO_4$) (Alfa Aesar); acetic acid (HCH_3COO) (Fisher Scientific); and sodium carbonate (Na_2CO_3) (JT Baker Chemical Co.). All chemicals were > 98.0% purity and used without further purification. To create a solution for each acid-base system, a salt containing the base was dissolved in solution and then mixed with a strong acid to control the pH. Bulk solution pH was measured by a pH probe (AP110, accumet Portable). Table 1 lists the pH, salt, and acid comprising each solution used to generate aerosol particles. Concentration values for each solution are provided in Table S1. Aerosols were generated from solutions using a Collison nebulizer (atomizer) operated with HEPA-filtered air and then impacted onto quartz substrates (Ted Pella, Inc.) using a Microanalysis Particle Sampler (MPS-3, California Measurements, Inc.). For the HCO_3^-/CO_3^{2-} system, generated aerosols were passed through two diffusion dryers prior to impaction in order to remove liquid phase water and increase the concentration of analytes in individual particles (concentration increased by a factor of ~100 on average). Particles from Stage 1 of the MPS (>2.8 μm equivalent aerodynamic diameter cut-point) were analyzed to ensure particles were larger than the Rayleigh diffraction limit (0.36 μm) and spot size (0.72 μm) for the Raman spectrometer (0.9 N.A. objective with a 532 nm laser). The projected area diameter (d_{pa}) size range for particles studied is determined by optical imaging and refers to the diameter of a circle with the same projected area as the particle. For the particles in this study, d_{pa} ranged from 1 - 15 μm, with an average of 6.3 μm. These d_{pa}'s are larger than aerodynamic or geometric diameters of the particles prior to impaction due to spreading upon impaction.

Table 6.1. Composition and pH of solutions used to generate aerosol particles, along with vibrational modes corresponding to the acid and conjugate base, for each acid-base system.

Acid-Base System	Bulk Solution pH	Solution Composition		Acid		Base	
		Salt	Acid	Mode	Freq.[#] (cm^{-1})	Mode	Freq.[#] (cm^{-1})
HNO_3/NO_3^-	< 0*	$NaNO_3$	HNO_3	$\nu_s(HNO_3)$	1306	$\nu_s(NO_3^-)$	1047
$HC_2O_4^-/C_2O_4^{2-}$	3.63	$(NH_4)_2C_2O_4$	HCl	ν(C-C) $HC_2O_4^-$	873	ν(C-C) $C_2O_4^{2-}$	907
	3.97						
HCH_3COO/CH_3COO^-	3.92	$NaCH_3COO$	HCl	ν(C-C) CH_3COO	890	ν(C-C) CH_3COO^-	927
HCO_3^-/CO_3^{2-}	10.47	Na_2CO_3	HCl	$\nu_s(HCO_3^-)$	1019	$\nu_s(CO_3^{2-})$	1067
HSO_4^-/SO_4^{2-} & $HC_2O_4^-/C_2O_4^{2-}$	0.39	$(NH_4)_2SO_4$, $(NH_4)_2C_2O_4$	H_2SO_4	$\nu_s(HSO_4^-)$	1053	$\nu_s(SO_4^{2-})$	983
	0.83						
	3.58			ν(C-C) $HC_2O_4^-$	873	ν(C-C) $C_2O_4^{2-}$	907
	3.99						

*pH below measurement range of pH probe
[#]Frequencies identified from calibration of standard compounds

6.2.2 Raman Microspectroscopy

Raman spectra for individual impacted particles were collected using a LabRAM HR Evolution Raman microspectrometer (Horiba, Ltd.) equipped with a Nd:YAG laser source (50 mW, 532 nm) and CCD detector, and coupled with a confocal optical microscope (100x 0.9 N.A. SLMPlan N Olympus objective). The instrument was calibrated against the Stokes Raman signal of pure Si at 520 cm^{-1} using a silicon wafer standard. Spectra from 500 to 1400 cm^{-1} were acquired for 5 s with three accumulations for the inorganic acid systems and 15 s with three accumulations for the organic acid systems and the mixture. A 600 groove/mm diffraction grating yielded spectral resolution of ~1.7 cm^{-1}. Spectra were collected at ambient temperature and relative humidity (RH), monitored with an RH sensor (EK-H5, Sensiron). A 2 μL droplet of each solution was also analyzed in order to compare bulk solution spectra with those of the particles.

6.2.3 Aerosol pH Calculation

The pH of individual aerosol particles was determined using the method described by Rindelaub et al. (Rindelaub et al., 2016a). Briefly, integrated peak areas of the vibrational modes corresponding to an acid (HA) and conjugate base (A^-) for each acid-base system were related to concentration using calibration curves (Figures B.1-B.5). The vibrational modes analyzed for each acid-base system are included in Table 1. The concentration of other ions present in the particle (those not directly involved in the acid-base equilibrium) were determined from the ratio of [ion]:[acid + conjugate base] (Table S1). Once the concentration of all ions present was determined, ionic strength (I) was calculated via Equation 6.1, where C_i and z_i represent the concentration of each ion and its corresponding charge, respectively.

Equation 6.1
$$I = \frac{1}{2}\sum C_i z_i^2$$

Molality units were used for concentration of each species, determined by converting molarity to molality using the density of the solution mixture. The solution densities were found by using the Laliberté model (Laliberte and Cooper, 2004), and were iteratively solved during molality conversions. Since the density calculations required concentrations of each solute in the solution mixture, the equivalent concentrations of each cation and anion were found by Clegg's equivalent fraction method (Clegg and Simonson, 2001), which assumes that all possible combinations of cation and anion are present as solute components.

Then the extended Debye-Hückel relationship (Equation 6.2) was applied to calculate the activity coefficient for each species in the acid-base equilibrium. In the extended Debye-Hückel relationship, A and B are constants characteristic of the solvent (water) and $å_i$ is the effective diameter of the ion in solution (Kielland, 1937; Garrels and Christ, 1965). Values for the constants used in the extended Debye- Hückel relationship can be found in Table S2.

Equation 6.2
$$-log\gamma_i = \frac{Az_i^2\sqrt{I}}{1+å_i B\sqrt{I}}$$

The concentrations of acid and conjugate base, their respective activity coefficients, and the acid dissociation constant, K_a, were then used to calculate [H^+] (Equation 6.3), and finally pH (Equation 6.4).

Equation 6.3
$$K_a = \frac{a_{H^+} * a_{A^-}}{a_{HA}} = \frac{([H^+]*\gamma_{H^+})([A^-]*\gamma_{A^-})}{[HA]*\gamma_{HA}}$$

Equation 6.4
$$\text{pH} = -log\left(a_{H^+}\right) = -log(\gamma_{H^+} * [H^+])$$

Note that an iterative method is needed to solve Equations. 6.1-6.3, since the value of $[H^+]$ is not known and is needed in the calculation of ionic strength and activity coefficients. As with the density calculations (discussed after Equation 6.1), Clegg's equivalent fraction method (Clegg and Simonson, 2001) was used to find the first initial value for $[H^+]$. This value is then used to solve for ionic strength (Equation 6.1), and subsequently the activity coefficients (Equation 6.2). Using the activity coefficients, Equation 6.3 is applied to calculate a new value for $[H^+]$. The initial value for $[H^+]$ is then iteratively changed until it equals that from the Equation 6.3 calculations.

6.3 Results and Discussion

6.3.1 Inorganic Acid-Base Equilibria Aerosol pH

Aerosol particle pH was evaluated for each acid and conjugate base system and is discussed in terms of inorganic acid systems (HNO_3/NO_3^- and HCO_3^-/CO_3^{2-}), organic acid systems ($HC_2O_4^-/C_2O_4^{2-}$ and CH_3COOH/CH_3COO^-), and a mixed inorganic-organic system ($HC_2O_4^-/C_2O_4^{2-}$ with HSO_4^-/SO_4^{2-}). Figure 6.2 shows the relative fraction of each inorganic species as a function of pH for the nitric acid and carbonic acid equilibriums, respectively. Since the pH was too low to be measured accurately with the pH probe, the pH of the bulk solution used to generate aerosol particles for the HNO_3/NO_3^- system was calculated to be between -1.1 and -1.4, based on the concentration of ions in solution. The pH of HNO_3/NO_3^- aerosol particles when calculated using the extended Debye-Hückel model varied from -1.2 to 0.090, with an average of -0.48. A histogram showing the pH for all particles measured (for the HNO_3/NO_3^- system and all systems discussed later) is included in the Supporting Information. The Raman spectrum of a representative HNO_3/NO_3^- particle (pH = -0.49, d_{pa} = 9.9 μm) is shown in Figure 6.2C, with the vibrational modes that were used to determine $[NO_3^-]$ and $[HNO_3]$ identified as $\nu_s(NO_3^-)$ at 1057 cm^{-1} and $\nu_s(HNO_3)$ at 1313 cm^{-1}, respectively (Ratcliffe and Irish, 1985; Waterland et al., 2001; Wren and Donaldson, 2012a; Jentzsch et al., 2013). In the inset, the shoulder of the $\nu_s(HNO_3)$ mode at 1344 cm^{-1} was attributed to the $\nu_a(NO_3^-)$ mode (Wren and Donaldson, 2012a; Jentzsch et al., 2013). As can be seen by the low intensity of the $\nu_s(HNO_3)$ mode relative to the $\nu_s(NO_3^-)$ mode, nitric acid was not conserved in the particle phase, a phenomenon that will be discussed further later. For comparison with an alternative prediction of pH, the multilayer adsorption isotherm based model from Dutcher et al. was also used to

determine the molalities and activities of the solutes present, and subsequently the activity of H^+ and pH (Dutcher et al., 2013). With the Dutcher model, particle pH values were closer than the values from extended Debye-Hückel model to the calculated pH values of the HNO_3/NO_3^- bulk solution, ranging from -1.4 to -0.88, with an average pH of -1.2. The pH of the particle corresponding to the Raman spectrum shown in Figure 6.2C was calculated with the Dutcher model to be -1.17.

The measured pH of the bulk solution used to generate aerosol particles for the HCO_3^-/CO_3^{2-} system was 10.47. HCO_3^-/CO_3^{2-} aerosol particles varied in pH from 9.9 to 10.4, with an average of 10.1. The $\nu_s(HCO_3^-)$ vibrational mode at 1023 cm^{-1} and $\nu_s(CO_3^{2-})$ vibrational mode at 1052 cm^{-1} that were used to determine $[HCO_3^-]$ and $[CO_3^{2-}]$, respectively (Rudolph et al., 2008), are shown in the Raman spectrum of a representative HCO_3^-/CO_3^{2-} particle (pH = 10.1, d_{pa} = 4.1 μm) in Figure 6.2D. The H_2CO_3/HCO_3^- equilibrium could not be studied, due to the equilibrium between aqueous phase H_2CO_3 with CO_2 and H_2O (Magid and Turbeck, 1968).

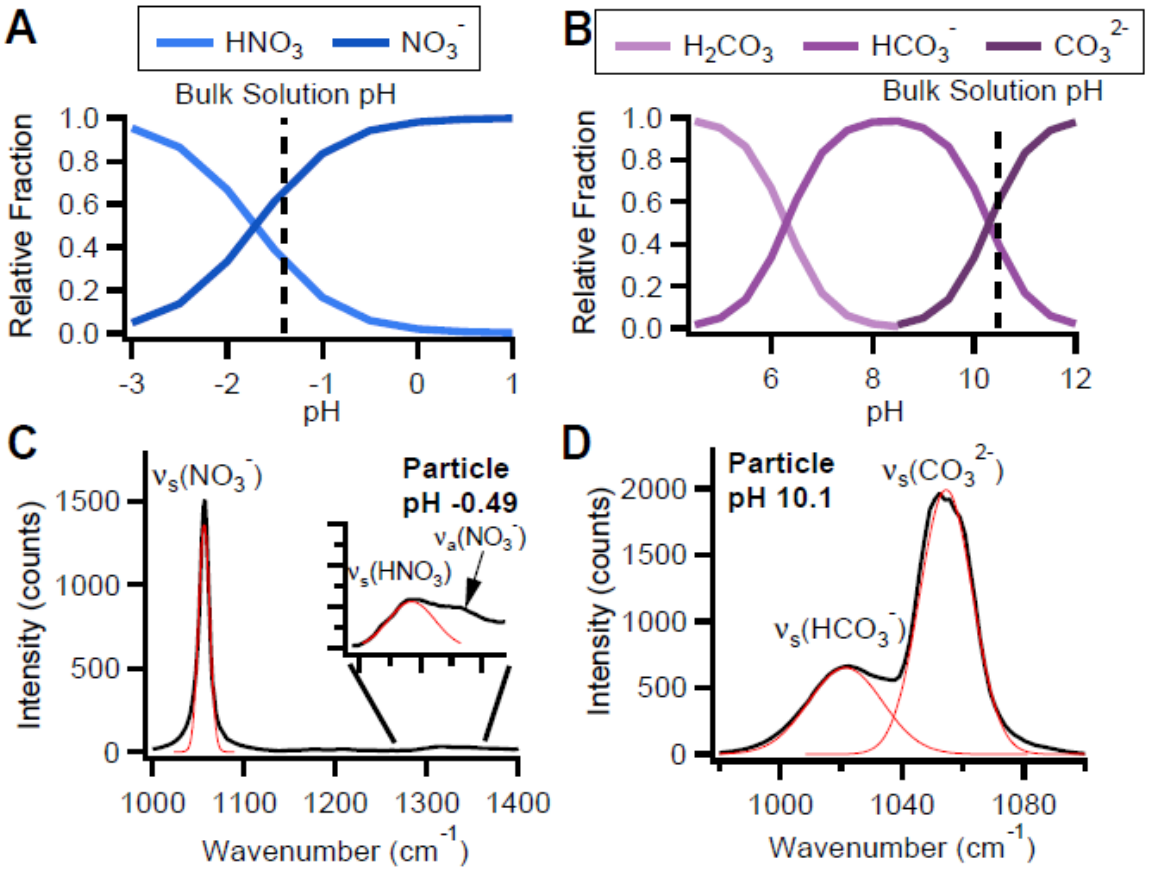

Figure 6.2. Relative fraction as a function of pH for (A) nitric acid equilibrium and (B) carbonic acid and bicarbonate equilibrium, with the pH of the bulk solutions used to generate aerosol particles indicated by the dashed line. Raman spectra for a (C) HNO_3/NO_3^- aerosol particle pH -0.49 and a (D) HCO_3^-/CO_3^{2-} aerosol particle pH 10.1. Red lines indicate Gaussian peak fits.

6.3.2 Organic Acid-Base Equilibria Aerosol pH

For the organic acids, the relative fractions of each species as a function of pH in the oxalic acid and acetic acid equilibriums are shown in Figure 6.3A and 6.3B, respectively. $HC_2O_4^-/C_2O_4^{2-}$ aerosol particles were atomized from two bulk solutions, with measured pH values of 3.63 and 3.97, respectively. Aerosol particle pH varied from 2.4 to 3.8 with an average of 3.0 and from 2.8 to 3.9 with an average of 3.3 for $HC_2O_4^-/C_2O_4^{2-}$ particles generated from the respective low and high pH bulk solutions. Raman spectra for two representative $HC_2O_4^-/C_2O_4^{2-}$ particles (pH = 2.9, d_{pa} = 15.0 μm and pH = 3.6, d_{pa} = 8.0 μm) are shown in Figure 6.3C. $[HC_2O_4^-]$ was determined from the $HC_2O_4^-$ ν(C-C) mode at 876 cm^{-1} and $[C_2O_4^{2-}]$ was determined from the $C_2O_4^{2-}$ ν(C-C) mode at 899 cm^{-1} (Ito and Bernstein, 1956; Gruen and Plane, 1967; de Villepin and Novak, 1971). Under appropriately acidic conditions, $H_2C_2O_4$ can be identified by its ν(C-C) mode at 850 cm^{-1} (Figure B.7) (Hibben, 1935). However, close proximity to the ν(C-C) mode of $HC_2O_4^-$ makes it difficult to fit the two modes accurately enough to determine their respective ion concentrations, thus limiting the use of the $H_2C_2O_4/HC_2O_4^-$ equilibrium system with this method for determining aerosol particle pH.

For the CH_3COOH/CH_3COO^- equilibrium system, particles were generated from a bulk solution with a measured pH of 3.92, yielding aerosol particle pH values of 3.8 to 4.2, with an average of 4.0. The Raman spectrum of a representative CH_3COOH/CH_3COO^- particle (pH = 4.1, d_{pa} = 4.4 μm) is shown in Figure 6.3D, with the CH_3COOH ν(C-C) mode used to calculate $[CH_3COOH]$ identified at 892 cm^{-1} and the CH_3COO^- ν(C-C) mode used to calculate $[CH_3COO^-]$ identified at 931 cm^{-1} (Ito and Bernstein, 1956; Ng and Shurvell, 1987; Nakabayashi et al., 1999). It should be noted that CH_3COOH measurements are most likely of acetic acid clusters, as CH_3COOH molecules can form dimers through hydrogen bonding interactions in aqueous environments (Nishi et al., 1999). Similar to nitric acid, low intensity of the ν(C-C) mode for CH_3COOH relative to CH_3COO^- indicates less acetic acid is present in the particle phase due to gas-particle partitioning and will be discussed in detail later.

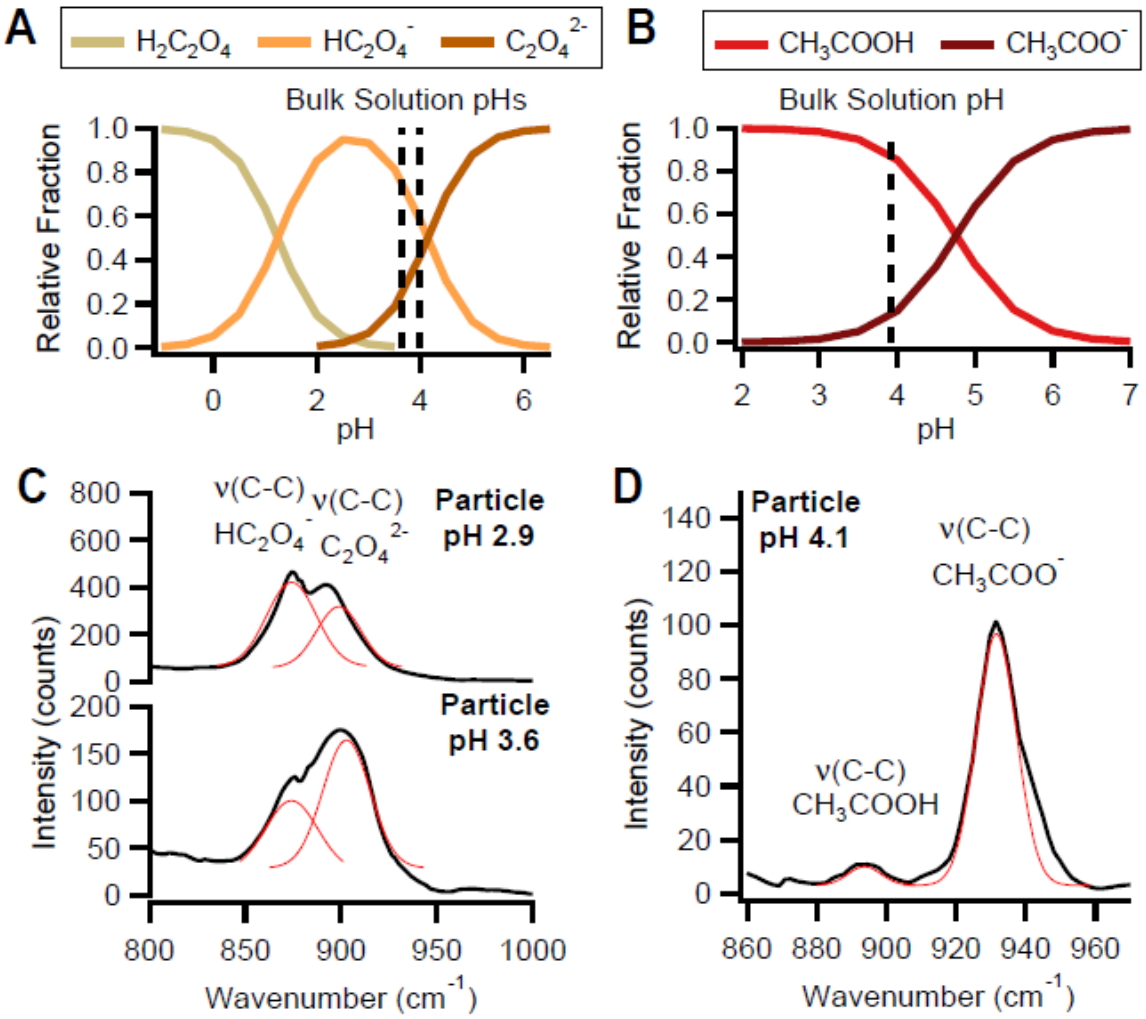

Figure 6.3. Relative fraction as a function of pH for (A) oxalic acid and bioxalate equilibrium and (B) acetic acid equilibrium, with the pH of the bulk solutions used to generate aerosol particles highlighted by the dashed line. Raman spectra for (C) $HC_2O_4^-/C_2O_4^{2-}$ aerosol particles pH 2.9 and 3.6 and (D) a CH_3COOH/CH_3COO^- aerosol particle pH 4.1. Red lines indicate Gaussian peak fits.

6.3.3 Mixed Acid-Base Equilibria Aerosol pH

The final set of particles were composed of both the $HC_2O_4^-/C_2O_4^{2-}$ and HSO_4^-/SO_4^{2-} equilibrium systems. Figure 6.4A shows the relative fraction of all species for both equilibrium systems as a function of pH. Particles were atomized from four bulk solutions of different pHs – 0.39, 0.83, 3.58, and 3.99. For particles generated from the two lower pH solutions, the HSO_4^-/SO_4^{2-} equilibrium was used to determine pH. Particle pH ranged from 0.91 to 1.3 with an average of 1.2 for the lowest pH set (bulk solution pH 0.39) and 1.5 to 1.8 with an average of 1.6 for the higher pH set (bulk solution pH 0.83). For particles generated from the two higher pH

solutions, the $HC_2O_4^-/C_2O_4^{2-}$ equilibrium was used to determine pH. Particle pH ranged from 3.6 to 4.7 with an average of 4.1 for the lower pH set (bulk solution pH 3.58) and 3.3 to 4.9 with an average of 3.7 for the higher pH set (bulk solution pH 3.99). Figure 6.4B shows spectra of a representative particle for which the HSO_4^-/SO_4^{2-} equilibrium was used to determine the pH (pH = 1.5, d_{pa} = 8.8 μm) and a representative particle for which the $HC_2O_4^-/C_2O_4^{2-}$ equilibrium was used to determine the pH (pH = 3.6, d_{pa} = 8.3 μm). Figure 6.4C shows the same spectra, focused closer on the spectral regions where the vibrational modes corresponding to the $HC_2O_4^-/C_2O_4^{2-}$ system and HSO_4^-/SO_4^{2-} system are located. Raman spectra of a representative particle (pH = 1.2, d_{pa} = 8.1 μm) generated from the pH 0.38 solution and a representative particle (pH = 3.9, d_{pa} = 4.4 μm) generated from the pH 3.58 solution are also shown in Figure 6.4C. For the HSO_4^-/SO_4^{2-} system, the $\nu_s(SO_4^{2-})$ and $\nu_s(HSO_4^-)$ modes were identified at 983 cm^{-1} and 1050 cm^{-1}, respectively, and used to determine $[SO_4^{2-}]$ and $[HSO_4^-]$ (Jentzsch et al., 2013; Rindelaub et al., 2016a). At the low pHs, all oxalate species were present in the form of oxalic acid and thus the ν(C-C) mode of $H_2C_2O_4$ at 850 cm^{-1} was used to determine $[H_2C_2O_4]$ (Hibben, 1935), which was included in calculations of ionic strength. For the $HC_2O_4^-/C_2O_4^{2-}$ system, the same ν(C-C) modes for $HC_2O_4^-$ and $C_2O_4^{2-}$ discussed previously for particles composed of only the $HC_2O_4^-/C_2O_4^{2-}$ equilibrium were used to determine pH. At the high pHs, all sulfate species present were in the form of sulfate and thus the $\nu_s(SO_4^{2-})$ mode was used to determine $[SO_4^{2-}]$ and incorporated into the calculations of ionic strength. Aerosol particle pH for particles composed of only $HC_2O_4^-/C_2O_4^{2-}$ was, on average, lower in comparison to particles of $HC_2O_4^-/C_2O_4^{2-}$ and HSO_4^-/SO_4^{2-} mixed composition, despite similar pH bulk solutions used to generate particles and using the $HC_2O_4^-/C_2O_4^{2-}$ equilibrium to calculate pH for both systems. This phenomenon can be explained by differences in particle ionic strength and H^+ activity and will be discussed later. Successful determination of pH for these mixed system particles shows the potential for this method to be applied to aerosol particles of more complex chemical compositions, potentially even ambient aerosol particles if distinguishable modes for an acid and its conjugate base are present and measurable.

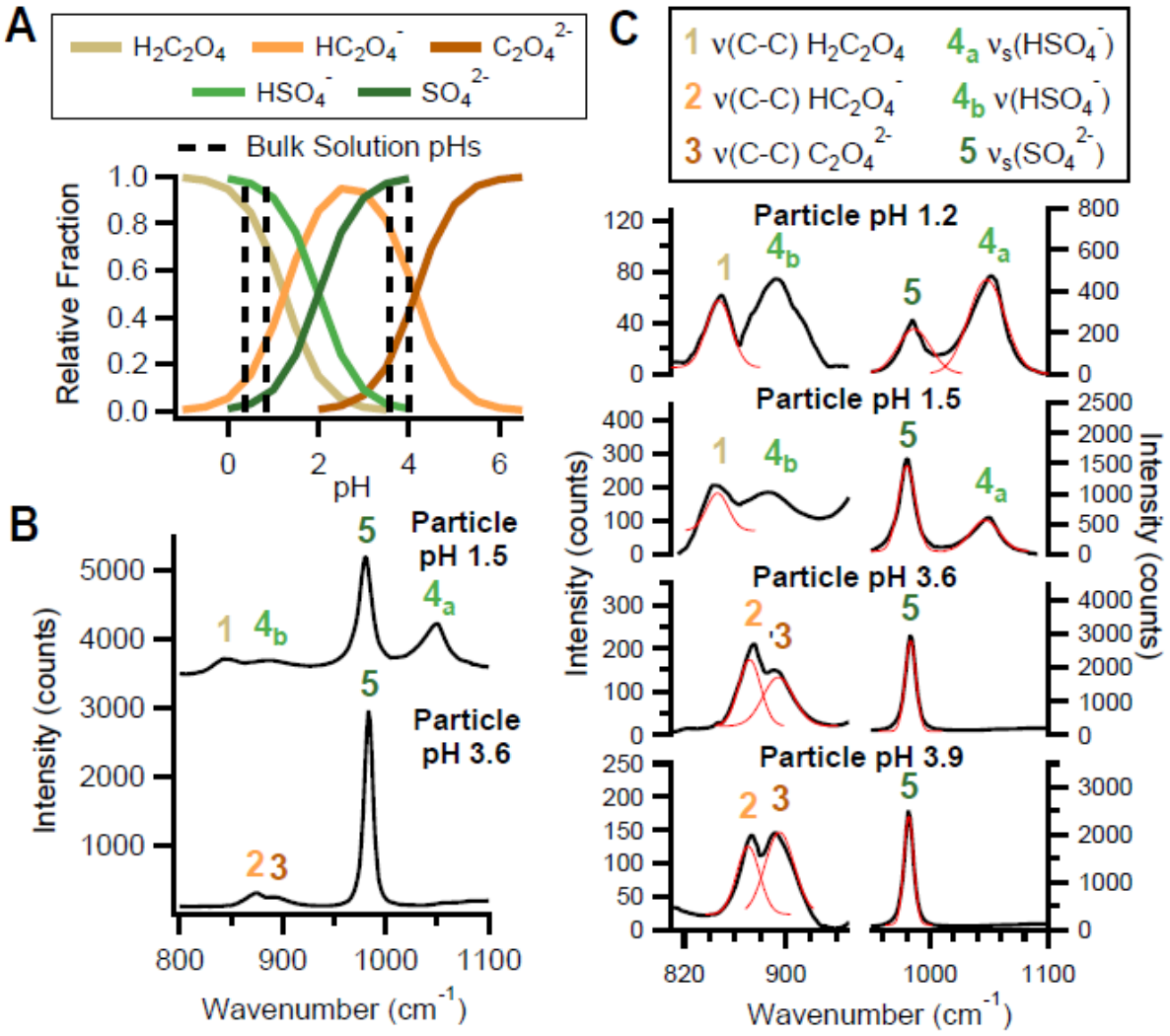

Figure 6.4. (A) Relative fraction as a function of pH for oxalic acid and bioxalate equilibrium and bisulfate equilibrium, with the pH of the bulk solutions used to generate oxalate-sulfate mixed aerosol particles highlighted by the dashed lines. (B) Full Raman spectra for $HC_2O_4^-$/$C_2O_4^{2-}$ and HSO_4^-/SO_4^{2-} mixed aerosol particles pH 1.5 and 3.2. (C) Raman spectra for $HC_2O_4^-$/$C_2O_4^{2-}$ and HSO_4^-/SO_4^{2-} aerosol particles pH 1.2, 1.5, 3.6, and 3.9 focused on spectral regions where ν(C-C) $HC_2O_4^-$, ν(C-C) $C_2O_4^{2-}$, $\nu_s(HSO_4^-)$, and $\nu_s(SO_4^{2-})$ are present. Red lines indicate Gaussian peak fits.

6.3.4 Observations of Gas-Particle Partitioning

As mentioned previously in the discussions of the HNO_3/NO_3^- and CH_3COOH/CH_3COO^- equilibrium systems, HNO_3 and CH_3COOH are not conserved in the generated aerosol particles relative to their respective conjugate bases due to gas-particle partitioning. To further explore this phenomenon, Figure 6.5 shows a comparison of spectra of the HNO_3/NO_3^- and CH_3COOH/CH_3COO^- particles to spectra of the bulk solutions from which the particles were

generated. The intensity of the vibrational modes corresponding to the acid for both systems is significantly larger in the bulk solution than in the particle, thus the [acid]:[base] ratio in the bulk solution is larger than that of the particle. This indicates nitric acid and acetic acid are partitioning from the particle to gas phase during the atomization process, most likely due to quicker loss of vapor because of increased surface to volume ratio for the aerosol particles versus the droplets and/or heating from the laser. Nitric acid and acetic acid exhibit this behavior more than oxalic acid and the other ion compounds because of their higher volatility. The value for the Henry's Law constant (k_H°) for nitric acid and acetic acid is ~ $2x10^3$ mol m^{-3} Pa^{-1} and ~ $4x10^1$ mol m^{-3} Pa^{-1}, respectively, in contrast to the larger k_H° of ~$6x10^6$ mol m^{-3} Pa^{-1} of oxalic acid (Sander, 2015). A limited number of particles were analyzed for the CH_3COOH/CH_3COO^- system, due to challenges associated with partitioning of CH_3COOH to the gas phase. For comparison, Raman spectra of bulk solutions and particles for the $HC_2O_4^-/C_2O_4^{2-}$ system and the $HC_2O_4^-/C_2O_4^{2-}$ and HSO_4^-/SO_4^{2-} mixed system that did not exhibit this partitioning behavior are shown in Figure B.8. The observation of decreased [acid]:[base] for aerosol particles for the HNO_3/NO_3^- and CH_3COOH/CH_3COO^- equilibrium systems could have implications for size-dependent particle acidity and particle phase reactions, such as acid-displacement in mixed sea salt and weak organic acid particles (Laskin et al., 2012).

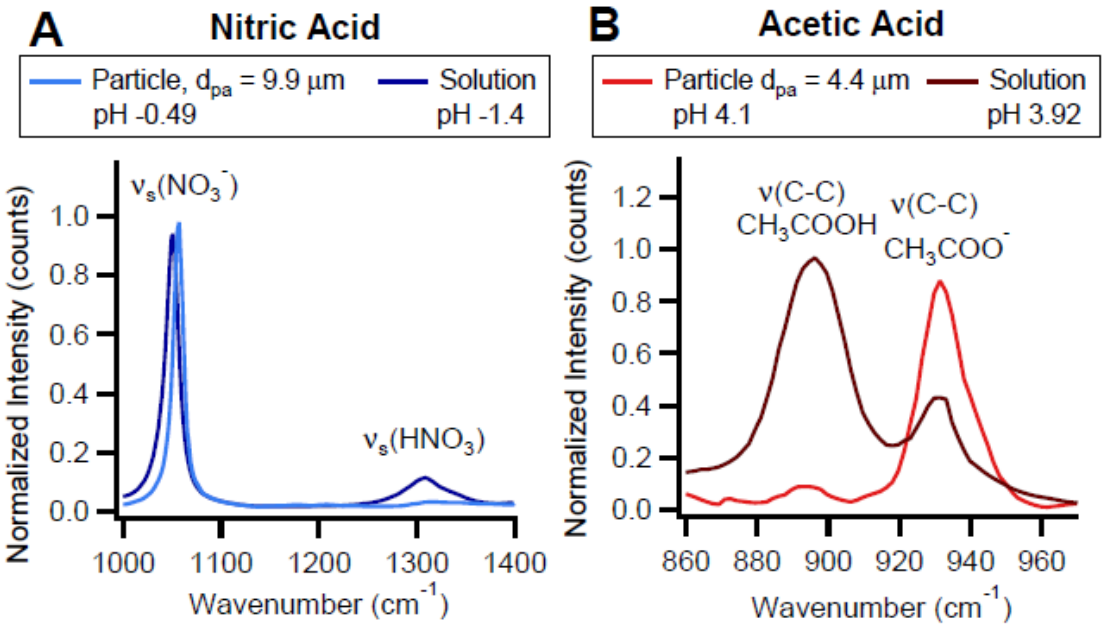

Figure 6.5. Raman spectra of a representative particle and the bulk solution for the A) HNO_3/NO_3^- and B) CH_3COOH/CH_3COO^- equilibrium systems. The spectra for the HNO_3/NO_3^- system were normalized to the $\nu_s(NO_3^-)$ mode and the spectra for the CH_3COOH/CH_3COO^- system were normalized to the ν(C-C) mode of CH_3COO^-.

6.3.5 H^+ Activity and Ionic Strength

In addition to measuring the pH of aerosol particles for each of these systems, trends were observed for H^+ activity coefficient, $\gamma(H^+)$, in relation to ionic strength and aerosol particle pH relative to the broadness of the vibrational modes analyzed. Across all of the acid-base systems, there is a negative relationship for $\gamma(H^+)$ as a function of ionic strength (Figure 6.6), with more $\gamma(H^+)$ sensitivity at lower ionic strength. However, the inorganic systems tend to have larger, more varied ionic strength with lower, less variable $\gamma(H^+)$. The inverse holds for the organic systems, which show larger, more varied $\gamma(H^+)$ with smaller and less variability in ionic strength. As mentioned earlier, even though particles were generated from bulk solutions of similar pH and the $HC_2O_4^-/C_2O_4^{2-}$ system was used to determine pH, particles composed of only $HC_2O_4^-/C_2O_4^{2-}$ had lower average pH than particles of $HC_2O_4^-/C_2O_4^{2-}$ and HSO_4^-/SO_4^{2-} mixed composition (average aerosol particle pH 3.2 and 4.0, respectively). Because of the inorganic component in the $HC_2O_4^-/C_2O_4^{2-}$ and HSO_4^-/SO_4^{2-} mixed particles, their $\gamma(H^+)$ was lower, thus decreasing the activity of H^+, making the particles less acidic. This observation supports that ion

behavior in mixed organic and inorganic particles is dictated by contributions from all chemical species present.

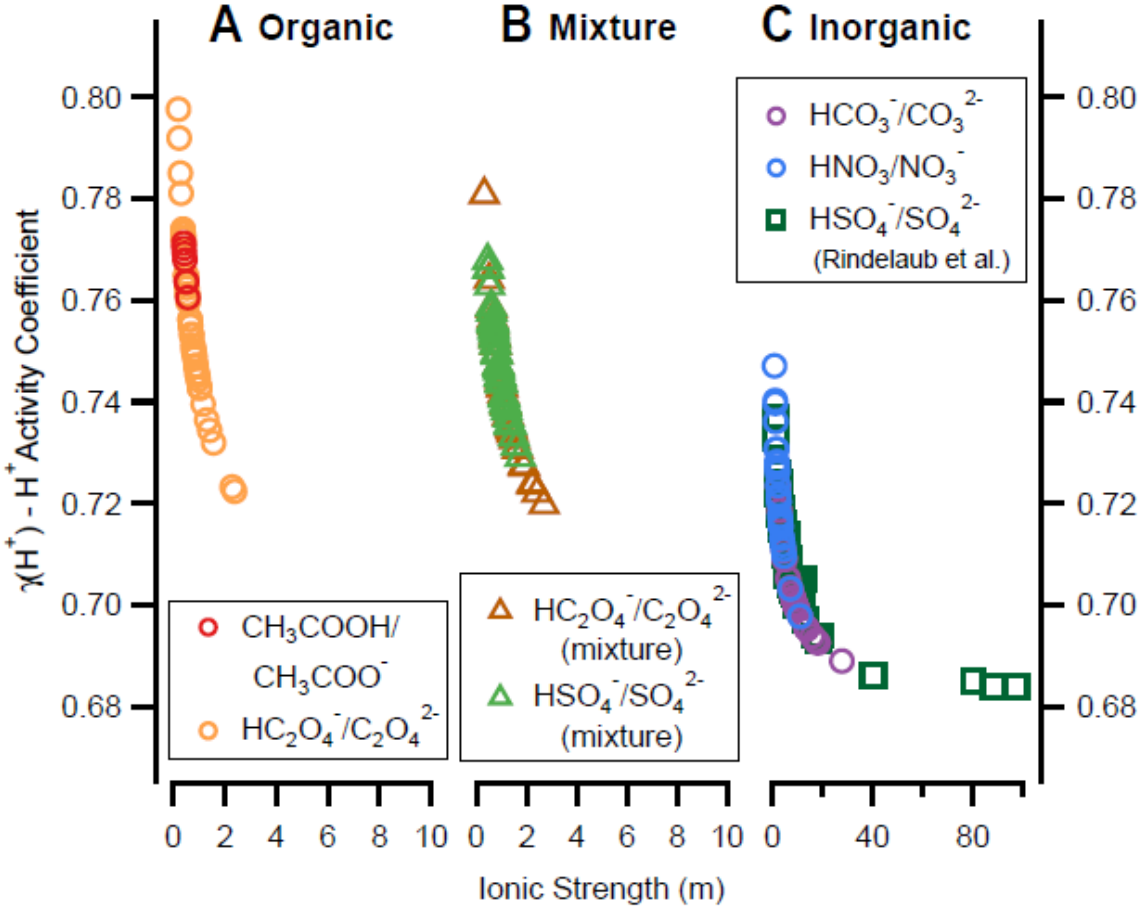

Figure 6.6. H^+ activity coefficient ($\gamma(H^+)$) as a function of ionic strength for each organic (A), mixture (B), and inorganic (C) acid-base system. Data for the HSO_4^-/SO_4^{2-} equilibrium from Rindelaub et al. is also included for comparison. Note the differing scales for ionic strength.

6.3.6 Hydrogen Bonding Effects

In addition to the relationship between $\gamma(H^+)$ and ionic strength, aerosol particle pH as a function of peak broadness (full width half maximum – fwhm) was explored (Figure 6.7). For vibrational modes corresponding to both the inorganic and organic acids, fwhm increased as particles became more acidic. The broadening of these modes may be attributed to different solvent binding conformations that occur as pH decreases and hydrogen bonding increases (Larkin, 2011). In the presence of more H_3O^+ ions and increased hydrogen bonding, there may be multiple solvent conformations, each with slightly different energies that form, leading to a

broader peak that encompasses all of these variations in structure. The correlation (r) values for this trend are: $\nu_s(HCO_3^-)$, -0.927; $\nu_s(HSO_4^-)$, -0.532; $\nu_s(HNO_3)$, -0.729; ν(C-C) CH_3COOH, -0.683; and ν(C-C) $HC_2O_4^-$, -0.513. Although there is a relatively strong correlation between aerosol particle pH and fwhm for ν(C-C) CH_3COOH, it is difficult to confidently identify a relationship due to the limited number of data points. A second aspect of pH versus peak width worth commenting on is the greater magnitude of broadening for the nitric acid peak versus the bicarbonate peak, which is attributed to significantly higher H_3O^+ concentration at pH -1 versus 10.

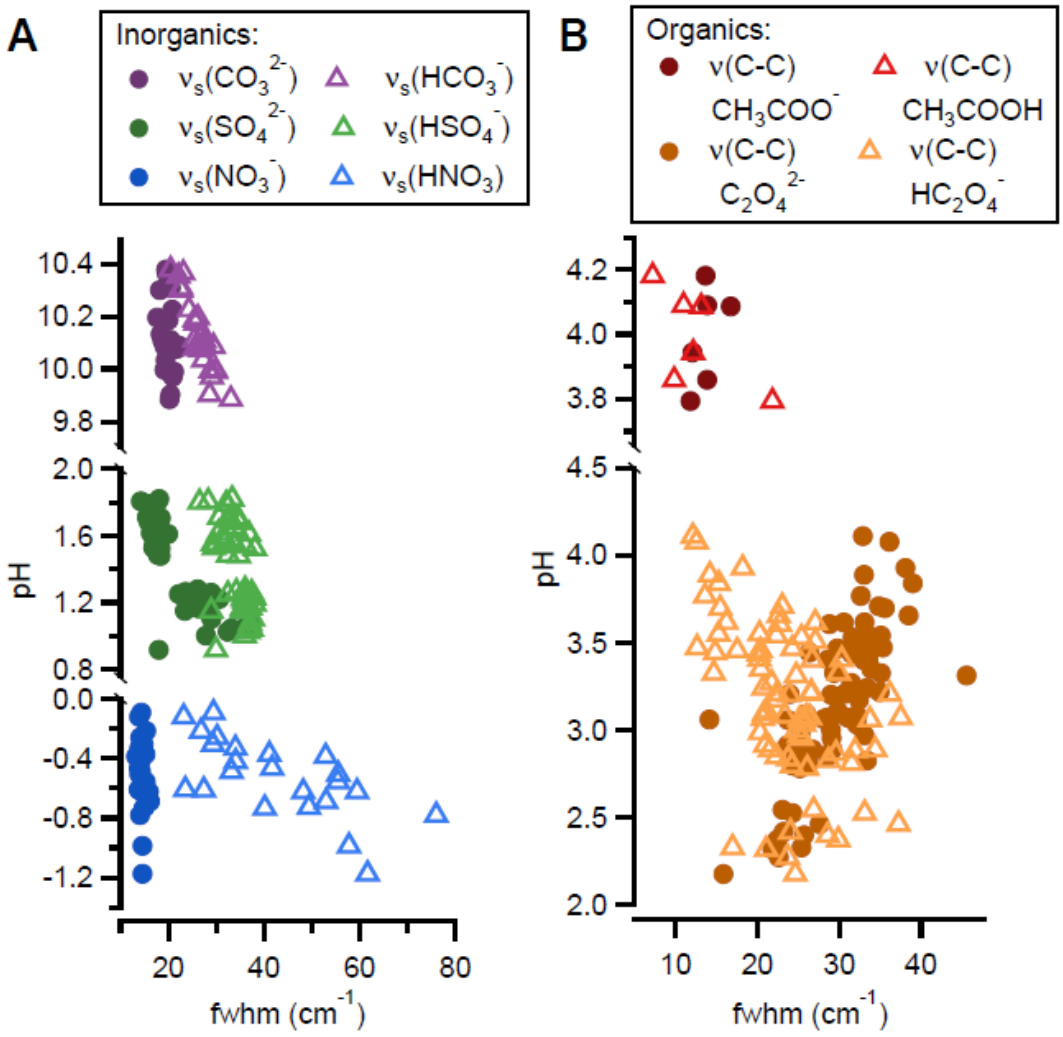

Figure 6.7. Aerosol particle pH as a function of the full width half maximum (fwhm) for (A) inorganic acids and bases and (B) organic acids and bases).

Additionally, it should be noted that the correlation between aerosol particle pH and fwhm of the vibrational mode corresponding to the acid species is not quite as strong for

$\nu_s(HSO_4^-)$, -0.532 and ν(C-C) $HC_2O_4^-$, -0.513. For HSO_4^-, this could be due to the extra oxygen atom (four oxygen compared to two or three of the other acid species), which creates more resonance and increases the electron density, thus reducing the impact of hydrogen bonding on the symmetric S-O stretch and limiting broadening of its peak in the Raman spectra. Comparison with results from Rindelaub et al. (Figure B.9) (Rindelaub et al., 2016a) shows a slightly stronger correlation between aerosol particle pH and $\nu_s(HSO_4^-)$ peak broadness (r = -0.659). For $HC_2O_4^-$, the impact of hydrogen bonding on peak fwhm is much less pronounced, since the analyzed vibrational mode corresponds to the C-C stretch of the backbone of the dicarboxylic acid, rather than a stretch containing an oxygen atom. However, according to density functional theory calculations (see Supporting Information for details on calculations), the ν(C-C) stretch is weakly coupled to the δ(O-C-O) bend, which is influenced by protonation and subsequent hydrogen bonding with decreasing pH.

In contrast to the acid species, for the inorganic base species, there was no correlation between aerosol particle pH and peak broadness. This observation is tentatively attributed to fewer solvent bonding conformations being possible for the more symmetric molecules, resulting in a consistently sharper peak. For the organic bases, the peak became narrower with decreasing pH, which could be due to increased concentration of the base species (oxalate or acetate) with decreasing pH, resulting in a more intense, and thus broader, peak. Because the ν(C-C) stretch for the organic base species is inherently broader than the symmetric stretch of the inorganic base species, this trend of increasing pH and ion concentration leading to increased peak broadness is only observed for the organic base species, though this is speculative and further work is needed to explain this phenomenon. While there may appear to be a relationship between aerosol particle pH and peak fwhm for $\nu_s(SO_4^{2-})$, this is an artifact of analyzing two samples with two distinctly different pHs, and thus two different populations of sulfate. When compared with results from Rindelaub et al. with aerosol particle pH varied over a broader range (Figure B.9) (Rindelaub et al., 2016a), it is clear that there is not a strong correlation (r = -0.471). Correlation (r) values for all acid and base species are provided in Table S3. Further work expanding the number of species studied and range of pH is needed to fully understand the relationship between aerosol particle pH and the ion interactions that dictate broadness of the vibrational modes corresponding to the species of the acid-base equilibrium systems.

6.4 Conclusions

In this study, pH was determined for individual laboratory generated aerosol particles of varying composition at ambient conditions using Raman microspectroscopic measurements of acid and conjugate base species and the extended Debye-Hückel relationship. The acid-base equilibrium systems tested included two inorganic (nitric acid/nitrate and bicarbonate/carbonate), two organic (bioxalate/oxalate and acetic acid/acetate), as well as a mixture of both inorganic and organic (bisulfate/sulfate and bioxalate/oxalate). In addition to aerosol particle pH measurements, this study explored gas-particle partitioning of volatile acid species and a few aspects of ion behavior in relation to particle pH. Nitric acid and acetic acid were found to partition from the particle to the gas phase due to increased surface to volume ratios and did so more than the other acid species because of their higher volatility. In terms of the impact of organic and inorganic components on ionic strength and H^+ activity, the inorganic particles had larger, more variable ionic strength with smaller, less change in the H^+ activity coefficient, while the organic particles had larger, more variable H^+ activity coefficient values with smaller, less change in ionic strength. Finally, the relationship between particle pH and peak broadness was explored and revealed unique trends in peak broadness with changing pH for both inorganic and organic acid and base species. These results show the potential for direct measurement of pH and ion behavior in individual aerosol particles and will enable future studies of more chemically complex particles, including ambient aerosol, which will improve understanding of their pH-dependent chemical processes and climate-relevant properties.

6.5 Acknowledgements

This work was supported by the National Science Foundation Grant No. CAREER-1654149 (Ault) and No. CAREER-1554936 (Dutcher), startup funds from the University of Michigan, and RLC was supported by the Susan Lipschutz Fellowship Award from the University of Michigan Rackham Graduate School. RLC performed Raman spectroscopy research with assistance from JLA. LN performed modeling and calculations with assistance from CSD.

Chapter 7. Direct Determination of Aerosol pH: Size-Resolved Measurements of Submicron and Supermicron Aqueous Particles

Adapted with permission from Craig, R. L., Peterson, P. K., Nandy, L., Lei, Z., Hossain, M. A., Camarena, S., Dodson, R. A., Cook, R. D., Dutcher, C. S., and Ault, A. P.: Direct Determination of Aerosol pH: Size-Resolved Measurements of Submicron and Supermicron Aqueous Particles, *Anal. Chem.*, 2018, under review with journal. Copyright 2018 American Chemical Society.

7.1 Introduction

Atmospheric aerosols have global impacts on human health (10% of global deaths annually) (Kim et al., 2015) and climate (due to effects on radiative forcing and cloud formation). (Pöschl, 2005). Despite their importance, mechanistic understanding is low for many key atmospheric processes, such as secondary organic aerosol (SOA) formation. Aerosol acidity is a critical property for SOA formation, specifically epoxide ring opening reactions, as the reaction rates of pH-dependent multiphase chemical processes can vary by five orders of magnitude within relevant atmospheric pH values (0-5), leading to lifetimes for key species that vary from minutes to weeks (Jang et al., 2002, 2003b; Limbeck et al., 2003; Iinuma et al., 2009; Eddingsaas et al., 2010; Surratt et al., 2010; Lin et al., 2012; Gaston et al., 2014; Riva et al., 2016c). Other multiphase chemical processes where acidic pH conditions are important include gas-aerosol phase partitioning (Jang et al., 2002), heterogeneous reactions (Gard et al., 1998; Bondy et al., 2017b), water uptake (Prenni et al., 2003; Ghorai et al., 2011), hydrolysis (Surratt et al., 2008; Hu et al., 2011; Rindelaub et al., 2015, 2016b), liquid-liquid phase separations (Ault et al., 2013a; You et al., 2014; Losey et al., 2016), metal ion dissolution and solubility (Chen et al., 2012; Longo et al., 2016; Fang et al., 2017), and photolysis and OH radical reaction chemistry (Liu et al., 2017c; Rapf et al., 2017; Witkowski and Gierczak, 2017). Recent work has predicted through indirect methods that aerosol particles are often acidic (Guo et al., 2015, 2016; Bougiatioti et al., 2016; Weber et al., 2016; Battaglia et al., 2017; Liu et al., 2017b), which has important implications for the processes listed above. However, in addition to a lack of direct measurements, there is both variability and uncertainty regarding atmospheric aerosol acidity due

to differing source contributions (Bougiatioti et al., 2016; Pozzer et al., 2017; Shi et al., 2017), seasonality (Kumar and Raman, 2016; Wu et al., 2017), and regional location, such as urban versus rural areas (Battaglia et al., 2017).

Aerosol acidity is difficult to measure due to the non-conservative nature of H^+ concentration and its dependence on relative humidity (RH) and aerosol liquid water content. As such, indirect filter-based measurements or proxy methods to predict pH are often used. Proxy methods include ion balance, molar ratio, phase partitioning, and thermodynamic equilibrium models, with the latter two regarded as the most accurate (Hennigan et al., 2015). For the phase partitioning method, gas and aerosol phase measurements of semi-volatile compounds, such as NH_3/NH_4^+, are used to indirectly measure pH (Keene et al., 2004; Young et al., 2013; Hennigan et al., 2015). Thermodynamic models, such as E-AIM (Clegg et al., 1992, 1998; Carslaw et al., 1995; Wexler and Clegg, 2002) and ISORROPIA-II (Nenes et al., 1998; Fountoukis and Nenes, 2007), predict aerosol pH based on measured chemical species (e.g., sulfate and ammonium concentrations), temperature, and RH and have been increasingly applied to evaluate aerosol acidity and variability (Guo et al., 2015, 2016; Bougiatioti et al., 2016; Weber et al., 2016; Battaglia et al., 2017; Liu et al., 2017b; Wu et al., 2017). Given the lack of approaches to directly measure pH, these models have driven our knowledge of aerosol acidity, but have also had few experimental measurements of pH to constrain their results. In particular, the thermodynamic models are most accurate when they can be constrained by measurements of both gas and aerosol phase chemical components (Hennigan et al., 2015; Murphy et al., 2017). Both the phase partitioning method and thermodynamic models are sensitive to input measurement values and their associated uncertainties, which can be high for species such as ammonia. Also, both assume gas-particle phase equilibrium, which is not always accurate, especially as aerosol often have low liquid water content or high ionic strength (Keene et al., 2004; Perraud et al., 2012; Hennigan et al., 2015; Shiraiwa et al., 2017). Additionally, neither method accounts for organic components, which are ubiquitous in the atmosphere (Kolb and Worsnop, 2012). This is a limitation as organic acids can influence acidity levels (Hennigan et al., 2015; Silvern et al., 2017). Direct measurement of aerosol pH is needed to provide an analytical determination of pH to constrain both model and proxy methods, particularly when the available methods disagree.

Currently, direct measurement of aerosol acidity is limited. One method uses colorimetric analysis integrated with a reflectance UV-Visible spectrometer to measure the proton

concentration of particles samples collected on dyed filters (Jang et al., 2008; Li and Jang, 2012). Another method uses Raman microspectroscopy to quantify concentrations from the vibrational modes of an acid and its conjugate base, allowing their equilibrium to be determined (Rindelaub et al., 2016a; Craig et al., 2017b). The concentrations are then combined with activity coefficient calculations to determine pH of individual particles (Rindelaub et al., 2016a; Craig et al., 2017b). Application of this method is limited though, as it has only been used to measure pH for laboratory-generated supermicron particles composed of simple chemical composition (Rindelaub et al., 2016a; Craig et al., 2017b).

Herein, we developed and applied a facile method for direct, quantitative, real-time measurement of size-resolved ensemble average (bulk) aerosol pH. This method uses pH indicator paper to colorimetrically determine aerosol acidity, thus eliminating the dependence on challenging particle composition measurements or isolation of specific acid/conjugate base species for direct pH measurement via Raman spectroscopy. While a limited number of studies have measured cloud and fog droplet acidity qualitatively with pH indicator paper method previously (Ganor et al., 1993; Ganor, 1999), this has not been explored quantitatively. Aerosol samples were collected on pH indicator paper using a multiple stage impactor, allowing size-resolved aerosol acidity to be measured. In this work, size-dependent trends in aerosol acidity were observed for $(NH_4)_2SO_4$-H_2SO_4 aerosol particles, with smaller particles having higher levels of acidity. This trend was confirmed with single particle pH measurements via the previously discussed spectroscopic method (Rindelaub et al., 2016a; Craig et al., 2017b). Lastly, preliminary ambient atmospheric measurements with pH indicator paper are presented to demonstrate the field capabilities of this method.

7.2 Methods

7.2.1 Laboratory-Generated Aerosol Samples

Standard solutions were prepared using 18.3 MΩ Milli-Q water and the following chemicals: ammonium sulfate $(NH_4)_2SO_4$ (Alfa Aesar) and sulfuric acid (H_2SO_4) (Sigma-Aldrich). All chemicals were > 98.0% purity and used without further purification. Solutions were 30 mM $(NH_4)_2SO_4$ with varying concentration of H_2SO_4 to control pH. Bulk solution pH values ranged from 0 to 5, as measured by a pH probe (AP110, accumet Portable). Aerosols were generated from solution using an atomizer operated with HEPA-filtered air and then impacted

onto pH indicator paper (MColorpHast pH Test Strips, Millipore Sigma) and quartz substrates (Ted Pella, Inc.) using a microanalysis particle sampler (MPS-3, California Measurements, Inc.). The MPS-3 consists of three stages with aerodynamic diameter (d_a) 50% size cuts of 2.5-5.0 μm, 0.40-2.5 μm, and < 0.40 μm for stages 1, 2, and 3, respectively. The chemical composition of the aerosol particles was chosen based on the ubiquity of sulfate in submicron atmospheric particles, which results in it being a common seed for SOA chambers study experiments (Riva et al., 2016c). The pH range was chosen based on predictions of acidic aerosol particles from previous studies (Guo et al., 2015, 2016; Bougiatioti et al., 2016; Weber et al., 2016; Battaglia et al., 2017; Liu et al., 2017b). Aerosol particles were not dried prior to impaction to ensure they were aqueous and the RH of the system was maintained at ~90%.

7.2.2 pH Indicator Paper Measurements

Aerosol pH for aqueous particles collected from each stage of the MPS on pH indicator paper was determined by colorimetric analysis of images collected immediately after sampling (Figure 7.1). pH indicator paper for the pH range 0-2.5 and 2.5-4.5 were used for this study. For the pH 0-2.5 paper, the indicator dye is thymol blue with a pK_a of 1.7 and for the pH 2.5-4.5 paper, the indicator dye is methyl orange with a pK_a of 3.47. An image of each sample, the corresponding pH color scale, and a blank pH indicator strip was collected with a standard cellular phone camera. The Red, Green, and Blue channels of the pH color scale were analyzed with a custom MATLAB script (Peterson, P. K., 2017. pH Paper Analysis. doi:10.5281/zenodo.1036797) created for this purpose to create a calibration curve relating the difference between the Green and Blue channels to pH^2. The pH of the sample was then determined using the calibration curve. The pH color scale is included in each picture to generate a calibration curve for each sample analyzed to account for differences between images. Uncertainty for each pH measurement is also calculated based on color variation within the sample. pH indicator paper measurements of bulk solution standards of $(NH_4)_2SO_4$-H_2SO_4 of varying pH were compared to pH probe measurements to confirm the accuracy of the pH indicator paper and image processing method (Figure F.1). Due to a small, systematic bias with the pH 2.5-4.5 indicator paper, a correction factor was applied to all measurements made with the higher range pH paper and further information is provided in Appendix F (Figure F.2). To confirm the color change on the pH indicator paper was due to aerosol particles rather than gas

or water vapor, a blank in which the particles were filtered out using a HEPA filter was collected and there was no observed color change on the pH indicator paper (Figure F.3). To account for potential differences in measured pH between calibration reference solutions and inorganic ions common in atmospheric aerosols, a range of aqueous inorganic solutions were tested with both pH probe and pH indicator paper (Figure F.4).

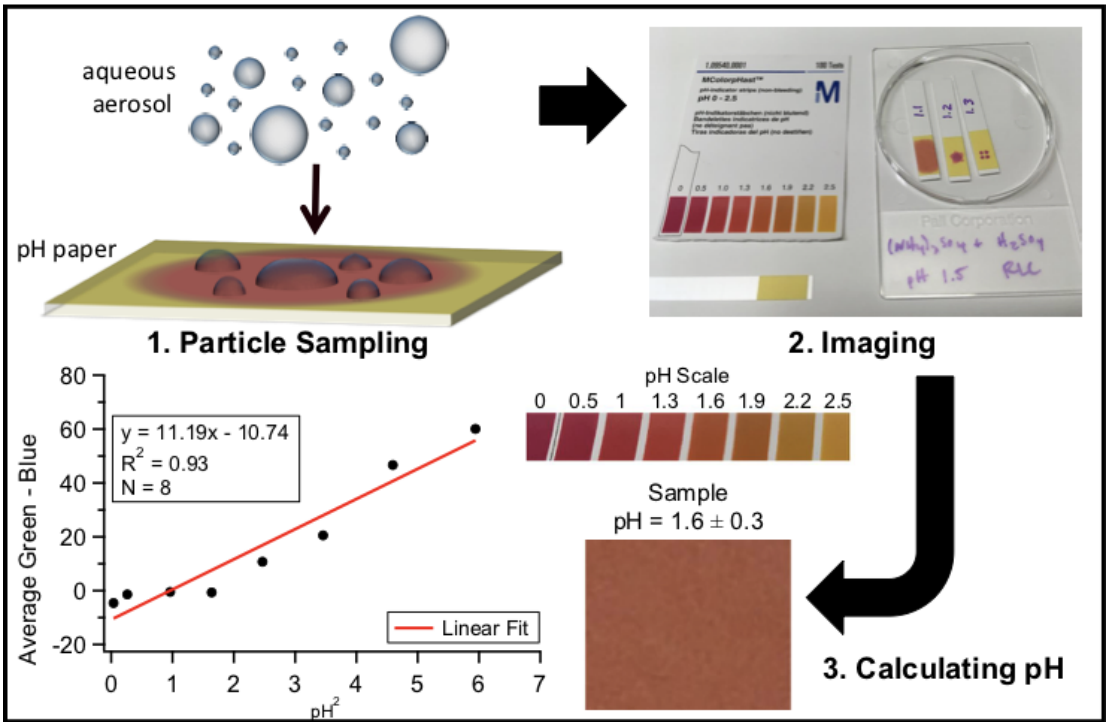

Figure 7.1 Schematic of pH indicator paper method for direct measurement of aerosol pH.

7.2.3 Raman Microspectroscopy

For comparison to the bulk aerosol pH from the pH indicator paper, the pH of individual particles was also determined using the Raman microspectroscopic method previously described (Rindelaub et al., 2016a; Craig et al., 2017b). Details on the Raman analysis are provided in Appendix F.

7.2.4 Size Distribution Characterization

Generated particles for each solution were also characterized by a scanning mobility particle sizer (SMPS, Model 3938, TSI Inc.) and aerodynamic particle sizer (APS, Model 3321, TSI Inc.). The SMPS was operated at a 10:1 sheath:aerosol flow ratio and provided mobility diameter (d_m) number and mass concentrations for the size range 14.1-763.5 nm. The APS

provided aerodynamic diameter (d_a) number and mass concentrations for the size range 0.542-19.81 μm. Aerosols were studied under high (~90%) and low (~45%) RH conditions. For the low RH condition, aerosols passed through two diffusion dryers prior to analysis. RH was monitored with an RH sensor (EK-H5, Sensiron).

7.2.5 Ambient Aerosol Samples

Ambient aerosol samples were also collected for pH indicator paper measurements using the MPS-3 impactor. Sampling was conducted at the University of Michigan Biological Station (UMBS) PROPHET Tower (Pellston, MI) in July 2016 and the University of Michigan Chemistry Building (Ann Arbor, MI) in August 2016.

7.3 Results and Discussion

7.3.1 pH Measurements of Standard Aerosol Samples

Herein, the first direct, quantitative measurements of size-resolved aerosol pH were made using pH indicator paper. Aerosol particles were generated from $(NH_4)_2SO_4$-H_2SO_4 solutions (pH range 0 – 4.5) and impacted onto the pH indicator paper using a cascade impactor with three stages. Changes in aerosol acidity as a function of particle size were primarily observed at acidities below the pK_a of HSO_4^- (1.99) (Lide, 2009), as shown in Figure 7.2. For aerosols generated from solutions with pH < 2.5, the aerosol pH of the coarse mode particles (d_a > 2.5 μm) was similar to the bulk solutions. In contrast, below a pH of 2.5, fine mode aerosol (d_a 0.4-2.5 μm) pH was lower than the bulk solution and coarse mode particles. Aerosol pH of the smallest sized particles (d_a < 0.4 μm) was even lower, indicating particle acidity increases (pH decreases) with decreasing particle size. It should be noted that the minimum pH value calculated with the pH indicator paper method is pH 0, which represents an upper bound of pH for samples generated from solutions with pH ≤ 1. The increasing acidity of smaller particles is likely related to aerosol water content and ammonia partitioning below the pK_a of bisulfate and is discussed in detail below.

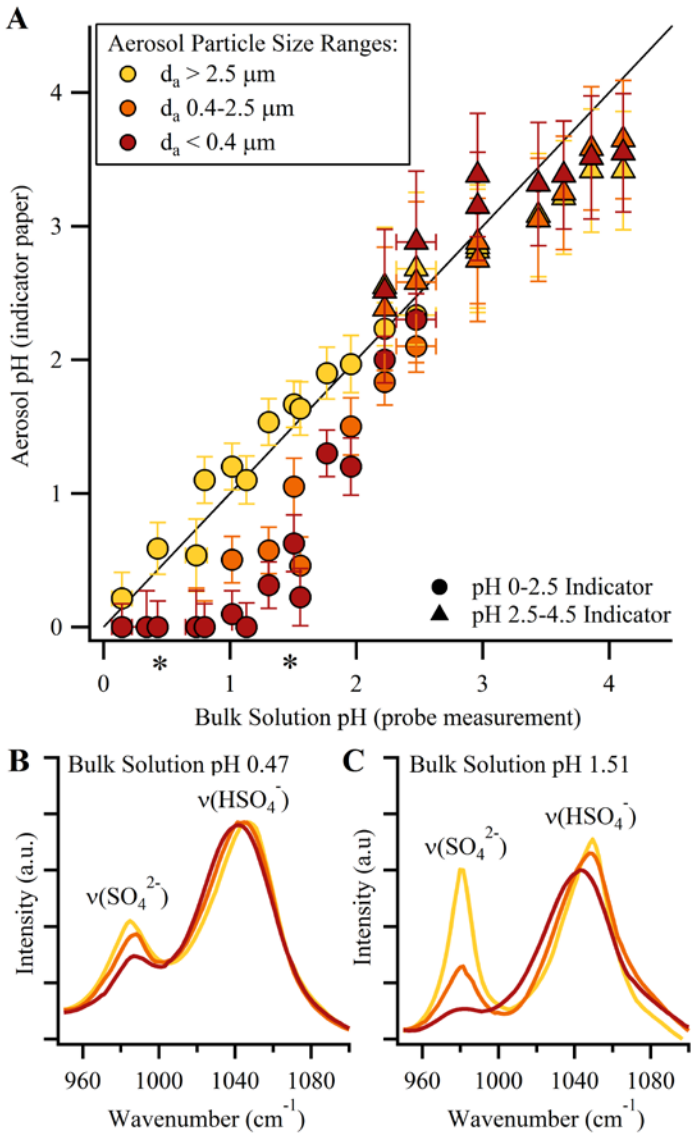

Figure 7.2 (A) pH indicator paper measurements of aerosol particles d_a > 2.5 μm (yellow), d_a 0.4 – 2.5 μm (orange), and d_a < 0.4 μm (red) as a function of the bulk solution pH from which the particles were generated. Raman spectra of the $\nu(SO_4^{2-})$ and $\nu(HSO_4^-)$ modes, normalized to the $\nu(HSO_4^-)$ mode, for particles generated from bulk solution (B) pH 0.47 and (C) pH 1.51 (corresponding to the data marked by the *).

Raman spectra collected from aerosol particles of various sizes corresponding to the pH paper measurement size ranges confirmed the observation of increased particle acidity with decreasing particle size (Figure 7.2B and 7.2C). As shown in Rindelaub et al. and Craig et al., the $\nu_s(SO_4^{2-})$ and $\nu_s(HSO_4^-)$ vibrational modes can be used to determine aerosol particle pH

based on the HSO_4^-/SO_4^{2-} acid-base equilibrium (Rindelaub et al., 2016a; Craig et al., 2017b). For spectra normalized to the intensity of the $\nu(HSO_4^-)$ mode, a clear decrease in the intensity of the $\nu(SO_4^{2-})$ mode, indicating increasing acidity (decreasing pH), is observed with decreasing particle size across all bulk solution pH systems. Raman spectra for the other systems between pH 0.15 – 2.05, the pH range for which aerosol particle pH can be determined spectroscopically for the HSO_4^-/SO_4^{2-} equilibrium, is provided in Appendix F (Figure F.4).

To further investigate the relationship between particle size and acidity, individual aerosol particle pH was determined spectroscopically for particles generated from bulk solution of pH 0.15 to pH 2.05. As shown in Figure 7.3, the single particle spectroscopic pH measurements corroborate the aerosol pH indicator paper measurements. Particles generated from bulk solutions of lower pH had higher acidity levels, as expected, and across all bulk solution pH systems, the $[HSO_4^-]/[SO_4^{2-}]$ ratio is higher and more varied for smaller sized particles, indicating higher levels of acidity and decreased uniformity within the aerosol population. When clustered according to the size ranges corresponding to the pH indicator paper measurements, increasing acidity with decreasing particle size can be clearly seen for systems both pH < 1 and pH > 1. As the pH indicator paper particle size ranges from inertial separation are based on aerodynamic diameter (d_a) rather than projected area diameter (d_{pa}) (Hinds, 1999), the measured d_{pa} of the individual particles analyzed by Raman was converted to d_a prior to clustering based on a spreading ratio of 4 (Sobanska et al., 2014; Bondy et al., 2017a). For bulk solution systems pH < 1, particles with aerodynamic diameter < 0.4 μm, 0.4 – 2.5 μm, and > 2.5 μm had median pH values of 0.23, 0.66, and 0.69, respectively. For bulk solution systems pH > 1, particles with aerodynamic diameter < 0.4 μm, 0.4 – 2.5 μm, and > 2.5 μm had median pH values of 0.63, 0.87, and 1.03, respectively. Considering the log scale of $[H^+]$ for pH, these differences of ~ 0.5 pH units correspond to a 3x increase in H^+ concentration as particle size decreases from supermicron to submicron for aerosol particles of the same population.

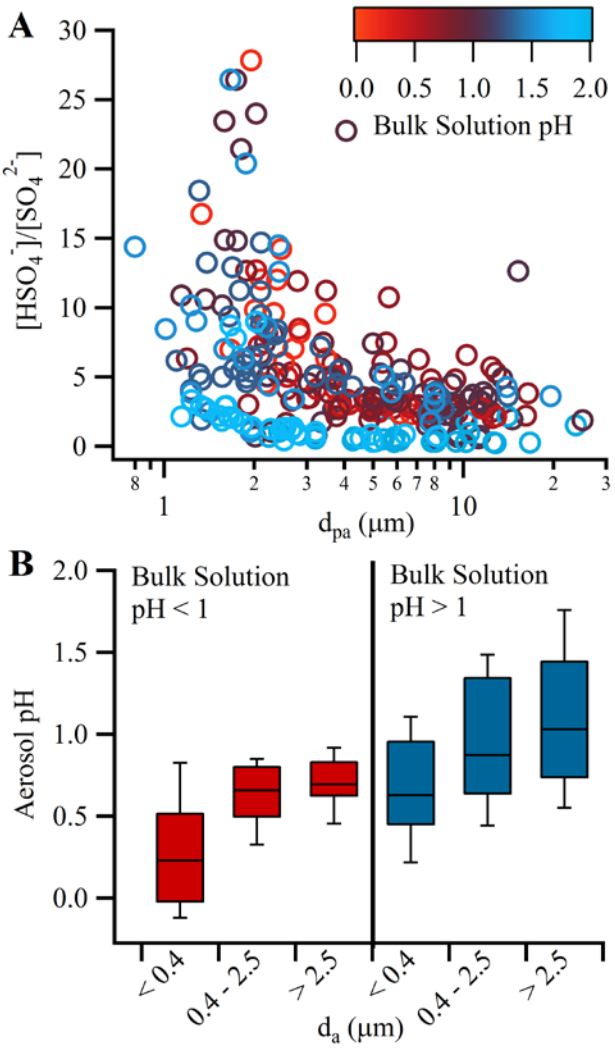

Figure 7.3 (A) $[HSO_4^-]/[SO_4^{2-}]$ as a function of d_{pa} for individual aerosol particles, with color representing the pH of the solution from which the particles were generated. (B) Box and whisker plot of aerosol pH as a function of d_a for individual particles, but grouped into size ranges corresponding to the pH indicator paper measurements. The centerline represents the median, the box outlines the inner quartiles, and the whiskers represent the 10th and 90th percentile.

The observed trend of increasing particle acidity with decreasing particle size is attributed to ammonia partitioning and water loss. Below the pK_a of bisulfate, loss of $NH_4^+{}_{(aq)}$ to $NH_{3(g)}$ partitioning leaves less $NH_4^+{}_{(aq)}$ present in the particle phase to neutralize sulfate species (Equation 7.1). Though direct measurements of $NH_{3(g)}$ and quantified $NH_4^+{}_{(aq)}$ were not available, this equilibrium likely plays a role and will be explored in future work.

Equation 7.1 $SO_4^{2-}(aq) + NH_4^+(aq) \rightarrow HSO_4^-(aq) + NH_3(g)$

Increased surface area-to-volume ratios for smaller particles compared to larger particles allows for greater loss of water and potential NH_3 diffusion from the particle to gas phase. With a lower water content, the molar concentration of chemical species (e.g. H^+) increases. Thus, in smaller sized particles [H^+] increases and pH decreases. Water content fraction by mass for each size range of particles for several pH systems was calculated based on comparison of mass concentration size distributions at wet and dry RH conditions. More details on the water content fraction calculation are provided in Appendix F. Increasing water content fraction was observed with increasing pH, as well as with increasing particle size, across all pH levels (Table F.1). Particle density, calculated as part of the Raman spectroscopic method to determine pH (Rindelaub et al., 2016a; Craig et al., 2017b), corroborated the water content fraction results, as particle density increased with decreasing particle size (Table F.1). These observations of water content fraction and particle density support the hypothesis that smaller particles contain less water and have higher concentrations of chemical species, leading to measured lower pH values. Both loss of $NH_4^+{}_{(aq)}$ due to $NH_{3(g)}$ partitioning and water loss lead to solutions that are no longer thermodynamically ideal water droplets with higher ionic strengths and higher levels of acidity.

This trend of increasing particle acidity with decreasing particle size has been indirectly observed for ambient aerosol previously (Ganor et al., 1993; Keene et al., 2002; Yao et al., 2007; Zhang et al., 2007a; Fang et al., 2017). The pH of coarse mode aerosol was reported to be higher than fine mode aerosol for several different particle types, including sea salt aerosol particles (Keene et al., 2002), fog and cloud droplets (Ganor et al., 1993), and urban aerosol particles (Yao et al., 2007; Zhang et al., 2007a; Fang et al., 2017). For these observations, aerosol pH was determined via extrapolation of pH measurements of diluted samples (Keene et al., 2002), ion balance (Yao et al., 2007), thermodynamic modeling (Zhang et al., 2007a; Fang et al., 2017), or a qualitative pH paper method (Ganor et al., 1993). Several hypotheses were proposed to explain the observed differences in acidity, including differing rates of HCl volatilization (Keene et al., 2002), dilution by condensation (Ganor et al., 1993), differing rates of neutralization (Yao et al., 2007), and size-dependent neutralization by mineral cations (Fang et al., 2017) or gas-phase NH_3 (Zhang et al., 2007a). Given the complex nature of aerosol particles in terms of chemical composition and atmospheric conditions, it is likely that there are many factors that influence

aerosol acidity with regards to particle size and further studies are needed to elucidate the potential mechanisms driving this phenomenon.

Direct comparison of aerosol pH from pH indicator paper and single particle pH from Raman microspectroscopy is presented in Figure 7.4. The Raman measurements represent the average pH for individual particles analyzed within each size range (converted from d_{pa} to d_a), with error bars indicating standard deviation. There is good agreement between the two methods across all size ranges. The largest deviation between the two methods is observed for particles generated from solution pH < 1.5 for the d_a 0.4-2.5 μm size range, with the Raman spectroscopically determined pH values ~0.5 pH units higher than the pH indicator paper determined pH values. This is most likely due to a limitation of the Raman spectroscopic method, as when one of the species in the bisulfate-sulfate equilibrium is more dominant, it is more difficult to accurately measure both vibrational modes. It should also be noted that the pH values plateau ~ pH 0 for particle size ranges d_a < 0.4 μm and d_a 0.4-2.5 μm because both methods have a lower limit of ~ pH 0. A comparison of pH indicator paper and Raman microspectroscopic aerosol pH measurements to model predicted aerosol pH is included in the Supporting Information.

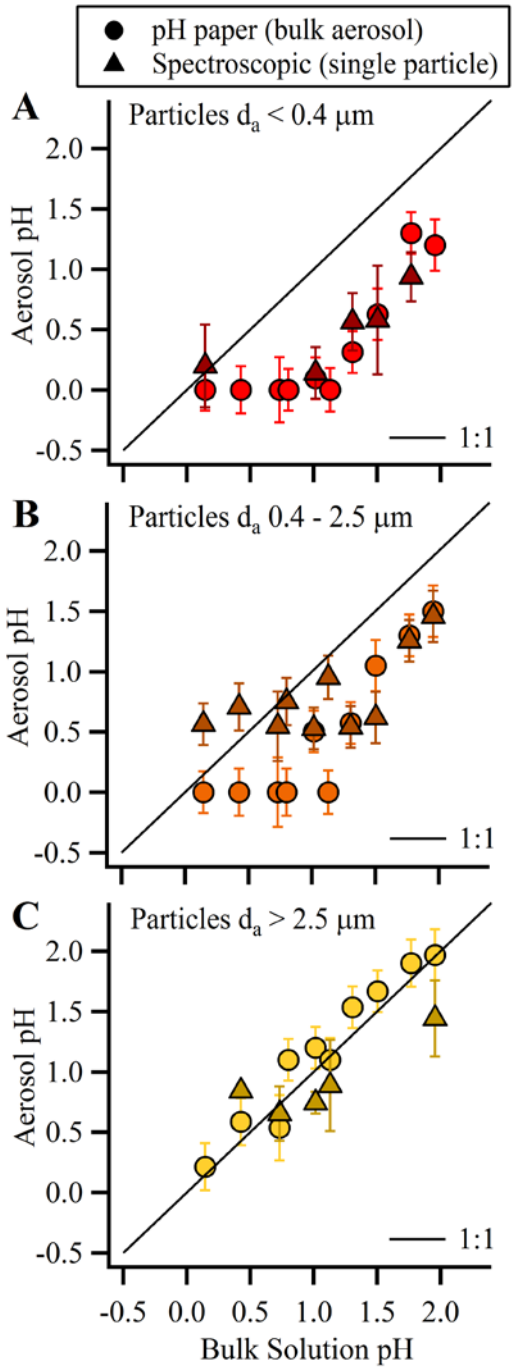

Figure 7.4 Aerosol pH as a function of the pH of the bulk solution from which the particles were generated to compare pH indicator paper and Raman spectroscopic methods for measuring aerosol pH for particles (A) d_a < 0.4 µm, (B) d_a 0.4-2.5 µm, and (C) d_a > 2.5 µm. Error bars for the pH indicator paper data corresponds to uncertainty in the measurements across multiple trials. Error bars for the Raman spectroscopic data corresponds to standard deviation of multiple trials.

7.3.2 pH Indicator Paper Method Limit of Detection

To investigate the detection limit of the pH indicator paper method, the minimum mass of particles needed to induce a quantifiable color change on the indicator paper for each size range was determined (Figure 7.5). The mass of particles impacted for each size range was calculated by integrating the area under the curve for mass concentration size distributions collected via SMPS and APS. The minimum mass required was determined by decreasing sampling time until a color change on the pH indicator paper was no longer distinguishable optically, both visually and by image processing script. RH, and consequently, aerosol liquid water content, plays an important role in how much particulate mass is required, as water is needed for the dye in the indicator paper to change and diffuse through the paper enough to be visible. For $(NH_4)_2SO_4$-H_2SO_4 particles for most size ranges and pH conditions at RH 90%, ~ 100 μg or less of aerosol mass is sufficient for an accurate aerosol pH measurement. As particle pH increases, the necessary mass of particles also increases, since $[H^+]$ becomes more dilute. The smaller particle sizes of the lowest pH system (pH 0.15) are the exception to this trend, most likely due to lower water content fraction (Table F.1), which requires a larger mass of particles for sufficient liquid water to induce a color change on the pH indicator paper. Concurrently, the larger sized particle range requires significantly more particulate mass, as both the mass and water content fraction of the larger particles is much greater than for those of the smaller sized particles. Specific mass values are provided in Table F.1. It should be noted that under lower RH conditions, it is likely that greater particle mass will be necessary for pH indicator paper measurements, as the aerosol liquid water content will be lower. Future work will thoroughly investigate the limitations with respect to aerosol water content and RH for the pH indicator paper method of measuring aerosol pH.

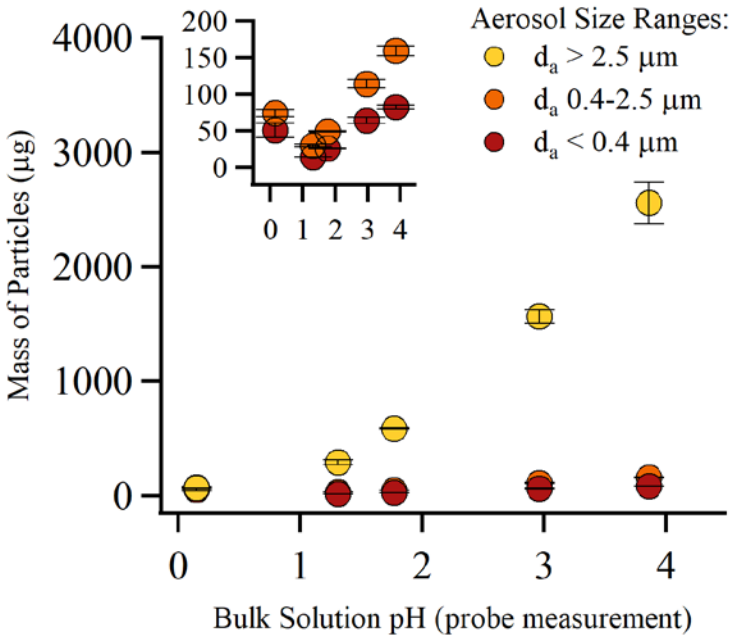

Figure 7.5 Minimum mass of particles needed to induce a measurable color change on the pH indicator paper for each particle size range for particles generated from solutions of varying pH. Error bars represent uncertainty in the calculation of the mass of particles based on multiple measurements of the mass concentration size distribution. Note - the error bars are difficult to see on this scale, so black error bars were used. Inset focuses on smaller mass range for d_a 0.4-2.5 µm and < 0.4 µm particles.

7.3.3 pH Measurements of Ambient Aerosol Samples

To demonstrate the potential for ambient sampling with this method, as well as to illustrate some potential challenges, ambient aerosol particle samples were collected at two locations – the UMBS near Pellston, MI and outside the University of Michigan Chemistry Building in Ann Arbor, MI, as shown in Figure 7.6. As discussed in the Methods section, the pH of solutions of varying inorganic ion composition was successfully measured with pH indicator paper, thus indicating this method could also be applied to measure the pH of ambient aerosol particles of varying chemical composition. Ambient RH was ~ 70%, 80%, and 60% at the time of sampling for the UMBS 1, UMBS2, and UM Chemistry samples, respectively. Ambient samples were collected for ~1 – 2 hours, demonstrating that pH indicator paper method can be run rapidly enough for semi-continuous measurements. For samples from both locations, aerosol acidity was primarily estimated to be ~pH 3 – 3.5 across the particle sizes measured. One sample from UMBS (Figure 7.6A) indicated that the smallest particles were more acidic (pH ~1.5),

though the color change was not uniform across the samples and other portions of the paper had pH close to 3. pH could only be qualitatively determined from visual inspection for these samples, as the pH indicator paper used for sampling was not compatible with the MATLAB script for more quantitative analysis. However, the ambient aerosol pH measurements agree with the pH measurements of the laboratory-generated particles of this study, as aerosol particles with lower acidity levels (~ pH 3 - 3.5) showed minimal difference in measured pH with regards to particle size. These preliminary results demonstrate the potential for ambient measurement, however, it should be noted that further testing with precisely controlled RH and aerosol water content are needed to utilize the pH indicator paper method quantitatively for ambient studies.

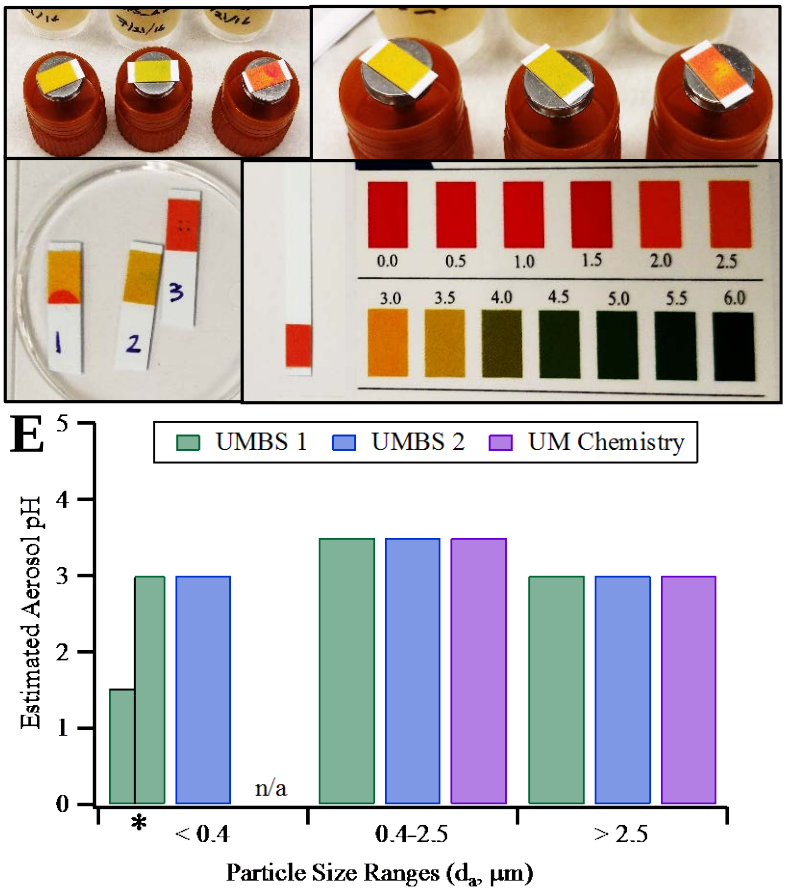

Figure 7.6 Images of ambient aerosol collected on pH indicator paper UMBS ((A) and (B)) and UM Chemistry building (C) with the pH indicator paper scale and blank (D). (E) Estimated aerosol pH based on comparison of the images to the color scale for each ambient sample. Note – two color changes corresponding to pH 1.5 and pH 3 were observed for the UMBS 1 < 0.4 µm sample, although pH 3 was more predominant and a color change was not observed on the paper for the UM Chemistry < 0.4 µm sample.

7.4 Conclusions

This study presents a facile method for direct measurement of aerosol pH through quantitative colorimetric analysis of aqueous aerosol samples. $(NH_4)_2SO_4$-H_2SO_4 aerosol particles of varying pH were generated and collected on pH indicator paper with a 3-stage impactor with aerodynamic size cuts of d_a < 0.4 μm, d_a 0.4 – 2.5 μm, and d_a > 2.5 μm, enabling analysis of size-resolved aerosol pH. For systems pH < 2, aerosol acidity increased with decreasing particle size, due to ammonia partitioning below the pK_a (1.99) of bisulfate and loss of water as surface area-to-volume ratios increased. Comparison with direct measurement of individual aerosol particle pH via a previously established spectroscopic method corroborated these results. The limit of detection for the pH indicator method in terms of particulate mass necessary for a measurable color change show that ~100 μg of particulate mass was needed for fine particles (< 2.5 μm), while the mass for more dilute, larger particles increased with pH, requiring total particulate masses of ~100 μg at pH 0 and ~2.5 mg at pH 4. Preliminary ambient measurements with sampling times of ~1 – 2 hours demonstrate the potential for atmospheric application of this method. Further work investigating the effect of RH and aerosol liquid water content is needed to make ambient sampling robust. Future studies of aerosol acidity enabled by this method of direct, real-time measurement of aerosol pH have the potential to constrain ambient aerosol acidity experimentally. This is needed as key processes, such as SOA formation in the Southeast U.S. and nitrate haze events in Beijing are strongly dependent on aerosol acidity, but pH values have thus far been determined indirectly and without measurement validation (Wang et al., 2016; Weber et al., 2016). Fundamental studies of aerosol acidity have the potential to increase understanding of pH-dependent multiphase chemical processes, which are needed to improve the predictive capability of atmospheric models focused on human health and climate.

7.5 Acknowledgements

This work was supported by the National Science Foundation through a CAREER Award to A. P. Ault (CHE-1654149), CAREER Award to C. Dutcher (AGS-1554936), and startup funds from the University of Michigan. RLC was partially supported by the Susan Lipschutz Fellowship Award from the University of Michigan Rackham Graduate School. RDC was supported by a Rackham Merit Fellowship Award from the University of Michigan Rackham Graduate School and the Marian P. and David M. Gates University of Michigan Biological

Station Graduate Student Fellowship. SC and MAH were supported by the Detroit Research Internship Summer Experience (D-RISE) program, funded by the National Science Foundation (CHE-1305777) to Dr. Nicolai Lehnert at U. Michigan and Dr. Ault's CAREER award, as well as the University of Michigan College of Literature, Science and the Arts, the University of Michigan Office of the Provost, and Cass Technical High School in Detroit, MI. RLC performed pH indicator paper research with assistance from MAH, SC, and RAD. RLC performed Raman research with assistance from ZL and MAH. RLC performed ambient sampling with assistance from RAD and RDC. PKP developed the MATLAB script. LN performed calculations with assistance from CSD. Dr. Simon Clegg is thanked for helpful discussions of ion activity.

Chapter 8. Conclusions and Future Directions

8.1 Conclusions

The ability of an atmospheric aerosol particles to impact climate by acting as cloud condensation nuclei (CCN) or ice nuclei (IN), as well as scatter and absorb solar radiation is determined by their physicochemical properties at the single particle level, specifically size, morphology, and chemical composition. The acidity of atmospheric aerosols is also critical, as many key multiphase chemical reactions involving aerosols are highly pH-dependent. These reactions impact processes, such as SOA formation and aging, which can modify the climate-relevant behavior of particles. However, determining aerosol mixing state is difficult as atmospheric particles are complex mixtures of organic and inorganic components, often with hundreds to thousands of different species present at femtogram to attogram levels, and can vary greatly particle-to-particle. Measuring the pH of atmospheric particles, which have minute volumes, is also an analytical challenge due to the non-conservative nature of the hydronium ion, particularly as most chemical aerosol measurements are made offline or under vacuum, where water content can be changed and acid-base equilibria shifted. To address some of the challenges of measuring the physicochemical properties of atmospheric aerosols, this dissertation has described the development and application of several novel analytical methods specifically focused on characterization of chemical composition and measurements of aerosol pH.

Chapter 2 presented a computer-controlled Raman microspectroscopic (CC-Raman) method for detailed physicochemical analysis of atmospheric aerosol particles. Raman microspectroscopy has a great deal of promise for identifying secondary species and their mixing with primary components, as it can provide detailed information on functional groups present, morphology, and internal structure. However, as with many other spectroscopic techniques, manual analysis by Raman microspectroscopy can be slow, limiting single particle statistics and the number of samples that can be analyzed. The CC-Raman method was shown to increase throughput and minimizes user bias for single particle Raman analysis. CC-Raman applied

automated mapping to increase analysis speed, allowing for up to 100 particles to be analyzed in an hour. CC-Raman was applied to both laboratory and ambient samples to demonstrate its utility for the characterization of both primary and, more importantly, secondary components (e.g. sulfate, nitrate, ammonium, and organic material). Reproducibility and precision were compared to computer controlled-scanning electron microscopy with energy dispersive X-ray spectroscopy (CCSEM-EDX). The greater sample throughput for CC-Raman showed the potential to improve particle statistics and advance understanding of aerosol particle composition and mixing state, and, thus, climate-relevant properties.

Chapters 3 and 4 discussed the development and application of surface enhanced Raman spectroscopy (SERS) to the study of atmospheric aerosol particles. Due to their small size, measurements of the complex composition of atmospheric aerosol particles are analytically challenging. Chapter 3 detailed the first use of SERS to detect trace organic and/or inorganic species present within both laboratory-generated and ambient aerosol particles that were collected via impaction on silver nanoparticle-coated substrates. The observations of complex chemical compositions of ambient SOA particles obtained with this new method demonstrated the power of SERS to probe difficult to detect inter- and intraparticle variability. The most abundant atmospheric aerosol are ~100 nm and difficult to characterize with traditional microspectroscopic methods. To address this challenge, Chapter 4 presented work that used Ag foil substrates to push SERS below the diffraction limit and towards more atmospherically-relevant particle sizes. SERS enhanced spectra were collected for both 150 nm size-selected polystyrene latex sphere (PSL) particles and ambient aerosol particles, which represents both the smallest individual aerosol particles analyzed by Raman microspectroscopy and the first time atmospheric particles were measured below the diffraction limit. SERS-enabled detection and identification of vibrational modes present in smaller, more atmospherically-relevant sized particles has the potential to improve understanding of aerosol composition and its evolution during multiphase atmospheric reactions critical to climate and health.

Chapters 5 and 6 described the development and expansion of a Raman microspectroscopic method for determining the pH of individual aerosol particles. In contrast to traditional indirect methods of estimating aerosol pH, this method coupling Raman microspectroscopy with extended Debye-Hückel activity calculations allowed for direct determination of acidity of individual particles based on measurements of acid and conjugate

base vibrational modes. Several atmospherically relevant inorganic and organic acid-base equilibria systems are compatible with this method, including HNO_3/NO_3^-, HSO_4^-/SO_4^{2-}, $HC_2O_4^-/C_2O_4^{2-}$, CH_3COOH/CH_3COO^-, and HCO_3^-/CO_3^{2-}, covering a broad pH range (-1 to 10). In addition to pH measurements, the effect of RH on particle acidity, gas-particle partitioning of acidic chemical species, and the relationship between ionic strength and H^+ activity were also studied with this method. These results indicate the potential for direct spectroscopic determination of pH in particles composed of more complicated chemical mixtures and the need to improve fundamental understanding of ion behavior in atmospheric particles.

In continuity with the aerosol acidity focus of Chapters 5 and 6, Chapter 7 detailed a novel and facile method for direct measurement of size-resolved bulk aerosol pH using pH indicator paper. Quantitative colorimetric image processing of cellular phone images was used to determine pH of $(NH_4)_2SO_4$-H_2SO_4 aqueous aerosol particles impacted onto pH-indicator paper for the pH range 0 – 4.5. A trend of increasing aerosol acidity with decreasing particle size was observed that is consistent with spectroscopic measurements of individual particle pH. Preliminary measurements of ambient aerosol pH were also explored and presented. These results show the potential for direct measurements of size-resolved atmospheric aerosol acidity, which is needed to improve fundamental understanding of critical pH-dependent multiphase atmospheric processes.

8.2 Future Directions

The research described in this dissertation focused primarily on the development of analytical methods for characterization of atmospheric aerosol chemical composition and mixing state as well as measuring aerosol pH. However, further work can be done to improve and optimize these methods, as well as apply them to learn more about the physicochemical properties of both laboratory-generated model systems and ambient aerosols.

In Chapter 2, the CC-Raman method was used to characterize the chemical composition, size, and morphology of a few laboratory-generated standard aerosol samples as well as ambient aerosol collected during the 2013 SOAS field campaign. However, this analysis of SOAS aerosol particles was preliminary and further work is required for more detailed characterization of aerosol mixing state. This would include more detailed assignments for detected vibrational

modes and proposed identification of specific chemical compounds present within particles, as well as comparison with data collected via other analytical techniques, such as CCSEM (Bondy et al., 2017b; Fraund et al., 2017), STXM-NEXAFS (O'Brien et al., 2015a) or single particle mass spectrometry (Hatch et al., 2011). In general, CC-Raman can be used for improved single particle Raman characterization for both laboratory and field aerosol studies due to its high-speed analysis and increased particle statistics.

In Chapters 3 and 4, SERS of submicron sized aerosol particles was explored using AgNP coated quartz, Ag foil, and a few other Ag substrates. While enhancements for many vibrational modes were observed, enhancement factors were highly variable, even for particles of similar size and chemical composition. There is potential to improve SERS enhancement in terms of both magnitude and variability if the SERS substrates can be optimized with respect to metal identity, nanoparticle shape, and configuration. These aspects can be investigated through more thorough substrate testing that includes commercial standards and substrates prepared via nanosphere lithography (Sharma et al., 2013; Schlucker, 2014), which allows for greater control of nanoparticle shape and orientation. Improved substrates would allow for more detailed characterization of the inorganic and organic vibrational modes detected from ambient aerosol particles, providing better understanding of inter- and intraparticle variability. Additionally, if SERS and CC-Raman can be combined, the potential of Raman characterization of aerosol mixing state for atmospherically relevant sized particles would greatly increase. However, this will require a substrate that does not interfere optically with the CC-Raman method as it differentiates particles from background for analysis.

Chapters 5 and 6 described a Raman microspectroscopic method for measuring the pH of individual aerosol particles, however, the method has been applied to a limited number of laboratory-generated aerosol particles of simple chemical compositions. In order to realize the full potential of this method, it will need to be tested with laboratory-generated particles of increasing chemical complexity. Examples of more complex particles include three or more component mixtures, particularly mixtures of acid-base equilibria systems with similar pK_a values, and particles collected during chamber experiments simulating atmospherically relevant compositions and conditions. By systematically increasing the complexity of particles, any complications in terms of ion behavior or interferences for particle pH measurements can be addressed. This will also allow for characterization of a broader range of acid-base equilibrium

systems, helping to improve this method and enable eventual pH measurements of ambient aerosol particles, which are exponentially more complex and have unknown composition.

The pH indicator method presented in Chapter 7 requires optimization to be able to be used for quantitative ambient aerosol pH measurements. This includes a thorough investigation of the effect of RH on pH measurements, as particles must have sufficient liquid water content in order to be able to induce a measureable color change on the pH indicator paper, as well as testing particles of varying chemical composition and phase state. Developing a better understanding for the impact of different environmental conditions is crucial for establishing the pH indicator paper method as a quantitatively accurate technique for real-time ambient aerosol pH measurements.

In addition to acidity measurements of ambient aerosol, both pH methods can be used to quantitatively investigate the role of acidity in pH-dependent aerosol processes through controlled laboratory experiments. For example, pH measurements of the inorganic and organic phases of LLPS particles can help improve understanding of the mechanism behind these phase transitions. Thus far, few studies have focused on pH impacts on LLPS, but previous work has found that increasing pH corresponds to a decrease in the separation RH (Losey et al., 2016) and that once LLPS occurs, the organic-rich phase is less acidic than the previously single phase particle (Dallemagne et al., 2016). However, these studies have investigated primarily large particles (20-200 μm) at pH levels higher than what thermodynamic models predict for atmospheric aerosols. Ongoing research using the pH measurement methods established in Chapters 5-7 investigates LLPS of laboratory-generated SOA particles composed of ammonium sulfate and polyethylene glycol 400 (PEG-400) at atmospherically relevant sizes and pH's. Preliminary work shows that LLPS particles of varying pH have different internal structures in terms of distribution of organic and inorganic chemical components (Figure 8.1). Further work quantitatively measuring the pH of the different phases present within the particles is necessary to determine the relationships between pH, RH, and LLPS particle structure.

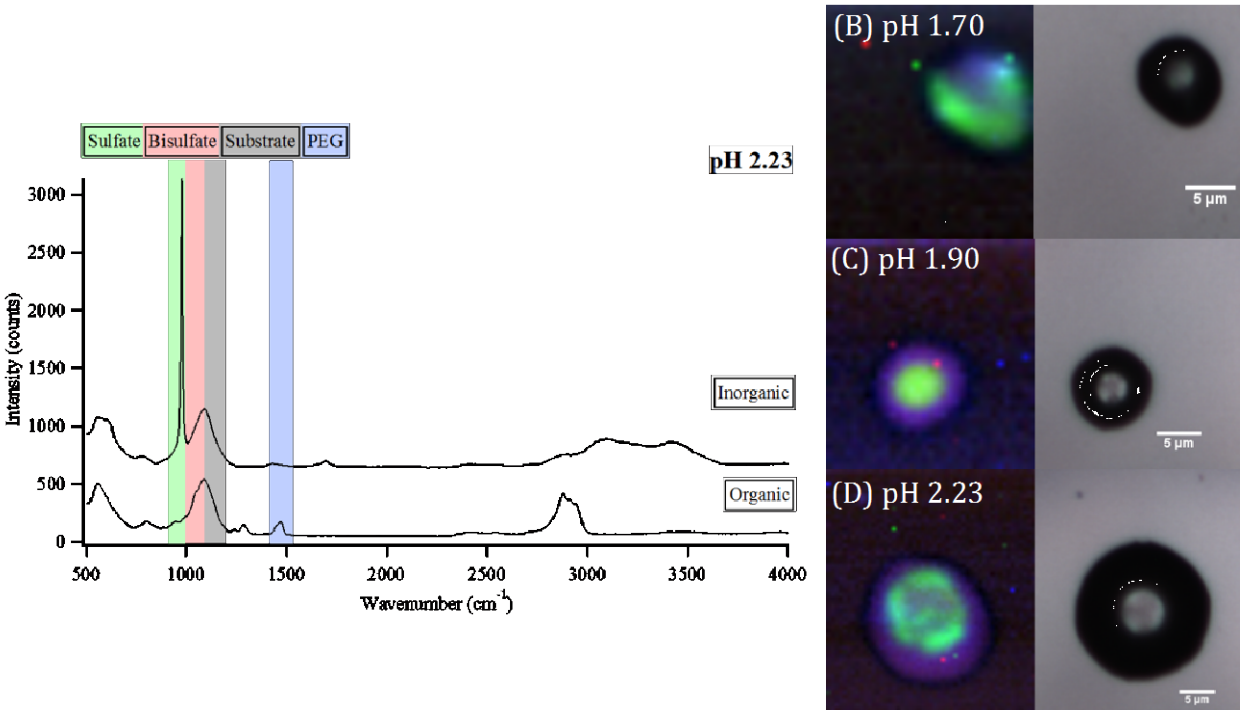

Figure 8.1 (A) Representative Raman spectra of inorganic and organic parts of LLPS particles composed of $(NH_4)_2SO_4/H_2SO_4$ and PEG-400. (B)-(D) Optical images and Raman maps of LLPS particles of varying pH. For the Raman maps, green, red, and blue correspond to the presence of sulfate, bisulfate, and PEG-400 species, respectively, determined by the intensity of their corresponding vibrational modes in the Raman spectra.

This dissertation presented the development and preliminary application of several novel analytical methods for characterization of atmospheric aerosol particles. Future studies that further refine these methods and apply them to measure aerosol mixing state and pH could have important implications for acidity-dependent multiphase aerosol processes and how aerosol particle composition and morphology influence climate effects. For example, these methods could be incorporated into field study analysis plans, characterizing the mixing state of ambient aerosols particles to correlate chemical composition with radiative forcing effects. The Southeast United States is a particularly interesting region for this type of analysis, as the observed radiative forcing trend has been one of cooling rather than warming, like most other regions globally. The cooling effect is potentially attributed to aerosol particles, but further work characterizing the mixing state and multiphase atmospheric processing of aerosols in this region is necessary to confirm this effect. The CC-Raman and SERS method are applicable for these studies, since the aerosol particles in the Southeast US often contain complex mixtures of

organic species, as the region is heavily forested but also home to anthropogenic emission sources. The pH methods are also applicable, as thermodynamic models have predicted Southeast US aerosol particles to be highly acidic (pH ~1). Additionally, all of these methods are well-suited for chamber studies that isolate and systematically study specific atmospheric processes. These techniques can be used to measure chemical composition and pH and their evolution over the course of an experiment. Chamber studies focused on key atmospheric reactions or physical processes will help improve identification of these phenomena occurring in the atmosphere in order to determine their impact on climate effects. Overall, the methods developed and presented in this dissertation can be applied to many different types of aerosol studies, both laboratory and field based, and will improve understanding of aerosol mixing state and pH to better predict or explain aerosol climate effects.

Appendix A. Computer-Controlled Raman Microspectroscopy (CC-Raman): A Method for the Rapid Characterization of Individual Atmospheric Aerosol Particles Supplemental Information[1]

A.1 Mixed Standard Aerosol Sample

Tables A.1-A.3 correspond to the mixed standard aerosol particle sample. Table A.1 lists the percent fraction for each identified cluster with standard error for the CC-Raman, CCSEM, and CPC methods. Standard error was calculated according to Equation A.1, where *F* is fraction and *N* is total population. Standard error for a sample was calculated with the total number of particles analyzed after similar clusters from each CC-Raman run were compiled for a given sample.

Equation A.1 $$\text{Standard Error} = \sqrt{\frac{F(1-F)}{N}}$$

Table A.2 lists the total fraction of particles containing L-alanine, ammonium sulfate, or sodium nitrate with standard error for the CC-Raman, CCSEM, and CPC methods. Table A.3 lists the percent fraction for each identified cluster with standard error for three trials of ~100 particles and the total particles analyzed for the CC-Raman method.

Table A.1 Cluster percent fractions with standard error for the CC-Raman, CCSEM, and CPC methods for the mixed standards sample.

Cluster	CC-Raman (%)	CCSEM (%)	CPC (%)
L-alanine	11 ± 2	11 ± 2	58.0 ± 0.6
L-alanine/$(NH_4)_2SO_4$	36 ± 3	17 ± 2	0
$(NH_4)_2SO_4$	16 ± 2	30 ± 3	36.1 ± 0.6
$(NH_4)_2SO_4/NaNO_3$	2.8 ± 0.9	8 ± 2	0
$NaNO_3$	5 ± 1	29 ± 3	5.9 ± 0.3
L-alanine/ $NaNO_3$	6 ± 1	6 ± 1	0
L-alanine/$(NH_4)_2SO_4$/ $NaNO_3$	24 ± 2	0	0

[1] Appendix A details supplemental information corresponding to Chapter 2

Table A.2 Total fraction of particles containing each compound with standard error for the CC-Raman, CCSEM, and CPC methods for the mixed standards sample.

Compound	CC-Raman (%)	CCSEM (%)	CPC (%)
L-alanine	77 ± 2	34 ± 3	58.0 ± 0.6
$(NH_4)_2SO_4$	78 ± 2	54 ± 3	36.1 ± 0.6
$NaNO_3$	37 ± 3	42 ± 3	5.9 ± 0.3

Table A.3 Cluster percent fractions with standard error for mixed standard samples for the CC-Raman method.

Sample	L-alanine (%)	L-alanine/ $(NH_4)_2SO_4$ (%)	$(NH_4)_2SO_4$ (%)	$(NH_4)_2SO_4$/ $NaNO_3$ (%)	$NaNO_3$ (%)	L-alanine/ $NaNO_3$ (%)	L-alanine/ $(NH_4)_2SO_4$/ $NaNO_3$ (%)
1	20 ± 4	34 ± 5	12 ± 3	8 ± 3	0.9 ± 0.9	11 ± 3	14 ± 3
2	2 ± 1	59 ± 5	10 ± 3	0	6 ± 2	3 ± 2	20 ± 4
3	13 ± 3	14 ± 3	26 ± 4	0	7 ± 2	3 ± 2	37 ± 5
Total	11 ± 2	36 ± 3	16 ± 2	2.8 ± 0.9	5 ± 1	6 ± 1	24 ± 2

The size distribution of mixed standards sample particles analyzed by CC-Raman and CCSEM is shown below in Figure A.1. Both methods measured projected area diameter and the mode was 1.64 μm and 1.12 μm for CC-Raman and CCSEM, respectively.

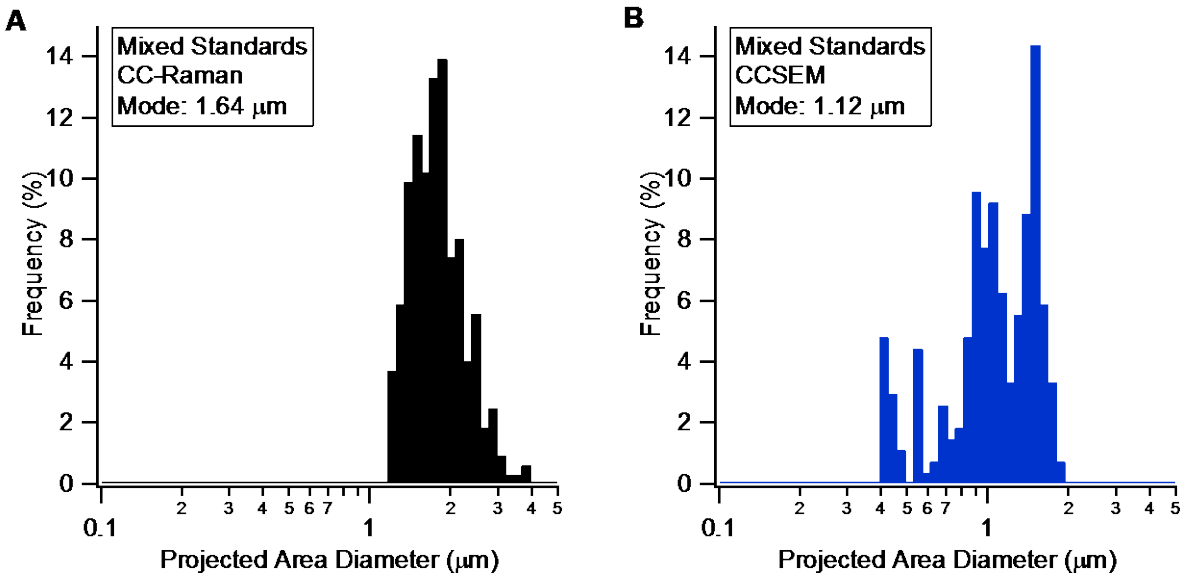

Figure A.1 Size distribution for mixed standards sample particles analyzed by (A) CC-Raman and (B) CCSEM.

A.2 Sulfate Standard Aerosol Particle Sample

Tables A.4 and A.5 correspond to the sulfate standard aerosol particle sample. Table A.4 lists the percent fraction for each identified cluster with standard error for the CC-Raman, CCSEM, and CPC methods. Table A.5 lists the total fraction of particles containing ammonium sulfate, calcium sulfate, magnesium sulfate, or sodium sulfate with standard error for the CC-Raman, CCSEM, and CPC methods.

Table A.4 Cluster percent fractions with standard error for the CC-Raman, CCSEM, and CPC methods for the sulfate standards sample.

Cluster	CC-Raman (%)	CCSEM (%)	CPC (%)
$(NH_4)_2SO_4$	29 ± 4	0	15.3 ± 0.3
$(NH_4)_2SO_4/CaSO_4$	5 ± 2	0	0
$CaSO_4$	0	20 ± 3	30.1 ± 0.4
$CaSO_4/MgSO_4$	12 ± 3	0	0
$MgSO_4$	0	23 ± 3	27.4 ± 0.4
Na_2SO_4	7 ± 2	14 ± 2	27.2 ± 0.4
$CaSO_4/MgSO_4/ Na_2SO_4$	13 ± 3	14 ± 2	0
$(NH_4)_2SO_4/MgSO_4/Na_2SO_4$	0	15 ± 2	0
$(NH_4)_2SO_4/CaSO_4/MgSO_4/ Na_2SO_4$	34 ± 4	14 ± 2	0

Table A.5 Total fraction of particles containing each compound with standard error for the CC-Raman, CCSEM, and CPC methods for the sulfate standards sample.

Compound	CC-Raman (%)	CCSEM (%)	CPC (%)
$(NH_4)_2SO_4$	68 ± 4	29 ± 3	15.3 ± 0.3
$CaSO_4$	64 ± 4	47 ± 3	30.1 ± 0.4
$MgSO_4$	60 ± 4	66 ± 3	27.4 ± 0.4
Na_2SO_4	54 ± 4	57 ± 3	27.2 ± 0.4

The size distribution of sulfate standards sample particles analyzed by CC-Raman and CCSEM is shown below in Figure A.2. Both methods measured projected area diameter and the mode was 1.59 μm and 0.82 μm for CC-Raman and CCSEM, respectively.

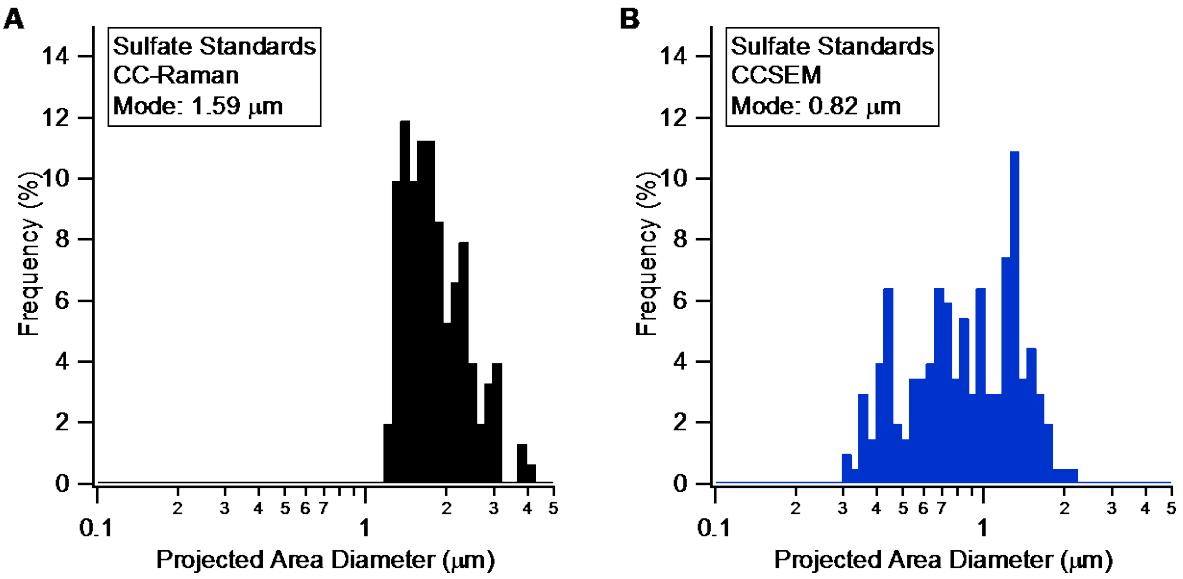

Figure A.2 Size distribution for sulfate standards sample particles analyzed by (A) CC-Raman and (B) CCSEM.

A.3 Ambient Aerosol Samples

Table A.6 corresponds to the ambient samples collected during the SOAS field campaign and lists the percent fraction with standard error for each general particle type cluster identified by the CC-Raman method.

Table A.6 Cluster percent fractions with standard error for SOAS samples.

Cluster	Fraction (%)
Trace Organic	60 ± 1
Organic	22 ± 1
Organic/Mineral	3.2 ± 0.5
Fluorescence	8.5 ± 0.8
Burning	6.5 ± 0.7

A size distribution for the SOAS aerosol particles was generated from CC-Raman and CCSEM measurements of projected area diameter (Figure A.3). Measured projected area diameters ranged from around 0.8 to 8.7 μm, with the mode at 1.53 μm for CC-Raman. Measured projected area diameters ranged from around 0.2 to 4.7 μm and yielded a bimodal distribution, with the larger mode at 1.20 μm for CCSEM.

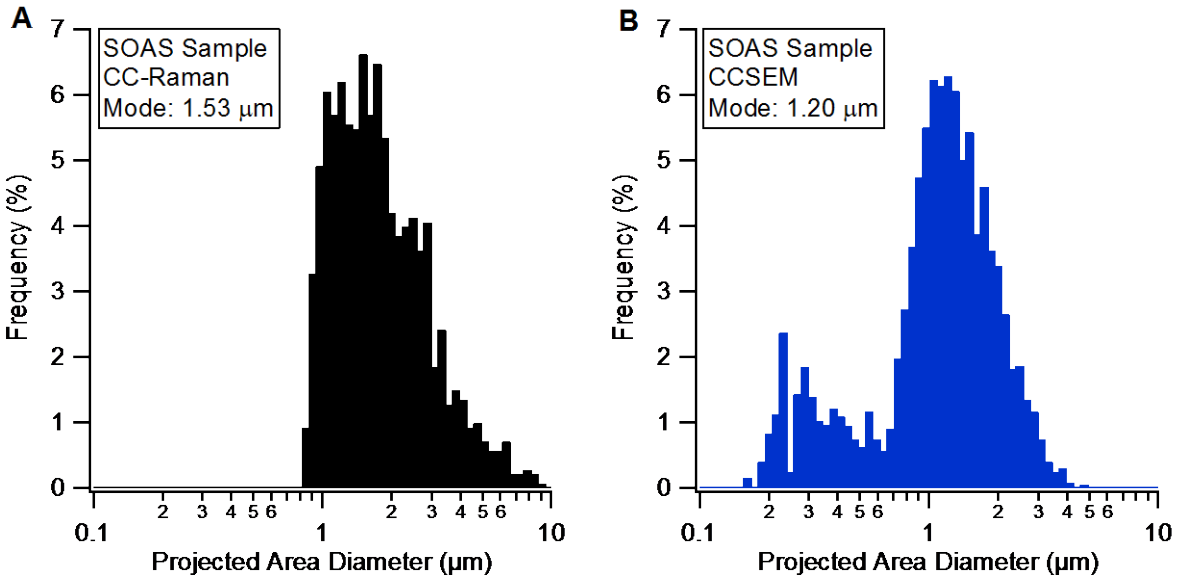

Figure A.3 (A) CC-Raman and (B) CCSEM determined size distributions for the SOAS aerosol particles.

In addition to the spectra corresponding to organic particles from the SOAS samples, spectra of organic/mineral mixed particles, particles that exhibited fluorescence, and particles containing graphitic soot species were also obtained (Figure A.4). Particles that exhibited artifacts of burning were included in the graphitic soot cluster due to the challenge associated with distinguishing burning from soot or other features. Figure A.5 shows a few optical images with representative graphitic soot particles highlighted. Although often observed together, fluorescence and burning features were observed independently of each other for most of the SOAS samples analyzed for this study. The organic/mineral mixed particles were found to contain either aluminum or silicon based on the vibrational modes at 518 and 636 cm^{-1} (Michaelian, 1986; Frost et al., 1997; Laskina et al., 2013).

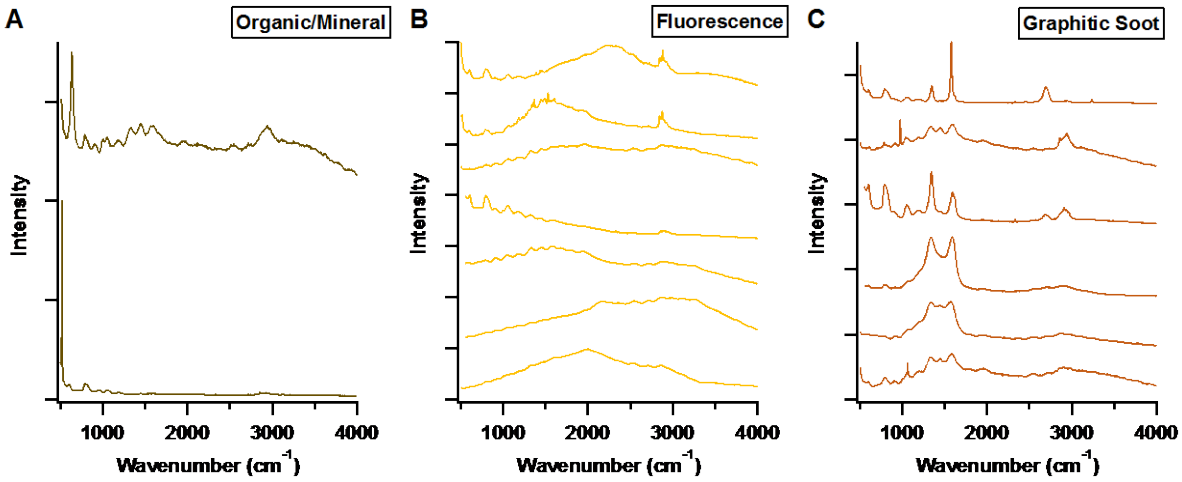

Figure A.4 Raman spectra of different observed types of A) organic/mineral particles, B) fluorescence, and C) graphitic soot from the SOAS aerosol particle samples.

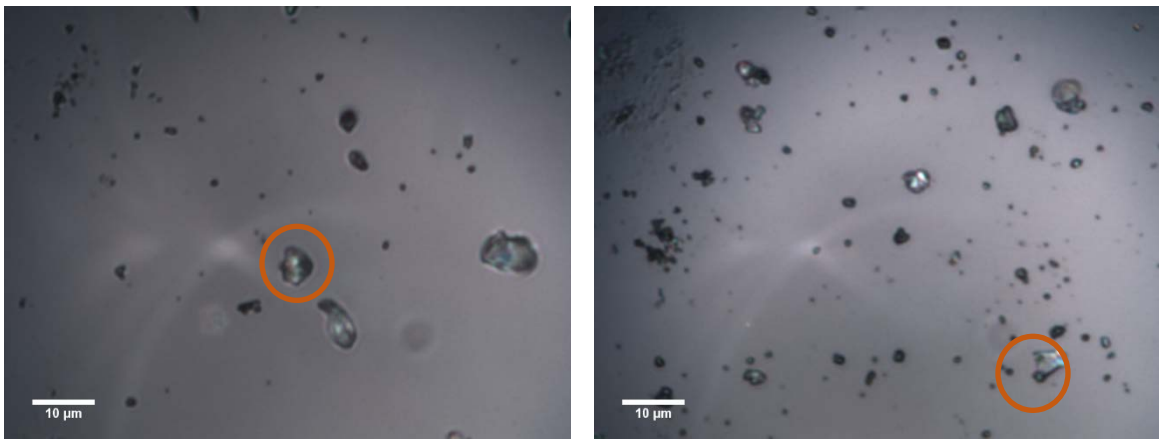

Figure A.5 Optical images of two SOAS samples with example soot particles highlighted.

A brief comparison between CC-Raman and CCSEM analysis for two of the SOAS samples is shown in Figure A.6. While there are not many direct comparisons between the clusters identified by CC-Raman and CCSEM, CC-Raman shows much more diversity in terms of secondary chemical components of organic and organic-containing particles. CCSEM cannot detect this diversity and rather classifies most particles in a general SOA cluster.

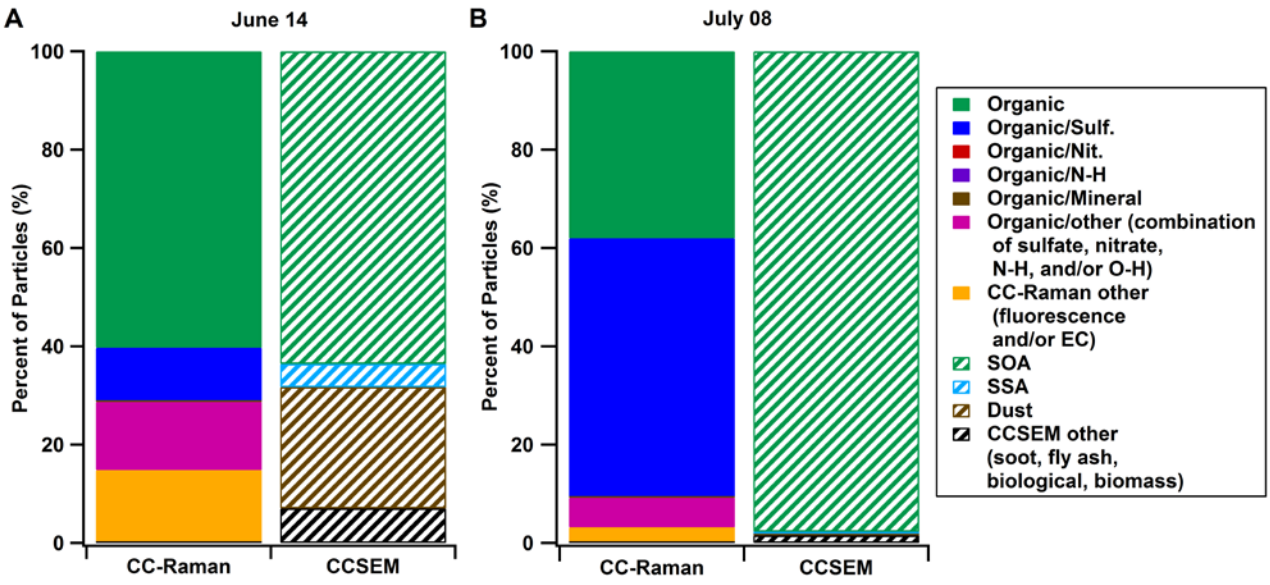

Figure A.6 CC-Raman and CCSEM identified classes of particles for A) June 14 and B) July 08 samples from the SOAS field campaign.

Table A.7 corresponds to the ambient samples collected during the SOAS field campaign and lists the percent fraction with standard error for each specific organic cluster identified by the CC-Raman method.

Table A.7 Organic cluster percent fractions with standard error for SOAS samples.

Cluster	Fraction (%)
Organic	1.0 ± 0.6
Organic/Sulf.	53 ± 3
Organic/Nit.	20 ± 2
Organic/O-H	11 ± 2
Organic/N-H	0.3 ± 0.3
Organic/Sulf./N-H	4 ± 1
Organic/Sulf./O-H	1.3 ± 0.7
Organic/Nit./O-H	9 ± 2
Organic/Sulf./Nit./N-H	0.3 ± 0.3
Organic/Sulf./N-H/O-H	0.3 ± 0.3

Appendix B. Surface Enhanced Raman Spectroscopy Enables Observations of Previously Undetectable Secondary Organic Aerosol Components at the Individual Particle Level Supplemental Information[2]

B.1 Ag Nanoparticle Characterization

TEM images were collected on a JEOL 2010F Analytical Electron Microscope. ImageJ 1.48 software was used to estimate projected area diameter and determine a size distribution. Absorbance spectra were collected using a Cary 50 UV-Vis spectrometer for the wavelength range 300-800 nm. Ten absorbance spectra were collected and averaged to determine mean absorbance maximum (λ_{max}) and full width half max (fwhm). λ_{max} corresponds to the average particle size, while fwhm absorption is related to particle dispersion. Figure S1a shows a TEM image of the Ag nanoparticles, which exhibit a mode at 52 nm for projected area diameter (Figure B.1b). The Ag colloidal solution had an absorption maximum at 415 nm and full width half maximum (fwhm) of 155 nm (Figure 2c). From Mie theory this is indicative of small, relatively monodispersed particles of the size from TEM (Mie, 1908).

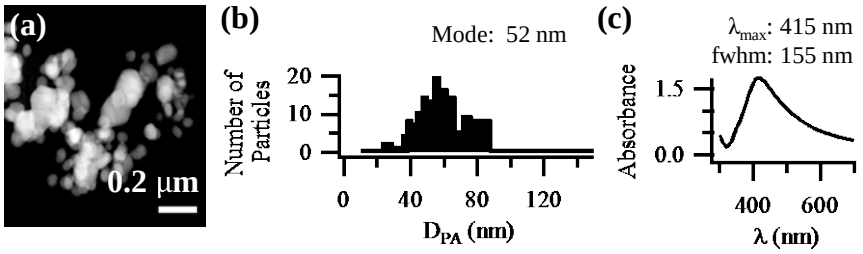

Figure B.1 (a) TEM image of Ag nanoparticles. (b) Size distribution of Ag nanoparticles with an average mode of 52 nm. (c) Absorbance spectrum of Ag colloidal solution with A_{max} at 415 nm and fwhm of 155 nm.

B.2 Raman Microspectroscopy and Mapping

A Horiba Labram HR Evolution Raman spectrometer coupled with a confocal optical microscope (100x Olympus objective) was used to collect Raman spectra. The Raman spectrometer was equipped with a Nd:YAG laser source (50 mW, 532 nm) and CCD detector. A

[2] Appendix B details supplemental information corresponding to Chapter 3

600 g/mm diffraction grating yielded spectral resolution of ~2 cm^{-1}. The instrument was calibrated against the Stokes Raman signal of pure Si at 520 cm^{-1} using a silicon wafer standard. Laser power was adjusted accordingly with ND filters to prevent damage to the sample. Spectra were collected for the range 100 to 4000 cm^{-1} with two accumulations at 1 s acquisition time for each particle analyzed. Raman maps were collected using computer-controlled XY Raman mapping, which recorded spectra automatically in a point-by-point scanning mode with a 0.5 μm step size. Each map spectrum was collected for the range 555 to 2175 cm^{-1} with two accumulations at 1 s acquisition time.

B.3 Calculations of Area, Volume, and Mass

To calculate the area, volume, and mass of a 3 μm aerosol particle, the following equations were used:

Equation B.1 $$A = \pi r^2$$

Equation B.2 $$V = \frac{4}{3}\pi r^3$$

Equation B.3 $$m = \rho V$$

where r = 1.5 x 10^{-6} m and average density (ρ) of 1.2 g/m^3 was assumed (typical for organic carbon containing aerosol particles). Area, volume, and mass were determined to be 7.1 μm^2, 1.4 x 10^{-12} m^3, and 1.7 pg, respectively.

The volume of the 10 nm spherical segment of the 3 μm aerosol particle that exhibits enhancement was calculated according to the following equation:

Equation B.4 $$V = \left(\frac{\pi}{6}\right)\left(3r_1^2 + 3r_2^2 + h\right)h$$

where r_1 = 1.5 x 10^{-6} m, r_2 = 1.4 x 10^{-6} m, and h = 1 x 10^{-8} m. The volume was determined to be 6.6 x 10^{-20} m^3. Mass of the 10 nm spherical segment was calculated according to Equation B.3 to be 1.7 fg. If approximately 100 chemical species are present within the 10 nm spherical segment that exhibits enhancement, the mean mass of each chemical species present is 790 ag.

B.4 Comparison of SERS-enhanced and Non-enhanced Spectra

Figure B.2 shows two examples of non-enhanced Raman spectra and three SERS-enhanced Raman spectra. The non-enhanced spectra were collected from aerosol particles impacted on quartz substrates and the SERS-enhanced spectra were collected from aerosol particles impacted on Ag nanoparticle coated quartz substrates. The SERS-enhanced spectra are the full spectra of the three particles from which specific regions highlighting certain vibrational modes are shown in Figure 3.3a.

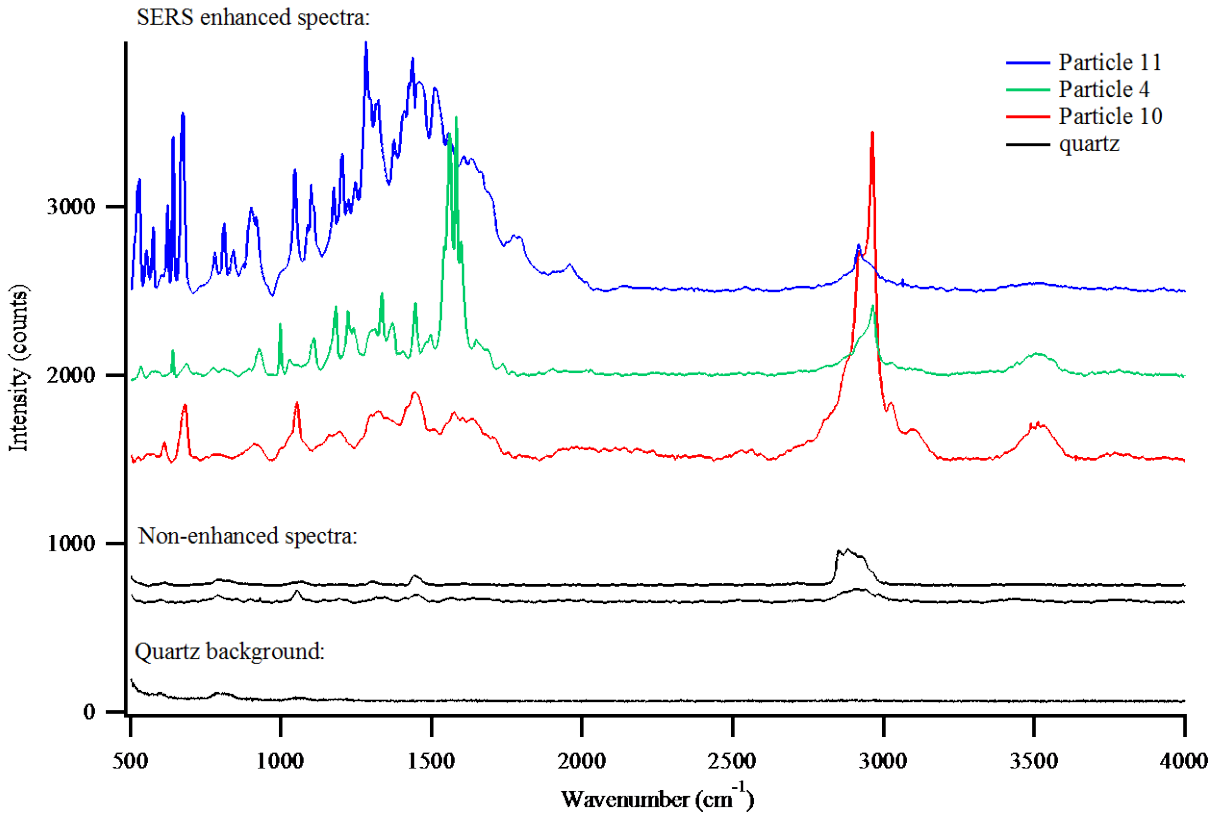

Figure B.2 Two non-enhanced Raman spectra collected (bottom), three SERS enhanced spectra (top), and a quartz background spectrum. The spectrum for Particle 11 corresponds to the spectra shown in Figure 3a for the $\nu(NO_3^-)$ vibrational mode, Particle 4 corresponds to δ(C-C), and Particle 10 corresponds to ν(C-H) and ν(O-H).

B.5 Red Shift of Nitrate Symmetric Stretch

The red shift observed in Figure 3.2 for the $\nu(NO_3^-)$ peak is likely due to the molecular geometry of the nitrate anion and its coupling to the nanoparticle surface. The strength of coupling that is observed between the SERS substrate and the nitrate anion is strongly dependent on the proximity of the nitrate to the silver nanoparticle surface, as well as the orientation and binding of the anion to that surface. Aqueous NO_3^-, which Ault et al. showed having a peak frequency of 1055 (similar to 1054 in Figure 3.2) and similar shift of 13 cm^{-1} from $NaNO_3$, may be able to bind more effectively with the silver nanoparticle surface, while nitrate in $NaNO_{3\,(s)}$ cannot bind as tightly due to the interaction with sodium or incorporation into a $NaNO_3$ solid or crystal. It is also possible that NO_3^- of a specific surface binding geometry, such as bidentate, contributes to the red shift. No sulfate peaks were observed to red shift, which is explainable by the fact that ammonium sulfate will effloresce to a crystal at a much higher RH (33%) (Cziczo et al., 1997) than $NaNO_3$ (values vary, but water remains to < 6%) (Li et al., 2006), meaning there is a greater chance of some aqueous NO_3^- being available to strongly couple to the nanoparticle surface. Further experiments will be needed to fully characterize this phenomenon.

B.6 SEM/EDX

Scanning electron microscopy (SEM) coupled with energy dispersive X-ray spectroscopy (EDX) was used to confirm both chemical composition and particle sizes. It should be noted that internal structure is substantially altered by the loss of water under the vacuum of the SEM, as can be seen by the effloresced salts within the particles below. SEM images and EDX spectra of particles impacted on silicon substrates were collected with an FEI Helios 650 Nanolab SEM/FIB. Figure B.3 shows several example particles within the 0.5-2 μm size range and their accompanying EDX spectra. The EDX spectra show the elemental composition of these representative particles to consist primarily of carbon, oxygen, aluminum (though some interference is present from the SEM stub), and sulfur, which is in agreement with the mainly organic, organosulfate, and mineral/dust vibrational modes observed in the SERS analysis. Organonitrate vibrational modes were detected through SERS, yet a peak at 0.39 kV in the EDX spectra indicative of nitrogen cannot be detected, most likely due to the difficulty of detecting a

N in trace amounts, as noted in previous work (Moffet et al., 2010b). While silicon is a common component of dust, the large silicon peak is primarily due to the silicon substrate.

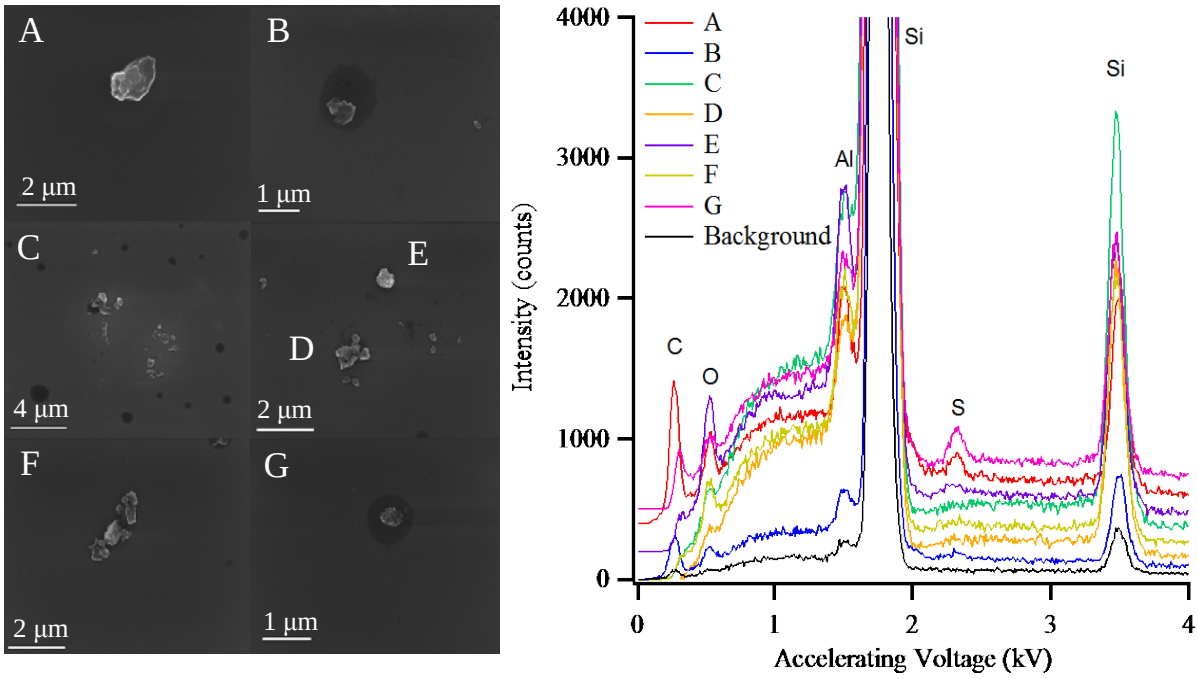

Figure B.3 SEM images of representative ambient aerosol particles (left) and accompanying EDX spectra for each particle (right).

B.7 Peak Assignments

Table B.1 list several preliminary peak assignments based on both calculated and experimentally collected spectra for several organic and organonitrate compounds representative of the type of compounds present in SOA. These compounds include isobutyl nitrate, ethyl hexyl nitrate, pinonic acid, alpha pinene oxide, isoprene nitrate, and mono-nitroglycerin. DFT calculations used B3LYP functional and 3-21G and 6-311G basis sets.

Table B.1 Vibrational mode assignments for organic and organonitrate compounds present in SOA.

Wavenumber (cm^{-1})	**Vibrational Mode**
625, 645	C-O wagging[c]
687	Aromatic stretching[d]
815, 843, 901	C-C stretching[c,d]
920, 924	C-H rocking[a,c]
998	C-H wagging[c]
1051, 1110, 1221	C-C stretching[c,e]
1282, 1324	C-H twisting[b]
1337, 1377	C-H wagging[c,e]
1354	C-H twisting[f]
1370	C-C stretching[c]
1370	C-H wagging[a]
1445, 1459, 1506, 1560, 1570, 1580	C-H bending[c,e,f]
1653	NO_3^- symmetric stretching[a,b,e,f]

[a]isobutyl nitrate, [b]ethyl hexyl nitrate, [c]pinonic acid, [d]alpha pinene oxide, [e], isoprene nitrate, [f]mono-nitroglycerin

B.8 Mapping Enhanced Regions

Figure B.4 focuses on the aerosol particle discussed in Figure 3.5, with the same optical image and mapped region. In addition to the $\nu_w(CH_2)$, $\nu(NO_3^-)$, and δ(C-C) vibrational modes indicated by green, blue, and red intensity on the map, a background representing regions of the particle not exhibiting enhancement is shown in gray. The non-enhanced background corresponds to 1950 cm^{-1}. SERS enhancement within this aerosol particle is concentrated near the edge of the particle on the lower right.

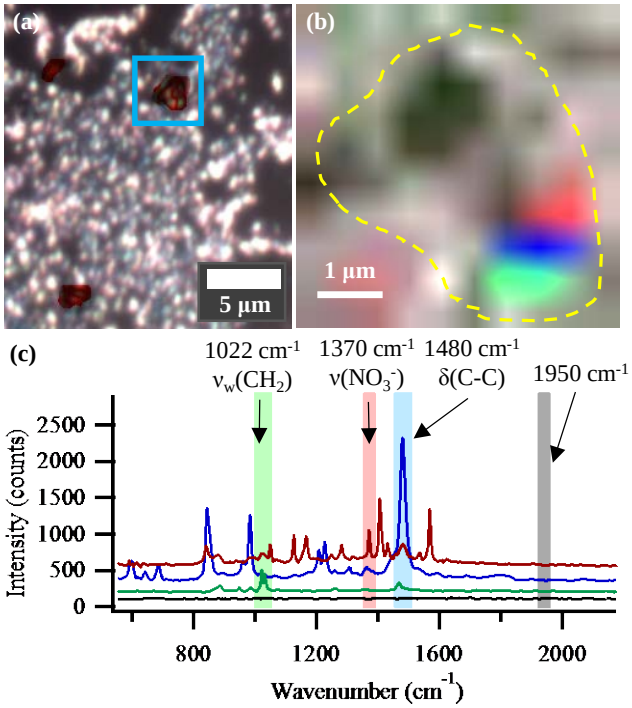

Figure B.4 (a) Optical image of aerosol particle, (highlighted in red) against SERS substrates, and mapped area (blue box). (b) Map of the aerosol particle (outlined in yellow dashes) showing the location of three different enhanced chemical species at 1022 cm^{-1} (green), 1370 cm^{-1} (red), and 1480 cm^{-1} (blue) against a background of non-enhancement (gray). (c) Raman spectra accompanying the mapped intensities. This is the same aerosol particle as shown in Figure 3.5.

Appendix C. Surface Enhanced Raman Spectroscopy of Submicron Sized Aerosol Particles: Breaking the Diffraction Limit Supplemental Information[3]

C.1 Testing Ag SERS Substratse

Several different Ag SERS substrates were tested for their application to aerosol particle studies. Ag nanoparticles (AgNPs) were synthesized according to the method by Leopold and Lendl (Leopold and Lendl, 2003). Briefly, a mixture of NaOH and hydroxylamine hydrochloride was added to a solution of $AgNO_3$. The size of the resulting nanoparticles depended on the speed of mixing of the two solutions. Rapid mixing led to smaller nanoparticles (~30 nm) while mixing dropwise led to larger nanoparticles (~60 nm). Ag bipyramidal nanoparticles were synthesized according to the method by Zhang et al. (Zhang et al., 2009). Briefly, a mixture of $AgNO_3$, sodium citrate, BSPP, and NaOH was irradiated with a mercury lamp for 18 hours. The resulting colloidal solutions of AgNPs and Ag bipyramids were drop-coated onto clean quartz slides and dried in a desiccator to create SERS substrates in the same manner as Craig et al. (Craig et al., 2015).

Laboratory-generated $(NH_4)_2SO_4$ particles were impacted onto the SERS substrates, as well as a plain quartz substrate and analyzed for SERS enhancement. Raman spectra were collected for 1 accumulation with 1 s acquisition time for the range of 200 – 1900 cm^{-1} and are shown in Figure C.1. Similar to the substrate comparison discussed in the main text, the Ag foil SERS substrate yielded the best spectral enhancement. Enhancement factors for the $\nu(SO_4^{2-})$ mode were calculated to be 5.6, 3.1, 2.8, and 2.4 for the Ag foil, AgNPs (large), Ag bipyramids, and AgNPs (small), respectively.

[3] Appendix C details supplemental information corresponding to Chapter 4

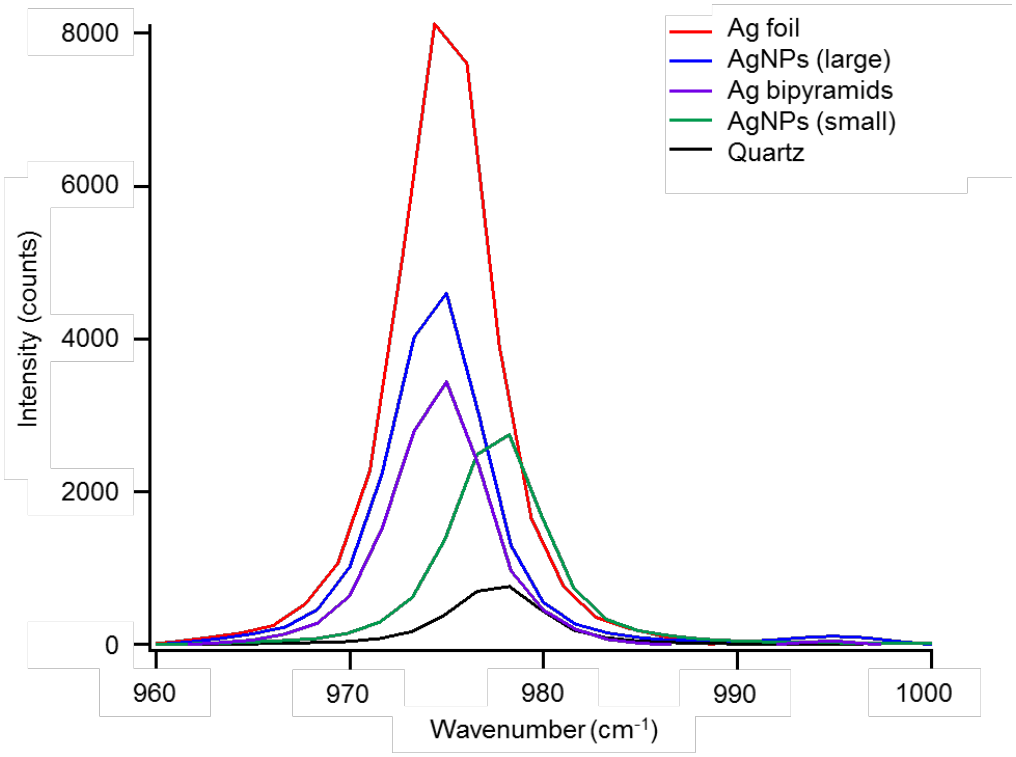

Figure C.1 Comparison of Raman spectra of $(NH_4)_2SO_4$ particles for different types of Ag SERS substrates. Enhancement factors were calculated to be 5.6, 3.1, 2.8, and 2.4 for the Ag foil, AgNPs (large), Ag bipyramids, and AgNPs (small), respectively.

C.2 Raman Spectra

All Raman spectra and the average spectrum for 400 nm, 600 nm, and 800 nm PSL particles from both quartz and Ag foil substrates are shown in Figures C.2-C.4. All Raman spectra and the average spectrum for 400 nm, 600 nm, and 800 nm $(NH_4)_2SO_4$ particles from both quartz and Ag foil substrates are shown in Figures C.5-C.7. All Raman spectra and the average spectrum for 400 nm, 600 nm, and 800 nm $NaNO_3$ particles from both quartz and Ag foil substrates are shown in Figures C.8-C.10.

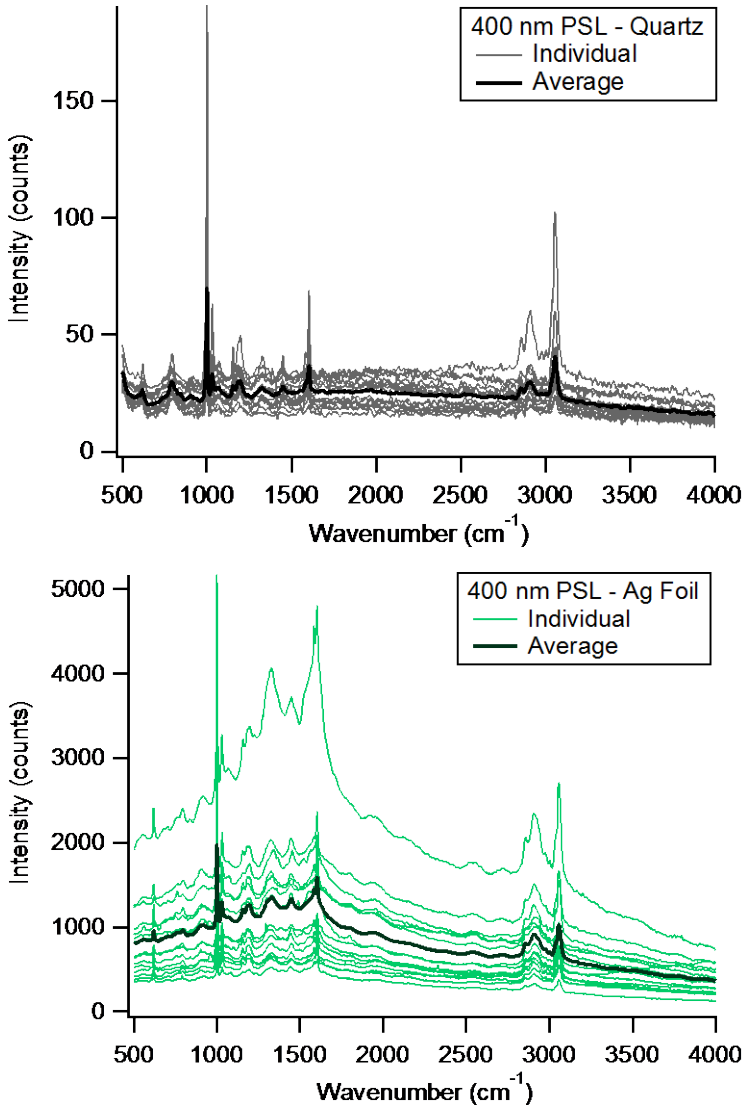

Figure C.2 Raman spectra for 400 nm PSL particles on quartz (top) and Ag foil (bottom) substrates.

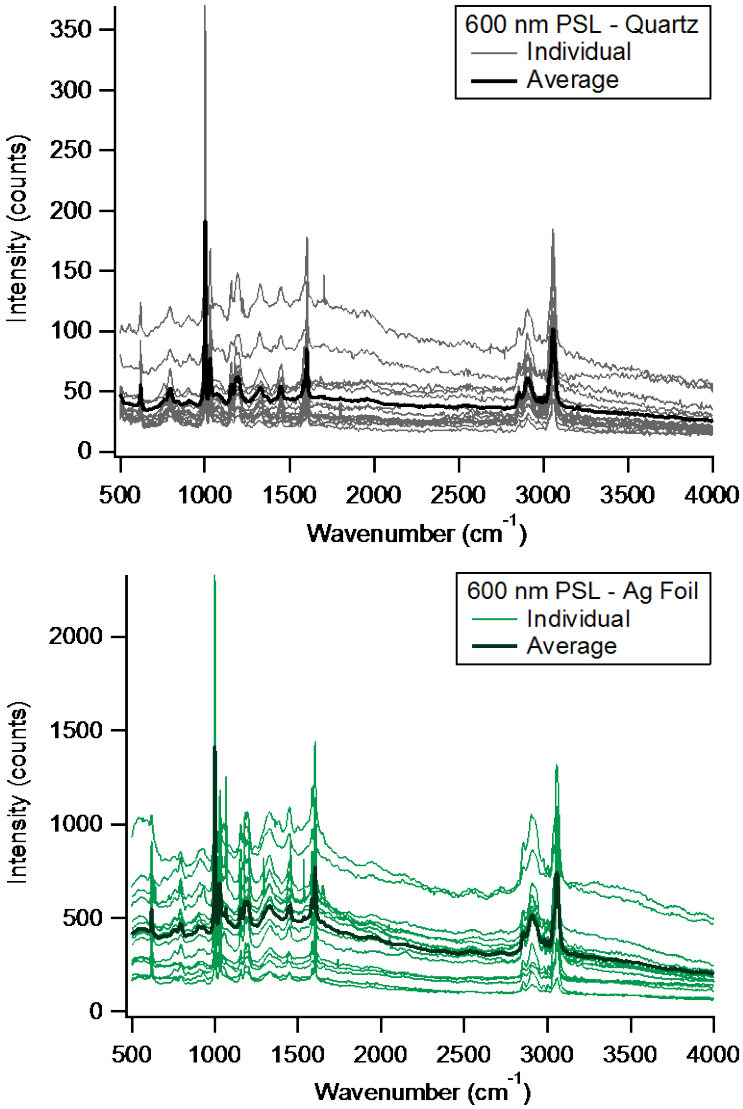

Figure C.3 Raman spectra for 600 nm PSL particles on quartz (top) and Ag foil (bottom) substrates.

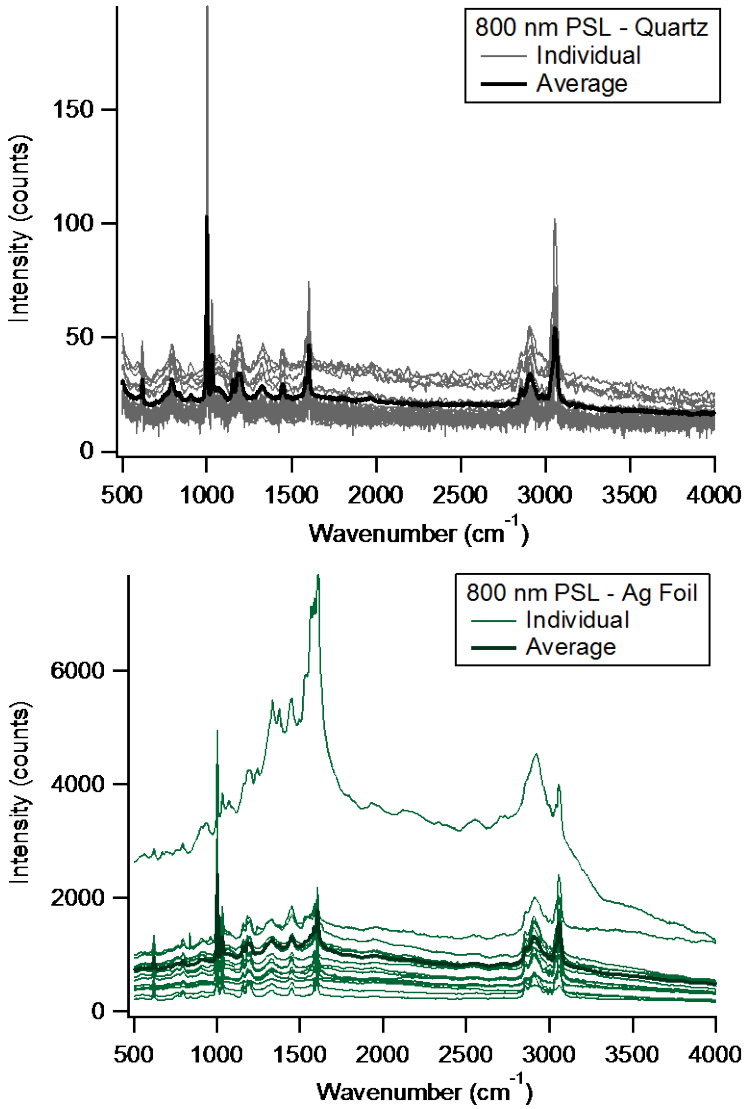

Figure C.4 Raman spectra for 800 nm PSL particles on quartz (top) and Ag foil (bottom) substrates.

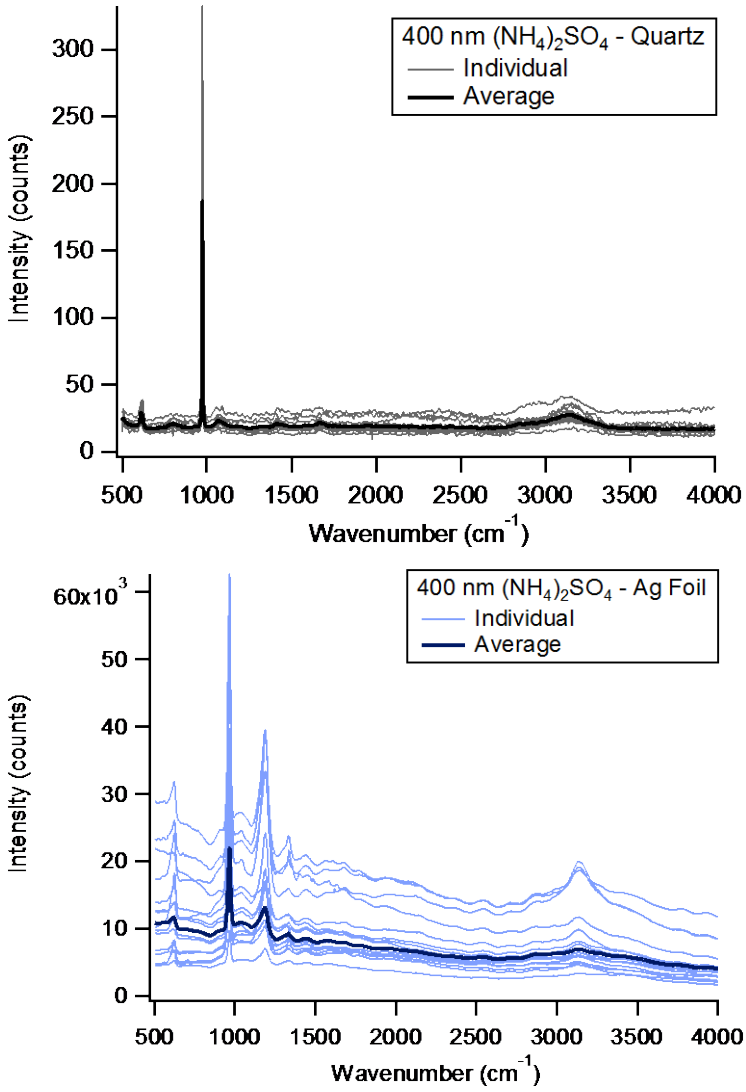

Figure C.5 Raman spectra for 400 nm $(NH_4)_2SO_4$ particles on quartz (top) and Ag foil (bottom) substrates.

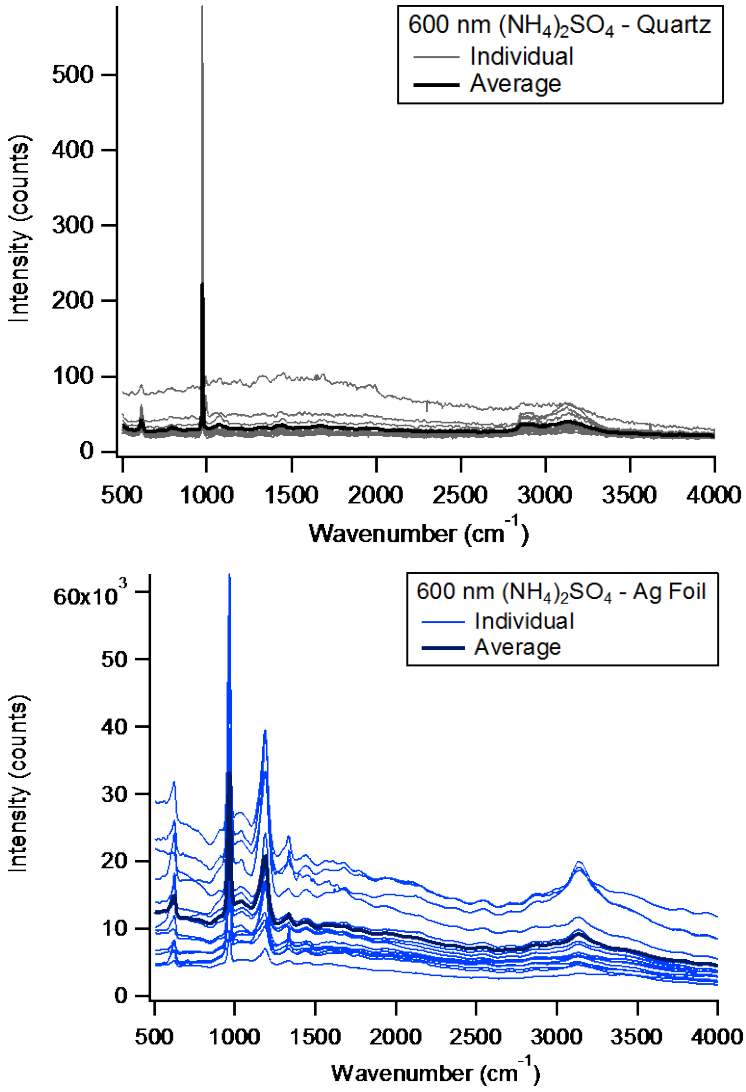

Figure C.6 Raman spectra for 600 nm $(NH_4)_2SO_4$ particles on quartz (top) and Ag foil (bottom) substrates.

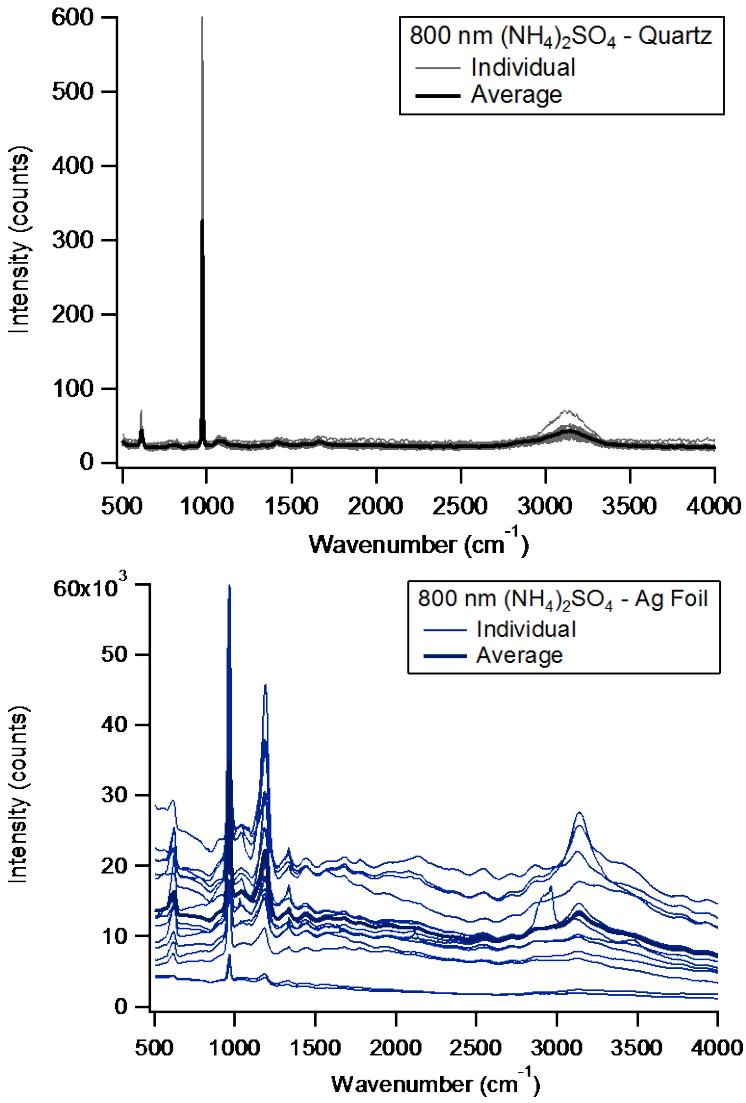

Figure C.7 Raman spectra for 800 nm $(NH_4)_2SO_4$ particles on quartz (top) and Ag foil (bottom) substrates.

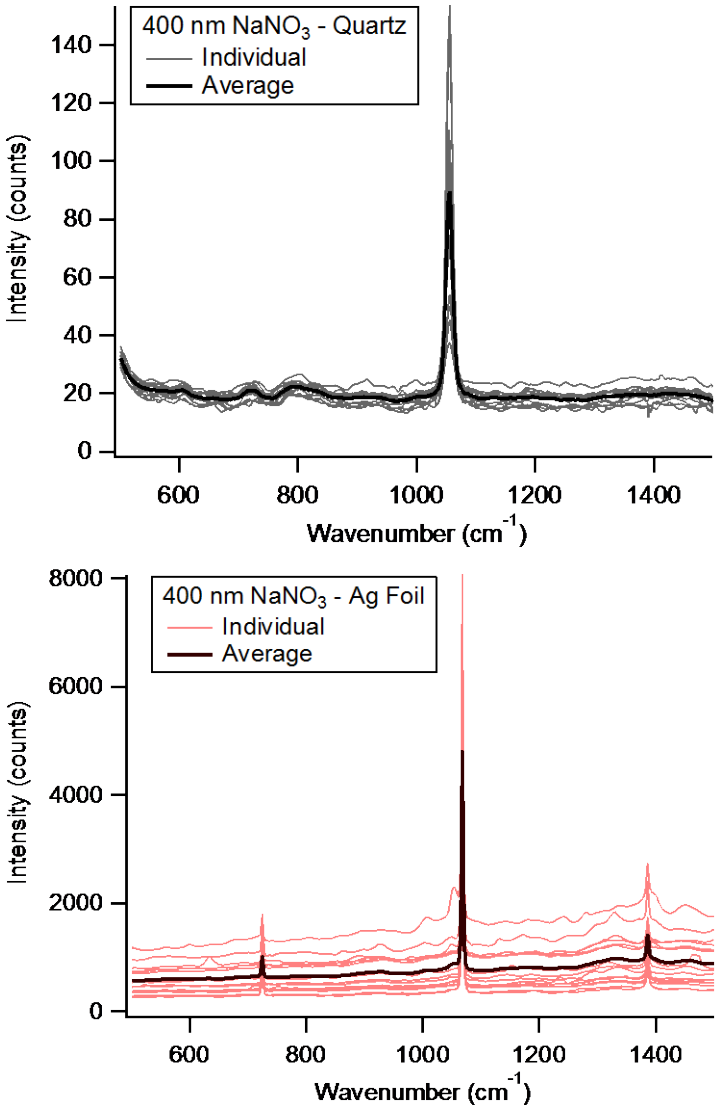

Figure C.8 Raman spectra for 400 nm $NaNO_3$ particles on quartz (top) and Ag foil (bottom) substrates.

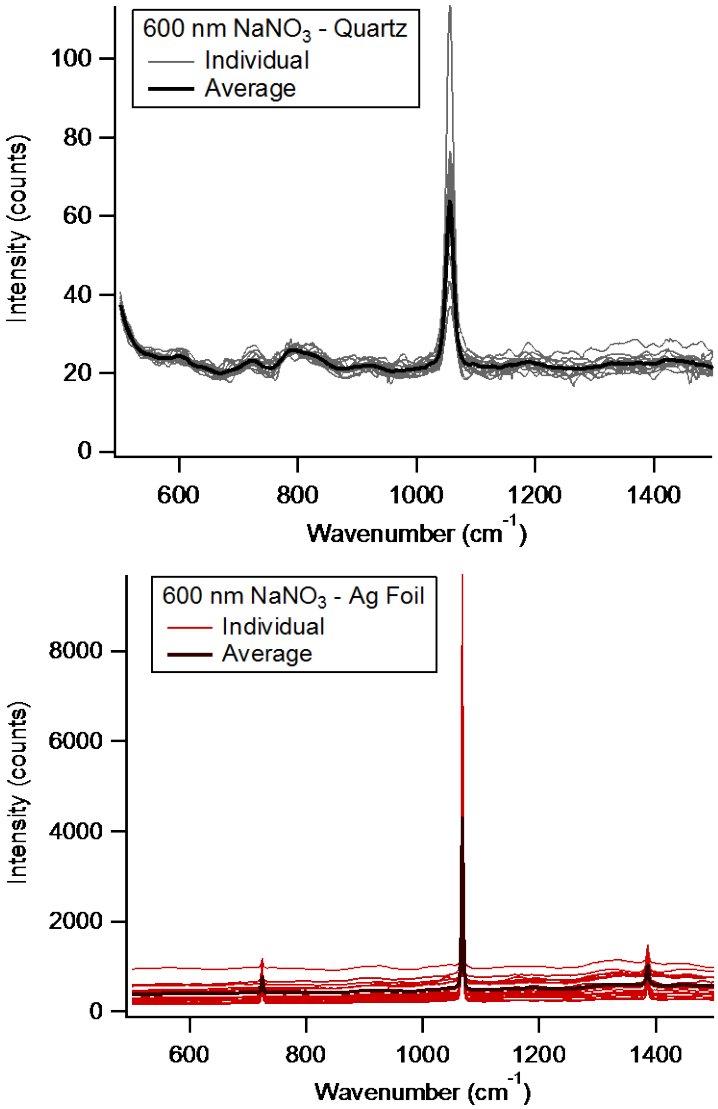

Figure C.9 Raman spectra for 600 nm $NaNO_3$ particles on quartz (top) and Ag foil (bottom) substrates.

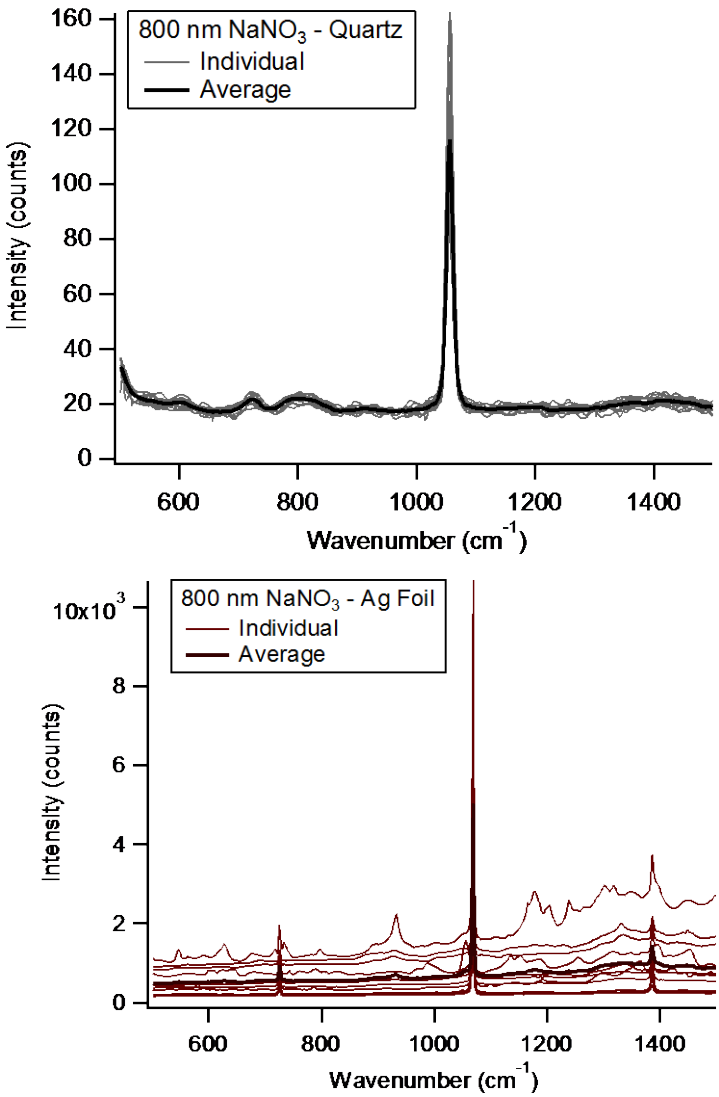

Figure C.10 Raman spectra for 800 nm $NaNO_3$ particles on quartz (top) and Ag foil (bottom) substrates.

C.3 Ambient Aerosol Sample Optical Images

SERS spectra were collected for 150 nm size-selected ambient aerosol particles with point-by-point automated mapping with 0.25 μm step size. Figure C.11 shows the Raman spectra and corresponding optical image for these sample with the mapped region and the location of the spectra highlighted. The ambient aerosol may appear larger in the optical image due to spreading upon impaction (Sobanska et al., 2014; Bondy et al., 2017a) or agglomeration, however, the large particles were avoided for this analysis.

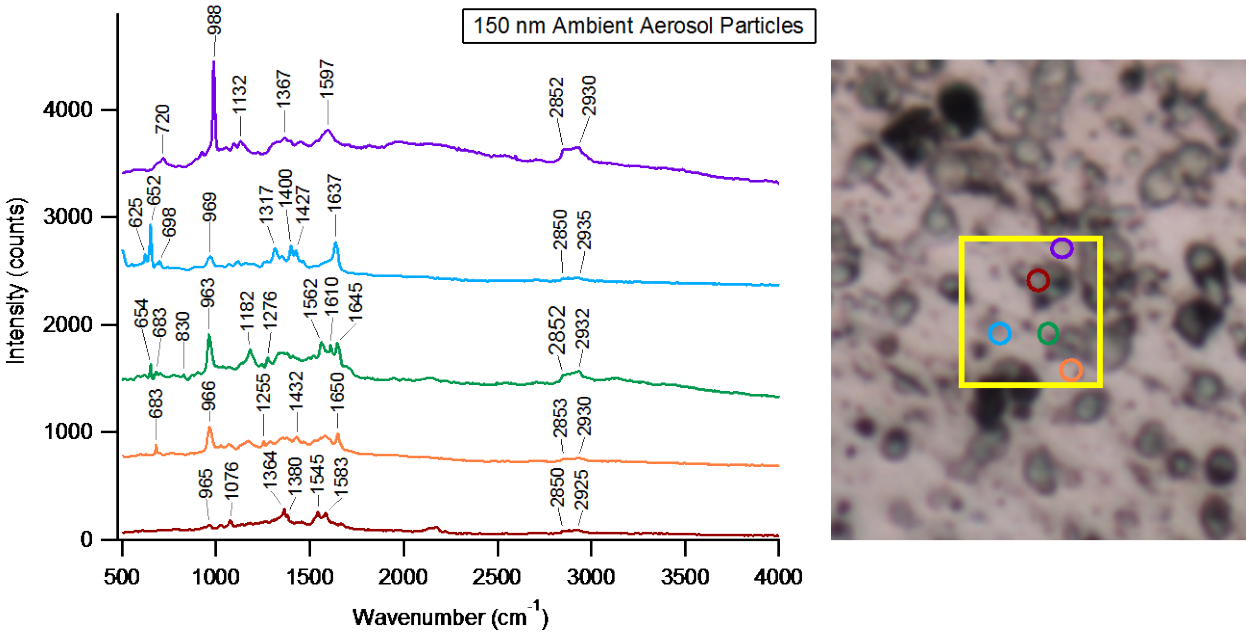

Figure C.11 Raman spectra for 150 nm size-selected ambient aerosol particles with color coordinated highlights for their respective locations within the mapped region (indicated by the yellow square).

Appendix D. Direct Measurement of pH in Individual Particle via Raman Microspectroscopy and Variation in Acidity with Relative Humidity Supplemental Information[4]

D.1 Bulk Solution Composition

Aerosol particles were generated from solutions of $MgSO_4$-H_2SO_4. The ratio of the concentration of Mg^{2+} to the concentration of total sulfate species (bisulfate + sulfate) for each bulk solution was used to determine the concentration of Mg^{2+} in individual particles (Table D.1).

Table D.1 Bulk solution composition

Bulk Solution pH	[$MgSO_4$] (mM)	[H_2SO_4] (mM)	[Mg^{2+}]/([HSO_4^- + SO_4^{2-}])
0.44	30	360	0.08
0.89	30	198	0.13
1.15	30	54	0.36
1.64	30	18	0.63
1.99	30	4.1	0.88

D.2 Comparison with Proxy Methods

To compare the Raman microspectroscopic method of measuring aerosol particle pH, the ion balance proxy method for calculating aerosol particle [H^+] was applied using the averaged data for [Mg^{2+}], [HSO_4^-], and [$H_2SO_4^{2-}$]. The ion balance method was unable to be used to calculate aerosol particle pH for bulk solution pH 1.64 and 1.99, as it resulted in negative [H^+] values. The results of the ion balance method, which have a significantly smaller correlation

[4] Appendix D details supplemental information corresponding to Chapter 5

factor and do not show an increase in pH with increasing relative humidity, are shown in Figure D.1.

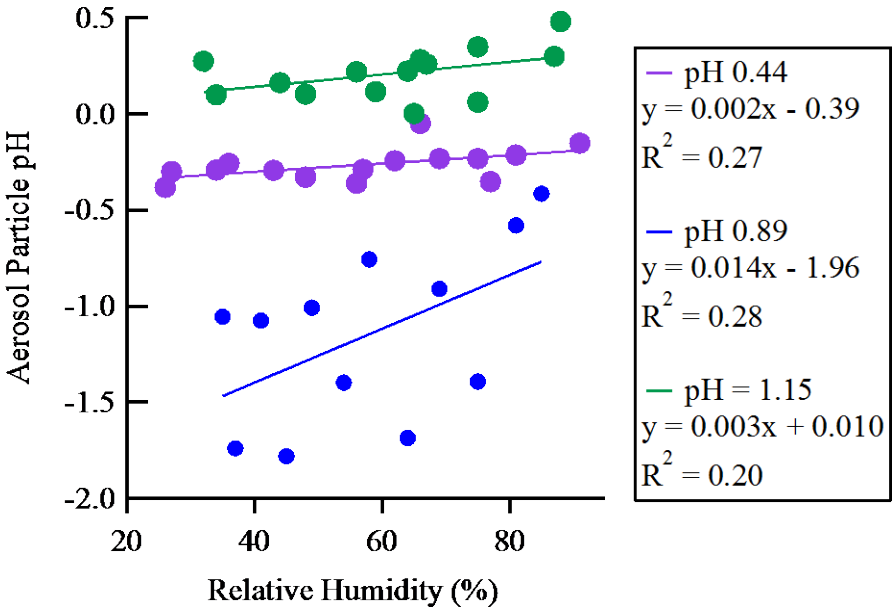

Figure D.1 Aerosol particle pH as a function of relative humidity for bulk solution pH 0.44, 0.89, and 1.15, as calculated by the ion balance proxy method for determining $[H^+]$ of an aerosol particle.

D.3 Relative Humidity Cycling

Table D.2 Average data from each cycle at each bulk solution pH..

Bulk Solution pH	Cycle	RH (%)	$[HSO_4^-]$ (m)	$[SO_4^{2-}]$ (m)	$[Mg^{2+}]$ (m)	$[SO_4^{2-}]/[HSO_4^-]$	I	γ (HSO_4^-)	γ (SO_4^{2-})	$\gamma(H^+)$	$[H^+]$ (m)	Aerosol Particle pH
0.44	1	26	3.527	0.222	0.300	0.070	3.959	0.528	0.078	0.714	2.305	-0.074
		34	3.018	0.110	0.250	0.036	3.525	0.531	0.079	0.715	2.590	-0.267
		43	2.745	0.242	0.239	0.098	3.691	0.532	0.081	0.716	2.714	0.003
		56	3.090	0.325	0.273	0.099	3.222	0.536	0.083	0.717	0.961	0.170
		62	2.237	0.295	0.203	0.134	2.439	0.549	0.091	0.722	0.651	0.337
		69	2.097	0.325	0.194	0.154	2.358	0.551	0.093	0.723	0.545	0.407
		77	2.697	0.466	0.253	0.163	3.063	0.541	0.086	0.719	0.554	0.402
		91	1.884	0.201	0.167	0.107	2.047	0.559	0.098	0.726	0.740	0.270
	2	27	3.102	0.102	0.256	0.036	3.935	0.527	0.078	0.714	3.334	-0.324
		36	2.607	0.175	0.223	0.067	2.804	0.542	0.086	0.719	1.410	0.012
		48	2.819	0.328	0.252	0.121	3.013	0.538	0.084	0.718	0.885	0.233
		57	2.566	0.295	0.229	0.115	2.711	0.544	0.087	0.720	0.760	0.264
		66	1.334	0.219	0.124	0.176	1.572	0.576	0.111	0.733	0.436	0.515
		75	2.061	0.343	0.192	0.163	2.381	0.551	0.092	0.723	0.559	0.412
		81	1.807	0.402	0.177	0.232	2.257	0.554	0.094	0.724	0.395	0.568
0.89	1	37	85.473	9.828	12.389	0.109	87.947	0.443	0.039	0.684	1.550	-0.025
		45	90.425	12.402	13.368	0.128	97.409	0.443	0.039	0.684	1.314	0.047
		54	40.402	3.767	5.742	0.093	40.074	0.451	0.041	0.686	1.709	-0.069
		64	61.678	14.573	9.913	0.212	80.203	0.448	0.040	0.685	0.784	0.271
		75	32.053	7.120	5.092	0.222	40.809	0.451	0.041	0.686	0.717	0.308
	2	35	17.847	1.821	2.557	0.102	18.362	0.471	0.049	0.693	1.365	0.025
		41	17.978	2.179	2.620	0.115	19.193	0.473	0.051	0.694	1.212	0.077
		49	16.565	1.393	2.334	0.083	16.558	0.473	0.050	0.694	1.642	-0.057

Bulk Solution pH	Cycle	RH (%)	$[HSO_4^-]$ (m)	$[SO_4^{2-}]$ (m)	$[Mg^{2+}]$ (m)	$[SO_4^{2-}]/[HSO_4^-]$	I	γ (HSO_4^-)	γ (SO_4^{2-})	$\gamma(H^+)$	$[H^+]$ (m)	Aerosol Particle pH
		58	8.435	1.100	1.240	0.130	9.366	0.490	0.058	0.700	0.940	0.183
		69	11.522	1.804	1.732	0.151	13.269	0.481	0.054	0.697	0.872	0.218
		81	5.239	0.848	0.791	0.172	6.220	0.515	0.072	0.709	0.643	0.362
		85	3.366	0.657	0.523	0.237	4.297	0.529	0.079	0.714	0.509	0.493
1.15	1	32	2.056	0.128	0.786	0.072	3.637	0.534	0.082	0.716	1.560	0.003
		44	2.411	0.224	0.948	0.105	4.091	0.528	0.078	0.714	1.083	0.162
		56	1.929	0.234	0.779	0.151	3.403	0.537	0.084	0.717	0.827	0.314
		66	1.467	0.243	0.616	0.164	2.717	0.545	0.088	0.720	0.531	0.420
		67	1.809	0.201	0.724	0.143	3.182	0.545	0.090	0.721	0.855	0.311
		75	1.305	0.194	0.540	0.237	2.409	0.560	0.100	0.726	0.578	0.511
		88	0.822	0.169	0.357	0.456	1.655	0.585	0.121	0.737	0.384	0.784
	2	34	3.282	0.150	1.235	0.076	5.742	0.529	0.080	0.714	2.661	-0.057
		48	2.242	0.371	0.941	0.156	4.051	0.531	0.080	0.715	0.614	0.361
		59	1.983	0.400	0.858	0.204	3.776	0.535	0.083	0.717	0.541	0.459
		64	1.755	0.267	0.728	0.157	3.161	0.537	0.083	0.717	0.588	0.383
		65	2.549	0.531	1.109	0.181	4.972	0.521	0.074	0.711	0.838	0.305
		75	2.555	0.392	1.061	0.175	4.519	0.528	0.079	0.714	0.671	0.369
		87	1.409	0.233	0.591	0.222	2.646	0.554	0.095	0.724	0.588	0.501
1.64	1	31	2.494	0.360	1.798	0.170	5.971	0.508	0.067	0.707	0.814	0.297
		41	2.259	0.134	1.508	0.073	5.416	0.515	0.071	0.709	2.005	-0.065
		53	3.194	0.432	2.285	0.141	7.451	0.500	0.063	0.704	0.838	0.241
		62	2.589	0.392	1.878	0.154	6.196	0.506	0.066	0.706	0.721	0.297
		75	2.438	0.415	1.797	0.174	5.963	0.513	0.070	0.709	0.641	0.361
		87	1.935	0.537	1.557	0.353	5.332	0.519	0.074	0.711	0.352	0.657
	2	32	2.698	0.406	1.956	0.167	6.426	0.513	0.071	0.709	0.706	0.337
		44	4.562	0.820	3.391	0.183	11.049	0.492	0.060	0.701	0.691	0.330

Bulk Solution pH	Cycle	RH (%)	$[HSO_4^-]$ (m)	$[SO_4^{2-}]$ (m)	$[Mg^{2+}]$ (m)	$[SO_4^{2-}]/[HSO_4^-]$	I	γ (HSO_4^-)	γ (SO_4^{2-})	$\gamma(H^+)$	$[H^+]$ (m)	Aerosol Particle pH
		56	4.168	0.975	3.240	0.266	10.761	0.501	0.065	0.704	0.493	0.504
		64	3.346	0.777	2.597	0.234	8.674	0.496	0.061	0.702	0.505	0.454
		70	4.299	1.163	3.441	0.286	11.579	0.491	0.059	0.700	0.442	0.524
		81	2.801	0.914	2.340	0.339	8.081	0.503	0.065	0.705	0.344	0.631
1.99	1	35	4.041	0.795	4.255	0.274	12.380	0.503	0.067	0.705	0.521	0.512
		46	3.332	1.100	3.900	0.403	11.840	0.489	0.058	0.700	0.350	0.651
		56	2.150	0.881	2.667	0.415	8.310	0.498	0.062	0.703	0.281	0.709
		67	1.511	0.769	2.007	0.689	6.408	0.512	0.069	0.708	0.199	0.920
		73	1.099	0.599	1.494	0.646	4.823	0.523	0.076	0.712	0.173	0.946
		77	0.965	0.535	1.320	0.777	4.272	0.532	0.081	0.716	0.160	1.022
		85	0.775	0.417	1.049	0.699	3.401	0.540	0.086	0.719	0.161	1.007
	2	39	2.795	0.744	3.114	0.279	9.332	0.497	0.062	0.703	0.440	0.526
		46	2.322	0.786	2.735	0.349	8.380	0.496	0.061	0.702	0.356	0.617
		59	1.732	0.837	2.260	0.484	7.176	0.502	0.064	0.704	0.233	0.786
		67	1.410	0.711	1.867	0.524	5.970	0.508	0.067	0.706	0.218	0.825
		78	1.184	0.670	1.631	0.734	5.281	0.518	0.073	0.710	0.175	0.968

Appendix E. Spectroscopic Determination of Aerosol pH from Acid-Base Equilibria in Inorganic, Organic, and Mixed Systems Supplemental Information[5]

E.1 Solution Preparation

To create a solution for each acid-base system, a salt containing the base was dissolved in solution and then mixed with a strong acid to control the pH. Table E.1 lists measured pH, the concentration of salt, and concentration of acid for each solution. The ratio of [ion]:[acid + conjugate base] that was used to determine the concentration of spectator ions (those not involved in the acid-base equilibrium) in each particle is also given.

Table E.1 Composition and pH of solutions used to generate particles for each acid-base system.

Acid-Base System	**pH**	**Salt**	**Acid**	**[ion]:[acid + conjugate base]**
HNO_3/NO_3^-	< 0*	0.085-0.096 M $NaNO_3$	8.81-9.63 M HNO_3	Na^+ - ~0.01:1
$HC_2O_4^-/C_2O_4^{2-}$	3.63	0.272 M $(NH_4)_2C_2O_4$	0.091 M HCl	NH_4^+ - 2:1 Cl^- - 0.33:1
	3.97	0.280 M $(NH_4)_2C_2O_4$	0.065 M HCl	NH_4^+ - 2:1 Cl^- - 0.23:1
HCH_3COO/CH_3COO^-	3.92	0.695 M $NaCH_3COO$	0.023 M HCl[#]	Cl^- - 0.03:1
HCO_3^-/CO_3^{2-}	10.47	0.038 M Na_2CO_3	0.010 M HCl	Na^+ - 2:1 Cl^- - 0.26:1
HSO_4^-/SO_4^{2-} & $HC_2O_4^-/C_2O_4^{2-}$	0.39	0.273 M $(NH_4)_2SO_4$, 0.273 M $(NH_4)_2C_2O_4$	0.795 M H_2SO_4	NH_4^+ - 0.81:1
	0.83	0.286 M $(NH_4)_2SO_4$, 0.286 M $(NH_4)_2C_2O_4$	0.476 M H_2SO_4	NH_4^+ - 1.09:1
	3.58	0.284 M $(NH_4)_2SO_4$, 0.283 M $(NH_4)_2C_2O_4$	0.057 M H_2SO_4	NH_4^+ - 1.82:1
	3.99	0.291 M $(NH_4)_2SO_4$, 0.291 M $(NH_4)_2C_2O_4$	0.033 M H_2SO_4	NH_4^+ - 1.89:1

*pH below measurement range of pH probe
[#]0.097 M HCH_3COO also added

E.2 Calibration Curves

[5] Appendix E details supplemental information corresponding to Chapter 6

Standard solutions were used to create calibration curves relating integrated peak area to concentration for each acid and conjugate base studied (Figures E.1-E.5). For all systems, the calibration curve for the base was created first. Then, to calibrate the acid species for the HNO_3/NO_3^-, HCO_3^-/CO_3^{2-}, HCH_3COO/CH_3COO^-, and HSO_4^-/SO_4^{2-} systems, the calibration curve for the base was used to determine [base] present in the acid-base equilibrium and subtracted from the total [acid + base] to determine [acid]. For the $HC_2O_4^-/C_2O_4^{2-}$ system, the acid calibration curve was created by relating the acid:total peak area ratio to the [acid]:[total acid + base] because of the close proximity of the analyzed vibrational modes. To confirm this method, the base:total peak area ratio related to the [base]:[total acid + base] was compared to the data for the $C_2O_4^{2-}$ calibration curve and was found to be consistent. To calibrate for $H_2C_2O_4$, HCl was added to standard solutions of $H_2C_2O_4$ to ensure the pH was low enough that $H_2C_2O_4$ was the only species present in the $H_2C_2O_4/ HC_2O_4^-$ equilibrium.

E.2.1. HNO_3/NO_3^-

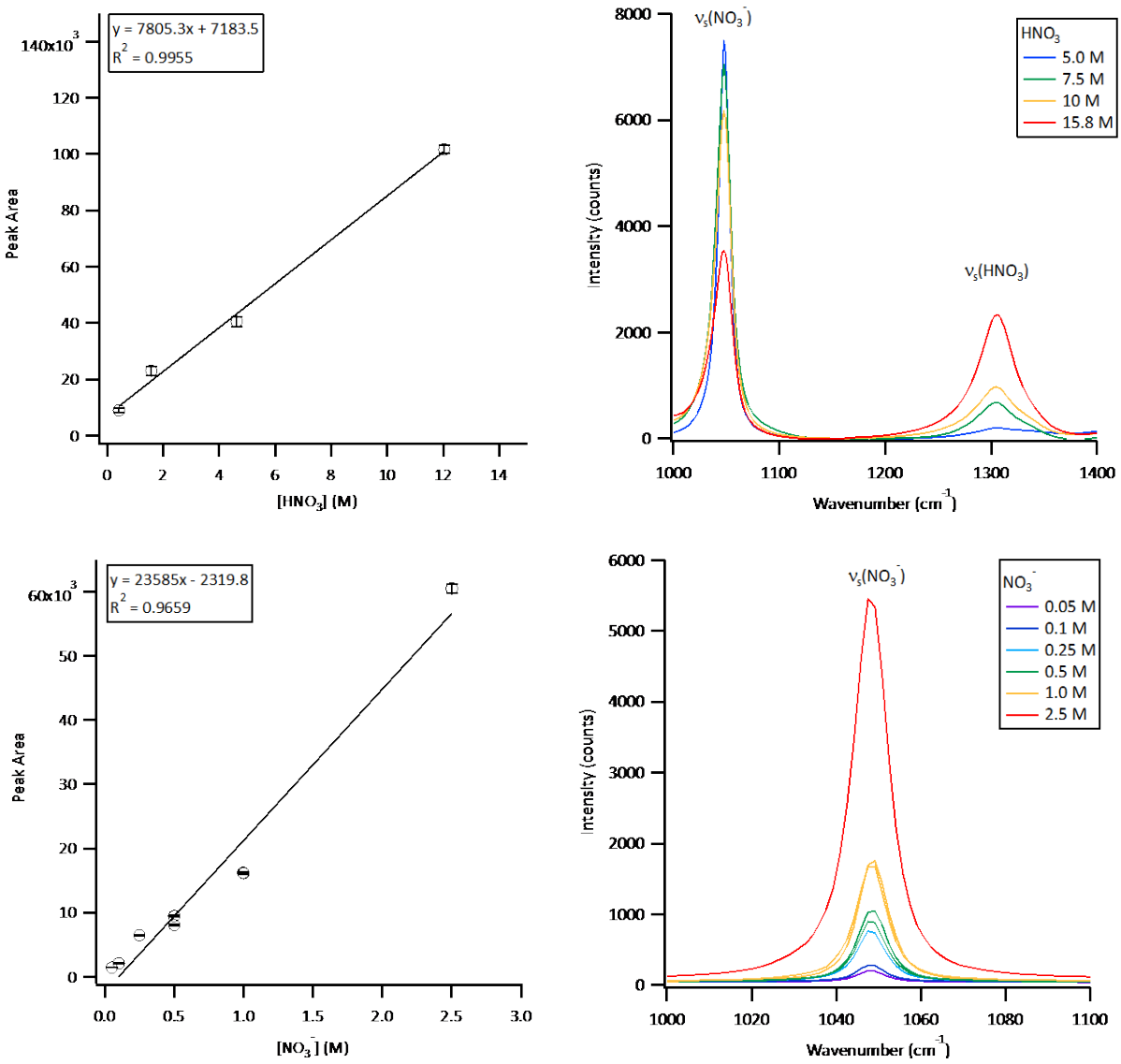

Figure E.1 Calibration curves relating integrated peak area to concentration for HNO_3 and NO_3^-, along with corresponding spectra for $\nu_s(NO_3^-)$ at 1047 cm^{-1} and $\nu_s(HNO_3)$ at 1306 cm^{-1}.

E.2.2. HCO_3^-/CO_3^{2-}

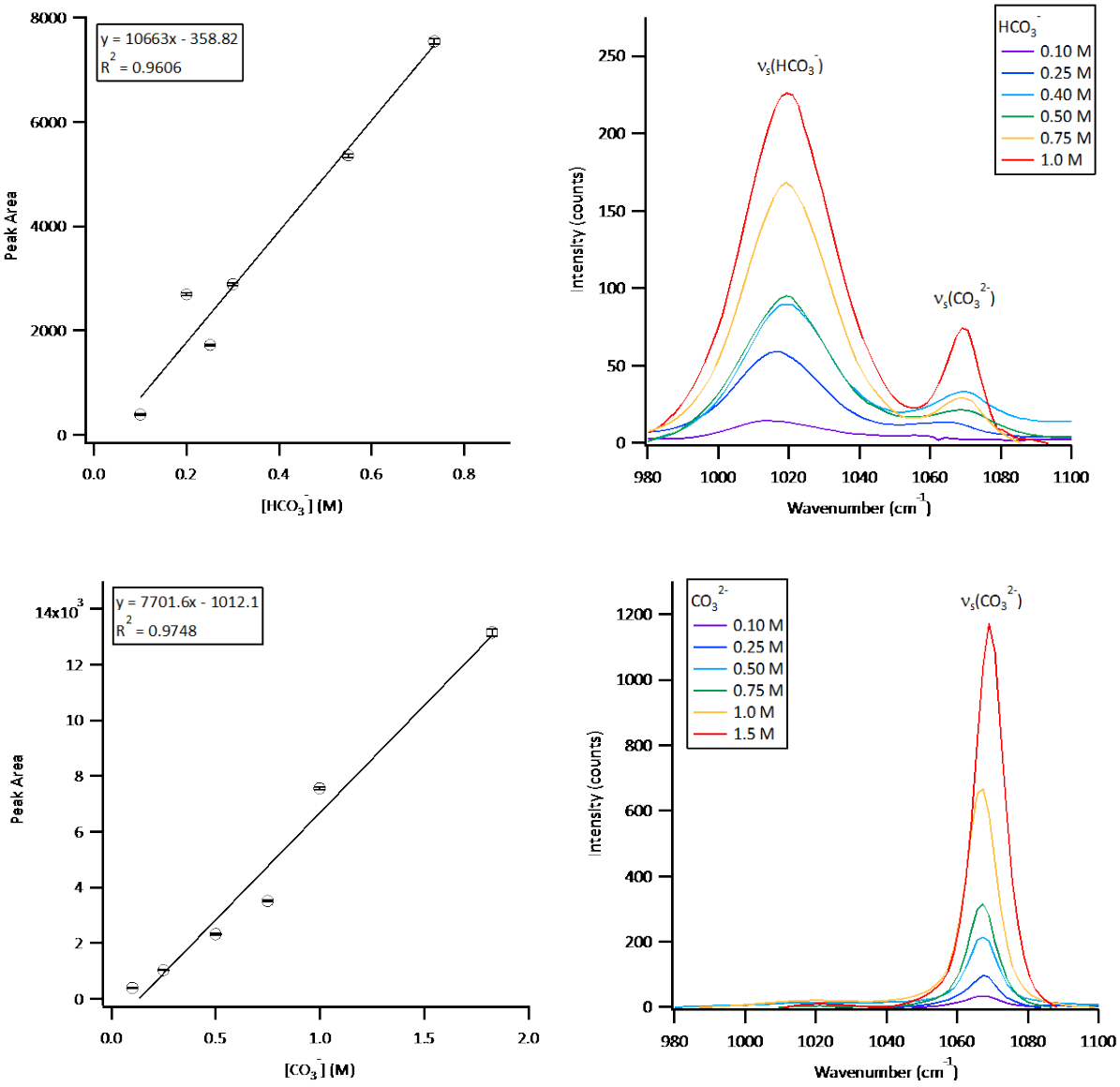

Figure E.2 Calibration curves relating integrated peak area to concentration for HCO_3^- and CO_3^{2-}, along with corresponding spectra for $\nu_s(CO_3^{2-})$ at 1067 cm^{-1} and $\nu_s(HCO_3^-)$ at 1019 cm^{-1}.

E.2.3. HSO_4^-/SO_4^{2-}

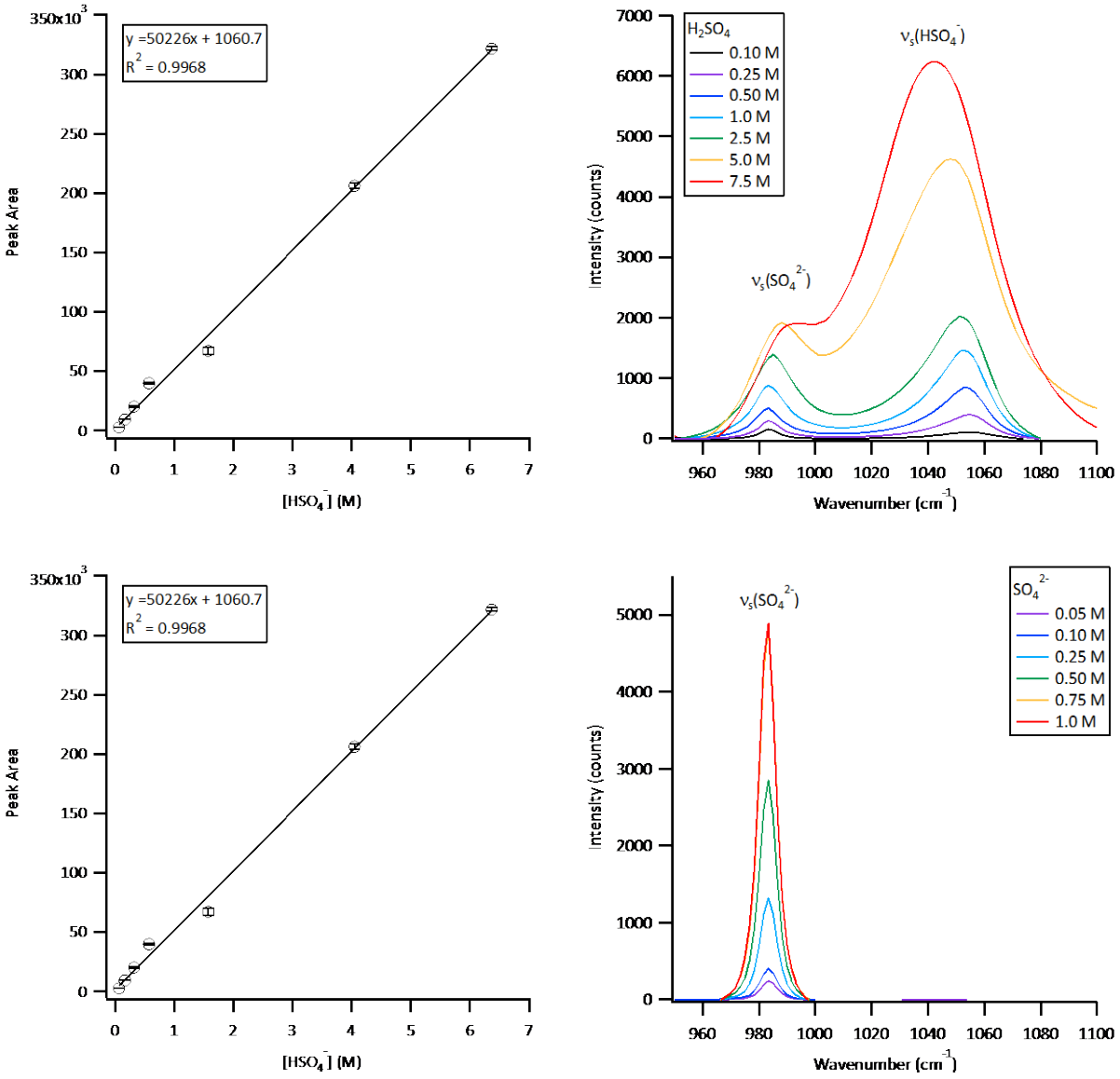

Figure E.3 Calibration curves relating integrated peak area to concentration for HSO_4^- and SO_4^{2-}, along with corresponding spectra for $\nu_s(SO_4^{2-})$ at 983 cm^{-1} and $\nu_s(HSO_4^-)$ at 1053 cm^{-1}.

E.2.4. $H_2C_2O_4/HC_2O_4^-/C_2O_4^{2-}$

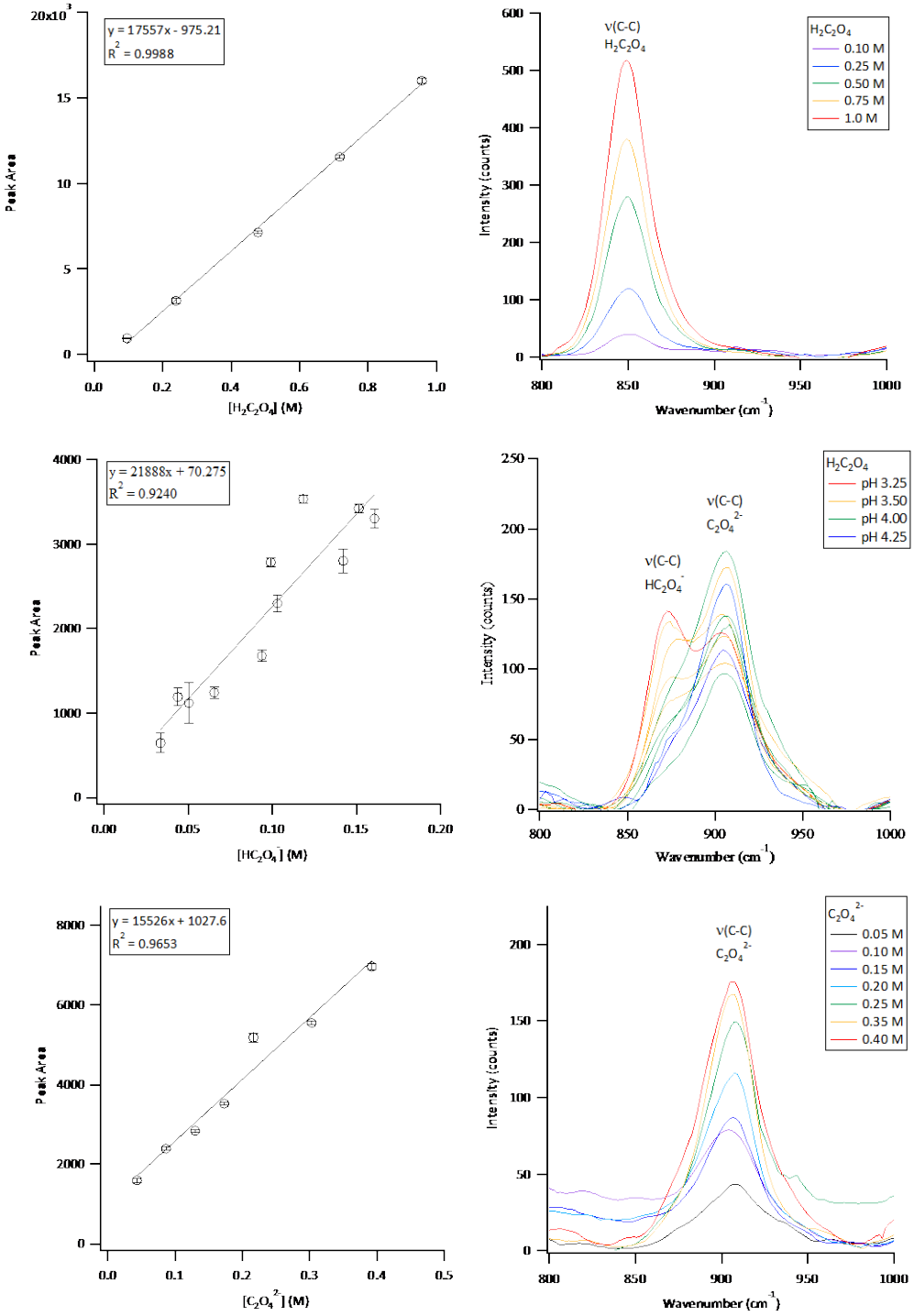

Figure E.4 Calibration curves relating integrated peak area to concentration for $H_2C_2O_4$, $HC_2O_4^-$, and $C_2O_4^{2-}$, along with corresponding spectra for ν(C-C) $H_2C_2O_4$ at 850 cm^{-1}, ν(C-C) $HC_2O_4^-$ at 873 cm^{-1}, and ν(C-C) $C_2O_4^{2-}$ at 907 cm^{-1}.

E.2.5. CH_3COOH/CH_3COO^-

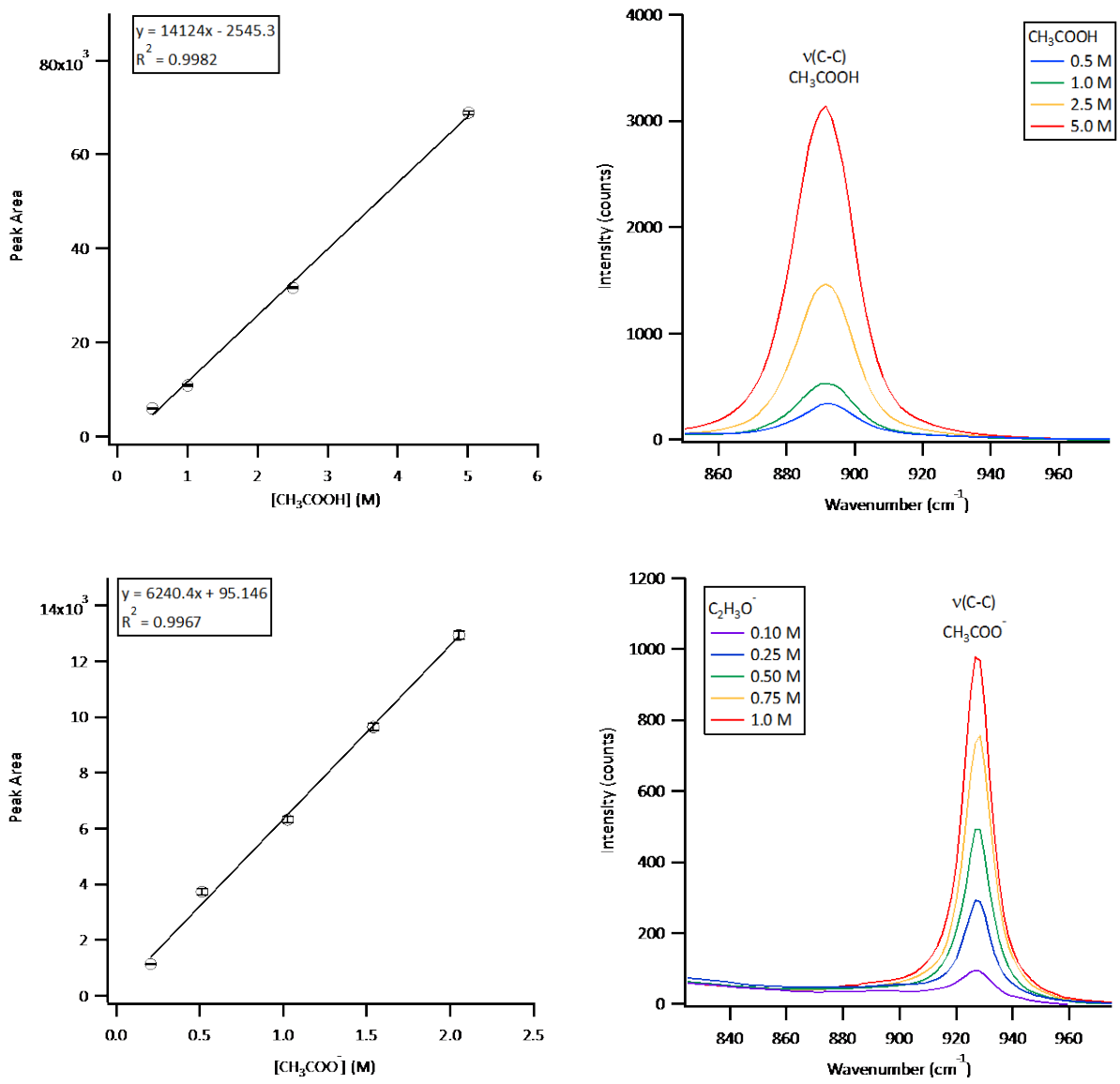

Figure E.5 Calibration curves relating integrated peak area to concentration for HCH_3COO and CH_3COO^-, along with corresponding spectra for ν(C-C) HCH_3COO at 890 cm^{-1} and ν(C-C) CH_3COO^- at 927 cm^{-1}.

E.3 Extended Debye-Hückel Relationship

The extended Debye-Hückel relationship (Equation 6.2) was applied to calculate the activity coefficient for each species in the acid-base equilibrium. In the extended Debye-Hückel relationship, *A* and *B* are constants characteristic of the solvent (water) and $å_i$ is the effective diameter of the ion in solution (Kielland, 1937; Garrels and Christ, 1965). The value for *A* 0.5085 and the value for *B* is $3.281x10^{-9}$. Values for $å_i$ are listed in Table B.2.

Table E.2 Effective diameter ($å_i$) values.

$å_i$ x 10^8	**Ion**
2.5	NH_4^+
3.0	Cl^-, NO_3^-
4.0	Na^+, HCO_3^-, HSO_4^-, SO_4^{2-}
4.5	CO_3^{2-}, $HC_2O_4^-$, $C_2O_4^{2-}$, CH_3COO^-
9	H^+

E.4 Particle pH Measurements

Although the aerosol particles studied for each system were all generated from the same solution, there was some variability in particle pH. Histograms for the measured particle pH for each acid-base system are given in Figure E.6.

A **B**

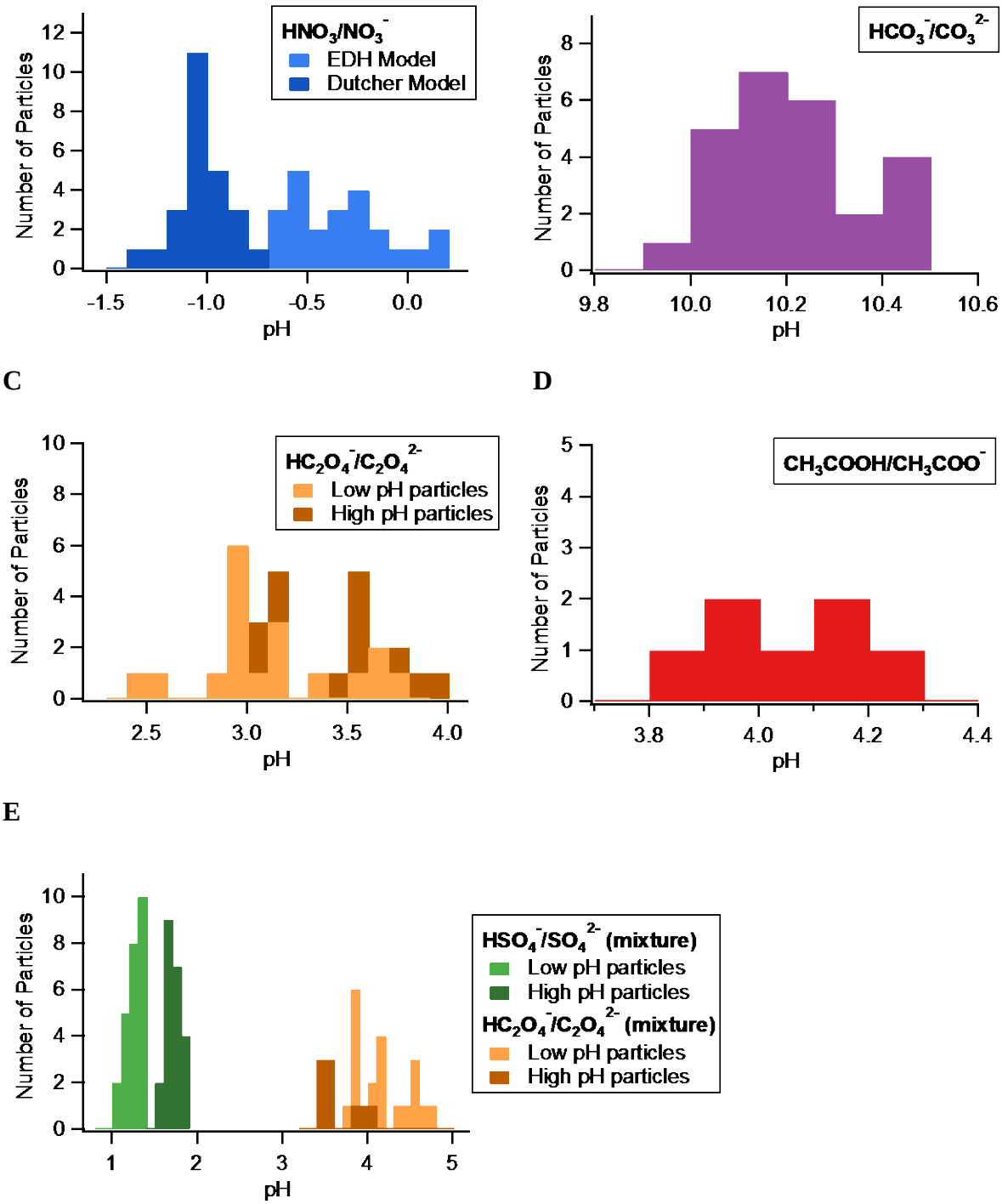

Figure E.6 Histograms for measured particle pH for A) HNO_3/NO_3^-, B) HCO_3^-/CO_3^{2-}, C) $HC_2O_4^-/C_2O_4^{2-}$, D) CH_3COOH/CH_3COO^-, and E) $HC_2O_4^-/C_2O_4^{2-}$ and HSO_4^-/SO_4^{2-} mixed acid-base equilibrium systems.

E.5 Oxalic Acid Measurements

To illustrate the challenges of using the $H_2C_2O_4/HC_2O_4^-$ equilibrium to determine aerosol particle pH, Figure E.7 shows Raman spectra of $H_2C_2O_4$, $HC_2O_4^-$, and $C_2O_4^{2-}$ standards, with the ν(C-C) mode for each of the compounds located at 850 cm^{-1}, 873 cm^{-1}, and 907 cm^{-1}, respectively. It is difficult to separate and accurately fit the ν(C-C) $H_2C_2O_4$ and ν(C-C) $HC_2O_4^-$ modes to determine their ion concentrations due to their close proximity (~20 cm^{-1}) and the shoulder-like nature of the ν(C-C) $HC_2O_4^-$ mode on the ν(C-C) $H_2C_2O_4$ mode.

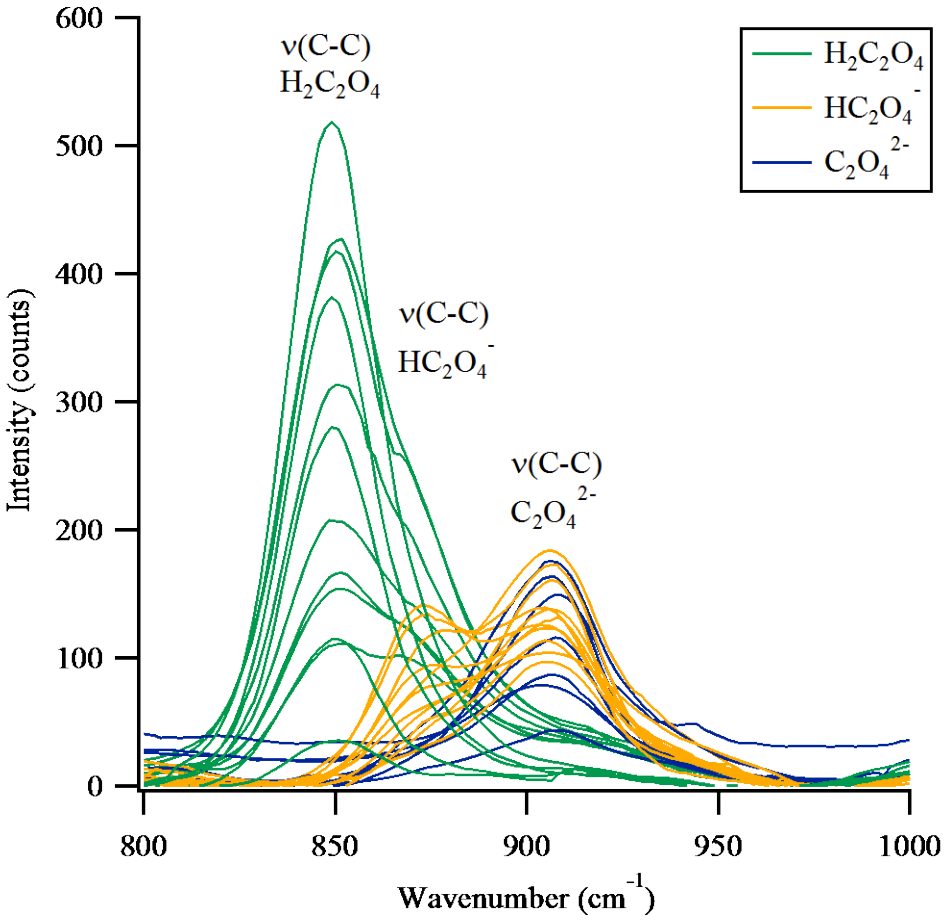

Figure E.7 Raman spectra of $H_2C_2O_4$ (green), $HC_2O_4^-$ (yellow), and $C_2O_4^{2-}$ (blue) standards.

E.6 Gas-Particle Partitioning

In contrast to the HNO_3/NO_3^- and CH_3COOH/CH_3COO^- equilibrium systems, the acid for the $HC_2O_4^-/C_2O_4^{2-}$ system, the $HC_2O_4^-/C_2O_4^{2-}$ and HSO_4^-/SO_4^{2-} mixed system, and the HCO_3^-/CO_3^{2-} system did partitioning from the particle to the gas phase. Representative Raman spectra showing this are given in Figure E.8 for the $HC_2O_4^-/C_2O_4^{2-}$ system and the $HC_2O_4^-/C_2O_4^{2-}$ and HSO_4^-/SO_4^{2-} mixed system. Spectra for the HCO_3^-/CO_3^{2-} system are not given, as low concentrations in the bulk solution did not provide visible intensity in the spectra.

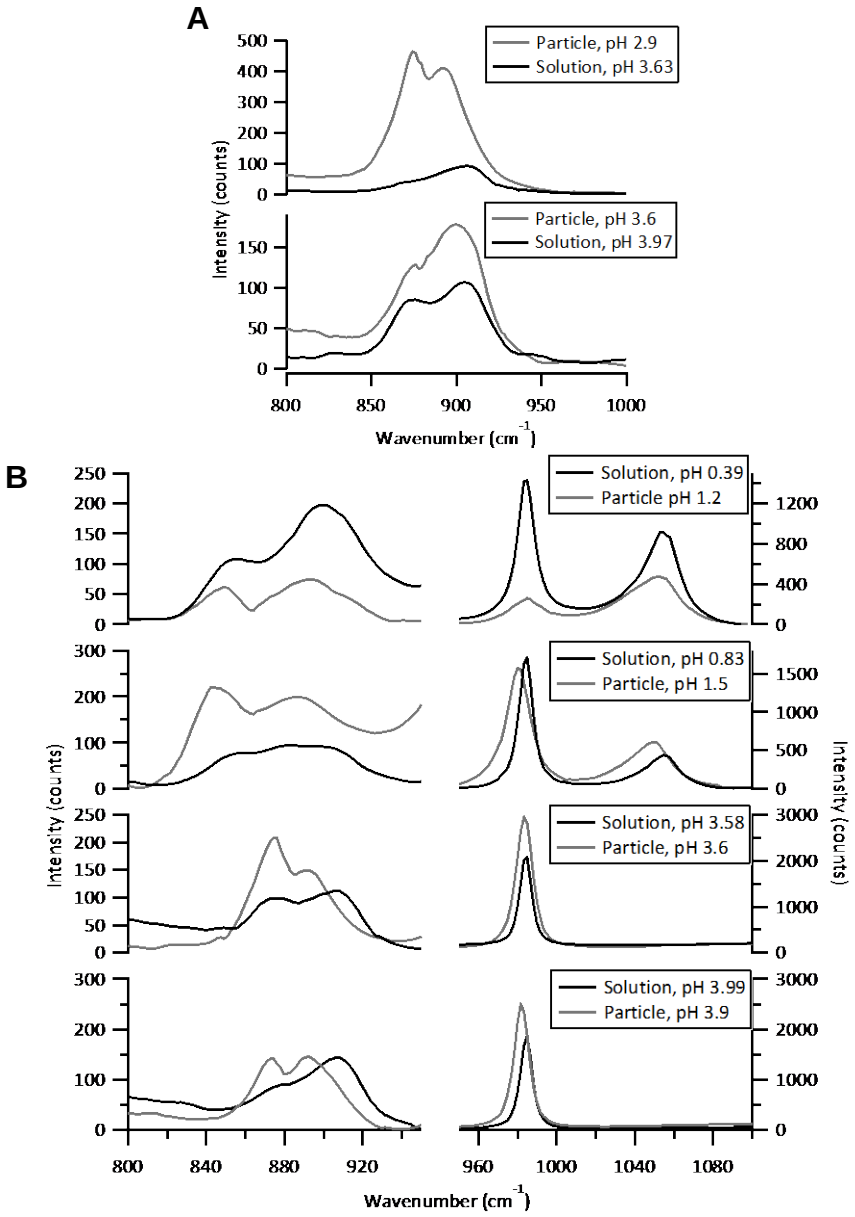

Figure E.8 Raman spectra of the bulk solution and representative particles for A) the $HC_2O_4^-/C_2O_4^{2-}$ system and B) the $HC_2O_4^-/C_2O_4^{2-}$ and HSO_4^-/SO_4^{2-} mixed system.

E.7 Dutcher Model

For improved predictions of pH for particles of the high ionic strength HNO_3/NO_3^- system, the multilayer adsorption isotherm based model from Dutcher et al. was used (Dutcher et al., 2013). The model includes arbitrary number of adsorbed monolayers and uses a power law relationship for aqueous solutions to determine adsorption energy parameter of water molecules with a solute by adjusting two parameters. The model (equations 27 and 28 in Dutcher et al.) (Dutcher et al., 2013) is used for finding the molalities and activities of the solutes present as a function of water activities, and subsequently the activities of the ions are determined. Treating RH data as equivalent to water activity and using it as input to the model, the molalities and activities of the solutes are calculated. Alternatively, using both RH data and the measured (converted) molality data, the model calculated the activities of each solute present in the solution mixture. The difference in pH using both methods for the nitrate system is not significant. However, the results shown in this work are from the latter method where the measured RH and concentration data were input to the model. For the HNO_3/NO_3^- particles, the activity of the acid (HNO_3) is found by the model, and the activity of the conjugate base ion (NO_3^-) is found by Equation E.1. Then, Equation 6.3 is finally used to determine the activity of the H^+, and therefore pH by Equation 6.4.

Equation E.0.1

$$a_{NO3-} = \sqrt{a_{HNO3} . a_{NaNO3}} .$$

E.8 Density Function Theory (DFT) Calculation

DFT optimization and frequency calculations were performed for $HC_2O_4^-$ and $C_2O_4^{2-}$ to investigate the behavior and potential coupling of the ν(C-C) vibrational mode. An optimization calculation was first performed using the B3LYP method with 3-21G basis set, following by an optimization and frequency calculation using the B3LYP method with 6-311G basis set (++, 2d, p). Both calculations were performed with water as the designated solvent. The calculations revealed that the ν(C-C) mode is coupled to the δ(O-C-O) bend for both ions, which for $HC_2O_4^-$, protonation and hydrogen bonding interactions, could contribute to the broadening of the corresponding peak with decreasing aerosol particle pH.

E.9 Particle pH and Peak Broadness Correlations

As discussed in the paper, the relationship between aerosol particle pH and the peak broadness of the all acid and base vibrational modes was explored. The correlation (r) values for this relationship for all inorganic and organic species analyzed are given in Table E.3. Figure E.9 shows aerosol particle pH as a function of the full width half maximum (fwhm) for the $\nu_s(HSO_4^-)$ and $\nu_s(SO_4^{2-})$, with data from both this study and Rindelaub et al. to confirm that there is no trend between aerosol particle pH and the broadness of the peak corresponding to $\nu_s(SO_4^{2-})$ (Rindelaub et al., 2016a).

Table E.3 Correlation (r) values for aerosol particle pH with peak broadness (fwhm) for the acid and base species for each acid-base system.

	Acid		**Base**	
	Mode	**r value**	**Mode**	**r value**
Inorganic	$\nu_s(HCO_3^-)$	-0.927	$\nu_s(CO_3^{2-})$	-0.265
	$\nu_s(HSO_4^-)$	-0.532*	$\nu_s(SO_4^{2-})$	-0.848[#]
	$\nu_s(HNO_3)$	-0.729	$\nu_s(NO_3^-)$	-0.152
Organic	ν(C-C) CH_3COOH	-0.683	ν(C-C) CH_3COO^-	0.548
	ν(C-C) $HC_2O_4^-$	-0.513	ν(C-C) $C_2O_4^{2-}$	0.714

*r = -0.659 when data from Rindelaub et al. is also included.
[#]r = -0.471 when data from Rindelaub et al. is also included.

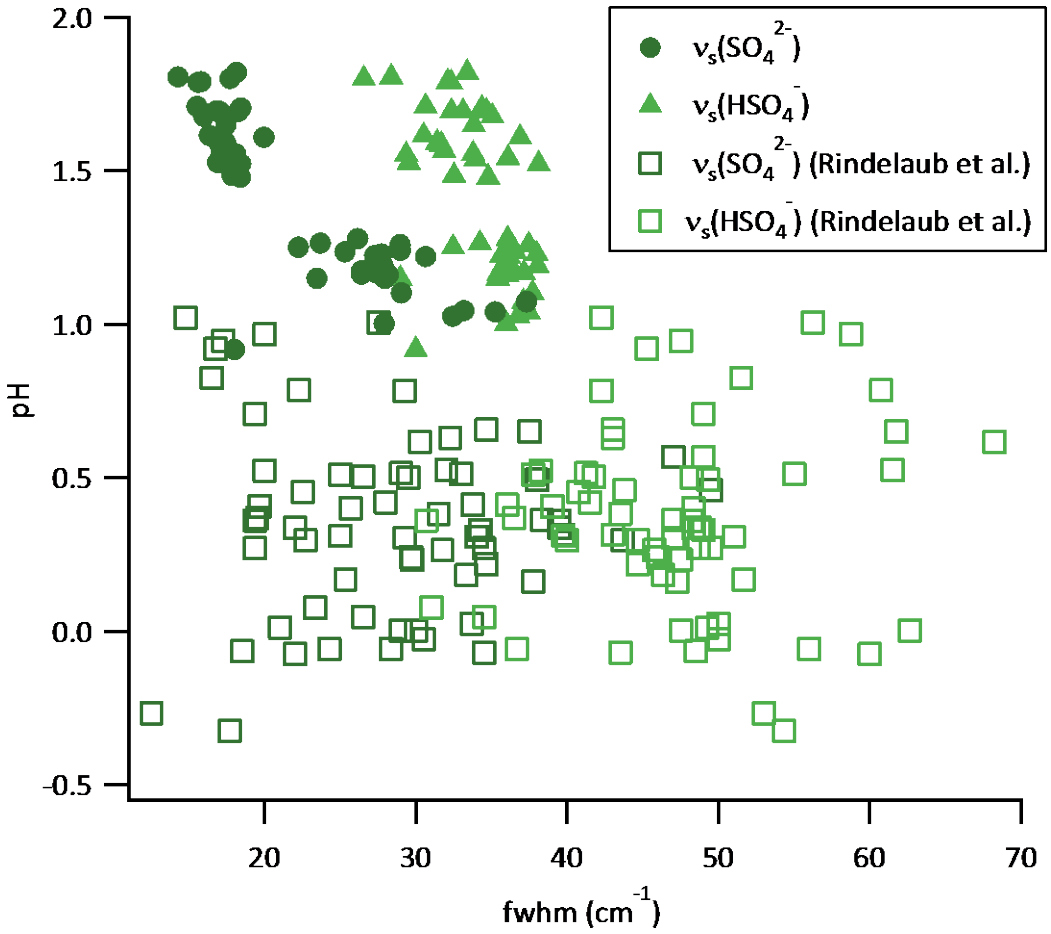

Figure E.9 Aerosol particle pH as a function of full width half maximum (fwhm) for the $\nu_s(SO_4^{2-})$ and $\nu_s(HSO_4^-)$ vibrational modes, with data from this study as well as from Rindelaub et al. (Rindelaub et al., 2016a).

Appendix F. Direct Determination of Aerosol pH: Size-Resolved Measurements of Submicron and Supermicron Aqueous Particles Supplemental Information[6]

F.1 pH Measurements of $(NH_4)_2SO_4$-H_2SO_4 Standard Solutions

pH indicator paper measurements of bulk solution standards of $(NH_4)_2SO_4$-H_2SO_4 of varying pH were compared to pH probe measurements to confirm the accuracy of the pH indicator paper method (Figure F.1). Good agreement was observed between the two pH measurement techniques. The pH indicator paper measurements showed slight deviation when approaching the limits of each paper's respective pH range, due to the pK_a values of the indicator dye in the paper. For the pH 0-2.5 paper, the indicator dye is thymol blue with a pK_a of 1.7 and for the pH 2.5-4.5 paper, the indicator dye is methyl orange with a pK_a of 3.47. At pH values at the limits of the indicator range, the dye is less effective, leading to pH measurements that may be slightly less accurate. Overall, the pH indicator paper measurements were both accurate and precise through multiple trials with each solution.

[6] Appendix F details supplemental information corresponding to Chapter 7

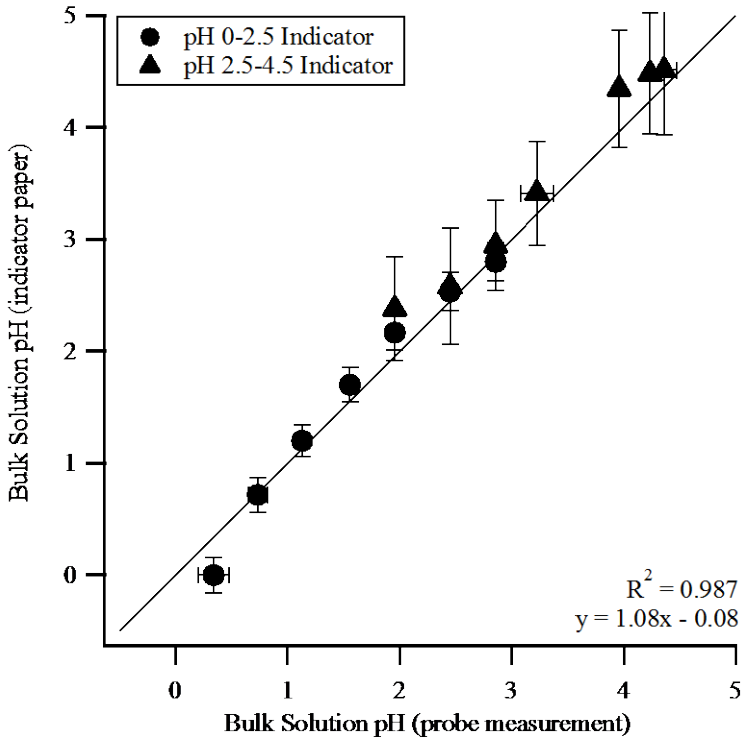

Figure F.1 Bulk solution pH as determined by pH indicator paper measurements in comparison to bulk solution pH measured by a pH probe. The solid line represents 1:1.

F.2 Correction Factor for pH Measurements with pH 2.5-4.5 Indicator Paper

pH measurements made with the pH 2.5-4.5 indicator paper showed a bias for consistently underestimating pH for the $(NH_4)_2SO_4$-H_2SO_4 solutions as well as hydrochloric acid (HCl) standard solutions (Figure F.2). The pH measurements for the HCl standards were fitted with a linear regression and a correction factor offsetting the y-intercept of the regression was applied, bringing the pH measurements into good agreement with the pH measurements via probe analysis. The y-intercept correction factor of -0.319 was applied to all subsequent pH measurements with the pH 2.5-4.5 indicator paper.

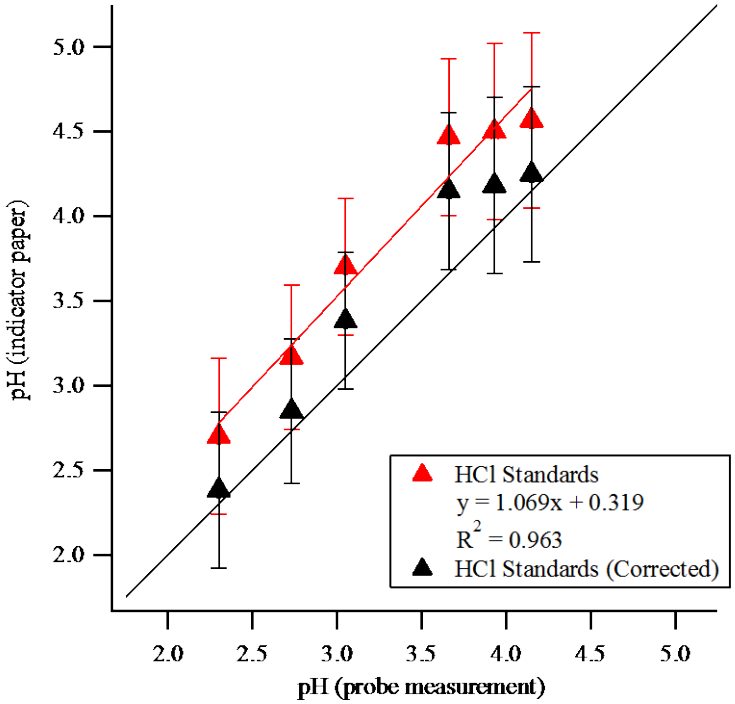

Figure F.2 Bulk solution pH measurements via pH 2.5-4.5 indicator paper as a function of bulk solution pH measurements via pH probe for HCl standard solutions.

F.3 Blank Aerosol Testing with pH Indicator Paper

To confirm the color change on the pH indicator paper was due to aerosol particles rather than gas or water vapor, an aerosol blank in which the particles were filtered out using a HEPA filter was collected and there was no observed color change on the pH indicator paper (Figure F.3). pH 0.5, 2, and 3 systems were tested.

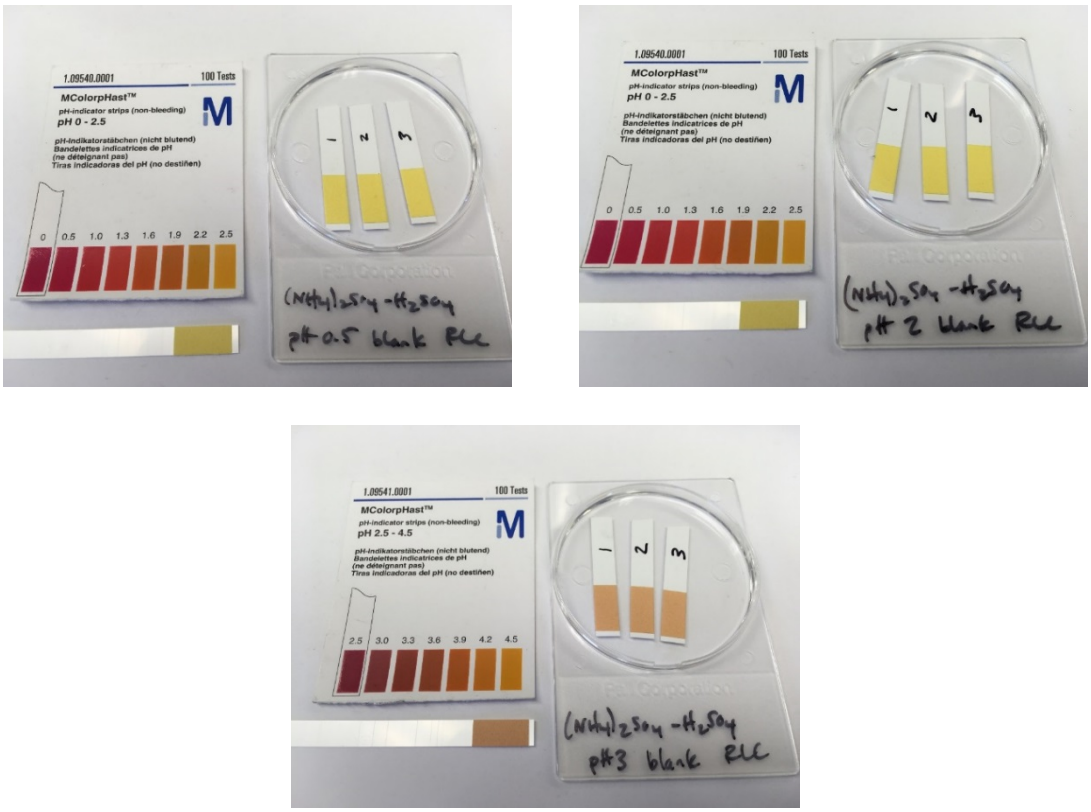

Figure F.3 Images of pH 0.5, 2, 3 systems tested with aerosol particles filtered out to determine influence of gases and/or water vapor on pH indicator paper color changes.

F.4 pH Indicator Paper Testing with Various Aqueous Inorganic Ion Systems

Systems of varying inorganic ion composition and pH were also tested with the pH 0-2.5 indicator paper to confirm its accuracy and applicability to a range of chemical compositions common in atmospheric aerosol particles (Figure F.4). Aerosol particle chemical compositions included $MgSO_4$-H_2SO_4, Na_2SO_4-H_2SO_4, Na_2CO_3-HCl, $NaNO_3$-HNO_3, and NH_4NO_3-HNO_3.

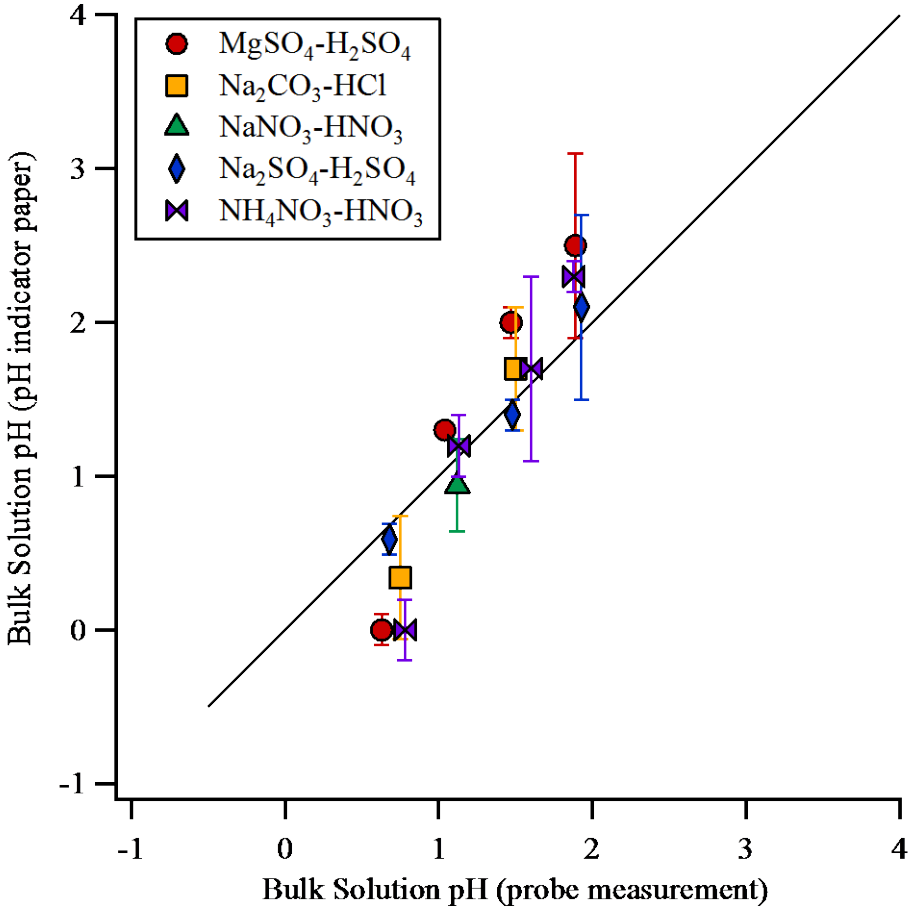

Figure F.4 Bulk solution pH as measured by pH indicator paper compared to bulk solution pH as measured by pH probe for systems of various inorganic ion composition.

F.5 Raman Analysis

Raman spectra for individual impacted particles were collected using a LabRAM HR Evolution Raman microspectrometer (Horiba, Ltd.) equipped with a Nd:YAG laser source (50 mW, 532 nm) and CCD detector, and coupled with a confocal optical microscope (100x 0.9 N.A. SLMPlan N Olympus objective). The instrument was calibrated against the Stokes Raman signal of pure Si at 520 cm^{-1} using a silicon wafer standard. Spectra from 500 to 1400 cm^{-1} were acquired for 15 s with three accumulations. A 600 groove/mm diffraction grating yielded spectral resolution of ~1.7 cm^{-1}. Spectra were collected at ambient temperature and RH (~35% or ~60%). Though the aerodynamic diameter for particles collected on the smallest stage (< 0.4 μm) is below the typical detectable particle size due to the diffraction limit of visible light and the 532

nm laser for the 100x objective, aqueous particles spread when impacted, causing a larger projected area diameter, which can be observed with typical spreading ratios (Sobanska et al., 2014; Bondy et al., 2017a).

F.6 Raman Spectra for Small, Medium, and Large Particle Sizes Under Various pH Conditions

Raman spectra were collected for aerosol particles of various sizes corresponding to the pH indicator paper measurement size ranges to further investigate the trend of increasing particle acidity with decreasing particle size. Figure F.5 shows spectra normalized to the $\nu(HSO_4^-)$ mode for the pH 0.15, pH 0.80, pH 1.01, pH 1.31, and pH 1.78 systems.

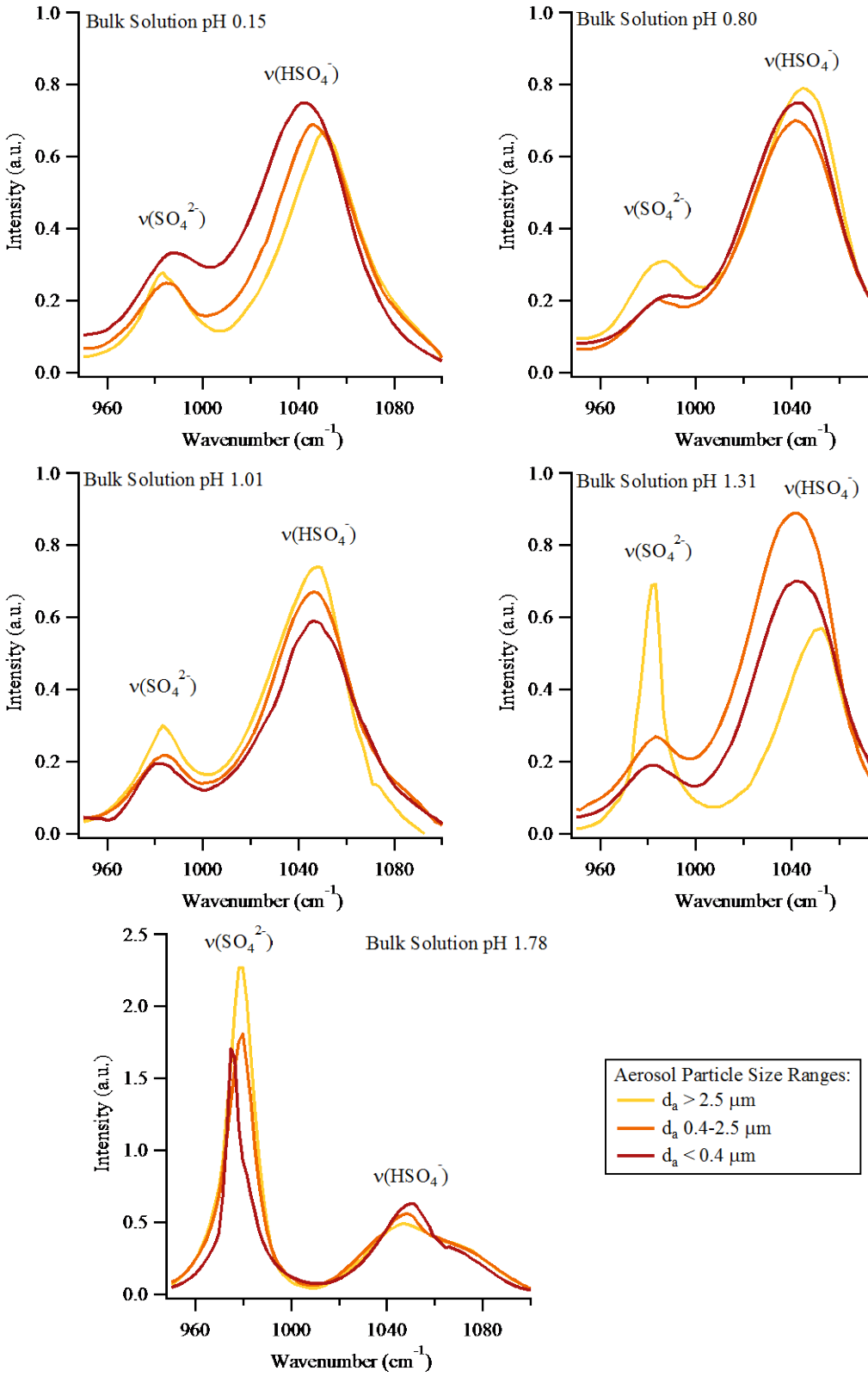

Figure F.5 Raman spectra normalized to the $\nu(HSO_4^-)$ mode for particles of various sizes generated from solution with pH ranging from 0.15 to 1.78.

F.7 Water Content Fraction and Particle Mass Limit Calculations

Water content fraction by mass for each size range of particles for several pH systems was calculated based on comparison of mass concentration size distributions at wet and dry RH conditions. Particle mass from the mass concentration size distribution was summed for all bins within a given particle size range for a wet and then dry RH condition. Then water content fraction was calculated by dividing the difference between wet and dry condition masses (m_{wet} and m_{dry}, respectively) by the wet condition mass, according to Equation F.1.

Equation F.0.1

$$\text{Water content fraction} = \frac{(m_{wet} - m_{dry})}{m_{wet}}$$

Water content fraction values, along with minimum particle mass needed to induce a measureable color change and average particle density, for several pH systems is provided in Table F.1. Minimum particle mass was calculated by again summing the mass from mass concentration size distributions for all bins within a given particle size range and then multiplying by sampling time to determine total mass of particles impacted.

Table F.1 Minimum particle mass, water content fraction, and average particle density for particles of various sizes for a range of pH systems.

		Bulk Solution pH				
		0.15	**1.31**	**1.77**	**2.96**	**3.86**
Particles d_a < 0.4 µm	**Mass (µg)**	50.8 ± 9.7	14.5 ± 0.2	25.6 ± 0.5	63.9 ± 4.0	82.9 ± 2.2
	Water Content Fraction	0.610 ± 0.225	0.814 ± 0.022	0.784 ± 0.027	0.804 ± 0.081	0.792 ± 0.034
	Average Particle Density (kg/m^3)	1040.8 ± 21.8	1056.5 ± 3.9	1048.1 ± 3.6	-	-
Particles d_a 0.4 µm – 2.5 µm	**Mass (µg)**	74.4 ± 5.2	30.1 ± 1.3	49.0 ± 0.8	114.5 ± 6.	159.3 ± 6.7
	Water Content Fraction	0.745 ± 0.091	0.729 ± 0.060	0.690 ± 0.064	0.693 ± 0.077	0.733 ± 0.056
	Average Particle Density (kg/m^3)	1016.8 ± 1.8	1040.7 ± 3.9	1034.3 ± 3.0	-	-
Particles d_a > 2.5 µm	**Mass (µg)**	67.4 ± 1.1	294.9 ± 19.9	584.1 ± 6.7	1565.5 ± 59.2	2560.0 ± 180.3
	Water Content Fraction	0.629 ± 0.070	0.992 ± 0.095	0.996 ± 0.016	0.997 ± 0.053	0.998 ± 0.100
	Average Particle Density (kg/m^3)	1018.6 ± 1.4	1025.4 ± 3.6	1022.9 ± 2.1	-	-

F.8 Thermodynamic Modeling

Thermodynamic models commonly used to predict aerosol acidity, such as E-AIM II (Clegg et al., 1992, 1998; Carslaw et al., 1995; Wexler and Clegg, 2002) and ISORROPIA-II (Nenes et al., 1998; Fountoukis and Nenes, 2007) use model inputs of temperature, RH, and chemical concentrations such as ammonium and sulfate. However, bisulfate concentrations – like those measured here – cannot be input independently into the models. If spectroscopically measured sulfate (SO_4^{2-}) and bisulfate (HSO_4^-) concentrations are combined and used as the nominal sulfate concentration input, an ion balance needed to run E-AIM would lead to erroneously high values of the input H^+ concentration. The users' input conditions may lead to an over-prediction in acidity when running the model. Indeed, Figure F.7 shows that when run in this manner, both models over predicted aerosol acidity, resulting in pH values ~1 – 2.5 pH units lower than the direct aerosol pH measurements. Again, this is most likely due to the challenges of accurately representing bisulfate and, possibly, in distinguishing between free and bound protons (H^+ vs HSO_4^-) within the model. These results illustrate the benefit of direct measurements of aerosol pH, at both the bulk and single particle level, to compare to and help constrain model predictions. Details on how the models were run and additional assumptions model are provided below for each model.

F.8.1 E-AIM.

E-AIM Model II (Clegg et al., 1992, 1998; Carslaw et al., 1995; Wexler and Clegg, 2002) (http://www.aim.env.uea.ac.uk/aim/aim.php) was used to determine bulk solution pH as well as aerosol pH for individual particles for each pH system. For bulk solution pH, model inputs included concentration of SO_4^{2-}, NH_4^+, and H^+. For aerosol pH, model inputs included temperature, relative humidity, and concentration of SO_4^{2-}, NH_4^+, and H^+. [SO_4^{2-}] was determined by combining spectroscopically measured concentrations of SO_4^{2-} and HSO_4^-. The ratio of [NH_4^+] to ([SO_4^{2-}] + [HSO_4^{2-}]) in each bulk solution was used to determine [NH_4^+] in the particles based on the measured [SO_4^{2-}] and [HSO_4^{2-}], in the same manner as Rindelaub et al. and Craig et al. (Rindelaub et al., 2016a; Craig et al., 2017b) The [H^+] input was determined from an ion balance with [SO_4^{2-}] and [NH_4^+]. Formation of all solids was prevented for each calculation. pH was then calculated from model determined [$H^+_{(aq)}$] (m) and activity coefficient according to Eq. F.2 (Figure F.6 and F.7).

Equation F.0.2 $$pH = -log([H^+] * \gamma_{H^+})$$

F.8.2 ISORROPIA-II.

ISORROPIA-II (Nenes et al., 1998; Fountoukis and Nenes, 2007) (http://nenes.eas.gatech.edu/ISORROPIA) was also used to determine aerosol pH for individual particles for each pH system. Model inputs included temperature, relative humidity, and concentration of SO_4^{2-} and NH_4^+. Similar to the concentration inputs for E-AIM, $[SO_4^{2-}]$ was determined by combining spectroscopically measured concentrations of SO_4^{2-} and HSO_4^-. The ratio of $[NH_4^+]$ to $([SO_4^{2-}] + [HSO_4^{2-}])$ in each bulk solution was used to determine $[NH_4^+]$ in the particles based on the measured $[SO_4^{2-}]$ and $[HSO_4^{2-}]$. Certainly, the model predictions are more accurate when inputs of both aerosol and gas phase chemical species are included (Hennigan et al., 2015; Murphy et al., 2017). However, with only aerosol phase concentration measurements, ISORROPIA-II was run in the reverse mode and to prevent precipitation of salts, the metastable state was specified. pH was calculated directly by the model (Figure F.7). In particular, differences between the ISORROPIA-II model and measurements shown here may be attributable to differences in the $[HSO_{4\,(aq)}^-]$ and $[SO_{4\,(aq)}^{2-}]$ ratios.

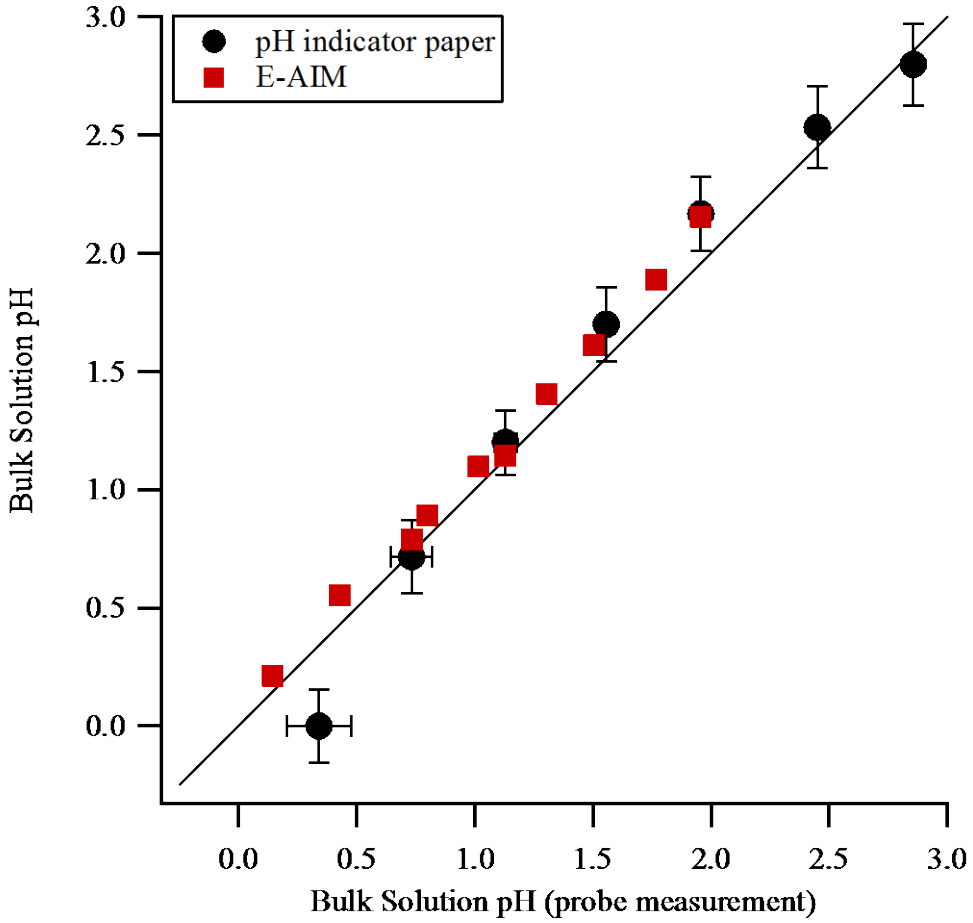

Figure F.6 Comparison of pH indicator paper measurements and E-AIM calculated pH with pH probe measurements for the bulk solutions from which the aerosol particles were generated.

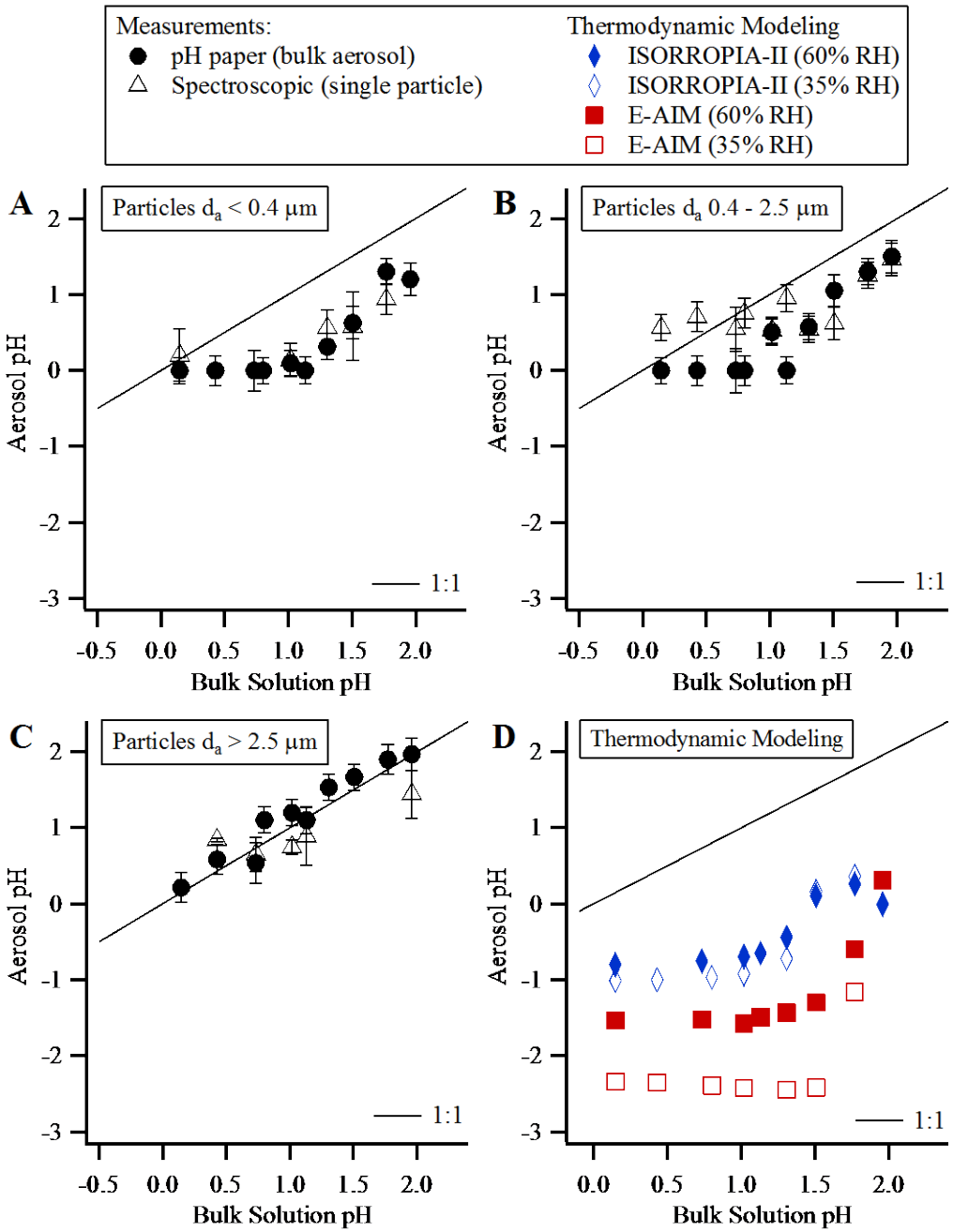

Figure F.7 Aerosol pH as a function of the pH of the bulk solution from which the particles were generated for particles (A) d_a < 0.4 µm, (B) d_a 0.4-2.5 µm, and (C) d_a > 2.5 µm, as measured by the pH indicator paper and Raman microspectroscopic methods, and (D) calculated by E-AIM and ISORROPIA-II thermodynamic models. Error bars for the pH indicator paper data correspond to uncertainty in the measurements across multiple trials. Error bars for the Raman spectroscopic data corresponds to standard deviation of multiple trials. On all graphs, the solid black line represents 1:1.

References

Abel, S. J.; Haywood, J. M.; Highwood, E. J.; Li, J.; Buseck, P. R. Evolution of Biomass Burning Aerosol Properties from an Agricultural Fire in Southern Africa. *Geophys. Res. Lett.* **2003**, *30* (15), 1783.

Alexander, D. T. L.; Crozier, P. A.; Anderson, J. R. Brown Carbon Spheres in East Asian Outflow and Their Optical Properties. *Science (80-.).* **2008**, *321* (5890), 833–836.

Allen, H. M.; Draper, D. C.; Ayres, B. R.; Ault, A.; Bondy, A.; Takahama, S.; Modini, R. L.; Baumann, K.; Edgerton, E.; Knote, C.; et al. Influence of Crustal Dust and Sea Spray Supermicron Particle Concentrations and Acidity on Inorganic NO3- Aerosol during the 2013 Southern Oxidant and Aerosol Study. *Atmos. Chem. Phys.* **2015**, *15* (18), 10669–10685.

Andreae, M. O.; Rosenfeld, D. Aerosol-Cloud-Precipitation Interactions. Part 1. The Nature and Sources of Cloud-Active Aerosols. *Earth-Science Rev.* **2008**, *89* (1–2), 13–41.

Ault, A. P.; Axson, J. L. Atmospheric Aerosol Chemistry: Spectroscopic and Microscopic Advances. *Anal. Chem.* **2017**, *89* (1), 430–452.

Ault, A. P.; Peters, T. M.; Sawvel, E. J.; Casuccio, G. S.; Willis, R. D.; Norris, G. A.; Grassian, V. H. Single-Particle SEM-EDX Analysis of Iron-Containing Coarse Particulate Matter in an Urban Environment: Sources and Distribution of Iron within Cleveland, Ohio. *Environ. Sci. Technol.* **2012**, *46* (8), 4331–4339.

Ault, A. P.; Guasco, T. L.; Ryder, O. S.; Baltrusaitis, J.; Cuadra-Rodriguez, L. A.; Collins, D. B.; Ruppel, M. J.; Bertram, T. H.; Prather, K. A.; Grassian, V. H. Inside versus Outside: Ion Redistribution in Nitric Acid Reacted Sea Spray Aerosol Particles as Determined by Single Particle Analysis. *J. Am. Chem. Soc.* **2013a**, *135* (39), 14528–14531.

Ault, A. P.; Zhao, D.; Ebben, C. J.; Tauber, M. J.; Geiger, F. M.; Prather, K. A.; Grassian, V. H. Raman Microspectroscopy and Vibrational Sum Frequency Generation Spectroscopy as Probes of the Bulk and Surface Compositions of Size-Resolved Sea Spray Aerosol Particles. *Phys. Chem. Chem. Phys.* **2013b**, *15* (17), 6206–6214.

Ault, A. P.; Moffet, R. C.; Baltrusaitis, J.; Collins, D. B.; Ruppel, M. J.; Cuadra-Rodriguez, L. A.; Zhao, D.; Guasco, T. L.; Ebben, C. J.; Geiger, F. M.; et al. Size-Dependent Changes in Sea Spray Aerosol Composition and Properties with Different Seawater Conditions. *Environ. Sci. Technol.* **2013c**, *47* (11), 5603–5612.

Ault, A. P.; Guasco, T. L.; Baltrusaitis, J.; Ryder, O. S.; Trueblood, J. V; Collins, D. B.; Ruppel, M. J.; Cuadra-Rodriguez, L. A.; Prather, K. A.; Grassian, V. H. Heterogeneous Reactivity of Nitric Acid with Nascent Sea Spray Aerosol: Large Differences Observed between and within Individual Particles. *J. Phys. Chem. Lett.* **2014**, *5* (15), 2493–2500.

Avzianova, E.; Brooks, S. D. Raman Spectroscopy of Glyoxal Oligomers in Aqueous Solutions. *Spectrochim. Acta Part A Mol. Biomol. Spectrosc.* **2013**, *101*, 40–48.

Axson, J. L.; May, N. W.; Colón-Bernal, I. D.; Pratt, K. A.; Ault, A. P. Lake Spray Aerosol: A Chemical Signature from Individual Ambient Particles. *Environ. Sci. Technol.* **2016a**, *50* (18), 9835–9845.

Axson, J. L.; Shen, H.; Bondy, A. L.; Landry, C. C.; Welz, J.; Creamean, J. M.; Ault, A. P.

Transported Mineral Dust Deposition Case Study at a Hydrologically Sensitive Mountain Site: Size and Composition Shifts in Ambient Aerosol and Snowpack. *Aerosol Air Qual. Research* **2016b**, *16* (3), 555–567.

Ayora, M. J.; Ballesteros, L.; Perez, R.; Ruperez, A.; Laserna, J. J. Detection of Atmospheric Contaminants in Aerosols by Surface-Enhanced Raman Spectrometry. *Anal. Chim. Acta* **1997**, *355*, 15–21.

Batonneau, Y.; Sobanska, S.; Laureyns, J.; Bremard, C. Confocal Microprobe Raman Imaging of Urban Tropospheric Aerosol Particles. *Environ. Sci. Technol.* **2006**, *40* (4), 1300–1306.

Battaglia, M. A.; Douglas, S.; Hennigan, C. J. Effect of the Urban Heat Island on Aerosol pH. *Environ. Sci. Technol.* **2017**, *51* (22), 13095–13103.

Bauer, S. E.; Ault, A.; Prather, K. A. Evaluation of Aerosol Mixing State Classes in the GISS modelE-MATRIX Climate Model Using Single-Particle Mass Spectrometry Measurements. *J. Geophys. Res. Atmos.* **2013**, *118* (17), 9834–9844.

Baustian, K. J.; Cziczo, D. J.; Wise, M. E.; Pratt, K. A.; Kulkarni, G.; Hallar, A. G.; Tolbert, M. A. Importance of Aerosol Composition, Mixing State, and Morphology for Heterogeneous Ice Nucleation: A Combined Field and Laboratory Approach. *J. Geophys. Res.* **2012**, *117*, D06217.

Bertram, A. K.; Martin, S. T.; Hanna, S. J.; Smith, M. L.; Bodsworth, A.; Chen, Q.; Kuwata, M.; Liu, A.; You, Y.; Zorn, S. R. Predicting the Relative Humidities of Liquid-Liquid Phase Separation, Efflorescence, and Deliquescence of Mixed Particles of Ammonium Sulfate, Organic Material, and Water Using the Organic-to-Sulfate Mass Ratio of the Particle and the Oxygen-to-Carbon Ele. *Atmos. Chem. Phys.* **2011**, *11* (21), 10995–11006.

Bigg, E. K.; Ono, A.; Williams, J. A. Chemical Tests for Individual Submicron Aerosol Particles. *Atmos. Environ.* **1974**, *8* (1), 1–13.

Bondy, A. L.; Kirpes, R. M.; Merzel, R. L.; Pratt, K. A.; Banaszak Holl, M. M.; Ault, A. P. Atomic Force Microscopy-Infrared Spectroscopy of Individual Atmospheric Aerosol Particles: Subdiffraction Limit Vibrational Spectroscopy and Morphological Analysis. *Anal. Chem.* **2017a**, *89* (17), 8594–8598.

Bondy, A. L.; Wang, B.; Laskin, A.; Craig, R. L.; Nhliziyo, M. V; Bertman, S. B.; Pratt, K. A.; Shepson, P. B.; Ault, A. P. Inland Sea Spray Aerosol Transport and Incomplete Chloride Depletion: Varying Degrees of Reactive Processing Observed during SOAS. *Environ. Sci. Technol.* **2017b**, *51* (17), 9533–9542.

Bondy, A. L.; Craig, R. L.; Zhang, Z.; Gold, A.; Surratt, J. D.; Ault, A. P. Isoprene-Derived Organosulfates: Vibrational Mode Analysis by Raman Spectroscopy, Acidity-Dependent Spectral Modes, and Observation in Individual Atmospheric Particles. *J. Phys. Chem. A* **2018**, *122* (1), 303–315.

Bones, D. L.; Reid, J. P.; Lienhard, D. M.; Krieger, U. K. Comparing the Mechanism of Water Condensation and Evaporation in Glassy Aerosol. *Proc. Natl. Acad. Sci.* **2012**, *109* (29), 11613–11618.

Bougiatioti, A.; Nikolaou, P.; Stavroulas, I.; Kouvarakis, G.; Weber, R.; Nenes, A.; Kanakidou, M.; Mihalopoulos, N. Particle Water and pH in the Eastern Mediterranean: Source Variability and Implications for Nutrient Availability. *Atmos. Chem. Phys.* **2016**, *16* (7), 4579–4591.

Bougiatioti, A.; Stavroulas, I.; Fourtziou, L.; Nikolaou, P.; Paraskevopoulou, D.; Kouvarakis, G.;

Nenes, A.; Mihalopoulos, N. Fine Particle Water and PH in an Urban and Remote Location and the Role of Biomass Burning. In *Perspectives on Atmospheric Science*; Karacostas, TS and Bais, AF and Nastos, P., Ed.; Springer Atmospheric Sciences; 2017; pp 837–843.

Bozlee, B. J.; Misra, A. K.; Sharma, S. K.; Ingram, M. Remote Raman and Fluorescence Studies of Mineral Samples. *Spectrochim. Acta Part A Mol. Biomol. Spectrosc.* **2005**, *61* (10), 2342–2348.

Broekhuizen, K.; Chang, R. Y. W.; Leaitch, W. R.; Li, S. M.; Abbatt, J. P. D. Closure between Measured and Modeled Cloud Condensation Nuclei (CCN) Using Size-Resolved Aerosol Compositions in Downtown Toronto. *Atmos. Chem. Phys.* **2006**, *6* (9), 2513–2524.

Bruynseels, F.; Van Grieken, R. Direct Detection of Sulfate and Nitrate Layers on Sampled Marine Aerosols by Laser Microprobe Mass Analysis. *Atmos. Environ.* **1985**, *19* (11), 1969–1970.

Buajarern, J.; Mitchem, L.; Reid, J. P. Characterizing Multiphase Organic/Inorganic/Aqueous Aerosol Droplets. *J. Phys. Chem. A* **2007**, *111* (37), 9054–9061.

Budisulistiorini, S. H.; Li, X.; Bairai, S. T.; Renfro, J.; Liu, Y.; Liu, Y. J.; McKinney, K. A.; Martin, S. T.; McNeill, V. F.; Pye, H. O. T.; et al. Examining the Effects of Anthropogenic Emissions on Isoprene-Derived Secondary Organic Aerosol Formation during the 2013 Southern Oxidant and Aerosol Study (SOAS) at the Look Rock, Tennessee Ground Site. *Atmos. Chem. Phys.* **2015**, *15* (15), 8871–8888.

Buseck, P. R.; Pósfai, M. Airborne Minerals and Related Aerosol Particles: Effects on Climate and the Environment. *Proc. Natl. Acad. Sci.* **1999**, *96* (7), 3372–3379.

Cao, G.; Jang, M. Effects of Particle Acidity and UV Light on Secondary Organic Aerosol

Formation from Oxidation of Aromatics in the Absence of NOx. *Atmos. Environ.* **2007**, *41* (35), 7603–7613.

Cappa, C. D.; Onasch, T. B.; Massoli, P.; Worsnop, D. R.; Bates, T. S.; Cross, E. S.; Davidovits, P.; Hakala, J.; Hayden, K. L.; Jobson, B. T.; et al. Radiative Absorption Enhancements Due to the Mixing State of Atmospheric Black Carbon. *Science (80-.).* **2012**, *337* (6098), 1078–1081.

Carslaw, K. S.; Clegg, S. L.; Brimblecombe, P. A Thermodynamic Model of the System HCl-HNO3-H2SO4-H2O, Including Solubilities of HBr, from <200 to 328 K. *J. Phys. Chem.* **1995**, *99* (29), 11557–11574.

Carslaw, K. S.; Boucher, O.; Spracklen, D. V; Mann, G. W.; Rae, J. G. L.; Woodward, S.; Kulmala, M. A Review of Natural Aerosol Interactions and Feedbacks within the Earth System. *Atmos. Chem. Phys.* **2010**, *10* (4), 1701–1737.

Casuccio, G. S.; Janocko, P. B.; Lee, R. J.; Kelly, J. F.; Dattner, S. L.; Mgebroff, J. S. The Use of Computer Controlled Scanning Electron Microscopy in Environmental Studies. *J. Air Pollut. Control Assoc.* **1983**, *33* (10), 937–943.

Casuccio, G. S.; Schlaegle, S. F.; Lersch, T. L.; Huffman, G. P.; Chen, Y.; Shah, N. Measurement of Fine Particulate Matter Using Electron Microscopy Techniques. *Fuel Process. Technol.* **2004**, *85*, 763–779.

Catelani, T.; Pratesi, G.; Zoppi, M. Raman Characterization of Ambient Airborne Soot and Associated Mineral Phases. *Aerosol Sci. Technol.* **2014**, *48* (1), 13–21.

Chan, C. K.; Ha, Z.; Choi, M. Y. Study of Water Activities of Aerosols of Mixtures of Sodium and Magnesium Salts. *Atmos. Environ.* **2000**, *34* (28), 4795–4803.

Chan, K. M.; Huang, D. D.; Li, Y. J.; Chan, M. N.; Seinfeld, J. H.; Chan, C. K. Oligomeric Products and Formation Mechanisms from Acid-Catalyzed Reactions of Methyl Vinyl Ketone on Acidic Sulfate Particles. *J. Atmos. Chem.* **2013**, *70* (1), 1–18.

Chan, M. N.; Surratt, J. D.; Chan, A. W. H.; Schilling, K.; Offenberg, J. H.; Lewandowski, M.; Edney, E. O.; Kleindienst, T. E.; Jaoui, M.; Edgerton, E. S.; et al. Influence of Aerosol Acidity on the Chemical Composition of Secondary Organic Aerosol from β-Caryophyllene. *Atmos. Chem. Phys.* **2011**, *11* (4), 1735–1751.

Chang, M.; Kim, S.; Sioutas, C. Experimental Studies on Particle Impaction and Bounce: Effects of Substrate Design and Material. *Atmos. Environ.* **1999**, *33* (15), 2313–2322.

Chen, H.; Laskin, A.; Baltrusaitis, J.; Gorski, C. A.; Scherer, M. M.; Grassian, V. H. Coal Fly Ash as a Source of Iron in Atmospheric Dust. *Environ. Sci. Technol.* **2012**, *46* (4), 2112–2120.

Chen, H.; Wang, M.; Yao, L.; Chen, J.; Wang, L. Uptake of Gaseous Alkylamides by Suspended Sulfuric Acid Particles: Formation of Ammonium/Aminium Salts. *Environ. Sci. Technol.* **2017**, *51* (20), 11710–11717.

Cheng, Y.; Su, H.; Koop, T.; Mikhailov, E.; Pöschl, U. Size Dependence of Phase Transitions in Aerosol Nanoparticles. *Nat. Commun.* **2015**, *6*, 5923.

Cheng, Y. F.; Eichler, H.; Wiedensohler, A.; Heintzenberg, J.; Zhang, Y. H.; Hu, M.; Herrmann, H.; Zeng, L. M.; Liu, S.; Gnauk, T.; et al. Mixing State of Elemental Carbon and Non-Light-Absorbing Aerosol Components Derived from in Situ Particle Optical Properties at Xinken in Pearl River Delta of China. *J. Geophys. Res. Atmos.* **2006**, *111* (D20), D20204.

Chu, Y.; Sauerwein, M.; Chan, C. K. Hygroscopic and Phase Transition Properties of Alkyl

Aminium Sulfates at Low Relative Humidities. *Phys. Chem. Chem. Phys.* **2015**, *17* (30), 19789–19796.

Ciobanu, V. G.; Marcolli, C.; Krieger, U. K.; Weers, U.; Peter, T. Liquid−Liquid Phase Separation in Mixed Organic/Inorganic Aerosol Particles. *J. Phys. Chem. A* **2009**, *113* (41), 10966–10978.

Clarke, A. D.; Shinozuka, Y.; Kapustin, V. N.; Howell, S.; Huebert, B.; Doherty, S.; Anderson, T.; Covert, D.; Anderson, J.; Hua, X.; et al. Size Distributions and Mixtures of Dust and Black Carbon Aerosol in Asian Outflow: Physiochemistry and Optical Properties. *J. Geophys. Res. Atmos.* **2004**, *109* (D15), D15S09.

Clegg, S. L.; Simonson, J. M. A BET Model of the Thermodynamics of Aqueous Multicomponent Solutions at Extreme Concentration. *J. Chem. Thermodyn.* **2001**, *33* (11), 1457–1472.

Clegg, S. L.; Pitzer, K. S.; Brimblecombe, P. Thermodynamics of Multicomponent, Miscible, Ionic Solutions. Mixtures Including Unsymmetrical Electrolytes. *J. Phys. Chem.* **1992**, *96* (23), 9470–9479.

Clegg, S. L.; Brimblecombe, P.; Wexler, A. S. Thermodynamic Model of the System H+−NH4+−SO42-−NO3-−H2O at Tropospheric Temperatures. *J. Phys. Chem. A* **1998**, *102* (12), 2137–2154.

Cortés, D. A.; Elrod, M. J. Kinetics of the Aqueous Phase Reactions of Atmospherically Relevant Monoterpene Epoxides. *J. Phys. Chem. A* **2017**, *121* (48), 9297–9305.

Coz, E.; Gómez-Moreno, F. J.; Pujadas, M.; Casuccio, G. S.; Lersch, T. L.; Artíñano, B. Individual Particle Characteristics of North African Dust under Different Long-Range

Transport Scenarios. *Atmos. Environ.* **2009**, *43* (11), 1850–1863.

Craig, R. L.; Bondy, A. L.; Ault, A. P. Surface Enhanced Raman Spectroscopy Enables Observations of Previously Undetectable Secondary Organic Aerosol Components at the Individual Particle Level. *Anal. Chem.* **2015**, *87* (15), 7510–7514.

Craig, R. L.; Bondy, A. L.; Ault, A. P. Computer-Controlled Raman Microspectroscopy (CC-Raman): A Method for the Rapid Characterization of Individual Atmospheric Aerosol Particles. *Aerosol Sci. Technol.* **2017a**, *51* (9), 1099–1112.

Craig, R. L.; Nandy, L.; Axson, J. L.; Dutcher, C. S.; Ault, A. P. Spectroscopic Determination of Aerosol pH from Acid–Base Equilibria in Inorganic, Organic, and Mixed Systems. *J. Phys. Chem. A* **2017b**, *121* (30), 5690–5699.

Creamean, J. M.; Axson, J. L.; Bondy, A. L.; Craig, R. L.; May, N. W.; Shen, H.; Weber, M. H.; Pratt, K. A.; Ault, A. P. Changes in Precipitating Snow Chemistry with Location and Elevation in the California Sierra Nevada. *J. Geophys. Res. - Atmos.* **2016**, *121* (12), 7296–7309.

Cziczo, D. J.; Nowak, J. B.; Hu, J. H.; Abbatt, J. P. D. Infrared Spectroscopy of Model Tropospheric Aerosols as a Function of Relative Humidity: Observation of Deliquescence and Crystallization. *J. Geophys. Res. Atmos.* **1997**, *102* (D15), 18843–18850.

Czoschke, N. M.; Jang, M. Acidity Effects on the Formation of α-Pinene Ozone SOA in the Presence of Inorganic Seed. *Atmos. Environ.* **2006**, *40* (23), 4370–4380.

Dallemagne, M. A.; Huang, X. Y.; Eddingsaas, N. C. Variation in pH of Model Secondary Organic Aerosol during Liquid–Liquid Phase Separation. *J. Phys. Chem. A* **2016**, *120* (18), 2868–2876.

Darer, A. I.; Cole-Filipiak, N. C.; O'Connor, A. E.; Elrod, M. J. Formation and Stability of Atmospherically Relevant Isoprene-Derived Organosulfates and Organonitrates. *Environ. Sci. Technol.* **2011**, *45* (5), 1895–1902.

Davies, J. F.; Miles, R. E. H.; Haddrell, A. E.; Reid, J. P. Influence of Organic Films on the Evaporation and Condensation of Water in Aerosol. *Proc. Natl. Acad. Sci. U. S. A.* **2013**, *110* (22), 8807–8812.

Deboudt, K.; Flament, P.; Choel, M.; Gloter, A.; Sobanska, S.; Colliex, C. Mixing State of Aerosols and Direct Observation of Carbonaceous and Marine Coatings on African Dust by Individual Particle Analysis. *J. Geophys. Res.* **2010**, *115*.

Deng, C.; Brooks, S. D.; Vidaurre, G.; Thornton, D. C. O. Using Raman Microspectroscopy to Determine Chemical Composition and Mixing State of Airborne Marine Aerosols over the Pacific Ocean. *Aerosol Sci. Technol.* **2014**, *48* (2), 193–206.

DePalma, J. W.; Kelleher, P. J.; Johnson, C. J.; Fournier, J. A.; Johnson, M. A. Vibrational Signatures of Solvent-Mediated Deformation of the Ternary Core Ion in Size-Selected [MgSO4Mg(H2O)n=4–11]2+ Clusters. *J. Phys. Chem. A* **2015**, *119* (30), 8294–8302.

Dette, H. P.; Koop, T. Glass Formation Processes in Mixed Inorganic/Organic Aerosol Particles. *J. Phys. Chem. A* **2015**, *119* (19), 4552–4561.

Devillepin, J.; Novak, A.; Bougeard, D. Alpha Phase and Beta Phase of Oxalic Acid, H2C2O4 - Vibrational Spectra, Normal Coordinate Calculations, and Intermolecular Forces. *Chem. Phys.* **1982**, *73* (3), 291–312.

Ding, X.; Wang, X.-M.; Zheng, M. The Influence of Temperature and Aerosol Acidity on Biogenic Secondary Organic Aerosol Tracers: Observations at a Rural Site in the Central

Pearl River Delta Region, South China. *Atmos. Environ.* **2011**, *45* (6), 1303–1311.

Doughty, D. C.; Hill, S. C. Automated Aerosol Raman Spectrometer for Semi-Continuous Sampling of Atmospheric Aerosol. *J. Quant. Spectrosc. Radiat. Transf.* **2017**, *188*, 103–117.

Duporté, G.; Flaud, P.-M.; Geneste, E.; Augagneur, S.; Pangui, E.; Lamkaddam, H.; Gratien, A.; Doussin, J.-F.; Budzinski, H.; Villenave, E.; et al. Experimental Study of the Formation of Organosulfates from α-Pinene Oxidation. Part I: Product Identification, Formation Mechanisms and Effect of Relative Humidity. *J. Phys. Chem. A* **2016**, *120* (40), 7909–7923.

Dutcher, C. S.; Ge, X.; Wexler, A. S.; Clegg, S. L. An Isotherm-Based Thermodynamic Model of Multicomponent Aqueous Solutions, Applicable over the Entire Concentration Range. *J. Phys. Chem. A* **2013**, *117* (15), 3198–3213.

Ebben, C. J.; Ault, A. P.; Ruppel, M. J.; Ryder, O. S.; Bertram, T. H.; Grassian, V. H.; Prather, K. A.; Geiger, F. M. Size-Resolved Sea Spray Aerosol Particles Studied by Vibrational Sum Frequency Generation. *J. Phys. Chem. A* **2013**, *117* (30), 6589–6601.

Eddingsaas, N. C.; VanderVelde, D. G.; Wennberg, P. O. Kinetics and Products of the Acid-Catalyzed Ring-Opening of Atmospherically Relevant Butyl Epoxy Alcohols. *J. Phys. Chem. A* **2010**, *114* (31), 8106–8113.

Edgerton, E. S.; Casuccio, G. S.; Saylor, R. D.; Lersch, T. L.; Hartsell, B. E.; Jansen, J. J.; Hansen, D. A. Measurements of OC and EC in Coarse Particulate Matter in the Southeastern United States. *J. Air Waste Manage. Assoc.* **2009**, *59* (1), 78–90.

Edney, E. O.; Kleindienst, T. E.; Jaoui, M.; Lewandowski, M.; Offenberg, J. H.; Wang, W.; Claeys, M. Formation of 2-Methyl Tetrols and 2-Methylglyceric Acid in Secondary Organic

Aerosol from Laboratory Irradiated isoprene/NOX/SO2/air Mixtures and Their Detection in Ambient PM2.5 Samples Collected in the Eastern United States. *Atmos. Environ.* **2005**, *39* (29), 5281–5289.

Eom, H. J.; Gupta, D.; Cho, H. R.; Hwang, H. J.; Hur, S. D.; Gim, Y.; Ro, C. U. Single-Particle Investigation of Summertime and Wintertime Antarctic Sea Spray Aerosols Using Low-Z Particle EPMA, Raman Microspectrometry, and ATR-FTIR Imaging Techniques. *Atmos. Chem. Phys.* **2016**, *16* (21), 13823–13836.

Fang, T.; Guo, H.; Zeng, L.; Verma, V.; Nenes, A.; Weber, R. J. Highly Acidic Ambient Particles, Soluble Metals, and Oxidative Potential: A Link between Sulfate and Aerosol Toxicity. *Environ. Sci. Technol.* **2017**, *51* (5), 2611–2620.

Feng, J. L.; Guo, Z. G.; Zhang, T. R.; Yao, X. H.; Chan, C. K.; Fang, M. Source and Formation of Secondary Particulate Matter in PM2.5 in Asian Continental Outflow. *J. Geophys. Res. - Atmos.* **2012**, *117* (D3).

Fierce, L.; Riemer, N.; Bond, T. C. Toward Reduced Representation of Mixing State for Simulating Aerosol Effects on Climate. *Bull. Am. Meteorol. Soc.* **2016**, *98* (5), 971–980.

Fountoukis, C.; Nenes, A. ISORROPIA II: A Computationally Efficient Thermodynamic Equilibrium Model for K+-Ca2+-Mg2+-NH42+-Na+-SO42--NO3--Cl--H2O Aerosols. *Atmos. Chem. Phys.* **2007**, *7* (17), 4639–4659.

Fountoukis, C.; Nenes, A.; Sullivan, A.; Weber, R.; Van Reken, T.; Fischer, M.; Matías, E.; Moya, M.; Farmer, D.; Cohen, R. C. Thermodynamic Characterization of Mexico City Aerosol during MILAGRO 2006. *Atmos. Chem. Phys.* **2009**, *9* (6), 2141–2156.

Fraund, M.; Pham, Q. D.; Bonanno, D.; Harder, H. T.; Wang, B.; Brito, J.; de Sá, S. S.; Carbone,

S.; China, S.; Artaxo, P.; et al. Elemental Mixing State of Aerosol Particles Collected in Central Amazonia during GoAmazon2014/15. *Atmosphere* . 2017.

Frost, R. L. Fourier Transform Raman Spectroscopy of Kaolinite, Dickite, and Halloysite. *Clays Clay Miner.* **1995**, *43* (2), 191–195.

Frost, R. L.; Thu Ha, T.; Kristof, J. FT-Raman Spectroscopy of the Lattice Region of Kaolinite and Its Intercalates. *Vib. Spectrosc.* **1997**, *13* (2), 175–186.

Froyd, K. D.; Murphy, S. M.; Murphy, D. M.; de Gouw, J. A.; Eddingsaas, N. C.; Wennberg, P. O. Contribution of Isoprene-Derived Organosulfates to Free Tropospheric Aerosol Mass. *Proc. Natl. Acad. Sci. U. S. A.* **2010**, *107* (50), 21360–21365.

Fu, Y.; Kuppe, C.; Valev, V. K.; Fu, H.; Zhang, L.; Chen, J. Surface-Enhanced Raman Spectroscopy: A Facile and Rapid Method for the Chemical Component Study of Individual Atmospheric Aerosol. *Environ. Sci. Technol.* **2017**, *51* (11), 6260–6267.

Gaffney, J. S.; Marley, N. A.; Smith, K. J. Characterization of Fine Mode Atmospheric Aerosols by Raman Microscopy and Diffuse Reflectance FTIR. *J. Phys. Chem. A* **2015**, *119* (19), 4524–4532.

Gajaraj, S.; Fan, C.; Lin, M.; Hu, Z. Quantitative Detection of Nitrate in Water and Wastewater by Surface-Enhanced Raman Spectroscopy. *Environ. Monit. Assess.* **2013**, *185* (7), 5673–5681.

Ganor, E. A Method for Identifying Sulfuric Acid in Single Cloud and Fog Droplets. *Atmos. Environ.* **1999**, *33* (26), 4235–4242.

Ganor, E.; Levin, Z.; Pardess, D. Determining the Acidity and Chemical Composition of Fog, Haze and Cloud Droplets in Israel. *Atmos. Environ. Part A. Gen. Top.* **1993**, *27* (12), 1821–

1832.

Gao, S.; Ng, N. L.; Keywood, M.; Varutbangkul, V.; Bahreini, R.; Nenes, A.; He, J.; Yoo, K. Y.; Beauchamp, J. L.; Hodyss, R. P.; et al. Particle Phase Acidity and Oligomer Formation in Secondary Organic Aerosol. *Environ. Sci. Technol.* **2004**, *38* (24), 6582–6589.

Gard, E. E.; Kleeman, M. J.; Gross, D. S.; Hughes, L. S.; Allen, J. O.; Morrical, B. D.; Fergenson, D. P.; Dienes, T.; E. Gälli, M.; Johnson, R. J.; et al. Direct Observation of Heterogeneous Chemistry in the Atmosphere. *Science (80-.).* **1998**, *279* (5354), 1184–1187.

Garrels, R. M.; Christ, C. L. *Solutions, Minerals, and Equilibria*; Harper & Row Publishers, Inc.: New York City, NY, 1965.

Gaston, C. J.; Riedel, T. P.; Zhang, Z.; Gold, A.; Surratt, J. D.; Thornton, J. A. Reactive Uptake of an Isoprene-Derived Epoxydiol to Submicron Aerosol Particles. *Environ. Sci. Technol.* **2014**, *48* (19), 11178–11186.

De Gelder, J.; De Gussem, K.; Vandenabeele, P.; Moens, L. Reference Database of Raman Spectra of Biological Molecules. *J. Raman Spectrosc.* **2007**, *38* (9), 1133–1147.

Gen, M.; Chan, C. K. Electrospray Surface-Enhanced Raman Spectroscopy (ES-SERS) for Probing Surface Chemical Compositions of Atmospherically Relevant Particles. *Atmos. Chem. Phys.* **2017**, *17* (22), 14025–14037.

Germani, M. S.; Buseck, P. R. Automated Scanning Electron Microscopy for Atmospheric Particle Analysis. *Anal. Chem.* **1991**, *63* (20), 2232–2237.

Ghorai, S.; Laskin, A.; Tivanski, A. V. Spectroscopic Evidence of Keto−enol Tautomerism in Deliquesced Malonic Acid Particles. *J. Phys. Chem. A* **2011**, *115* (17), 4373–4380.

Ghorai, S.; Wang, B.; Tivanski, A.; Laskin, A. Hygroscopic Properties of Internally Mixed Particles Composed of NaCl and Water-Soluble Organic Acids. *Environ. Sci. Technol.* **2014**, *48* (4), 2234–2241.

Glasius, M.; Goldstein, A. H. Recent Discoveries and Future Challenges in Atmospheric Organic Chemistry. *Environ. Sci. Technol.* **2016**, *50* (6), 2754–2764.

Grassian, V. H. Particle Chemistry in the Environment: Challenges and Opportunities. *J. Phys. Chem. Lett.* **2015**, *6* (19), 3880–3881.

Gruen, E. C.; Plane, R. A. Raman Study of Aqueous Metal Oxalate Complexes and Related Oxalates. *Inorg. Chem.* **1967**, *6* (6), 1123–1127.

Guasco, T. L.; Cuadra-Rodriguez, L. A.; Pedler, B. E.; Ault, A. P.; Collins, D. B.; Zhao, D.; Kim, M. J.; Ruppel, M. J.; Wilson, S. C.; Pomeroy, R. S.; et al. Transition Metal Associations with Primary Biological Particles in Sea Spray Aerosol Generated in a Wave Channel. *Environ. Sci. Technol.* **2014**, *48* (2), 1324–1333.

Guo, H.; Xu, L.; Bougiatioti, A.; Cerully, K. M.; Capps, S. L.; Hite Jr, J. R.; Carlton, A. G.; Lee, S. H.; Bergin, M. H.; Ng, N. L.; et al. Fine-Particle Water and pH in the Southeastern United States. *Atmos. Chem. Phys.* **2015**, *15* (9), 5211–5228.

Guo, H.; Sullivan, A. P.; Campuzano-Jost, P.; Schroder, J. C.; Lopez-Hilfiker, F. D.; Dibb, J. E.; Jimenez, J. L.; Thornton, J. A.; Brown, S. S.; Nenes, A.; et al. Fine Particle pH and the Partitioning of Nitric Acid during Winter in the Northeastern United States. *J. Geophys. Res. - Atmos.* **2016**, *121* (17), 10,310-355,376.

Guo, H.; Liu, J.; Froyd, K. D.; Roberts, J. M.; Veres, P. R.; Hayes, P. L.; Jimenez, J. L.; Nenes, A.; Weber, R. J. Fine Particle pH and Gas–particle Phase Partitioning of Inorganic Species

in Pasadena, California, during the 2010 CalNex Campaign. *Atmos. Chem. Phys.* **2017**, *17* (9), 5703–5719.

Haes, A. J.; Van Duyne, R. P. A Unified View of Propagating and Localized Surface Plasmon Resonance Biosensors. *Anal. Bioanal. Chem.* **2004**, *379* (7–8), 920–930.

Hallquist, M.; Wenger, J. C.; Baltensperger, U.; Rudich, Y.; Simpson, D.; Claeys, M.; Dommen, J.; Donahue, N. M.; George, C.; Goldstein, A. H.; et al. The Formation, Properties and Impact of Secondary Organic Aerosol: Current and Emerging Issues. *Atmos. Chem. Phys.* **2009**, *9* (14), 5155–5236.

Han, Y.; Stroud, C. A.; Liggio, J.; Li, S. M. The Effect of Particle Acidity on Secondary Organic Aerosol Formation from α-Pinene Photooxidation under Atmospherically Relevant Conditions. *Atmos. Chem. Phys.* **2016**, *16* (21), 13929–13944.

Hatch, L. E.; Creamean, J. M.; Ault, A. P.; Surratt, J. D.; Chan, M. N.; Seinfeld, J. H.; Edgerton, E. S.; Su, Y.; Prather, K. A. Measurements of Isoprene-Derived Organosulfates in Ambient Aerosols by Aerosol Time-of-Flight Mass Spectrometry - Part 1: Single Particle Atmospheric Observations in Atlanta. *Environ. Sci. Technol.* **2011**, *45* (12), 5105–5111.

Hennigan, C. J.; Izumi, J.; Sullivan, A. P.; Weber, R. J.; Nenes, A. A Critical Evaluation of Proxy Methods Used to Estimate the Acidity of Atmospheric Particles. *Atmos. Chem. Phys.* **2015**, *15* (5), 2775–2790.

Hibben, J. H. The Raman Spectra of Oxalic Acid. *J. Chem. Phys.* **1935**, *3* (11), 675–679.

Hinds, W. C. *Aerosol Technology: Properties, Behavior, and Measurement of Airborne Particles*; John Wiley & Sons, Inc.: New York, USA, 1999.

Hood, G. C.; Redlich, O.; Reilly, C. A. Ionization of Strong Electrolytes. III. Proton Magnetic

Resonance in Nitric, Perchloric, and Hydrochloric Acids. *J. Chem. Phys.* **1954**, *22* (12), 2067–2071.

Hopkins, R. J.; Mitchem, L.; Ward, A. D.; Reid, J. P. Control and Characterisation of a Single Aerosol Droplet in a Single-Beam Gradient-Force Optical Trap. *Phys. Chem. Chem. Phys.* **2004**, *6* (21), 4924–4927.

Hopkins, R. J.; Desyaterik, Y.; Tivanski, A. V; Zaveri, R. A.; Berkowitz, C. M.; Tyliszczak, T.; Gilles, M. K.; Laskin, A. Chemical Speciation of Sulfur in Marine Cloud Droplets and Particles: Analysis of Individual Particles from the Marine Boundary Layer over the California Current. *J. Geophys. Res. - Atmos.* **2008**, *113* (D4).

Hu, K. S.; Darer, A. I.; Elrod, M. J. Thermodynamics and Kinetics of the Hydrolysis of Atmospherically Relevant Organonitrates and Organosulfates. *Atmos. Chem. Phys.* **2011**, *11* (16), 8307–8320.

Hughes, L. S.; Allen, J. O.; Bhave, P.; Kleeman, M. J.; Cass, G. R.; Liu, D. Y.; Fergenson, D. P.; Morrical, B. D.; Prather, K. A. Evolution of Atmospheric Particles along Trajectories Crossing the Los Angeles Basin. *Environ. Sci. Technol.* **2000**, *34* (15), 3058–3068.

Iinuma, Y.; Müller, C.; Berndt, T.; Böge, O.; Claeys, M.; Herrmann, H. Evidence for the Existence of Organosulfates from β-Pinene Ozonolysis in Ambient Secondary Organic Aerosol. *Environ. Sci. Technol.* **2007a**, *41* (19), 6678–6683.

Iinuma, Y.; Müller, C.; Böge, O.; Gnauk, T.; Herrmann, H. The Formation of Organic Sulfate Esters in the Limonene Ozonolysis Secondary Organic Aerosol (SOA) under Acidic Conditions. *Atmos. Environ.* **2007b**, *41* (27), 5571–5583.

Iinuma, Y.; Boge, O.; Kahnt, A.; Herrmann, H. Laboratory Chamber Studies on the Formation of

Organosulfates from Reactive Uptake of Monoterpene Oxides. *Phys. Chem. Chem. Phys.* **2009**, *11* (36), 7985–7997.

Irish, D. E.; Chen, H. Raman Spectral Study of Bisulfate-Sulfate Systems. II. Constitution, Equilibriums, and Ultrafast Proton Transfer in Sulfuric Acid. *J. Phys. Chem.* **1971**, *75* (17), 2672–2681.

Ito, K.; Bernstein, H. J. The Vibrational Spectra of the Formate, Acetate, and Oxalate Ions. *Can. J. Chem.* **1956**, *34* (2), 170–178.

Ivleva, N. P.; Messerer, A.; Yang, X.; Niessner, R.; Pöschl, U. Raman Microspectroscopic Analysis of Changes in the Chemical Structure and Reactivity of Soot in a Diesel Exhaust Aftertreatment Model System. *Environ. Sci. Technol.* **2007a**, *41* (10), 3702–3707.

Ivleva, N. P.; McKeon, U.; Niessner, R.; Pöschl, U. Raman Microspectroscopic Analysis of Size-Resolved Atmospheric Aerosol Particle Samples Collected with an ELPI: Soot, Humic-like Substances, and Inorganic Compounds. *Aerosol Sci. Technol.* **2007b**, *41* (7), 655–671.

Jacobs, M. I.; Burke, W. J.; Elrod, M. J. Kinetics of the Reactions of Isoprene-Derived Hydroxynitrates: Gas Phase Epoxide Formation and Solution Phase Hydrolysis. *Atmos. Chem. Phys.* **2014**, *14* (17), 8933–8946.

Jacobson, M. Z. Strong Radiative Heating due to the Mixing State of Black Carbon in Atmospheric Aerosols. *Nature* **2001**, *409* (6821), 695–697.

Jambers, W.; Bock, L. De; Grieken, R. Van. Recent Advances in the Analysis of Individual Environmental Particles: A Review. *Analyst* **1995**, *120*, 681–692.

Jang, M.; Kamens, R. M. Atmospheric Secondary Aerosol Formation by Heterogeneous Reactions of Aldehydes in the Presence of a Sulfuric Acid Aerosol Catalyst. *Environ. Sci.*

Technol. **2001**, *35* (24), 4758–4766.

Jang, M.; Czoschke, N. M.; Lee, S.; Kamens, R. M. Heterogeneous Atmospheric Aerosol Production by Acid-Catalyzed Particle-Phase Reactions. *Science (80-.).* **2002**, *298* (5594), 814–817.

Jang, M.; Lee, S.; Kamens, R. M. Organic Aerosol Growth by Acid-Catalyzed Heterogeneous Reactions of Octanal in a Flow Reactor. *Atmos. Environ.* **2003a**, *37* (15), 2125–2138.

Jang, M.; Carroll, B.; Chandramouli, B.; Kamens, R. M. Particle Growth by Acid-Catalyzed Heterogeneous Reactions of Organic Carbonyls on Preexisting Aerosols. *Environ. Sci. Technol.* **2003b**, *37* (17), 3828–3837.

Jang, M.; Cao, G.; Paul, J. Colorimetric Particle Acidity Analysis of Secondary Organic Aerosol Coating on Submicron Acidic Aerosols. *Aerosol Sci. Technol.* **2008**, *42* (6), 409–420.

Jaoui, M.; Corse, E. W.; Lewandowski, M.; Offenberg, J. H.; Kleindienst, T. E.; Edney, E. O. Formation of Organic Tracers for Isoprene SOA under Acidic Conditions. *Atmos. Environ.* **2010**, *44* (14), 1798–1805.

Jasse, B.; Chao, R. S.; Koenig, J. L. Laser Raman Scattering in Uniaxially Oriented Atactic Polystyrene. *J. Polym. Sci. Polym. Phys. Ed.* **1978**, *16* (12), 2157–2169.

Jentzsch, P. V.; Kampe, B.; Ciobota, V.; Roesch, P.; Popp, J. Inorganic Salts in Atmospheric Particulate Matter: Raman Spectroscopy as an Analytical Tool. *Spectrochim. Acta Part A Mol. Biomol. Spectrosc.* **2013**, *115*, 697–708.

Jordanov, N.; Zellner, R. Investigations of the Hygroscopic Properties of Ammonium Sulfate and Mixed Ammonium Sulfate and Glutaric Acid Micro Droplets by Means of Optical Levitation and Raman Spectroscopy. *Phys. Chem. Chem. Phys.* **2006**, *8* (23), 2759–2764.

Jung, H.-J.; Eom, H.-J.; Kang, H.-W.; Moreau, M.; Sobanska, S.; Ro, C.-U. Combined Use of Quantitative ED-EPMA, Raman Microspectrometry, and ATR-FTIR Imaging Techniques for the Analysis of Individual Particles. *Analyst* **2014**, *139* (16), 3949–3960.

Katrinak, K. A.; Rez, P.; Buseck, P. R. Structural Variations in Individual Carbonaceous Particles from an Urban Aerosol. *Environ. Sci. Technol.* **1992**, *26* (10), 1967–1976.

Keene, W. C.; Pszenny, A. A. P.; Maben, J. R.; Sander, R. Variation of Marine Aerosol Acidity with Particle Size. *Geophys. Res. Lett.* **2002**, *29* (7), 4–5.

Keene, W. C.; Pszenny, A. A. P.; Maben, J. R.; Stevenson, E.; Wall, A. Closure Evaluation of Size-Resolved Aerosol pH in the New England Coastal Atmosphere during Summer. *J. Geophys. Res. - Atmos.* **2004**, *109* (D23).

Keller, E. L.; Brandt, N. C.; Cassabaum, A. A.; Frontiera, R. R. Ultrafast Surface-Enhanced Raman Spectroscopy. *Analyst* **2015**, *140* (15), 4922–4931.

Kerminen, V.-M.; Hillamo, R.; Teinilä, K.; Pakkanen, T.; Allegrini, I.; Sparapani, R. Ion Balances of Size-Resolved Tropospheric Aerosol Samples: Implications for the Acidity and Atmospheric Processing of Aerosols. *Atmos. Environ.* **2001**, *35* (31), 5255–5265.

Kielland, J. Individual Activity Coefficients of Ions in Aqueous Solutions. *J. Am. Chem. Soc.* **1937**, *59* (9), 1675–1678.

Kiendler-Scharr, A.; Mensah, A. A.; Friese, E.; Topping, D.; Nemitz, E.; Prevot, A. S. H.; Äijälä, M.; Allan, J.; Canonaco, F.; Canagaratna, M.; et al. Ubiquity of Organic Nitrates from Nighttime Chemistry in the European Submicron Aerosol. *Geophys. Res. Lett.* **2016**, *43*, 7735–7744.

Kim, K.-H.; Kabir, E.; Kabir, S. A Review on the Human Health Impact of Airborne Particulate

Matter. *Environ. Int.* **2015**, *74* (Supplement C), 136–143.

Kleinman, S. L.; Frontiera, R. R.; Henry, A. I.; Dieringer, J. A.; Van Duyne, R. P. Creating, Characterizing, and Controlling Chemistry with SERS Hot Spots. *Phys. Chem. Chem. Phys.* **2013**, *15* (1), 21–36.

Knopf, D. A.; Luo, B. P.; Krieger, U. K.; Koop, T. Thermodynamic Dissociation Constant of the Bisulfate Ion from Raman and Ion Interaction Modeling Studies of Aqueous Sulfuric Acid at Low Temperatures. *J. Phys. Chem. A* **2003**, *107* (21), 4322–4332.

Koenig, J. L.; Angood, A. C. Raman Spectra of Poly(ethylene Glycols) in Solution. *J. Polym. Sci. Part A-2* **1970**, *8* (10), 1787-.

Kolb, C. E.; Worsnop, D. R. Chemistry and Composition of Atmospheric Aerosol Particles. *Annu. Rev. Phys. Chem.* **2012**, *63* (1), 471–491.

Koop, T.; Bookhold, J.; Shiraiwa, M.; Pöschl, U. Glass Transition and Phase State of Organic Compounds: Dependency on Molecular Properties and Implications for Secondary Organic Aerosols in the Atmosphere. *Phys. Chem. Chem. Phys.* **2011**, *13* (43), 19238–19255.

Koutrakis, P.; Wolfson, J. M.; Spengler, J. D. An Improved Method for Measuring Aerosol Strong Acidity: Results from a Nine-Month Study in St Louis, Missouri and Kingston, Tennessee. *Atmos. Environ.* **1988**, *22* (1), 157–162.

Kruus, P.; Hayes, A. C.; Adams, W. Determination of Ratios of Sulfate to Bisulfate Ions in Aqueous Solutions by Raman Spectroscopy. *J. Solution Chem.* **1985**, *14* (2), 117–128.

Kumar, S.; Raman, R. S. Inorganic Ions in Ambient Fine Particles over a National Park in Central India: Seasonality, Dependencies between SO_4^{2-}, NO_3^-, and NH_4^+, and Neutralization of Aerosol Acidity. *Atmos. Environ.* **2016**, *143* (Supplement C), 152–163.

Kuwata, M.; Liu, Y.; McKinney, K.; Martin, S. T. Physical State and Acidity of Inorganic Sulfate Can Regulate the Production of Secondary Organic Material from Isoprene Photooxidation Products. *Phys. Chem. Chem. Phys.* **2015**, *17* (8), 5670–5678.

Kwamena, N. O. A.; Buajarern, J.; Reid, J. P. Equilibrium Morphology of Mixed Organic/Inorganic/Aqueous Aerosol Droplets: Investigating the Effect of Relative Humidity and Surfactants. *J. Phys. Chem. A* **2010**, *114* (18), 5787–5795.

Lal, V.; Khalizov, A. F.; Lin, Y.; Galvan, M. D.; Connell, B. T.; Zhang, R. Heterogeneous Reactions of Epoxides in Acidic Media. *J. Phys. Chem. A* **2012**, *116* (24), 6078–6090.

Laliberte, M. A Model for Calculating the Heat Capacity of Aqueous Solutions, with Updated Density and Viscosity Data. *J. Chem. Eng. Data* **2009**, *54* (6), 1725–1760.

Laliberte, M.; Cooper, W. E. Model for Calculating the Density of Aqueous Electrolyte Solutions. *J. Chem. Eng. Data* **2004**, *49* (5), 1141–1151.

Larkin, P. *Infrared and Raman Spectroscopy; Principles and Spectral Interpretation*; Elsevier: Waltham, MA, 2011.

Laskin, A.; Cowin, J. P. Automated Single-Particle SEM/EDX Analysis of Submicrometer Particles down to 0.1 Mm. *Anal. Chem.* **2001**, *73* (5), 1023–1029.

Laskin, A.; Cowin, J. P.; Iedema, M. J. Analysis of Individual Environmental Particles Using Modern Methods of Electron Microscopy and X-Ray Microanalysis. *J. Electron Spectros. Relat. Phenomena* **2006**, *150* (2–3), 260–274.

Laskin, A.; Moffet, R. C.; Gilles, M. K.; Fast, J. D.; Zaveri, R. A.; Wang, B.; Nigge, P.; Shutthanandan, J. Tropospheric Chemistry of Internally Mixed Sea Salt and Organic Particles: Surprising Reactivity of NaCl with Weak Organic Acids. *J. Geophys. Res.* -

Atmos. **2012**, *117* (D15).

Laskin, A.; Gilles, M. K.; Knopf, D. A.; Wang, B.; China, S. Progress in the Analysis of Complex Atmospheric Particles. *Annu. Rev. Anal. Chem.* **2016**, *9* (1), 117–143.

Laskina, O.; Young, M. A.; Kleiber, P. D.; Grassian, V. H. Infrared Extinction Spectroscopy and Micro-Raman Spectroscopy of Select Components of Mineral Dust Mixed with Organic Compounds. *J. Geophys. Res. - Atmos.* **2013**, *118* (12), 6593–6606.

Laskina, O.; Morris, H. S.; Grandquist, J. R.; Qin, Z.; Stone, E. A.; Tivanski, A. V; Grassian, V. H. Size Matters in the Water Uptake and Hygroscopic Growth of Atmospherically Relevant Multicomponent Aerosol Particles. *J. Phys. Chem. A* **2015**, *119* (19), 4489–4497.

Lee, A. K. Y.; Chan, C. K. Single Particle Raman Spectroscopy for Investigating Atmospheric Heterogeneous Reactions of Organic Aerosols. *Atmos. Environ.* **2007**, *41* (22), 4611–4621.

Lee, A. K. Y.; Ling, T. Y.; Chan, C. K. Understanding Hygroscopic Growth and Phase Transformation of Aerosols Using Single Particle Raman Spectroscopy in an Electrodynamic Balance. *Faraday Discuss.* **2008**, *137* (0), 245–263.

Lee, B. H.; Mohr, C.; Lopez-Hilfiker, F. D.; Lutz, A.; Hallquist, M.; Lee, L.; Romer, P.; Cohen, R. C.; Iyer, S.; Kurtén, T.; et al. Highly Functionalized Organic Nitrates in the Southeast United States: Contribution to Secondary Organic Aerosol and Reactive Nitrogen Budgets. *Proc. Natl. Acad. Sci.* **2016**, *113* (6), 1516–1521.

Lee, S.-H.; Allen, H. C. Analytical Measurements of Atmospheric Urban Aerosol. *Anal. Chem.* **2012**, *84* (3), 1196–1201.

Lehmpuhl, D. W.; Ramirez-Aguilar, K. A.; Michel, A. E.; Rowlen, K. L.; Birks, J. W. Physical and Chemical Characterization of Atmospheric Aerosols by Atomic Force Microscopy.

Anal. Chem. **1999**, *71* (2), 379–383.

Leopold, N.; Lendl, B. A New Method for Fast Preparation of Highly Surface-Enhanced Raman Scattering (SERS) Active Silver Colloids at Room Temperature by Reduction of Silver Nitrate with Hydroxylamine Hydrochloride. *J. Phys. Chem. B* **2003**, *107* (24), 5723–5727.

Lewandowski, M.; Jaoui, M.; Offenberg, J. H.; Krug, J. D.; Kleindienst, T. E. Atmospheric Oxidation of Isoprene and 1,3-Butadiene: Influence of Aerosol Acidity and Relative Humidity on Secondary Organic Aerosol. *Atmos. Chem. Phys.* **2015**, *15* (7), 3773–3783.

Li, J.; Jang, M. Aerosol Acidity Measurement Using Colorimetry Coupled With a Reflectance UV-Visible Spectrometer. *Aerosol Sci. Technol.* **2012**, *46* (8), 833–842.

Li, J.; Pósfai, M.; Hobbs, P. V; Buseck, P. R. Individual Aerosol Particles from Biomass Burning in Southern Africa: 2, Compositions and Aging of Inorganic Particles. *J. Geophys. Res. Atmos.* **2003**, *108* (D13), n/a-n/a.

Li, J.; Jang, M.; Beardsley, R. L. Dialkylsulfate Formation in Sulfuric Acid-Seeded Secondary Organic Aerosol Produced Using an Outdoor Chamber under Natural Sunlight. *Environ. Chem.* **2016**, *13* (4), 590–601.

Li, X.-H.; Wang, F.; Lu, P.-D.; Dong, J.-L.; Wang, L.-Y.; Zhang, Y.-H. Confocal Raman Observation of the Efflorescence/Deliquescence Processes of Individual NaNO3 Particles on Quartz. *J. Phys. Chem. B* **2006**, *110* (49), 24993–24998.

Lide, D. R. *CRC Handbook of Chemistry and Physics : A Ready-Reference Book of Chemical and Physical Data*; CRC Press: Boca Raton, Fla., 2009.

Liggio, J.; Li, S.-M. Reactive Uptake of Pinonaldehyde on Acidic Aerosols. *J. Geophys. Res. Atmos.* **2006**, *111* (D24), n/a--n/a.

Liggio, J.; Li, S.-M. A New Source of Oxygenated Organic Aerosol and Oligomers. *Atmos. Chem. Phys.* **2013**, *13* (6), 2989–3002.

Lightstone, J. M.; Onasch, T. B.; Imre, D.; Oatis, S. Deliquescence, Efflorescence, and Water Activity in Ammonium Nitrate and Mixed Ammonium Nitrate/Succinic Acid Microparticles. *J. Phys. Chem. A* **2000**, *104* (41), 9337–9346.

Limbeck, A.; Kulmala, M.; Puxbaum, H. Secondary Organic Aerosol Formation in the Atmosphere via Heterogeneous Reaction of Gaseous Isoprene on Acidic Particles. *Geophys. Res. Lett.* **2003**, *30* (19).

Lin, Y.-H.; Zhang, Z.; Docherty, K. S.; Zhang, H.; Budisulistiorini, S. H.; Rubitschun, C. L.; Shaw, S. L.; Knipping, E. M.; Edgerton, E. S.; Kleindienst, T. E.; et al. Isoprene Epoxydiols as Precursors to Secondary Organic Aerosol Formation: Acid-Catalyzed Reactive Uptake Studies with Authentic Compounds. *Environ. Sci. Technol.* **2012**, *46* (1), 250–258.

Lin, Y.-H.; Budisulistiorini, S. H.; Chu, K.; Siejack, R. A.; Zhang, H.; Riva, M.; Zhang, Z.; Gold, A.; Kautzman, K. E.; Surratt, J. D. Light-Absorbing Oligomer Formation in Secondary Organic Aerosol from Reactive Uptake of Isoprene Epoxydiols. *Environ. Sci. Technol.* **2014**, *48* (20), 12012–12021.

Liu, D.; Whitehead, J.; Alfarra, M. R.; Reyes-Villegas, E.; Spracklen, D. V.; Reddington, C. L.; Kong, S.; Williams, P. I.; Ting, Y.-C.; Haslett, S.; et al. Black-Carbon Absorption Enhancement in the Atmosphere Determined by Particle Mixing State. *Nat. Geosci.* **2017a**, *10*, 184.

Liu, M.; Song, Y.; Zhou, T.; Xu, Z.; Yan, C.; Zheng, M.; Wu, Z.; Hu, M.; Wu, Y.; Zhu, T. Fine Particle pH during Severe Haze Episodes in Northern China. *Geophys. Res. Lett.* **2017b**.

Liu, M. J.; Wiegel, A. A.; Wilson, K. R.; Houle, F. A. Aerosol Fragmentation Driven by Coupling of Acid–Base and Free-Radical Chemistry in the Heterogeneous Oxidation of Aqueous Citric Acid by OH Radicals. *J. Phys. Chem. A* **2017c**, *121* (31), 5856–5870.

Liu, Y.; Laskin, A. Hygroscopic Properties of CH(3)SO(3)Na, CH(3)SO(3)NH(4), (CH(3)SO(3))(2)Mg, and (CH(3)SO(3))(2)Ca Particles Studied by Micro-FTIR Spectroscopy. *J. Phys. Chem. A* **2009**, *113* (8), 1531–1538.

Liu, Y.; Liggio, J.; Staebler, R.; Li, S.-M. Reactive Uptake of Ammonia to Secondary Organic Aerosols: Kinetics of Organonitrogen Formation. *Atmos. Chem. Phys.* **2015**, *15* (23), 13569–13584.

Longo, A. F.; Feng, Y.; Lai, B.; Landing, W. M.; Shelley, R. U.; Nenes, A.; Mihalopoulos, N.; Violaki, K.; Ingall, E. D. Influence of Atmospheric Processes on the Solubility and Composition of Iron in Saharan Dust. *Environ. Sci. Technol.* **2016**, *50* (13), 6912–6920.

Lopez-Hilfiker, F. D.; Mohr, C.; D'Ambro, E. L.; Lutz, A.; Riedel, T. P.; Gaston, C. J.; Iyer, S.; Zhang, Z.; Gold, A.; Surratt, J. D.; et al. Molecular Composition and Volatility of Organic Aerosol in the Southeastern U.S.: Implications for IEPOX Derived SOA. *Environ. Sci. Technol.* **2016**, *50* (5), 2200–2209.

Losey, D. J.; Parker, R. G.; Freedman, M. A. pH Dependence of Liquid–liquid Phase Separation in Organic Aerosol. *J. Phys. Chem. Lett.* **2016**, *7* (19), 3861–3865.

Mabrouk, K. Ben; Kauffmann, T. H.; Aroui, H.; Fontana, M. D. Raman Study of Cation Effect on Sulfate Vibration Modes in Solid State and in Aqueous Solutions. *J. Raman Spectrosc.* **2013**, *44* (11), 1603–1608.

Mael, L. E.; Jacobs, M. I.; Elrod, M. J. Organosulfate and Nitrate Formation and Reactivity from

Epoxides Derived from 2-Methyl-3-Buten-2-Ol. *J. Phys. Chem. A* **2015**, *119* (19), 4464–4472.

Magid, E.; Turbeck, B. O. The Rates of the Spontaneous Hydration of CO2 and the Reciprocal Reaction in Neutral Aqueous Solutions between 0° and 38°. *Biochim. Biophys. Acta - Gen. Subj.* **1968**, *165* (3), 515–524.

Malard, L. M.; Pimenta, M. A.; Dresselhaus, G.; Dresselhaus, M. S. Raman Spectroscopy in Graphene. *Phys. Rep.* **2009**, *473* (5–6), 51–87.

Mamane, Y.; Willis, R.; Conner, T. Evaluation of Computer-Controlled Scanning Electron Microscopy Applied to an Ambient Urban Aerosol Sample. *Aerosol Sci. Technol.* **2001**, *34* (1), 97–107.

Marais, E. A.; Jacob, D. J.; Jimenez, J. L.; Campuzano-Jost, P.; Day, D. A.; Hu, W.; Krechmer, J.; Zhu, L.; Kim, P. S.; Miller, C. C.; et al. Aqueous-Phase Mechanism for Secondary Organic Aerosol Formation from Isoprene: Application to the Southeast United States and Co-Benefit of SO2 Emission Controls. *Atmos. Chem. Phys.* **2016**, *16* (3), 1603–1618.

Marcolli, C.; Luo, B.; Peter, T. Mixing of the Organic Aerosol Fractions: Liquids as the Thermodynamically Stable Phases. *J. Phys. Chem. A* **2004**, *108* (12), 2216–2224.

Maria, S. F.; Russell, L. M.; Turpin, B. J.; Porcja, R. J. FTIR Measurements of Functional Groups and Organic Mass in Aerosol Samples over the Caribbean. *Atmos. Environ.* **2002**, *36* (33), 5185–5196.

McLaughlin, R. P.; Bird, B.; Reid, P. J. Vibrational Analysis of Isopropyl Nitrate and Isobutyl Nitrate. *Spectrochim. Acta Part A Mol. Biomol. Spectrosc.* **2002**, *58* (12), 2571–2580.

McMurry, P. H.; Wang, X.; Park, K.; Ehara, K. The Relationship between Mass and Mobility for

Atmospheric Particles: A New Technique for Measuring Particle Density. *Aerosol Sci. Technol.* **2002**, *36* (2), 227–238.

McNeill, V. F. Aqueous Organic Chemistry in the Atmosphere: Sources and Chemical Processing of Organic Aerosols. *Environ. Sci. Technol.* **2015**, *49* (3), 1237–1244.

McNeill, V. F.; Patterson, J.; Wolfe, G. M.; Thornton, J. A. The Effect of Varying Levels of Surfactant on the Reactive Uptake of N2O5 to Aqueous Aerosol. *Atmos. Chem. Phys.* **2006**, *6* (6), 1635–1644.

Metzger, S.; Mihalopoulos, N.; Lelieveld, J. Importance of Mineral Cations and Organics in Gas-Aerosol Partitioning of Reactive Nitrogen Compounds: Case Study Based on MINOS Results. *Atmos. Chem. Phys.* **2006**, *6* (9), 2549–2567.

Michaelian, K. H. The Raman Spectrum of Kaolinite #9 at 21 C. *Can. J. Chem. Can. Chim.* **1986**, *64* (2), 285–289.

Mie, G. Articles on the Optical Characteristics of Turbid Tubes, Especially Colloidal Metal Solutions. *Ann. Phys.* **1908**, *25* (3), 377–445.

Miller, Y.; Chaban, G. M.; Zhou, J.; Asmis, K. R.; Neumark, D. M.; Benny Gerber, R. Vibrational Spectroscopy of (SO42−)·(H2O)n Clusters, n=1–5: Harmonic and Anharmonic Calculations and Experiment. *J. Chem. Phys.* **2007**, *127* (9), 94305.

Mitchem, L.; Buajarern, J.; Ward, A. D.; Reid, J. P. A Strategy for Characterizing the Mixing State of Immiscible Aerosol Components and the Formation of Multiphase Aerosol Particles through Coagulation. *J. Phys. Chem. B* **2006**, *110* (28), 13700–13703.

Moffet, R. C.; Prather, K. A. In-Situ Measurements of the Mixing State and Optical Properties of Soot with Implications for Radiative Forcing Estimates. *Proc. Natl. Acad. Sci.* **2009**, *106*

(29), 11872–11877.

Moffet, R. C.; Henn, T.; Laskin, A.; Gilles, M. K. Automated Chemical Analysis of Internally Mixed Aerosol Particles Using X-Ray Spectromicroscopy at the Carbon K-Edge. *Anal. Chem.* **2010a**, *82* (19), 7906–7914.

Moffet, R. C.; Henn, T. R.; Tivanski, A. V; Hopkins, R. J.; Desyaterik, Y.; Kilcoyne, A. L. D.; Tyliszczak, T.; Fast, J.; Barnard, J.; Shutthanandan, V.; et al. Microscopic Characterization of Carbonaceous Aerosol Particle Aging in the Outflow from Mexico City. *Atmos. Chem. Phys.* **2010b**, *10* (3), 961–976.

Moffet, R. C.; Tivanski, A. V; Gilles, M. K. Chapter 17: Scanning Transmission X-Ray Microscopy: Applications in Atmospheric Research. In *Fundamentals and Applications in Aerosol Spectroscopy*; Signorell, R., Reid, J. P., Eds.; Taylor & Francis Group: Boca Raton, FL, 2011.

Moffet, R. C.; Rodel, T. C.; Kelly, S. T.; Yu, X. Y.; Carroll, G. T.; Fast, J.; Zaveri, R. A.; Laskin, A.; Gilles, M. K. Spectro-Microscopic Measurements of Carbonaceous Aerosol Aging in Central California. *Atmos. Chem. Phys.* **2013**, *13* (20), 10445–10459.

Möhler, O.; Büttner, S.; Linke, C.; Schnaiter, M.; Saathoff, H.; Stetzer, O.; Wagner, R.; Krämer, M.; Mangold, A.; Ebert, V.; et al. Effect of Sulfuric Acid Coating on Heterogeneous Ice Nucleation by Soot Aerosol Particles. *J. Geophys. Res. Atmos.* **2005**, *110* (D11), D11210.

Moteki, N.; Kondo, Y. Effects of Mixing State on Black Carbon Measurements by Laser-Induced Incandescence. *Aerosol Sci. Technol.* **2007**, *41* (4), 398–417.

Murphy, D. M.; Thomson, D. S. Chemical Composition of Single Aerosol Particles at Idaho Hill: Negative Ion Measurements. *J. Geophys. Res. Atmos.* **1997**, *102* (D5), 6353–6368.

Murphy, J. G.; Gregoire, P. K.; Tevlin, A. G.; Wentworth, G. R.; Ellis, R. A.; Markovic, M. Z.; VandenBoer, T. C. Observational Constraints on Particle Acidity Using Measurements and Modelling of Particles and Gases. *Faraday Discuss.* **2017**, *200* (0), 379–395.

Myhre, G.; Shindell, D.; Breon, F.-M.; Collins, W.; Fuglestvedt, J.; Huang, J.; Koch, D.; Lamarque, J.-F.; Lee, D.; Mendoza, B.; et al. Anthropogenic and Natural Radiative Forcing. In *Climate Change 2013: The Physical Science Basis. Contribution of Working Group I to the Fifth Assessment Report of the Intergovernmnetal Panel on Climate Change*; Stocker, T. F., Qin, D., Plattner, G.-K., Tignor, M., Allen, S. K., Boschung, J., Nauels, A., Xia, Y., Bex, V., Midgley, P. M., Eds.; Cambridge University Press: Cambridge, United Kingdom and New York, NY, USA, 2013; pp 659–740.

Nakabayashi, T.; Kosugi, K.; Nishi, N. Liquid Structure of Acetic Acid Studied by Raman Spectroscopy and Ab Initio Molecular Orbital Calculations. *J. Phys. Chem. A* **1999**, *103* (43), 8595–8603.

Nenes, A.; Pandis, S. N.; Pilinis, C. ISORROPIA: A New Thermodynamic Equilibrium Model for Multiphase Multicomponent Inorganic Aerosols. *Aquat. Geochemistry* **1998**, *4* (1), 123–152.

Ng, J. B.; Shurvell, H. F. Application of Factor Analysis and Band Contour Resolution Techniques to the Raman Spectra of Acetic Acid in Aqueous Solution. *J. Phys. Chem.* **1987**, *91* (2), 496–500.

Nie, S.; Emory, S. R. Probing Single Molecules and Single Nanoparticles by Surface-Enhanced Raman Scattering. *Science (80-.).* **1997**, *275* (5303), 1102–1106.

Nishi, N.; Nakabayashi, T.; Kosugi, K. Raman Spectroscopic Study on Acetic Acid Clusters in

Aqueous Solutions: Dominance of Acid−acid Association Producing Microphases. *J. Phys. Chem. A* **1999**, *103* (50), 10851–10858.

Noble, C. A.; Prather, K. A. Real-Time Single Particle Mass Spectrometry: A Historical Review of a Quarter Century of the Chemical Analysis of Aerosols. *MASS Spectrom. Rev.* **2000**, *19* (4), 248–274.

Northcross, A. L.; Jang, M. Heterogeneous SOA Yield from Ozonolysis of Monoterpenes in the Presence of Inorganic Acid. *Atmos. Environ.* **2007**, *41* (7), 1483–1493.

O'Brien, R. E.; Nguyen, T. B.; Laskin, A.; Laskin, J.; Hayes, P. L.; Liu, S.; Jimenez, J. L.; Russell, L. M.; Nizkorodov, S. A.; Goldstein, A. H. Probing Molecular Associations of Field-Collected and Laboratory-Generated SOA with Nano-DESI High-Resolution Mass Spectrometry. *J. Geophys. Res.* **2013**, *118* (2), 1042–1051.

O'Brien, R. E.; Neu, A.; Epstein, S. A.; MacMillan, A. C.; Wang, B. B.; Kelly, S. T.; Nizkorodov, S. A.; Laskin, A.; Moffet, R. C.; Gilles, M. K. Physical Properties of Ambient and Laboratory-Generated Secondary Organic Aerosol. *Geophys. Res. Lett.* **2014**, *41* (12), 4347–4353.

O'Brien, R. E.; Wang, B.; Laskin, A.; Riemer, N.; West, M.; Zhang, Q.; Sun, Y.; Yu, X.-Y.; Alpert, P.; Knopf, D. A.; et al. Chemical Imaging of Ambient Aerosol Particles: Observational Constraints on Mixing State Parameterization. *J. Geophys. Res. Atmos.* **2015a**, *120* (18), 9591–9605.

O'Brien, R. E.; Wang, B.; Kelly, S. T.; Lundt, N.; You, Y.; Bertram, A. K.; Leone, S. R.; Laskin, A.; Gilles, M. K. Liquid–Liquid Phase Separation in Aerosol Particles: Imaging at the Nanometer Scale. *Environ. Sci. Technol.* **2015b**, *49* (8), 4995–5002.

Offenberg, J. H.; Lewandowski, M.; Edney, E. O.; Kleindienst, T. E.; Jaoui, M. Influence of Aerosol Acidity on the Formation of Secondary Organic Aerosol from Biogenic Precursor Hydrocarbons. *Environ. Sci. Technol.* **2009**, *43* (20), 7742–7747.

Ofner, J.; Deckert-Gaudig, T.; Kamilli, K. A.; Held, A.; Lohninger, H.; Deckert, V.; Lendl, B. Tip-Enhanced Raman Spectroscopy of Atmospherically Relevant Aerosol Nanoparticles. *Anal. Chem.* **2016**, *88* (19), 9766–9772.

Okada, K. Number-Size Distribution and Formation Process of Submicrometer Sulfate-Containing Particles in the Urban Atmosphere of Nagoya. *Atmos. Environ.* **1985**, *19* (5), 743–757.

Parsons, M. T.; Knopf, D. A.; Bertram, A. K. Deliquescence and Crystallization of Ammonium Sulfate Particles Internally Mixed with Water-Soluble Organic Compounds. *J. Phys. Chem. A* **2004**, *108* (52), 11600–11608.

Pathak, R. K.; Yao, X. H.; Chan, C. K. Sampling Artifacts of Acidity and Ionic Species in PM2.5. *Environ. Sci. Technol.* **2004**, *38* (1), 254–259.

Pathak, R. K.; Wu, W. S.; Wang, T. Summertime PM2.5 Ionic Species in Four Major Cities of China: Nitrate Formation in an Ammonia-Deficient Atmosphere. *Atmos. Chem. Phys.* **2009**, *9* (5), 1711–1722.

Pathak, R. K.; Wang, T.; Ho, K. F.; Lee, S. C. Characteristics of Summertime PM2.5 Organic and Elemental Carbon in Four Major Chinese Cities: Implications of High Acidity for Water-Soluble Organic Carbon (WSOC). *Atmos. Environ.* **2011**, *45* (2), 318–325.

Perraud, V.; Bruns, E. A.; Ezell, M. J.; Johnson, S. N.; Yu, Y.; Alexander, M. L.; Zelenyuk, A.; Imre, D.; Chang, W. L.; Dabdub, D.; et al. Nonequilibrium Atmospheric Secondary Organic

Aerosol Formation and Growth. *Proc. Natl. Acad. Sci.* **2012**, *109* (8), 2836–2841.

Petzold, A.; Veira, A.; Mund, S.; Esselborn, M.; Kiemle, C.; Weinzierl, B.; Hamburger, T.; Ehret, G.; Lieke, K.; Kandler, K. Mixing of Mineral Dust with Urban Pollution Aerosol over Dakar (Senegal): Impact on Dust Physico-Chemical and Radiative Properties. *Tellus B* **2011**, *63* (4), 619–634.

Pierre, M. C. S.; Mackie, P. M.; Roca, M.; Haes, A. J. Correlating Molecular Surface Coverage and Solution-Phase Nanoparticle Concentration to Surface-Enhanced Raman Scattering Intensities. *J. Phys. Chem. C* **2011**, *115* (38), 18511–18517.

Pimenta, M. A.; Dresselhaus, G.; Dresselhaus, M. S.; Cancado, L. G.; Jorio, A.; Saito, R. Studying Disorder in Graphite-Based Systems by Raman Spectroscopy. *Phys. Chem. Chem. Phys.* **2007**, *9* (11), 1276–1290.

Poehlker, C.; Huffman, J. A.; Pöschl, U. Autofluorescence of Atmospheric Bioaerosols - Fluorescent Biomolecules and Potential Interferences. *Atmos. Meas. Tech.* **2012**, *5* (1), 37–71.

Pope, C. A.; Dockery, D. W. Health Effects of Fine Particulate Air Pollution: Lines That Connect. *J. Air Waste Manage. Assoc.* **2006**, *56* (6), 709–742.

Pöschl, U. Atmospheric Aerosols: Composition, Transformation, Climate and Health Effects. *Angew. Chemie-International Ed.* **2005**, *44* (46), 7520–7540.

Pósfai, M.; Anderson, J. R.; Buseck, P. R.; Shattuck, T. W.; Tindale, N. W. Constituents of a Remote Pacific Marine Aerosol: A Tem Study. *Atmos. Environ.* **1994**, *28* (10), 1747–1756.

Pósfai, M.; Anderson, J. R.; Buseck, P. R.; Sievering, H. Soot and Sulfate Aerosol Particles in the Remote Marine Troposphere. *J. Geophys. Res. Atmos.* **1999**, *104* (D17), 21685–21693.

Pósfai, M.; Simonics, R.; Li, J.; Hobbs, P. V; Buseck, P. R. Individual Aerosol Particles from Biomass Burning in Southern Africa: 1. Compositions and Size Distributions of Carbonaceous Particles. *J. Geophys. Res. Atmos.* **2003**, *108* (D13), n/a-n/a.

Pozzer, A.; Tsimpidi, A. P.; Karydis, V. A.; de Meij, A.; Lelieveld, J. Impact of Agricultural Emission Reductions on Fine-Particulate Matter and Public Health. *Atmos. Chem. Phys.* **2017**, *17* (20), 12813–12826.

Prather, K. A.; Hatch, C. D.; Grassian, V. H. Analysis of Atmospheric Aerosols. *Annu. Rev. Anal. Chem.* **2008**, *1*, 485–514.

Pratt, K. A.; Prather, K. A. Mass Spectrometry of Atmospheric aerosols—Recent Developments and Applications. Part I: Off-Line Mass Spectrometry Techniques. *Mass Spectrom. Rev.* **2012a**, *31* (1), 1–16.

Pratt, K. A.; Prather, K. A. Mass Spectrometry of Atmospheric aerosols—Recent Developments and Applications. Part II: On-Line Mass Spectrometry Techniques. *Mass Spectrom. Rev.* **2012b**, *31* (1), 17–48.

Prenni, A. J.; DeMott, P. J.; Kreidenweis, S. M. Water Uptake of Internally Mixed Particles Containing Ammonium Sulfate and Dicarboxylic Acids. *Atmos. Environ.* **2003**, *37* (30), 4243–4251.

Ramanathan, V.; Crutzen, P. J.; Kiehl, J. T.; Rosenfeld, D. Aerosols, Climate, and the Hydrological Cycle. *Science (80-.).* **2001**, *294*, 2119–2124.

Rapf, R. J.; Dooley, M. R.; Kappes, K.; Perkins, R. J.; Vaida, V. pH Dependence of the Aqueous Photochemistry of α-Keto Acids. *J. Phys. Chem. A* **2017**, *121* (44), 8368–8379.

Ratcliffe, C. I.; Irish, D. E. Vibrational Spectral Studies of Solutions at Elevated Temperatures

and Pressures. VII. Raman Spectra and Dissociation of Nitric Acid. *Can. J. Chem.* **1985**, *63* (12), 3521–3525.

Riemer, N.; West, M. Quantifying Aerosol Mixing State with Entropy and Diversity Measures. *Atmos. Chem. Phys.* **2013**, *13* (22), 11423–11439.

Rindelaub, J. D.; McAvey, K. M.; Shepson, P. B. The Photochemical Production of Organic Nitrates from α-Pinene and Loss via Acid-Dependent Particle Phase Hydrolysis. *Atmos. Environ.* **2015**, *100*, 193–201.

Rindelaub, J. D.; Craig, R. L.; Nandy, L.; Bondy, A. L.; Dutcher, C. S.; Shepson, P. B.; Ault, A. P. Direct Measurement of pH in Individual Particles via Raman Microspectroscopy and Variation in Acidity with Relative Humidity. *J. Phys. Chem. A* **2016a**, *120* (6), 911–917.

Rindelaub, J. D.; Borca, C. H.; Hostetler, M. A.; Slade, J. H.; Lipton, M. A.; Slipchenko, L. V; Shepson, P. B. The Acid-Catalyzed Hydrolysis of an Alpha-Pinene-Derived Organic Nitrate: Kinetics, Products, Reaction Mechanisms, and Atmospheric Impact. *Atmos. Chem. Phys.* **2016b**, *16* (23), 15425–15432.

Riva, M.; Tomaz, S.; Cui, T.; Lin, Y.-H.; Perraudin, E.; Gold, A.; Stone, E. A.; Villenave, E.; Surratt, J. D. Evidence for an Unrecognized Secondary Anthropogenic Source of Organosulfates and Sulfonates: Gas-Phase Oxidation of Polycyclic Aromatic Hydrocarbons in the Presence of Sulfate Aerosol. *Environ. Sci. Technol.* **2015**, *49* (11), 6654–6664.

Riva, M.; Da Silva Barbosa, T.; Lin, Y. H.; Stone, E. A.; Gold, A.; Surratt, J. D. Chemical Characterization of Organosulfates in Secondary Organic Aerosol Derived from the Photooxidation of Alkanes. *Atmos. Chem. Phys.* **2016a**, *16* (17), 11001–11018.

Riva, M.; Budisulistiorini, S. H.; Zhang, Z.; Gold, A.; Surratt, J. D. Chemical Characterization of

Secondary Organic Aerosol Constituents from Isoprene Ozonolysis in the Presence of Acidic Aerosol. *Atmos. Environ.* **2016b**, *130*, 5–13.

Riva, M.; Budisulistiorini, S. H.; Chen, Y.; Zhang, Z.; D'Ambro, E. L.; Zhang, X.; Gold, A.; Turpin, B. J.; Thornton, J. A.; Canagaratna, M. R.; et al. Chemical Characterization of Secondary Organic Aerosol from Oxidation of Isoprene Hydroxyhydroperoxides. *Environ. Sci. Technol.* **2016c**, *50* (18), 9889–9899.

Riva, M.; Bell, D. M.; Hansen, A.-M. K.; Drozd, G. T.; Zhang, Z.; Gold, A.; Imre, D.; Surratt, J. D.; Glasius, M.; Zelenyuk, A. Effect of Organic Coatings, Humidity and Aerosol Acidity on Multiphase Chemistry of Isoprene Epoxydiols. *Environ. Sci. Technol.* **2016d**, *50* (11), 5580–5588.

Ro, C.-U.; Osán, J.; Van Grieken, R. Determination of Low-Z Elements in Individual Environmental Particles Using Windowless EPMA. *Anal. Chem.* **1999**, *71* (8), 1521–1528.

Rosen, H.; Novakov, T. Raman Scattering and the Characterisation of Atmospheric Aerosol Particles. *Nature* **1977**, *266* (5604), 708–710.

Rosen, H.; Hansen, A. D. A.; Gundel, L.; Novakov, T. Identification of the Optically Absorbing Component in Urban Aerosols. *Appl. Opt.* **1978**, *17* (24), 3859–3861.

Rousseau, D. L.; Miller, R. E.; Leroi, G. E. Raman Spectrum of Crystalline Sodium Nitrate. *J. Chem. Phys.* **1968**, *48* (8), 3409.

Le Ru, E. C.; Blackie, E.; Meyer, M.; Etchegoin, P. G. Surface Enhanced Raman Scattering Enhancement Factors: A Comprehensive Study. *J. Phys. Chem. C* **2007**, *111* (37), 13794–13803.

Rudolph, W. W.; Irmer, G.; Konigsberger, E. Speciation Studies in Aqueous HCO3--CO32-

Solutions. A Combined Raman Spectroscopic and Thermodynamic Study. *Dalt. Trans.* **2008**, No. 7, 900–908.

Ruehl, C. R.; Wilson, K. R. Surface Organic Monolayers Control the Hygroscopic Growth of Submicrometer Particles at High Relative Humidity. *J. Phys. Chem. A* **2014**, *118* (22), 3952–3966.

Russell, L. M.; Maria, S. F.; Myneni, S. C. B. Mapping Organic Coatings on Atmospheric Particles. *Geophys. Res. Lett.* **2002**, *29* (16), 24–26.

Russell, L. M.; Bahadur, R.; Hawkins, L. N.; Allan, J.; Baumgardner, D.; Quinn, P. K.; Bates, T. S. Organic Aerosol Characterization by Complementary Measurements of Chemical Bonds and Molecular Fragments. *Atmos. Environ.* **2009**, *43* (38), 6100–6105.

Ryder, O. S.; Ault, A. P.; Cahill, J. F.; Guasco, T. L.; Riedel, T. P.; Cuadra-Rodriguez, L. A.; Gaston, C. J.; Fitzgerald, E.; Lee, C.; Prather, K. A.; et al. On the Role of Particle Inorganic Mixing State in the Reactive Uptake of N2O5 to Ambient Aerosol Particles. *Environ. Sci. Technol.* **2014**, *48* (3), 1618–1627.

Ryder, O. S.; Campbell, N. R.; Morris, H.; Forestieri, S.; Ruppel, M. J.; Cappa, C.; Tivanski, A.; Prather, K.; Bertram, T. H. Role of Organic Coatings in Regulating N2O5 Reactive Uptake to Sea Spray Aerosol. *J. Phys. Chem. A* **2015**, *119* (48), 11683–11692.

Ryu, J.; Ro, C.-U. Attenuated Total Reflectance FT-IR Imaging and Quantitative Energy Dispersive-Electron Probe X-Ray Microanalysis Techniques for Single Particle Analysis of Atmospheric Aerosol Particles. *Anal. Chem.* **2009**, *81* (16), 6695–6707.

Sadezky, A.; Muckenhuber, H.; Grothe, H.; Niessner, R.; Pöschl, U. Raman Microspectroscopy of Soot and Related Carbonaceous Materials: Spectral Analysis and Structural Information.

Carbon N. Y. **2005**, *43* (8), 1731–1742.

Sander, R. Compilation of Henry's Law Constants (Version 4.0) for Water as Solvent. *Atmos. Chem. Phys.* **2015**, *15* (8), 4399–4981.

Saukko, E.; Zorn, S.; Kuwata, M.; Keskinen, J.; Virtanen, A. Phase State and Deliquescence Hysteresis of Ammonium-Sulfate-Seeded Secondary Organic Aerosol. *Aerosol Sci. Technol.* **2015**, *49* (7), 531–537.

Schill, S. R.; Collins, D. B.; Lee, C.; Morris, H. S.; Novak, G. A.; Prather, K. A.; Quinn, P. K.; Sultana, C. M.; Tivanski, A. V; Zimmermann, K.; et al. The Impact of Aerosol Particle Mixing State on the Hygroscopicity of Sea Spray Aerosol. *ACS Cent. Sci.* **2015**, *1* (3), 132–141.

Schlucker, S. Surface-Enhanced Raman Spectroscopy: Concepts and Chemical Applications. *Angew. Chemie-International Ed.* **2014**, *53* (19), 4756–4795.

Schnaiter, M.; Linke, C.; Möhler, O.; Naumann, K. H.; Saathoff, H.; Wagner, R.; Schurath, U.; Wehner, B. Absorption Amplification of Black Carbon Internally Mixed with Secondary Organic Aerosol. *J. Geophys. Res. Atmos.* **2005**, *110* (D19), D19204.

Schwarzmeier, K.; Knauer, M.; Ivleva, N. P.; Niessner, R.; Haisch, C. Bioaerosol Analysis Based on a Label-Free Microarray Readout Method Using Surface-Enhanced Raman Scattering. *Anal. Bioanal. Chem.* **2013**, *405* (16), 5387–5392.

Sears, W. M.; Hunt, J. L.; Stevens, J. R. Raman Scattering from Polymerizing Styrene. I. Vibrational Mode Analysis. *J. Chem. Phys.* **1981**, *75* (4), 1589–1598.

Seinfeld, J. H.; Pandis, S. N. *Atmospheric Chemistry and Physics: From Air Pollution to Climate Change*, Third Edit.; John Wiley & Sons, Inc.: Hoboken, NJ, 2016.

Semeniuk, T. A.; Wise, M. E.; Martin, S. T.; Russell, L. M.; Buseck, P. R. Hygroscopic Behavior of Aerosol Particles from Biomass Fires Using Environmental Transmission Electron Microscopy. *J. Atmos. Chem.* **2007**, *56* (3), 259–273.

Sengupta, A.; Laucks, M. L.; Dildine, N.; Drapala, E.; Davis, E. J. Bioaerosol Characterization of Surface-Enhanced Raman Spectroscopy (SERS). *Aerosol Sci.* **2005**, *36*, 651–664.

Sharma, B.; Frontiera, R. R.; Henry, A.-I.; Ringe, E.; Van Duyne, R. P. SERS: Materials, Applications, and the Future. *Mater. Today* **2012**, *15* (1–2), 16–25.

Sharma, B.; Cardinal, M. F.; Kleinman, S. L.; Greeneltch, N. G.; Frontiera, R. R.; Blaber, M. G.; Schatz, G. C.; Van Duyne, R. P. High-Performance SERS Substrates: Advances and Challenges. *Mrs Bull.* **2013**, *38* (8), 615–624.

Shen, H.; Peters, T. M.; Casuccio, G. S.; Lersch, T. L.; West, R. R.; Kumar, A.; Kumar, N.; Ault, A. P. Elevated Concentrations of Lead in Particulate Matter on the Neighborhood-Scale in Delhi, India As Determined by Single Particle Analysis. *Environ. Sci. Technol.* **2016**, *50* (10), 4961–4970.

Shi, G.; Xu, J.; Peng, X.; Xiao, Z.; Chen, K.; Tian, Y.; Guan, X.; Feng, Y.; Yu, H.; Nenes, A.; et al. pH of Aerosols in a Polluted Atmosphere: Source Contributions to Highly Acidic Aerosol. *Environ. Sci. Technol.* **2017**, *51* (8), 4289–4296.

Shiraiwa, M.; Kondo, Y.; Moteki, N.; Takegawa, N.; Miyazaki, Y.; Blake, D. R. Evolution of Mixing State of Black Carbon in Polluted Air from Tokyo. *Geophys. Res. Lett.* **2007**, *34* (16), L16803.

Shiraiwa, M.; Li, Y.; Tsimpidi, A. P.; Karydis, V. A.; Berkemeier, T.; Pandis, S. N.; Lelieveld, J.; Koop, T.; Pöschl, U. Global Distribution of Particle Phase State in Atmospheric

Secondary Organic Aerosols. *Nat. Commun.* **2017**, *8*, 15002.

Silvern, R. F.; Jacob, D. J.; Kim, P. S.; Marais, E. A.; Turner, J. R.; Campuzano-Jost, P.; Jimenez, J. L. Inconsistency of Ammonium-Sulfate Aerosol Ratios with Thermodynamic Models in the Eastern US: A Possible Role of Organic Aerosol. *Atmos. Chem. Phys.* **2017**, *17* (8), 5107–5118.

Sivaprakasam, V.; Hart, M. B.; Eversole, J. D. Surface Enhanced Raman Spectroscopy of Individual Suspended Aerosol Particles. *J. Phys. Chem. C* **2017**, *121* (40), 22326–22334.

Slade, J. H.; Knopf, D. A. Multiphase OH Oxidation Kinetics of Organic Aerosol: The Role of Particle Phase State and Relative Humidity. *Geophys. Res. Lett.* **2014**, *41* (14), 5297–5306.

Smith, E.; Dent, G. *Modern Raman Spectroscopy: A Practical Approach*; John Wiley & Sons Ltd: West Sussex, England, 2005.

Smith, M. L.; You, Y.; Kuwata, M.; Bertram, A. K.; Martin, S. T. Phase Transitions and Phase Miscibility of Mixed Particles of Ammonium Sulfate, Toluene-Derived Secondary Organic Material, and Water. *J. Phys. Chem. A* **2013**, *117* (36), 8895–8906.

Sobanska, S.; Coeur, C.; Maenhaut, W.; Adams, F. SEM-EDX Characterisation of Tropospheric Aerosols in the Negev Desert (Israel). *J. Atmos. Chem.* **2003**, *44* (3), 299–322.

Sobanska, S.; Hwang, H.; Choel, M.; Jung, H. J.; Eom, H. J.; Kim, H.; Barbillat, J.; Ro, C. U. Investigation of the Chemical Mixing State of Individual Asian Dust Particles by the Combined Use of Electron Probe X-Ray Microanalysis and Raman Microspectrometry. *Anal. Chem.* **2012**, *84* (7), 3145–3154.

Sobanska, S.; Falgayrac, G.; Rimetz-Planchon, J.; Perdrix, E.; Bremard, C.; Barbillat, J. Resolving the Internal Structure of Individual Atmospheric Aerosol Particle by the

Combination of Atomic Force Microscopy, ESEM-EDX, Raman and ToF-SIMS Imaging. *Microchem. J.* **2014**, *114*, 89–98.

Song, C.; Gyawali, M.; Zaveri, R. A.; Shilling, J. E.; Arnott, W. P. Light Absorption by Secondary Organic Aerosol from α-Pinene: Effects of Oxidants, Seed Aerosol Acidity, and Relative Humidity. *J. Geophys. Res. Atmos.* **2013**, *118* (20), 11,741-11,749.

Song, J.; Peng, P. Surface Characterization of Aerosol Particles in Guangzhou, China: A Study by XPS. *Aerosol Sci. Technol.* **2009**, *43* (12), 1230–1242.

Song, X.-H.; Hopke, P. K.; Fergenson, D. P.; Prather, K. A. Classification of Single Particles Analyzed by ATOFMS Using an Artificial Neural Network, ART-2A. *Anal. Chem.* **1999**, *71* (4), 860–865.

Song, Y. C.; Ryu, J.; Malek, M. A.; Jung, H. J.; Ro, C. U. Chemical Speciation of Individual Airborne Particles by the Combined Use of Quantitative Energy-Dispersive Electron Probe X-Ray Microanalysis and Attenuated Total Reflection Fourier Transform-Infrared Imaging Techniques. *Anal. Chem.* **2010**, *82* (19), 7987–7998.

Staudt, S.; Kundu, S.; Lehmler, H. J.; He, X. R.; Cui, T. Q.; Lin, Y. H.; Kristensen, K.; Glasius, M.; Zhang, X. L.; Weber, R. J.; et al. Aromatic Organosulfates in Atmospheric Aerosols: Synthesis, Characterization, and Abundance. *Atmos. Environ.* **2014**, *94*, 366–373.

Stefaniak, E. A.; Buczynska, A.; Novakovic, V.; Kuduk, R.; Grieken, R. Van. Determination of Chemical Composition of Individual Airborne Particles by SEM/EDX and Micro-Raman Spectrometry: A Review. *J. Phys. Conf. Ser.* **2009**, *162* (1), 12019.

Surratt, J. D.; Lewandowski, M.; Offenberg, J. H.; Jaoui, M.; Kleindienst, T. E.; Edney, E. O.; Seinfeld, J. H. Effect of Acidity on Secondary Organic Aerosol Formation from Isoprene.

Environ. Sci. Technol. **2007a**, *41* (15), 5363–5369.

Surratt, J. D.; Kroll, J. H.; Kleindienst, T. E.; Edney, E. O.; Claeys, M.; Sorooshian, A.; Ng, N. L.; Offenberg, J. H.; Lewandowski, M.; Jaoui, M.; et al. Evidence for Organosulfates in Secondary Organic Aerosol. *Environ. Sci. Technol.* **2007b**, *41* (2), 517–527.

Surratt, J. D.; Gomez-Gonzalez, Y.; Chan, A. W. H.; Vermeylen, R.; Shahgholi, M.; Kleindienst, T. E.; Edney, E. O.; Offenberg, J. H.; Lewandowski, M.; Jaoui, M.; et al. Organosulfate Formation in Biogenic Secondary Organic Aerosol. *J. Phys. Chem. A* **2008**, *112* (36), 8345–8378.

Surratt, J. D.; Chan, A. W. H.; Eddingsaas, N. C.; Chan, M. N.; Loza, C. L.; Kwan, A. J.; Hersey, S. P.; Flagan, R. C.; Wennberg, P. O.; Seinfeld, J. H. Reactive Intermediates Revealed in Secondary Organic Aerosol Formation from Isoprene. *Proc. Natl. Acad. Sci. U. S. A.* **2010**, *107* (15), 6640–6645.

Takahama, S.; Gilardoni, S.; Russell, L. M.; Kilcoyne, A. L. D. Classification of Multiple Types of Organic Carbon Composition in Atmospheric Particles by Scanning Transmission X-Ray Microscopy Analysis. *Atmos. Environ.* **2007**, *41* (40), 9435–9451.

Takahama, S.; Johnson, A.; Russell, L. M. Quantification of Carboxylic and Carbonyl Functional Groups in Organic Aerosol Infrared Absorbance Spectra. *Aerosol Sci. Technol.* **2013**, *47* (3), 310–325.

Tan, Y.; Perri, M. J.; Seitzinger, S. P.; Turpin, B. J. Effects of Precursor Concentration and Acidic Sulfate in Aqueous Glyoxal-OH Radical Oxidation and Implications for Secondary Organic Aerosol. *Environ. Sci. Technol.* **2009**, *43* (21), 8105–8112.

Tanner, R. L.; Olszyna, K. J.; Edgerton, E. S.; Knipping, E.; Shaw, S. L. Searching for Evidence

of Acid-Catalyzed Enhancement of Secondary Organic Aerosol Formation Using Ambient Aerosol Data. *Atmos. Environ.* **2009**, *43* (21), 3440–3444.

Trebs, I.; Metzger, S.; Meixner, F. X.; Helas, G.; Hoffer, A.; Rudich, Y.; Falkovich, A. H.; Moura, M. A. L.; da Silva, R. S.; Artaxo, P.; et al. The NH4+-NO3−-Cl−-SO42−-H2O Aerosol System and Its Gas Phase Precursors at a Pasture Site in the Amazon Basin: How Relevant Are Mineral Cations and Soluble Organic Acids? *J. Geophys. Res. - Atmos.* **2005**, *110* (D7).

Utsunomiya, S.; Jensen, K. A.; Keeler, G. J.; Ewing, R. C. Direct Identification of Trace Metals in Fine and Ultrafine Particles in the Detroit Urban Atmosphere. *Environ. Sci. Technol.* **2004**, *38* (8), 2289–2297.

Veghte, D. P.; Altaf, M. B.; Freedman, M. A. Size Dependence of the Structure of Organic Aerosol. *J. Am. Chem. Soc.* **2013**, *135* (43), 16046–16049.

Venkateswarlu, P.; Bist, H. D.; Jain, Y. S. Laser Excited Raman Spectrum of Ammonium Sulfate Single Crystal. *J. Raman Spectrosc.* **1975**, *3* (2–3), 143–151.

Vieira-Filho, M.; Pedrotti, J. J.; Fornaro, A. Water-Soluble Ions Species of Size-Resolved Aerosols: Implications for the Atmospheric Acidity in São Paulo Megacity, Brazil. *Atmos. Res.* **2016**, *181* (Supplement C), 281–287.

de Villepin, J.; Novak, A. Vibrational Spectra of and Isotope Effect in Hydrogen Bonded Potassium Hydrogen Oxalate. *Spectrosc. Lett.* **1971**, *4* (1–2), 1–8.

Virtanen, A.; Joutsensaari, J.; Koop, T.; Kannosto, J.; Yli-Pirila, P.; Leskinen, J.; Makela, J. M.; Holopainen, J. K.; Poeschl, U.; Kulmala, M.; et al. An Amorphous Solid State of Biogenic Secondary Organic Aerosol Particles. *Nature* **2010**, *467* (7317), 824–827.

Virtanen, A.; Kannosto, J.; Kuuluvainen, H.; Arffman, A.; Joutsensaari, J.; Saukko, E.; Hao, L.; Yli-Pirilä, P.; Tiitta, P.; Holopainen, J. K.; et al. Bounce Behavior of Freshly Nucleated Biogenic Secondary Organic Aerosol Particles. *Atmos. Chem. Phys.* **2011**, *11* (16), 8759–8766.

Wang, G.; Zhang, R.; Gomez, M. E.; Yang, L.; Levy Zamora, M.; Hu, M.; Lin, Y.; Peng, J.; Guo, S.; Meng, J.; et al. Persistent Sulfate Formation from London Fog to Chinese Haze. *Proc. Natl. Acad. Sci.* **2016**, *113* (48), 13630–13635.

Wang, J.; Cubison, M. J.; Aiken, A. C.; Jimenez, J. L.; Collins, D. R. The Importance of Aerosol Mixing State and Size-Resolved Composition on CCN Concentration and the Variation of the Importance with Atmospheric Aging of Aerosols. *Atmos. Chem. Phys.* **2010a**, *10* (15), 7267–7283.

Wang, L.; Lal, V.; Khalizov, A. F.; Zhang, R. Heterogeneous Chemistry of Alkylamines with Sulfuric Acid: Implications for Atmospheric Formation of Alkylaminium Sulfates. *Environ. Sci. Technol.* **2010b**, *44* (7), 2461–2465.

Wang, T.; Liu, Z.; Wang, W.; Ge, M. Uptake Kinetics of Three Epoxides into Sulfuric Acid Solution. *Atmos. Environ.* **2012**, *56*, 58–64.

Waterland, M. R.; Stockwell, D.; Kelley, A. M. Symmetry Breaking Effects in NO3−: Raman Spectra of Nitrate Salts and Ab Initio Resonance Raman Spectra of Nitrate–water Complexes. *J. Chem. Phys.* **2001**, *114* (14), 6249–6258.

Weber, R. J.; Guo, H.; Russell, A. G.; Nenes, A. High Aerosol Acidity despite Declining Atmospheric Sulfate Concentrations over the Past 15 Years. *Nat. Geosci.* **2016**, *9* (4), 282–285.

Wexler, A. S.; Clegg, S. L. Atmospheric Aerosol Models for Systems Including the Ions H+, NH4+, Na+, SO42−, NO3−, Cl−, Br−, and H2O. *J. Geophys. Res. - Atmos.* **2002**, *107* (D14), ACH 14-1-ACH 14-14.

Wise, M. E.; Biskos, G.; Martin, S. T.; Russell, L. M.; Buseck, P. R. Phase Transitions of Single Salt Particles Studied Using a Transmission Electron Microscope with an Environmental Cell. *Aerosol Sci. Technol.* **2005**, *39* (9), 849–856.

Witkowski, B.; Gierczak, T. Cis-Pinonic Acid Oxidation by Hydroxyl Radicals in the Aqueous Phase under Acidic and Basic Conditions: Kinetics and Mechanism. *Environ. Sci. Technol.* **2017**.

Wong, J. P. S.; Lee, A. K. Y.; Abbatt, J. P. D. Impacts of Sulfate Seed Acidity and Water Content on Isoprene Secondary Organic Aerosol Formation. *Environ. Sci. Technol.* **2015**, *49* (22), 13215–13221.

Worobiec, A.; Potgieter-Vermaak, S.; Brooker, A.; Darchuk, L.; Stefaniak, E.; Van Grieken, R. Interfaced SEM/EDX and Micro-Raman Spectrometry for Characterisation of Heterogeneous Environmental Particles - Fundamental and Practical Challenges. *Microchem. J.* **2010**, *94* (1), 65–72.

Wren, S. N.; Donaldson, D. J. Glancing-Angle Raman Study of Nitrate and Nitric Acid at the Air–aqueous Interface. *Chem. Phys. Lett.* **2012a**, *522*, 1–10.

Wren, S. N.; Donaldson, D. J. How Does Deposition of Gas Phase Species Affect pH at Frozen Salty Interfaces? *Atmos. Chem. Phys.* **2012b**, *12* (21), 10065–10073.

Wren, S. N.; Donaldson, D. J. Laboratory Study of pH at the Air–ice Interface. *J. Phys. Chem. C* **2012c**, *116* (18), 10171–10180.

Wu, X.; Deng, J.; Chen, J.; Hong, Y.; Xu, L.; Yin, L.; Du, W.; Hong, Z.; Dai, N.; Yuan, C.-S. Characteristics of Water-Soluble Inorganic Components and Acidity of PM2.5 in a Coastal City of China. *Aerosol Air Qual. Res.* **2017**, *17* (9), 2152–2164.

Xu, L.; Guo, H.; Boyd, C. M.; Klein, M.; Bougiatioti, A.; Cerully, K. M.; Hite, J. R.; Isaacman-VanWertz, G.; Kreisberg, N. M.; Knote, C.; et al. Effects of Anthropogenic Emissions on Aerosol Formation from Isoprene and Monoterpenes in the Southeastern United States. *Proc. Natl. Acad. Sci.* **2015**, *112* (1), 37–42.

Xu, L.; Middlebrook, A. M.; Liao, J.; de Gouw, J. A.; Guo, H.; Weber, R. J.; Nenes, A.; Lopez-Hilfiker, F. D.; Lee, B. H.; Thornton, J. A.; et al. Enhanced Formation of Isoprene-Derived Organic Aerosol in Sulfur-Rich Power Plant Plumes during Southeast Nexus. *J. Geophys. Res. Atmos.* **2016**, *121* (18), 11,111-137,153.

Yacovitch, T. I.; Wende, T.; Jiang, L.; Heine, N.; Meijer, G.; Neumark, D. M.; Asmis, K. R. Infrared Spectroscopy of Hydrated Bisulfate Anion Clusters: $HSO_4^-(H_2O)_{1–16}$. *J. Phys. Chem. Lett.* **2011**, *2* (17), 2135–2140.

Yao, X.; Ling, T. Y.; Fang, M.; Chan, C. K. Size Dependence of in Situ pH in Submicron Atmospheric Particles in Hong Kong. *Atmos. Environ.* **2007**, *41* (2), 382–393.

Yeung, M. C.; Chan, C. K. Water Content and Phase Transitions in Particles of Inorganic and Organic Species and Their Mixtures Using Micro-Raman Spectroscopy. *Aerosol Sci. Technol.* **2010**, *44* (4), 269–280.

You, Y.; Bertram, A. K. Effects of Molecular Weight and Temperature on Liquid–liquid Phase Separation in Particles Containing Organic Species and Inorganic Salts. *Atmos. Chem. Phys.* **2015**, *15* (3), 1351–1365.

You, Y.; Renbaum-Wolff, L.; Carreras-Sospedra, M.; Hanna, S. J.; Hiranuma, N.; Kamal, S.; Smith, M. L.; Zhang, X.; Weber, R. J.; Shilling, J. E.; et al. Images Reveal That Atmospheric Particles Can Undergo Liquid–liquid Phase Separations. *Proc. Natl. Acad. Sci. U. S. A.* **2012**, *109* (33), 13188–13193.

You, Y.; Renbaum-Wolff, L.; Bertram, A. K. Liquid–liquid Phase Separation in Particles Containing Organics Mixed with Ammonium Sulfate, Ammonium Bisulfate, Ammonium Nitrate or Sodium Chloride. *Atmos. Chem. Phys.* **2013**, *13* (23), 11723–11734.

You, Y.; Smith, M. L.; Song, M.; Martin, S. T.; Bertram, A. K. Liquid–liquid Phase Separation in Atmospherically Relevant Particles Consisting of Organic Species and Inorganic Salts. *Int. Rev. Phys. Chem.* **2014**, *33* (1), 43–77.

Young, A. H.; Keene, W. C.; Pszenny, A. A. P.; Sander, R.; Thornton, J. A.; Riedel, T. P.; Maben, J. R. Phase Partitioning of Soluble Trace Gases with Size-Resolved Aerosols in near-Surface Continental Air over Northern Colorado, USA, during Winter. *J. Geophys. Res. - Atmos.* **2013**, *118* (16), 9414–9427.

Zhang, H.; Worton, D. R.; Lewandowski, M.; Ortega, J.; Rubitschun, C. L.; Park, J.-H.; Kristensen, K.; Campuzano-Jost, P.; Day, D. A.; Jimenez, J. L.; et al. Organosulfates as Tracers for Secondary Organic Aerosol (SOA) Formation from 2-Methyl-3-Buten-2-Ol (MBO) in the Atmosphere. *Environ. Sci. Technol.* **2012a**, *46* (17), 9437–9446.

Zhang, H.; Lin, Y.-H.; Zhang, Z.; Zhang, X.; Shaw, S. L.; Knipping, E. M.; Weber, R. J.; Gold, A.; Kamens, R. M.; Surratt, J. D. Secondary Organic Aerosol Formation from Methacrolein Photooxidation: Roles of NO*x* Level, Relative Humidity and Aerosol Acidity. *Environ. Chem.* **2012b**, *9* (3), 247–262.

Zhang, H.; Zhang, Z.; Cui, T.; Lin, Y.-H.; Bhathela, N. A.; Ortega, J.; Worton, D. R.; Goldstein, A. H.; Guenther, A.; Jimenez, J. L.; et al. Secondary Organic Aerosol Formation via 2-Methyl-3-Buten-2-Ol Photooxidation: Evidence of Acid-Catalyzed Reactive Uptake of Epoxides. *Environ. Sci. Technol. Lett.* **2014**, *1* (4), 242–247.

Zhang, J.; Li, S.; Wu, J.; Schatz, G. C.; Mirkin, C. A. Plasmon-Mediated Synthesis of Silver Triangular Bipyramids. *Angew. Chemie-International Ed.* **2009**, *48* (42), 7787–7791.

Zhang, Q.; Canagaratna, M. R.; Jayne, J. T.; Worsnop, D. R.; Jimenez, J.-L. Time- and Size-Resolved Chemical Composition of Submicron Particles in Pittsburgh: Implications for Aerosol Sources and Processes. *J. Geophys. Res. Atmos.* **2005**, *110* (D7), D07S09.

Zhang, Q.; Jimenez, J. L.; Worsnop, D. R.; Canagaratna, M. A Case Study of Urban Particle Acidity and Its Influence on Secondary Organic Aerosol. *Environ. Sci. Technol.* **2007a**, *41* (9), 3213–3219.

Zhang, Q.; Jimenez, J. L.; Canagaratna, M. R.; Allan, J. D.; Coe, H.; Ulbrich, I.; Alfarra, M. R.; Takami, A.; Middlebrook, A. M.; Sun, Y. L.; et al. Ubiquity and Dominance of Oxygenated Species in Organic Aerosols in Anthropogenically-Influence Norther Hemisphere Midlatitudes. *Geophys. Res. Lett.* **2007b**, *34*, LI3801.

Zhang, R.; Khalizov, A. F.; Pagels, J.; Zhang, D.; Xue, H.; McMurry, P. H. Variability in Morphology, Hygroscopicity, and Optical Properties of Soot Aerosols during Atmospheric Processing. *Proc. Natl. Acad. Sci. U. S. A.* **2008**, *105* (30), 10291–10296.

Zhang, X.; Zhang, Y.; Li, Q. Ab Initio Studies on the Chain of Contact Ion Pairs of Magnesium Sulfate in Supersaturated State of Aqueous Solution. *J. Mol. Struct. THEOCHEM* **2002**, *594* (1–2), 19–30.

Zhang, Y.; Chen, Y.; Lambe, A. T.; Olson, N. E.; Lei, Z.; Craig, R. L.; Zhang, Z.; Gold, A.; Onasch, T. B.; Jayne, J. T.; et al. Effect of the Aerosol-Phase State on Secondary Organic Aerosol Formation from the Reactive Uptake of Isoprene-Derived Epoxydiols (IEPOX). *Environ. Sci. Technol. Lett.* **2018**, DOI: 10.1021/acs.estlett.8b00044.

Zhang, Y. H.; Chan, C. K. Study of Contact Ion Pairs of Supersaturated Magnesium Sulfate Solutions Using Raman Scattering of Levitated Single Droplets. *J. Phys. Chem. A* **2000**, *104* (40), 9191–9196.

Zhao, L.-J.; Zhang, Y.-H.; Wei, Z.-F.; Cheng, H.; Li, X.-H. Magnesium Sulfate Aerosols Studied by FTIR Spectroscopy: Hygroscopic Properties, Supersaturated Structures, and Implications for Seawater Aerosols. *J. Phys. Chem. A* **2006**, *110* (3), 951–958.

Zhou, Q.; Pang, S.-F.; Wang, Y.; Ma, J.-B.; Zhang, Y.-H. Confocal Raman Studies of the Evolution of the Physical State of Mixed Phthalic Acid/Ammonium Sulfate Aerosol Droplets and the Effect of Substrates. *J. Phys. Chem. B* **2014**, *118* (23), 6198–6205.

Ziemann, P. J.; Atkinson, R. Kinetics, Products, and Mechanisms of Secondary Organic Aerosol Formation. *Chem. Soc. Rev.* **2012**, *41* (19), 6582–6605.